Development and preclinical validation of molecular and nanoparticulate probes for imaging of fibrin

Development and Preclinical Validation of Molecular and Nanoparticulate Probes for Imaging of Fibrin

Financial support by the Dutch Heart Foundation for the publication of this thesis is gratefully acknowledged.

This research was performed within the framework of the Center for Translational Molecular Medicine, project PARISk (grant 01C-202), and was supported by a grant of the Dutch Heart Foundation (DHF-2008-T094).

Support by Philips Research, PerkinElmer and Lipoid GmbH for the printing of this thesis is gratefully acknowledged.

A catalogue record is available from the Eindhoven University of Technology Library

ISBN: 978-90-386-3745-7

Cover design: L.W.E. Starmans

Printed by: Ipskamp Drukkers, the Netherlands

Development and Preclinical Validation of Molecular and Nanoparticulate Probes for Imaging of Fibrin

PROEFSCHRIFT

Ter verkrijging van de graad van doctor aan de Technische Universiteit Eindhoven,
op gezag van de rector magnificus prof.dr.ir. C.J. van Duijn,
voor een commissie aangewezen door het College voor Promoties,
in het openbaar te verdedigen op donderdag 18 december 2014 om 16:00 uur

door

Lucas Wijnand Elisabeth Starmans

geboren te Heerlen

Dit proefschrift is goedgekeurd door de promotoren en de samenstelling van de promotiecommissie is als volgt:

Voorzitter:	prof. dr. P.A.J. Hilbers
1e Promotor:	prof. dr. H. Grüll
Copromotor:	prof. dr. K. Nicolay
Leden:	prof. dr. S. Aime (University of Torino)
	prof. dr. J.W. Bulte (Johns Hopkins University)
	prof. dr. ir. L. Brunsveld
	prof. dr. M.J.A.P. Daemen (UvA-AMC)
	prof. dr. O.C. Boerman (RUN)

Contents

Dedicated to “**Granddad Stramproy”** and **“Grandma Sjömmert”**

Chapter 1

Introduction

This chapter is based on:

Starmans, L. W.; Rossin, R.; Nicolay, K.; Grull, H. Nuclear imaging strategies for visualization of fibrin deposition in disease: a comprehensive review. *In preparation.*

1.1 Formation and structure of fibrin and the role of fibrin in disease processes

Fibrin is an insoluble protein that plays a key role in hemostasis and wound healing.[1] Normally not present in the body, fibrin is formed by thrombin-induced polymerization of its precursor, fibrinogen.[2] Fibrinogen is a 340 kDa soluble glycoprotein that is abundantly present in plasma (1.5 – 4.5 g/L).[3] Fibrinogen comprises two sets of Aα, Bβ and γ-polypeptide chains, which display molecular masses of 66.5, 52 and 46.5 kDa, respectively.[4] The structure of fibrinogen is often portrayed as consisting of two outer D domains, which are each attached by a coil-coil segment to the central E domain (Fig. 1). Thrombin, activated by injury or contact with foreign surfaces, induces fibrin polymerization by cleavage of fibrinopeptides A (FpA) and B (FpB) from the fibrinogen Aα and Bβ-chains, respectively.[2, 4-5] Cleavage of the FpA is faster than for FpB and exposes a binding site in the E-domain (E_A) which is complementary to a binding-pocket in the D-domain (D_A). Binding of the exposed E_A-site to the D_A-binding pocket of neighboring fibrinogen molecules leads to formation of two-stranded protofibrils, initializing fibrin polymerization (Fig. 1). FpB cleavage exposes an additional binding site in the E-domain (E_B) which interacts with a complementary epitope in the D-domain (D_B). In addition, cleavage of FpB is associated with the release of the αC-domain from the central fibrinogen region, making the αC-domains available for intermolecular interactions and thereby contributing to lateral aggregation of the protofibrils into fibrin fibers (Fig. 1). Activated Factor XIII (FXIIIa) subsequently stabilizes the formed network of fibrin fibers by catalyzing transglutaminase reactions that covalently cross-link fibrin γ-chains and α-chains.[6-7] In addition, FXIIIa cross-links α2-antiplasmin into the fibrin network, thereby decreasing the vulnerability of the fibrin network against plasmin-induced fibrinolysis.

Besides its physiological function in hemostasis and wound healing, fibrin deposition plays an important role in several disease processes. Fibrin is a key component of thrombi, which are the root of severe thrombotic disorders such as stroke, myocardial infarction, pulmonary embolism (PE) and deep venous thrombosis (DVT). Fibrin is present in all thrombi, fresh and aged, as well as arterial and venous. For example, fibrin was present in all the thrombi that were obtained in a study investigating patients with acute stroke.[8] In addition to thrombosis, fibrin is of importance in atherosclerosis as deposition of fibrin frequently occurs in atherosclerotic plaques and correlates with plaque progression.[9-10] Fibrin deposition in plaques is associated with plaque erosion, dysfunctional endothelium and presence of intraplaque *vasa vasorum* and hemorrhage.[11-14] Cancer is another disease of interest with respect to fibrin deposition as fibrin is present in a variety of malignant tumor lesions.[15] Intratumoral fibrin deposition induces formation of tumor stroma and protects cancer cells by impeding natural killer cell-mediated elimination.[16-17] In addition, deposition of fibrin provides a scaffold that aids tumor angiogenesis and intratumoral storage of growth factors.[15, 17] For several tumor types, such as small cell lung carcinoma, renal cell carcinoma and malignant melanoma, fibrin formation has been linked to tumor progression and, for these tumor types, therapy with anticoagulants and fibrinolytic activators yielded favorable responses.[18] Finally, deposition of fibrin has been shown to accelerate neurovascular damage and neuroinflammation in mouse models of Alzheimer's disease, implicating fibrin as a potential critical factor in Alzheimer's disease.[19]

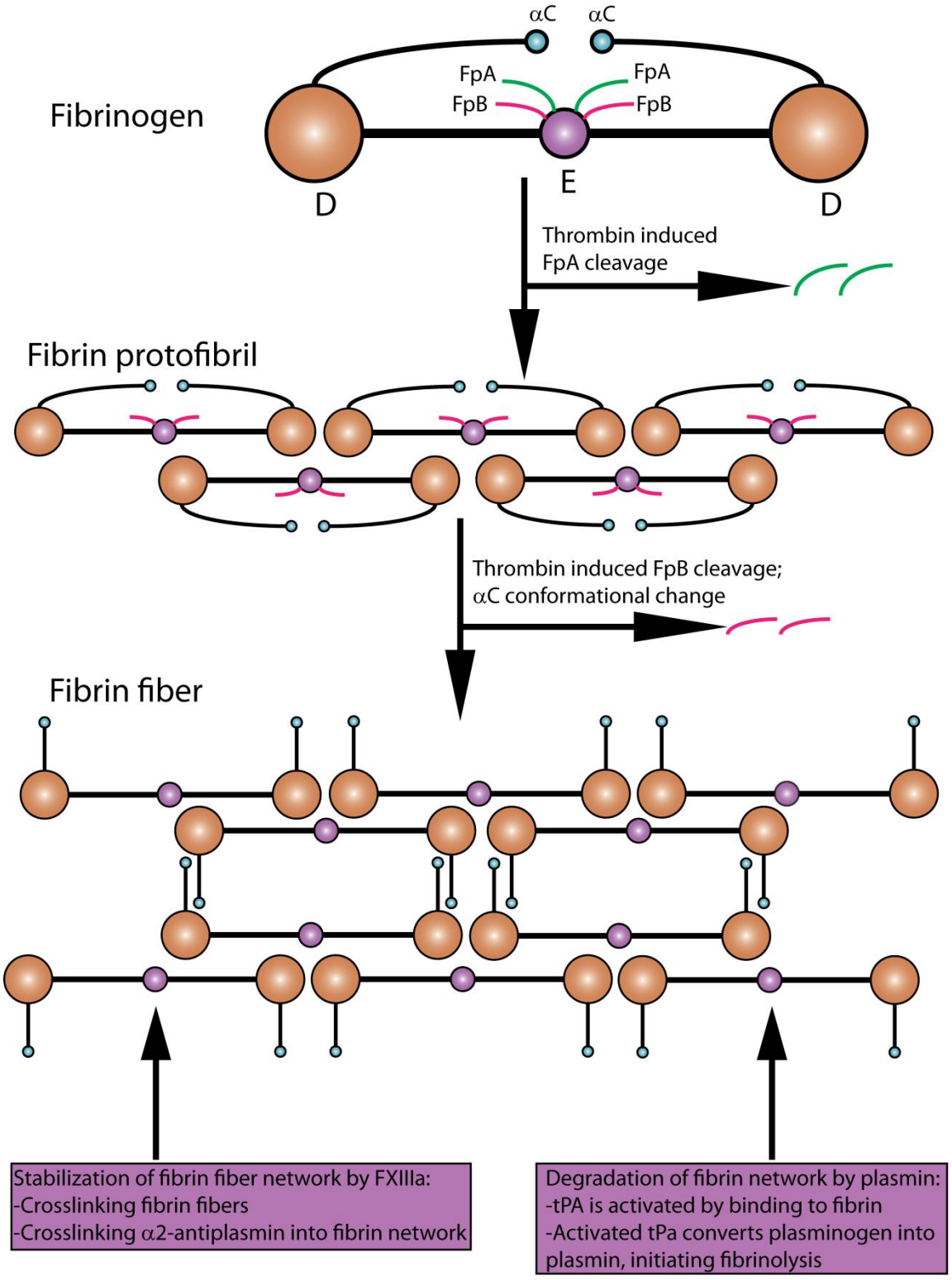

Figure 1. *Schematic representation of fibrinogen and its conversion into a fibrin fiber. First, thrombin cleaves FpA, yielding fibrin protofibrils. Subsequently, FpB is cleaved and this cleavage is associated with a conformational change of the αC-domain, leading to lateral aggregation of protofibrils into fibrin fibers. FpA= fibrinopeptide A; FpB = fibrinopeptide B; FXIIIa = activated factor 13; tPA = tissue-type plasminogen activator. Adapted from La Corte and coworkers with permission of Elsevier.*[20]

1.2 Rationale for nuclear imaging of fibrin deposition

The important role of fibrin deposition in these multiple severe disease processes motivates efforts to develop methodologies to noninvasively localize and quantify pathologic fibrin deposition. Molecular imaging strategies are ideally suited for this task. Molecular imaging can be described as a method to noninvasively visualize and quantify biological processes at the molecular level *in vivo*.[21-22] In general, molecular imaging methodologies require the injection of probes / contrast agents, which are either activated by or targeted to a pathological process of interest. After injection of such a targeted / activatable probe into the subject, the probe will accumulate in the region of interest and yield a physical signal that can be detected by the imaging instrument of choice. For instance, nuclear imaging technologies use probes that are radioactive to detect the presence and localization of the probes, whereas magnetic resonance imaging (MRI) probes should alter the proton magnetization in order to provide contrast on (proton) MR images. To allow molecular imaging of pathological fibrin deposition, probes should bind in a specific fashion to an epitope on the fibrin molecule (Fig. 2). Fibrin is an attractive target for molecular imaging as it is virtually absent in normal tissues and generally expressed in high quantities in diseases. Estimated fibrin concentrations in chronic human thrombi are in excess of 30 μM.[23]

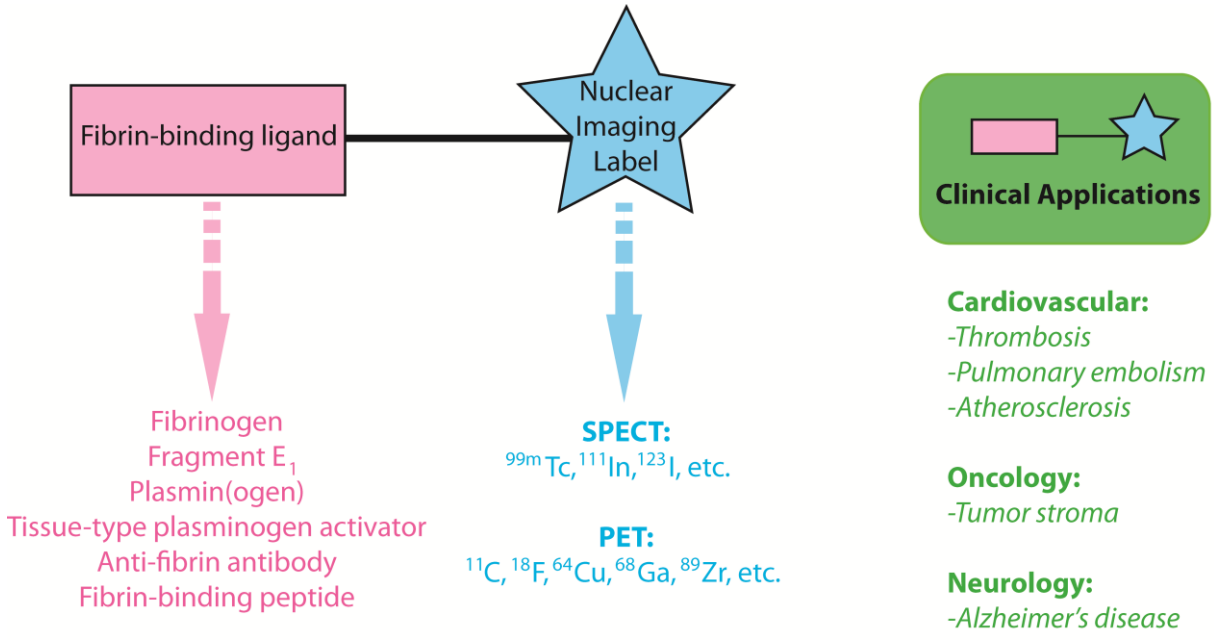

Figure 2. *Schematic representation of a fibrin-specific tracer for nuclear imaging, containing 2 entities: one component (ligand) binding to fibrin and a nuclear label that can be detected by nuclear imaging scanners. Clinical application areas of such fibrin-specific nuclear imaging tracers include cardiovascular, oncological and neurological diseases.*

Potential advantages of fibrin-specific molecular imaging for thrombosis diagnosis include providing the ability of direct whole-body detection of thrombi with high sensitivity, yielding essentially a "one stop shop" methodology. Currently, detection of thrombi and emboli involves a myriad of different imaging

modalities, including coronary angiography, carotid and pelvic ultrasound, transesophageal echocardiography (TEE), ventilation-perfusion lung scanning (V/Q), MRI and CT, each characterized by their own set of strengths and weaknesses.[24-29] Both coronary angiography and TEE are invasive methods, providing a strong drive to develop noninvasive alternatives such as molecular imaging. With respect to atherosclerosis, imaging of fibrin deposition has the potential to yield insights with respect to plaque biology.[30] Such an approach might ultimately yield means to assess plaque vulnerability, i.e. the risk of plaque rupture, which is the main cause of myocardial infarction and stroke. In oncology, fibrin-specific imaging may aid in characterization of tumor lesions, especially with respect to angiogenesis and metastatic potential, two biological hallmarks of cancer.[31] Furthermore, molecular imaging probes that allow visualization of intratumoral fibrin deposition are ideally suited as companion diagnostics for fibrin-targeted cytotoxic immunotherapy, which is currently being investigated as solid tumor therapeutic.[32] Finally, molecular imaging of fibrin deposition might aid in further elucidation of the pathological processes in Alzheimer's disease and in the quest for potential treatments.

The potential of fibrin-specific molecular imaging strategies to yield critical information regarding these cardiovascular, oncologic and neurologic disease processes has spurred the development of numerous fibrin-specific probes over the past half century. Nuclear imaging has been the major modality of choice for development of these probes. For this purpose, radiolabeled proteins of the coagulation system and radiolabeled fibrin-binding antibodies and peptides have been explored. Nuclear imaging entails the detection of gamma rays which are emitted upon the decay of radioactive isotopes and includes single photon emission computed tomography (SPECT) and positron emission tomography (PET). SPECT detects gamma rays which are a direct result of radioactive decay with ^{99m}Tc, ^{111}In and ^{123}I as commonly employed radionuclides. PET tracers emit positrons, which upon annihilation with electrons convert into two 511 keV gamma photons at an angle of essentially 180 degrees, and these photons are subsequently detected by the PET scanner. Frequently employed PET radionuclides are ^{11}C, ^{18}F, ^{64}Cu, ^{68}Ga and ^{89}Zr. SPECT and PET offer quantitative information with high sensitivity and yield hot-spot like images, which are relatively easy to comprehend and analyze. In addition, nuclear imaging requires injection of minute amounts of imaging tracers into patients, and as a consequence, regulatory agencies frequently require less demanding toxicity studies for clinical approval of nuclear imaging tracers compared to contrast agents developed for other imaging modalities. Therefore, translational efforts in the field of nuclear imaging to transfer novel imaging agents from bench to bedside are typically less challenging than for imaging agents developed for other imaging modalities. All in all, nuclear imaging is the prime modality for development of novel molecular imaging probes displaying high clinical translational potential.

This chapter (**Chapter 1**) will review the current armature of nuclear molecular imaging strategies employed to noninvasively visualize fibrin deposition in disease. In addition, this chapter will provide the aim and outline of this thesis.

1.3 Strategies for nuclear imaging of fibrin deposition

1.3.1 Radiolabeled fibrinogen

Fibrinogen is the precursor of fibrin and is incorporated under the action of thrombin into the fibrin polymer matrix as it forms. Radiolabeling of fibrinogen was therefore one of the first strategies employed to enable noninvasive imaging of fibrin deposition *in vivo*. The concept of employing radiolabeled fibrinogen to detect fibrin deposition was pioneered by Hobbs and Davies in 1960, who injected ^{131}I-fibrinogen into rabbits to detect the *in situ* formation of thrombi using an external scintillation counter. They were the first to suggest that such an approach might translate into a valuable clinical test for the detection of DVT.[33] This hypothesis was verified by Nanson and colleagues in a clinical study employing ^{131}I-fibrinogen to detect DVT located in the legs.[34] Fibrinogen radiolabeled with ^{125}I was subsequently introduced as a superior alternative for external scintillation counting of fibrin deposition,[35] as ^{125}I displays a longer half-life, softer gamma radiation and lower total body radiation. The ^{125}I-fibrinogen uptake test (FUT) has successfully been employed for identification of high risk patient populations,[36] and verification of clinically suspected DVT.[37] In addition, the FUT has been instrumental in elucidating the pathological process of DVT,[38] evaluating therapeutic regimens in patients with confirmed DVT,[39-40] and in assessing efficacies of prophylactic therapies for patients at risk for developing DVT.[41-42]

Charkes *et al.* reported the first fibrin imaging experiments in humans using an ^{131}I-fibrinogen scintigraphy strategy in 1974.[43] The advantage of fibrinogen scintigraphy with respect to the FUT is that it is not restricted to the extremities and thus is for instance able to detect DVT in the iliac veins, which are regarded as an important site of PE origin. Fibrinogen scintigraphy was subsequently optimized by DeNardo and coworkers by using ^{123}I-fibrinogen.[44-45] Unlike ^{131}I, ^{123}I decay does not include beta emissions, resulting in lower radiation exposure, and does not display photon emissions of multiple energies, yielding superior spatial resolution. Figure 3 shows typical examples of ^{123}I-fibrinogen scintigraphic images which were obtained for thrombus diagnostic purposes, displaying the potential of ^{123}I-fibrinogen scintigraphy for visualization of fibrin deposition. Although ^{123}I-fibrinogen scintigraphy was used in routine clinical practice for diagnosis of DVT by DeNardo *et al.*,[46] the lack of general availability of ^{123}I-fibrinogen likely explains the limited use of ^{123}I-fibrinogen scintigraphy in the clinical setting.[47] In addition to ^{123}I-labeling of fibrinogen, labeling techniques were developed for other short-lived radioisotopes displaying favorable emission characteristics, such as ^{67}Ga, ^{77}Br and ^{99m}Tc.[48-50]

One of the main disadvantages of employing radiolabeled fibrinogen for imaging of fibrin deposition is the slow clearance of fibrinogen from the circulation. Its half life in blood is approximately 120 h.[51] This results in high levels of background signal stemming from blood vessels, if fibrin imaging is attempted during the first few days post injection (PI) of radiolabeled fibrinogen. In an attempt to resolve this problem, Welch and coworkers prepared heavily iodinated fibrinogen (25 atoms of iodine per molecule), which shows similar clottability with respect to conventionally iodinated fibrinogen (<0.5 atoms of iodine per molecule), but is cleared substantially faster from the circulation and therefore shows higher thrombus to blood ratios at earlier time points after injection.[52] This approach allowed visualization of

femoral vein thrombi in dogs as early as 4 h PI of highly iodinated ^{123}I-fibrinogen.[53] An alternative approach to decrease high blood background signal is to convert radiolabeled fibrinogen, prior to injection, into radiolabeled soluble fibrin, which displays a significantly shorter half life in blood (<10 h).[54] Iodine-131-soluble fibrin was shown to accumulate in coronary artery thrombi in the same extent as conventionally labeled ^{125}I-fibrinogen, whereas the thrombus to blood ratios were more than doubled for soluble fibrin with respect to fibrinogen.[55]

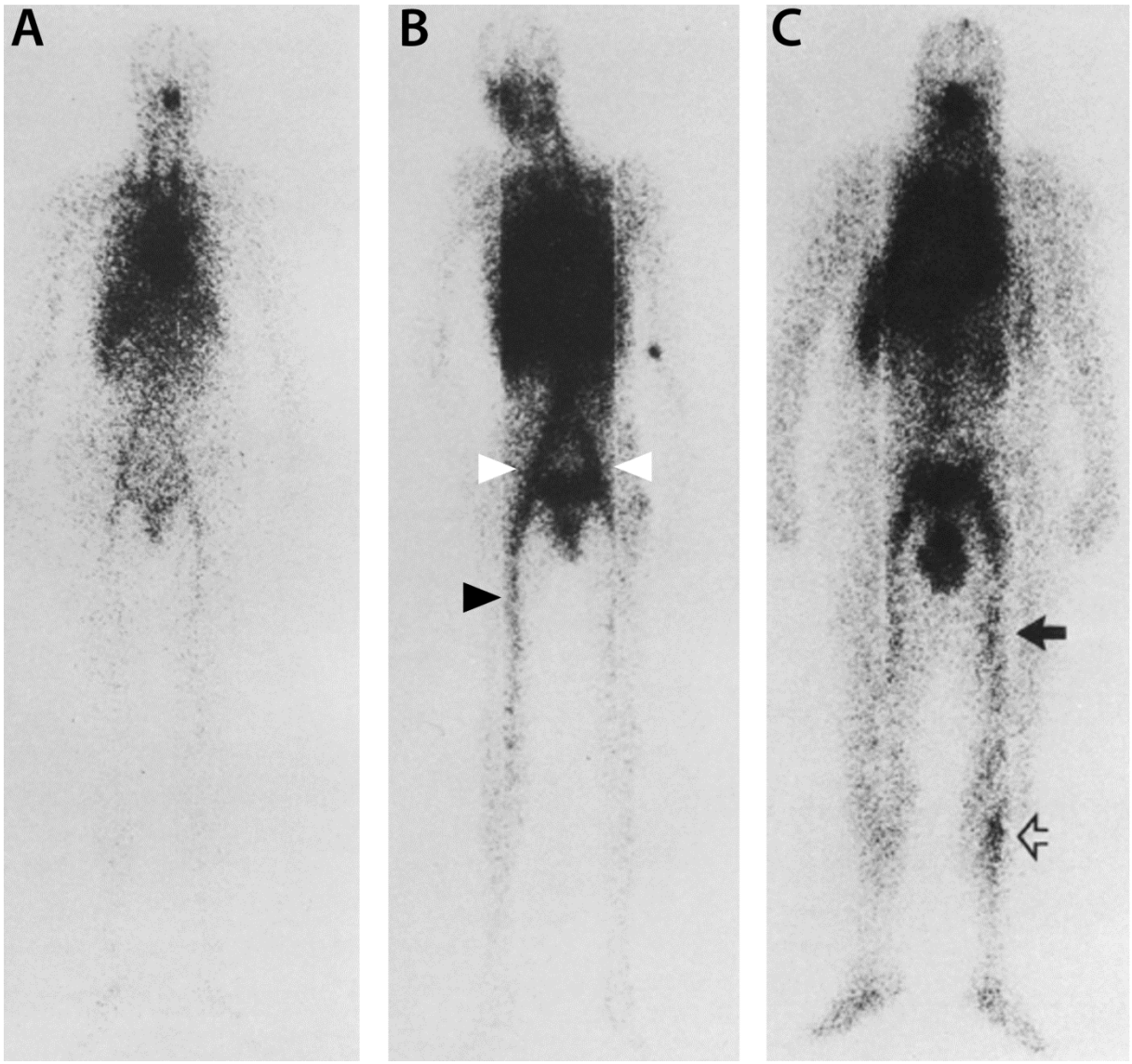

Figure 3. *Scintigraphic imaging using ^{123}I-fibrinogen. (A) Normal pattern of distribution in a patient without thrombosis at 24 hr post injection showing that there is a high level of tracer remaining in the circulation, as well as that there is a significant uptake of the tracer in the paranasal and vaginal area. (B) Thrombophlebitis of both iliac veins (white arrowheads) and right femoropopliteal vein (black arrowhead). (C) Thrombophlebitis of venous system of both lower extremities. Irregular pattern is observed in left femoral vein (black arrow) and in the left calf (open arrow). Reprinted from Denardo et al. with permission from Elsevier.*[46]

Important limitations of fibrinogen scintigraphy and the FUT for detection of thrombosis are: 1) fibrinogen is not taken up avidly by older thrombi,[56] 2) anticoagulants are known to interfere with the incorporation of fibrinogen into the fibrin matrix,[57] and 3) radiolabeled fibrinogen is prepared from blood obtained from donors, and therefore poses a risk of blood borne pathogen transmission.[58] These largely unresolved limitations in combination with the emergence of ultrasound imaging and the D-dimer blood assay for diagnosis of DVT have ultimately led to the abandonment of the FUT and fibrinogen scintigraphy in clinical routine.

Radiolabeled fibrinogen has also been investigated for noninvasive detection of pathological fibrin deposition in conditions other than DVT. Matsuura *et al.* showed that Ga^{67}-dialdehyde starch-deferoxamine-fibrinogen (^{67}Ga-DAS-DFO-fibrinogen) scintigraphy enables detection of bronchogenic carcinoma and also microthrombi in the region of a hepatoma.[59] Mettinger and coworkers investigated the potential of ^{123}I-fibrinogen to detect atherosclerotic plaques located in the carotid artery, and found that there was a significant accumulation of activity in the plaque 4 h PI.[60] This plaque signal subsequently disappeared within 20 h PI, suggesting that perhaps the high activity in the plaque after 4 h might have not necessarily been related to fibrin deposition, but rather due to increased permeability of the intima, resulting in passive accumulation of serum proteins, including fibrinogen.

1.3.2 Radiolabeled Fragment E_1

Fragment E_1 is an enzymatic breakdown product of fibrin and is produced by plasmin digestion of cross-linked fibrin polymers.[61] The molecular weight of Fragment E_1 is 60 kDa and Fragment E_1 contains the N-terminal region of fibrin, including portions of all six chains of the fibrin molecule. Fragment E_1 encompasses the thrombin activated binding sites E_B of the fibrin molecule that are involved in lateral aggregation of fibrin strands.[62] These E_B sites are complementary to D_B binding sites located on the fibrin D-domain, which are activated by the alignment of the D-domains of fibrin monomers upon polymerization. Therefore, Fragment E_1 does bind to fibrin dimers and cross-linked fibrin, but not to fibrinogen of fibrin monomers, and is thus likely suited as imaging agent for detection of fibrin deposition in disease.

Knight and coworkers investigated radiolabeled fragment E_1 as tracer for thrombosis imaging.[63] Fragment E_1 was labeled with ^{131}I and was stable in citrated human plasma for over 4 days.[64] Iodine-131-fragment E_1 was evaluated in a venous thrombosis (VT) pig model with thrombi ranging from 1 h up to 5 days of age. Twenty-four h PI of ^{131}I-fragment E_1, the thrombus to blood ratio was 43 (range 10-108) for 1-6 h old thrombi and 29 (range 8-107) for 1-5 days old thrombi.[64] The biodistribution of ^{131}I-fragment E_1 was investigated in healthy mice and showed rapid blood clearance and liver uptake within minutes PI. Subsequent biodistribution profiles at later time points PI (> 20 min PI) resembled that of free iodide, as radioactivity uptake was high in thyroid gland, stomach, kidneys and urine. Likely, the iodine label was released due to degradation of fragment E_1 in the liver with subsequent redistribution of free $^{131}I^-$.

Techniques were also developed for labeling of Fragment E_1 with ^{111}In and ^{99m}Tc.[65-66] These labeling procedures were performed using the DD(E) complex instead of Fragment E_1 in order to protect the E_B sites from chemical modification. After labeling, the DD(E) complex was dissociated and radiolabeled Fragment E_1 was obtained that had retained its functional activity. In contrast, ^{111}In- and ^{99m}Tc-labeling of Fragment E_1, without shielding the E_B sites using the DD(E) complex, yielded significantly less functional active Fragment E_1. Technetium-99m-Fragment E_1 was evaluated in rabbit and dog VT models.[66] The scintigraphic images allowed thrombus delineation within 20-60 min PI and biodistribution at 4 h PI showed thrombus to blood ratios of 8 and 16 for the rabbit and dog VT model, respectively.

A clinical study investigating the diagnostic accuracy of ^{123}I-labeled Fragment E_1 enrolled 10 patients suspected of DVT.[67] Contrast venography was employed as golden standard, yielding a positive DVT diagnosis for 5 patients. Upon injection of ^{123}I-Fragment E_1 (37 MBq, 75 µg), the radiotracer cleared rapidly from circulation, with a half-life of 20 min in patients diagnosed with DVT and a half-life of 90 min in patients without DVT. The decrease in half-life was attributed to binding of Fragment E_1 to circulating fibrin oligomers, which are present in patients with DVT and are cleared rapidly by the reticuloendothelial system. All 5 patients with confirmed DVT showed focal uptake of Fragment E_1 in scintigraphic images obtained within 30 min PI, whereas the 5 patients without DVT did not show focal hotspots. Figure 4 shows an example of a positive DVT diagnosis on both contrast venography and ^{123}I-Fragment E_1 scintigraphy images in a patient that had undergone a total hip replacement procedure. All patients with confirmed DVT received heparin and it was concluded that the heparin treatment did not affect thrombus binding of Fragment E_1. Images acquired several h PI did not display focal uptake of Fragment E_1 in thrombi anymore. This was likely due to plasmic digestion of Fragment E_1 on the clot surface, resulting in Fragment E_3, which does not bind to fibrin, and thus dissociates from the thrombus. A subsequent clinical study enrolling 20 patients with DVT showed a diagnostic sensitivity of 95% (19/20) for ^{123}I-Fragment E_1 scintigraphy.[68]

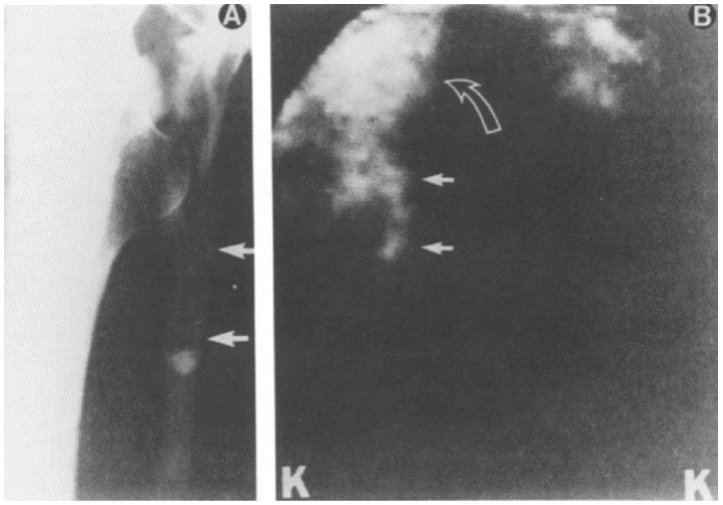

Figure 4. *Thrombus imaging in a patient 5 days post total hip replacement. (A) Radiograph of the right hip using contrast venography, showing intraluminal filling defects (arrows), representing thrombosis. (B) ^{123}I-fragment E_1 scintigraphy performed within 30 min post injection showing diffuse radiotracer uptake around the implanted hip prosthesis (curved arrow) and focal tracer localization corresponding to the thrombus (straight arrow). K indicates the level of the knees. Reprinted from Knight et al. with permission from the publisher.*[67]

Compared to radiolabeled fibrinogen, Fragment E_1 has a faster blood clearance, thus allowing imaging at earlier time points PI, and is better suited for imaging of older thrombi and thrombi in patients undergoing heparin therapy. Radiolabeled Fragment E_1 has the drawback of being vulnerable to plasmic degradation after binding to the thrombus, prohibiting imaging at later time points PI. In addition, similarly to radiolabeled fibrinogen, Fragment E_1 is prepared from blood obtained from donors, and therefore poses a risk to transmit blood borne pathogens.

1.3.3 Radiolabeled plasmin(ogen)

Plasmin is a proteolytic enzyme that plays a key role in fibrinolysis and is formed by activation of plasminogen, its precursor. Plasmin(ogen) is able to bind to fibrin,[69-71] and this was the rationale for an extensive series of preclinical and clinical studies investigating the potential of radiolabeled plasmin(ogen) as tracer for detection of DVT. Ouchi and coworkers injected ^{131}I-plasmin in dogs with femoral vein thrombosis and used a portable gamma spectrometer to detect the blood clots.[72] Subsequently, ^{123}I-plasminogen was employed to allow visualization of venous thrombosis in dogs using scintigraphic imaging.[73]

Studies in human subjects were performed using ^{99m}Tc-labeled plasmin,[74] which was distributed by NOVO Industri A/S (Denmark). Deacon and colleagues were the first to report successful detection of DVT in patients employing the ^{99m}Tc-plasmin test.[75] In their study, 20 patients clinically suspected of DVT were injected with 20 MBq of ^{99m}Tc-plasmin, and the radioactivity at predefined positions of the leg was counted 15-30 min PI using a portable scintillation counter. The results were compared to contrast venography, which was considered the golden standard, yielding a sensitivity of 100% (5/5) and specificity of 80% (12/15) for ^{99m}Tc-plasmin-based DVT detection. Subsequent studies, enrolling larger number of patients suspected of DVT (n=63-394), showed similar sensitivity (91-100%), but lower specificity (33-55%) for the ^{99m}Tc-plasmin test as DVT diagnostic.[76-80] Clinical studies investigating ^{99m}Tc-plasmin scintigraphic imaging, as an alternative of the previously employed radioactivity counting method, yielded comparable sensitivity (93-100%) and specifity (50-83%) in patients with clinically suspected DVT.[81-83] The above studies indicate that ^{99m}Tc-plasmin-based strategies offer high sensitivity, but suffer from a relatively low specificity. Figure 5 displays a typical example of ^{99m}Tc-plasmin scintigraphy in a patient with DVT. The ^{99m}Tc-plasmin test for detection of DVT has been utilized in numerous studies investigating prophylactic regimens for prevention of DVT.[84-88]

Besides the high sensitivity, another advantage of the ^{99m}Tc-plasmin test for detection of DVT is the rapid blood clearance of plasmin, which permits diagnosis within 1 h PI. However, the low specificity of the ^{99m}Tc-plasmin test requires confirmation of DVT diagnosis by a more specific test, such as for instance venography. The rather low specificity should likely be attributed to blood stasis and plasmin accumulation in areas of inflammation.[76] In addition, true positive ^{99m}Tc-plasmin tests were found to mainly reflect haemodynamic changes, which are secondary to DVT, rather than specific binding of ^{99m}Tc-plasmin to the thrombus.[82, 89-91] Thus, a plasmin-based approach does not seem well suited to allow specific imaging of fibrin deposition in disease.

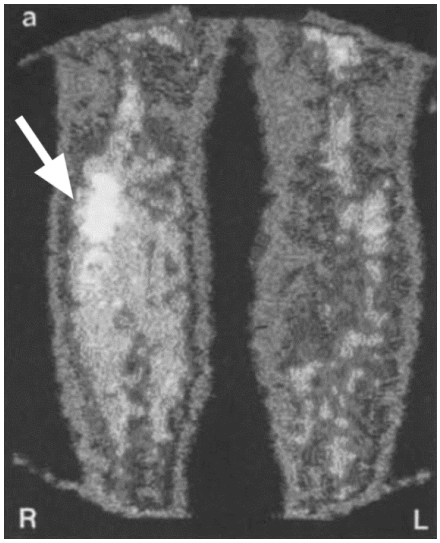

Figure 5. *^{99m}Tc-plasmin scintigraphy of knee and calf region. Right leg (R) knee region signal (arrow) is higher than in corresponding region of the left leg (L), indicating DVT. Reprinted from Dahlborn and coworkers with kind permission from Springer Science and Business Media.*[81]

1.3.4 Radiolabeled tissue-type plasminogen activator (tPA)

tPA is a serine protease that plays an important role in the thrombolytic cascade by converting plasminogen into plasmin.[92] In the absence of fibrin, tPA has a rather low affinity for plasminogen and therefore does not potently convert plasminogen into plasmin. In the presence of fibrin, tPA binds specifically to fibrin, which in turn increases the affinity of tPA towards plasminogen, causing potent plasminogen activation and subsequently thrombolysis.[93] Recombinant-tPA (rtPA) has been extensively investigated as thrombolytic agent and is currently employed in clinical practice for treatment of acute myocardial infarction and ischemic stroke.[94-96]

In addition, rtPA has been evaluated as imaging tracer to allow visualization of fibrin deposition in thrombi. Hnatowich and colleagues labeled rtPA with ^{111}In and showed that in normal mice ^{111}In-rtPA mainly accumulated in liver and kidneys.[97] Furthermore, ^{111}In-rtPA displayed rapid blood clearance ($t_{1/2}$ = 5 min) in dogs and within 1 h PI it allowed scintigraphic detection of fibrin deposited onto a thrombogenic catheter placed in the descending aorta of a dog. In rodent (rat) and feline thrombosis models, scintigraphy with ^{99m}Tc-labeled rtPA successfully visualized thrombi within 30 min PI.[98-101] However, image quality was not optimal due to low absolute uptake of tracer and, as the tracer uptake was transient, positive delineation of thrombi was only possible within 10-20 min PI. Uehara and coworkers investigated ^{131}I-tPA in an de-endothelialization thrombosis rabbit model and found lesion to blood ratios of less than 1.5.[102] Therefore, the investigators concluded that radiolabeled tPA may not be appropriate as tracer for detection of thrombosis.

The fibrinolytic activity of rtPA might be a limiting factor for scintigraphic detection of thrombosis using radiolabeled rtPA, as the clots that bind rtPA will become prone to rtPA induced lysis, effectively removing the imaging target and the bound radiolabeled tracer from the thrombus. The clot accumulation of ^{99m}Tc-rtPA was significantly prolonged after administration of an antifibrinolytic agent (aprotinin), suggesting that fibrinolysis indeed hampered accumulation of tracer in the thrombi.[99] To circumvent this problem associated with the fibrinolytic activity of rtPA for scintigraphic detection of

thrombosis, several investigators studied the use of inactivated-rtPA, which binds to fibrin without causing fibrinolysis.[103-106] Inactivated ^{111}In-rtPA allowed clear visualization of jugular vein thrombosis in rabbits using scintigraphy at 1 h PI, notably also in a subgroup of rabbits that received anticoagulant therapy after thrombus induction.[104] In addition, SPECT imaging using inactivated ^{123}I-rtPA permitted detection of femoral and pulmonary thrombi in dogs.[105-106]

In a clinical phase III trial, 79 patients suspected of DVT were injected with inactivated ^{99m}Tc-rtPA (640 MBq) and scintigraphic images were obtained 4 h PI.[107] Contrast venography was performed as the golden standard. The sensitivity of inactivated ^{99m}Tc-rtPA scintigraphy for detection of DVT was 93% and 86% and the specificity was 92% and 93% for proximal and calf vein thrombosis, respectively. Technetium-99m-labeled rtPA scintigraphy seemed unaffected by heparin therapy in the patients. In a subsequent study, the accuracy of inactivated ^{99m}Tc-rtPA scintigraphy was evaluated for DVT diagnosis in asymptomatic postoperative patients (n=53), using contrast venography as golden standard.[108] Scintigraphic scanning with inactivated ^{99m}Tc-rtPA displayed a sensitivity of 93% and specificity of 91%. In 2007, Brighton and coworkers assessed the aging of thrombi over 30 days in patients with acute DVT (n=74) using inactivated ^{99m}Tc-rtPA scintigraphy.[109] 72% of the thrombi persisting at day 7 and none of the thrombi persisting at day 30 showed ^{99m}Tc-rtPA uptake on the scintigrams. The authors of the study therefore concluded that inactivated ^{99m}Tc-rtPA scintigraphy allows differentiating new from old thrombi and has high sensitivity and specificity for detection of acute DVT in symptomatic and asymptomatic patients. A typical ^{99m}Tc-rtPA scintigraph of normal calves is shown in Figure 6A. Figure 6B-D displays sequential ^{99m}Tc-rtPA scintigraphs of the calves of a patient with confirmed thrombosis at day 1, 7 and 30, illustrating the potential of ^{99m}Tc-rtPA scintigraphy to specifically visualize fresh thrombi. A drawback of employing radiolabeled rtPA for visualization of fibrin deposition is the high liver and spleen uptake, which likely prohibits the use radiolabeled rtPA for imaging of fibrin deposition in these organs and nearby structures.

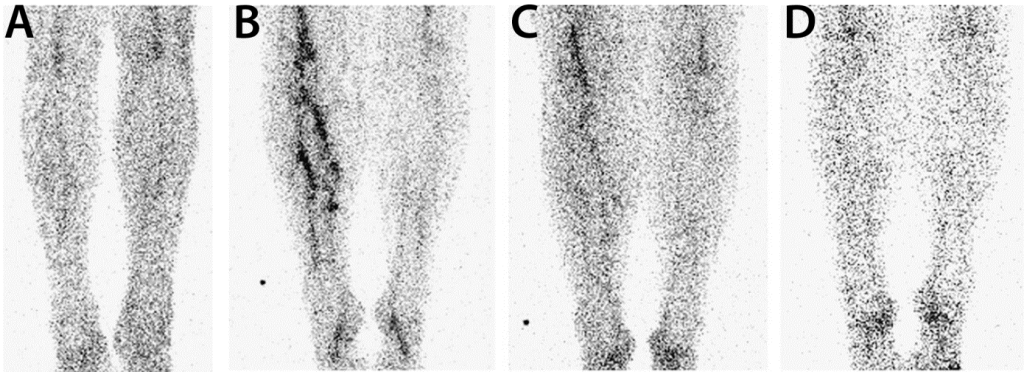

Figure 6. *^{99m}Tc-rtPA scintigraphy of the calve region at 4 h post tracer injection. (A) Normal uptake in calves without thrombosis. (B-D) Sequential images obtained at (B) day 1, (C) day 7 and (D) day 30 in a patient with DVT in the calf. Ultrasound imaging was positive for calf thrombosis up to day 30, whereas ^{99m}Tc-rtPA scintigraphy was only positive on day 1 and day 7, illustrating the potential of ^{99m}Tc-rtPA scintigraphy for specific visualization of fresh thrombi. This research was originally published in JNM.[109] © by the Society of Nuclear Medicine and Molecular Imaging, Inc.*

1.3.5 Radiolabeled polyclonal antibodies against fibrinogen and fibrin

In the 1960's, Spar *et al.* initiated the exploration of ^{131}I-labeled polyclonal antibodies against fibrinogen and fibrin for detection of fibrin deposition in tumors using scintigraphy. Anti-fibrin(ogen) polyclonal antibodies were extracted from serum of rabbits immunized by intravenous injection of the antigen. The anti-fibrinogen antibodies bind to circulating fibrinogen upon injection into the blood stream, and the resulting antibody-fibrinogen complex is subsequently incorporated into forming fibrin clots. In a Murphy-Sturm lymphosarcoma rat model, ^{131}I-labeled antibody against rat fibrinogen was shown to localize significantly in the tumors,[110] and the administration of a therapeutic dose (37-148 MBq) of ^{131}I-labeled antibodies resulted in rapid and permanent tumor regression.[111] Studies in dogs with spontaneous tumors showed preferential ^{131}I-labeled antibody localization in certain types of tumors,[112] most likely due to variations in fibrin content. This suggests that not all tumor types are suited to be diagnosed or treated with antibodies against fibrinogen. In subsequent clinical trials in human patients with various types of tumors, scintigraphy with anti-fibrinogen antibodies allowed detection of 54-75% of all tumors, including mammary carcinomas, malignant melanomas, bronchogenic carcinoma, osteogenic sarcomas, hypernephromas and primary brain tumors.[113-115] Figure 7 displays a ^{131}I-labeled anti-fibrinogen antibody photoscan of a patient with reoccurring brain cancer, showing increased accumulation of the anti-fibrinogen antibody in the tumor. Radioimmunotherapy with anti-fibrinogen ^{131}I-labeled antibodies resulted in a substantial remission of clinical symptoms in a subset of patients showing the highest tumor uptake.[114-115] Besides oncology, ^{131}I-labeled polyclonal antibodies against fibrinogen were successfully employed in dogs for detection of venous and intracardiac thrombosis,[116-117] and in humans for detection of PE, atrial and venous thrombi.[117-119]

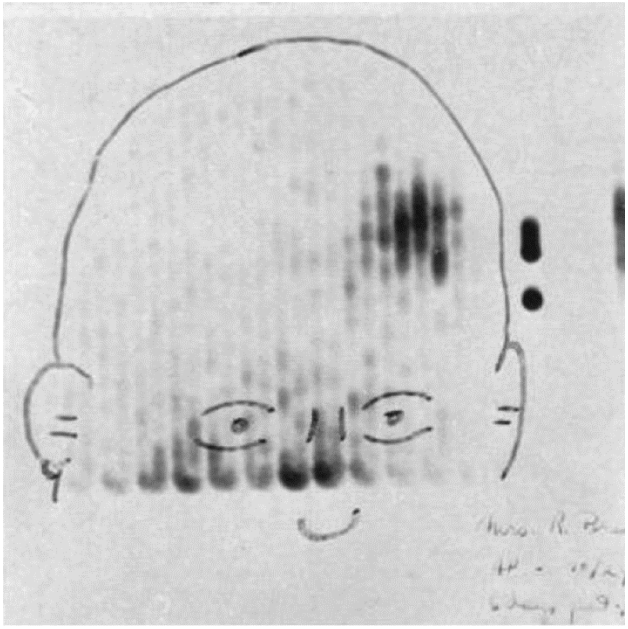

Figure 7. *^{131}I-labeled anti-fibrinogen antibody photoscan of a patient with reoccurring brain cancer (6 days post injection), showing increased accumulation of the anti-fibrin(ogen) antibody in the brain lesion. This research was originally published in JNM.[114] © by the Society of Nuclear Medicine and Molecular Imaging, Inc.*

The antibody-fibrinogen complex has a rather slow clearance from blood, and therefore at least a 24 h delay after injection of the radiolabeled antibodies is usually required to allow delineation of the target from the background activity. Injection of goat antiserum to rabbit globulin to remove circulating ^{131}I-labeled (rabbit) antibody against fibrinogen, successfully decreased background levels of radioactivity.[120] This clearing strategy was subsequently employed in a preclinical study in order to achieve improved thrombus delineation in the obtained scintigrams.[116]

Bosnjakovic and coworkers introduced a ^{131}I-labeled polyclonal antibody which was reactive to fibrin, but not to fibrinogen,[121] and showed that this antibody was capable of detecting DVT in a clinical study.[122] This strategy has the advantage that the antibody binds directly to the fibrin-containing thrombus, instead of binding first to circulating fibrinogen, and thus might be a more suitable option for detection of older thrombi which do not avidly take up fibrinogen.

1.3.6 Radiolabeled monoclonal antibodies (mAbs) against fibrin

A major disadvantage of employing polyclonal antibodies is that the serum obtained from immunized animals contains antibodies that differ in affinity and quantity with respect to the various epitopes on the antigen, and that the specificities of the obtained antibodies may differ dramatically from animal to animal. The development of the hybridoma cell technology in 1975,[123] which allows monoclonal antibody production, overcame the limitations of the polyclonal technique. A considerable number of monoclonal antibodies have been reported that recognize sites on fibrin which are not exposed on fibrinogen (Table 1).

1.3.6.1 Anti-α and anti-β chain N-terminus mAbs

Several antibodies have been developed that specifically recognize the N-terminus of the fibrin α or β chain. These sites are exposed by thrombin-induced cleavage of fibrinopeptides A and B from the fibrinogen molecule, resulting in the formation of fibrin. Scheefers-Borchel *et al.* developed a mAb, designated as Anti-Fbn 17, which specifically binds to the N-terminus of fibrin α chains and therefore might be used to image fibrin deposition in disease.[124] However, fibrin polymerizes spontaneously through binding of the α chain N-terminus to a site on an adjacent fibrin molecule, rendering the α chain N-terminus epitope nonaccessible for antibody binding. Consequently, no *in vivo* diagnostic applications employing specific antibodies against the fibrin α chain N-terminus have been reported.

Multiple antibodies have been raised against the fibrin β chain N-terminus, which remains accessible during the initial stages of fibrin polymerization. Monoclonal antibodies 59D8, 55D10, 64C5 and ZFB076.3 were obtained by immunizing mice with the heptapeptide Gly-His-Arg-Pro-Leu-Asp-Lys,[125-126] which is identical to the sequence of first seven amino acids of human fibrin β chain. T2G1s, a β chain N-terminus specific mAb with binding characteristics similar to 59D8, was developed by immunizing mice with the T(N)-DSK fragment,[127] which is obtained by cleaving fibrinogen using cyanogen bromide and thrombin.

Table 1. *Anti-fibrin monoclonal antibodies for nuclear imaging of fibrin deposition*

Antibody	Epitope Recognized	Dissociation Constant (K_d)	Species specificity	Preclinical Nuclear Imaging Studies	Clinical Studies: Safety and Nuclear Imaging
Anti-Fbn 17	N-terminus of fibrin α chain[124]	NS	Specific: human[124]	-	-
T2G1s	N-terminus of fibrin β chain[127]	Human fibrin, ^{125}I-T2G1s intact, $F(ab')_2$, Fab' and ^{111}In-$F(ab')_2$: 30 nM[131]	Specific: human, dog, rabbit[127-128, 132]	^{131}I- and ^{111}In-T2G1s, $F(ab')_2$ and Fab': VT in dogs[128, 133-136] ^{99m}Tc-T2G1s Fab': VT (dogs and rabbits), arterial thrombosis (AT) (dogs)[129-130, 132]	^{99m}Tc-T2G1s Fab': safety, VT and AT imaging (phase I-III)[137-139]
59D8	N-terminus of fibrin β chain[125]	NS	Specific: human, dog Not specific: chicken, cow, pig, sheep[125, 140]	^{111}In-59D8 Fab': VT (dogs and rabbits) and PE (rabbits)[141] ^{90}Y-59D8 Fab': β-imaging and radioimmunotherapy of ovarian carcinoma in mice[142-143]	^{111}In-59D8 Fab': safety, VT imaging[144-150]
55D10	N-terminus of fibrin β chain[125]	NS	Specific: human[125]	-	-
64C5	N-terminus of fibrin β chain[125]	NS	Specific: human, dog[125, 151] Not specific: chicken[152]	^{111}In-64C5: PE in dogs[151]	-
ZFB076.3	N-terminus of fibrin β chain[126]	Human fibrin monomer, ^{111}In-ZFB076.3: 5 nM[126]	Specific: human, dog[126, 153]	^{111}In-ZFB076.3: VT in dogs[153-155]	-
102-10 mAb	Fibrin β chain amino acids 201-216[156]	NS	Specific: human, mouse, rat[156]	^{89}Zr-102-11 mAb: mouse skin carcinoma[156]	-
DD-3B6/22	Fibrin D-dimer[157]	Human D-dimer, DD-3B6/22 intact and $F(ab')_2$: 0.3 and 1.6 nM, respectively[158]	Specific: human, baboon[157, 159] Not specific: dog, pig, rabbit, rat[158, 160]	^{131}I-DD-3B6/22: VT (human fibrin) in rabbits,[161] human D-dimer beads in rats (subcutaneous) and in rabbits (venous)[158, 160] ^{131}I-DD-3B6/22 $F(ab')_2$: human D-dimer beads in rabbits (venous)[158] ^{111}In-DD-3B6/22: VT (human fibrin) in dogs[155] ^{99m}Tc-DI3B6/22 Fab': VT in baboons,[159] human D-dimer beads in rabbits (venous)[162] ^{99m}Tc-DI3B6/22-80B3 Fab': PE and VT (human fibrin) in dogs[163]	^{99m}Tc-DI3B6/22 Fab': safety, DVT and PE imaging,[164] and 2 tumor imaging case reports[165] ^{99m}Tc-DI3B6/22-80B3 Fab': safety, dosimetry, DVT and PE imaging (phase I-II)[166-170]
DD-1C3/108	Fibrin D-dimer[157]	NS	Specific: human[157] Not specific: rat[160]	^{131}I-DD-1C3/108: subcutaneous human D-dimer beads in rats[160]	-
MA-15C5	Fibrin D-dimer[171]	Human D-dimer, ^{125}I-MA-15C5: 3 nM[171] ^{123}I-MA-15C5 $F(ab')_2$: 1 nM; Fab': 53 nM[172]	Specific: human Not specific: rabbit[171]	^{123}I-MA-15C5 $F(ab')_2$ and Fab': VT in rabbits (human plasma clot)[172]	-

Antibody	Epitope Recognized	Dissociation Constant (K_d)	Species specificity	Preclinical Nuclear Imaging Studies	Clinical Studies: Safety and Nuclear Imaging
TRF1 (F60/43/8)	Fibrin D-dimer[173-174]	Human cross-linked fibrin, TRF1: 0.6 nM[174]	Specific: human, rabbit[174]	^{131}I-TRF1 F(ab')$_2$: VT and AT in rabbits[174]	^{99m}Tc-TRF1 F(ab')$_2$: safety, VT and atherosclerosis[175-176]
GC4	Plasmin digested fibrin(ogen) D region[10]	NS	Specific: human, dog[136]	^{131}I-GC4: VT in dogs[136]	-
Y22	Non cross-linked fibrin D-domain[177-178]	NS	Specific: human, dog, rabbits, rats, sheep Not specific: mouse, pig[178]	^{99m}Tc-Y22: VT (rabbits, rats) and abdominal thrombosis (rabbits)[178-179]	-
MA-8D3	Non cross-linked fibrin D-domain[171]	Human D-dimer, ^{125}I-MA-8D3: 6 nM[171]	Specific: human Not specific: rabbit[171]	-	-
DG1	Non cross-linked fibrin D-domain[180]	Human fibrin, DG1: 1.2 nM[180]	Specific: human Not specific: rat[180]	-	-
TD-1	Cross-link region of fibrin DD/E[181]	Human DD/E, TD-1: 14 nM[181]	Specific: human[181]	-	-
1H10	Fibrin E-region[182]	Human fibrin clot, 1H10: 4 nM[183]	Specific: human, baboon, dog, pig Not specific: rabbit, sheep[184]	-	-
5F3	Fibrin E-region[182]	Human fibrin clot, 5F3: 4 nM[183]	Specific: human, baboon, dog, pig Not specific: rabbit, sheep[184]	-	-
MH-1	Cross-linked fibrin[185]	Cross-linked human fibrin, ^{125}I-MH-1: 0.67 nM[185]	Specific: human, rabbit Not specific: horse, dog, mouse ,rat, baboon, goat [185]	^{99m}Tc-Dextran-MH-1 Fab': VT in rabbits[186]	^{99m}Tc-MH-1 Fab': case report cardiopulmonary thromboembolism [187]
NIBn 123	X-oligomers (plasmin digested, large cross-linked fibrin fragments)[188]	Human X-oligomer, NIBn 123: 1.3 and 0.1 nM[161]	Specific: human[188]	^{131}I-NIBn 123: VT in rabbits (human fibrin)[161]	-
3E6	NS	NS	Specific: dog[189]	^{131}I-3E6: AT in dogs[189]	-
SZ-58	NS	Human cross-linked fibrin, SZ-58: 5 nM[190]	Specific: human, dog, guinea pig, rabbit, sheep[190]	-	-
SZ-63	NS	Human cross-linked fibrin, SZ-63: 4 nM[190]	Specific: human, dog, guinea pig, rabbit, sheep, pig[190-191]	^{99m}Tc-SZ-63: AT and VT in dogs[191]	-

NS= not specified

Rosebrough and coworkers evaluated ^{131}I-labeled T2G1s for scintigraphic imaging in a model of acute VT which was obtained by inserting a thrombogenic coil in the femoral vein of dogs 30 min before tracer injection.[128] As intact antibodies have a long circulation half-life, a 24 h delay was necessary to visualize the thrombotic area. The imaging protocol was subsequently improved by using ^{99m}Tc-T2G1s Fab' fragments, which allowed diagnosis of acute VT and arterial thrombosis (AT) in dogs with a much shorter delay time (2-4 h).[129-130] Indium-111-labeled 59D8 Fab' fragments showed comparable characteristics and diagnostic capabilities with respect to ^{99m}Tc-T2G1s Fab' fragments in an acute VT canine model.[130] Similar absolute thrombus uptake 4 h PI was found for 59D8 and T2G1s Fab', whereas the blood clearance of ^{99m}Tc-T2G1s Fab' was slightly faster, yielding a modest (1.6 fold) increase in thrombus to blood ratio at 4 h PI for T2G1s Fab' with respect to 59D8 Fab´. Both antibody fragments showed similar biodistribution profiles at 4 h PI, which were indicative of renal clearance. Kidney uptake was high for both antibody fragments (0.48 ± 0.06 and 0.35 ± 0.09% ID/g for ^{99m}Tc-T2G1s Fab' and ^{111}In-59D8 Fab', respectively), whereas uptake in other organs such as blood, liver, spleen, lung and muscle was low (<0.06% ID/g).

In addition to thrombosis imaging, 59D8 Fab' has been employed for radioimmunotherapy.[142-143] Intratumoral injections of ca. 20 MBq of ^{90}Y-59D8 Fab' resulted in significantly increased survival time and decreased tumor growth with respect to free ^{90}Y in a subcutaneous mouse model of human ovarian carcinoma. However, the clinical application of radioimmunoconjugates usually involves intravenous administration rather than intratumoral injection. Therefore, preclinical radioimmunotherapy studies employing systemic administration of ^{90}Y-59D8 Fab' should be carried out to more accurately gauge the clinical potential of such a fibrin-targeted radiation therapy strategy.

1.3.6.2 Clinical studies: anti-β chain N-terminus mAbs

A number of clinical studies were performed to investigate the safety and accuracy of thrombosis imaging using ^{99m}Tc-T2G1s Fab' and ^{111}In-59D8 Fab´.[137-139, 144-150] No adverse reactions and no significant increase in human anti-mouse antibody (HAMA) were observed after injection of T2G1s and 59D8 Fab'. A multicenter phase III clinical trial of ^{99m}Tc-T2G1s Fab' enrolled 153 patients suspected of acute DVT.[138] Patients were injected with ca. 0.7 GBq ^{99m}Tc-T2G1s Fab' and imaged at 0, 1.5 and 4-6 h PI using scintigraphy (Fig. 8). Contrast venography was performed as the gold standard to confirm presence of DVT. Figure 8A displays typical ^{99m}Tc-T2G1s Fab' leg scintigraphs of a healthy patient, showing relatively little uptake in both legs. Figure 8B shows ^{99m}Tc-T2G1s Fab' leg scintigraphs obtained from a patient with DVT in the left calf, knee and thigh, displaying high signal in the thrombosed areas. The diagnostic sensitivity of ^{99m}Tc-T2G1s Fab' scintigraphy for proximal DVT was 79% and specificity was 82%. Stratton *et al.* performed a clinical study which enrolled 18 patients with chronic AT (>2 months).[139] Patients were injected with ca. 0.7 GBq ^{99m}Tc-T2G1s Fab' and imaged at 0, 2 and 4-24 h PI. This study showed a relatively low sensitivity of 61%.

The results of six clinical trials regarding the diagnostic performance of ^{111}In-59D8 Fab' in patients with VT are summarized in Table 2. A total of 186 patients, of which most were clinically suspected of DVT,

were enrolled in these studies. All patients were injected with approximately 0.5 mg (75 MBq) ^{111}In-59D8 Fab' and anti-fibrin images were acquired at several time points up to 24 h PI. These images at different time points were subsequently jointly employed for diagnostic purposes. Contrast venography was performed as the golden standard for DVT diagnosis. Combining the six clinical studies, a diagnostic sensitivity of 88% and specificity of 85% was reported for ^{111}In-59D8 Fab'. Imaging at time points beyond 2-4 h PI generally did not improve the diagnostic accuracy. Thus, in comparison to ^{99m}Tc-T2G1s Fab', which displayed 79% sensitivity and 82% specificity, ^{111}In-59D8 Fab´ provided higher diagnostic accuracy for detection of VT.

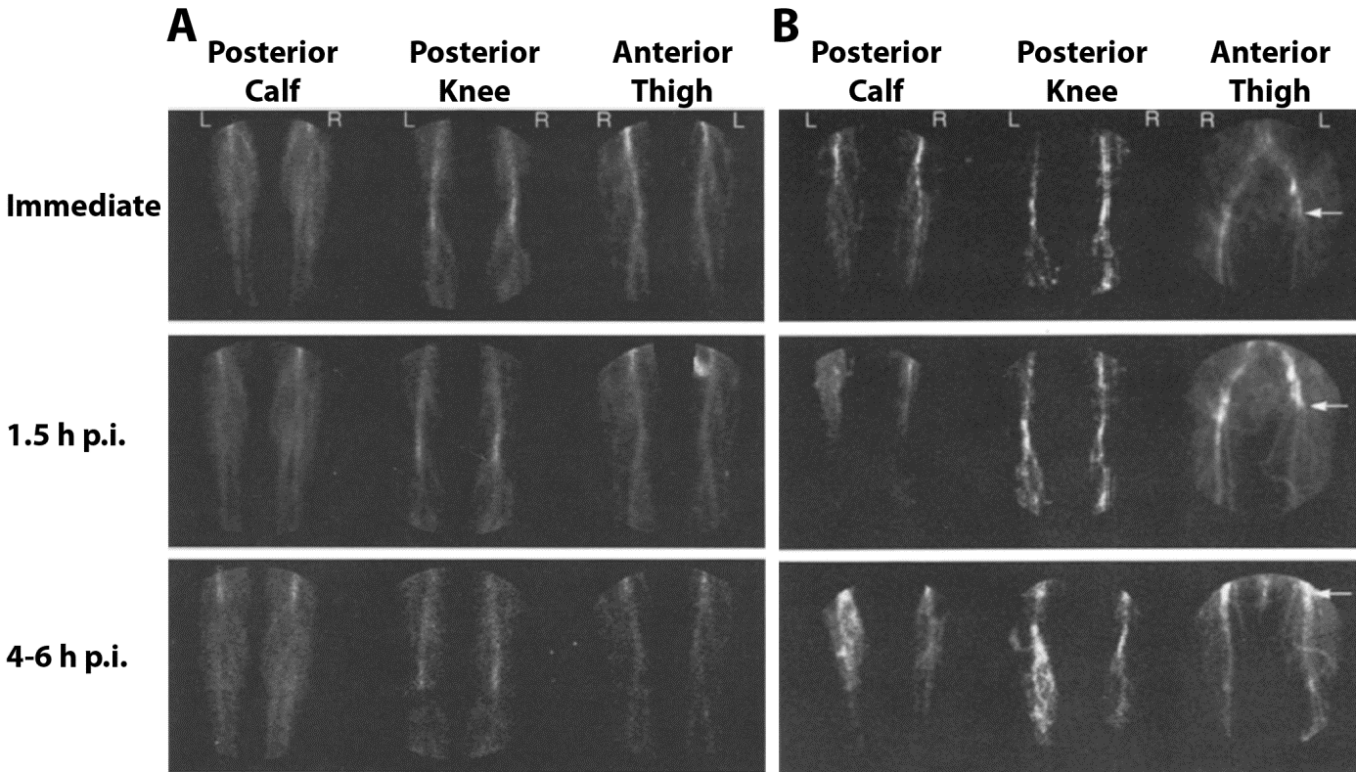

Figure 8. *^{99m}Tc-T2G1s Fab' scintigraphy of the legs immediately, 1.5 h and 4-6 h PI. (A) Low radiotracer uptake in legs without thrombosis. (B) Scintigraphic images of a case evaluated as positive for acute DVT in the left calf, knee and thigh region (white arrow).Reprinted from Manspeaker et al. with permission from Elsevier.*[138]

These clinical trials also showed that parameters such as thrombus age and heparin therapy might influence the diagnostic accuracy of fibrin β chain N-terminus directed mAbs. For instance, Lusiani *et al.* reported that the sensitivity of ^{111}In-59D8 Fab' increased from 78% to 100% by excluding patients who displayed symptoms for longer than 30 days.[149] Similarly, Jung and coworkers showed that the sensitivity increased from 84% to 92% by excluding patients with symptoms for longer than 10 days.[148] A possible explanation for these results is that older thrombi display a more organized structure, which decreases the accessibility of the fibrin β chain N-termini as these N-termini associate to adjacent fibrin polymers via hydrogen bonding during thrombus organization.[126] Thus, only newly formed areas on the

surface of thrombi will have highly accessible fibrin β chain N-termini and consequently, older, non-propagating thrombi will likely display less binding spots for specific mAbs targeting fibrin β chain N-termini. This hypothesis might explain the low sensitivity (61%) observed in an clinical study investigating ^{99m}Tc-T2G1s Fab' for detection of chronic AT (>2 months).[139]

Table 2. *^{111}In-59D8 Fab' clinical studies*

Investigators	**Patient population (number of patients / number of patients receiving heparin)**	**Time delay: injection - imaging**	**% Sensitivity (number of true positive tests / number of patients with thrombosis)**	**% Specificity (number of true negative tests / number of patients without thrombosis)**
Aronen *et al.*[145]	Clinically suspected DVT (14/NS)	1-4 and 20-28 h	100 (7/7)	67 (6/9)
Lusiani *et al.*[149]	Acute DVT (10/8), Chronic DVT (3/3), Superficial VT (5/4), No VT (7/5)	0.5, 3, 6 and 24 h	78 (14/18)	92 (11/12)
Jung *et al.*[148]	Clinically suspected DVT (52/23)	2 h	84 (26/31)	81 (17/21)
Alavi *et al.*[144]	Clinically suspected DVT (33/14)	4-6 and 24 h	97 (28/29)	75 (3/4)
De Faucal *et al.*[146]	Clinically suspected DVT (44/27)	3 and 18 h	85 (29/34)	100 (10/10)
Vorne *et al.*[150]	Clinically suspected DVT (18/6)	2, 4-6 and 20 h	92 (11/12)	100 (6/6)
Overall	-	-	**88 (115/131)**	**85 (53/62)**

NS= not specified

Heparin therapy suppresses thrombus propagation, thus reducing the areas consisting of newly formed fibrin, and prevents the replacement of antigenic sites lost due to endogenous fibrinolysis. Thus, heparinization likely leads to decreased thrombus uptake of anti-fibrin β chain N-terminus mAbs.[138] Morris and coworkers showed that heparin therapy in dogs resulted in significantly decreased sensitivity of an ^{111}In-labeled anti-fibrin β chain N-terminus mAb (ZFB076.3) for detection of acute VT.[153] Clinical studies using anti-fibrin β chain N-terminus mAbs displayed somewhat more ambiguous results with respect to heparin therapy. Alavi *et al.* showed that for thrombi located in the thigh region, the sensitivity of ^{111}In-59D8 Fab' was 100% in patients without heparin therapy, whereas the sensitivity was reduced to 54% in heparinized patients.[144] In contrast, De Faucal[146], Jung[148] and Lusiani,[149] did not

observe negative effects due to heparinization, although it was not excluded that sensitivity could have been higher without heparin therapy. It is likely that heparin treatment decreases anti-fibrin β chain N-terminus mAb uptake in thrombi, but that the actual level of reduction in mAb uptake determines whether sensitivity will be significantly affected.

1.3.6.3 Anti-D-dimer mAbs

During the fibrin polymerization process, D-regions of 2 separate fibrin monomers bind covalently, resulting in formation of D-dimers. These newly formed D-dimers contain epitopes which are not present on fibrinogen and fibrin monomers. Unlike the N-termini of α and β fibrin chains, the D-dimer epitope is exposed on polymerized fibrin regardless of thrombus propagation. Thus, anti-D-dimer mAbs are expected to bind fresh and older thrombi, with and without heparin administration.[192] Consequently, mAbs directed against the D-dimer region might be more apt for diagnosis of VT and PE in comparison with anti-fibrin N-terminus α and β chains mAbs, especially since patients suspected of acute DVT are recommended to receive anticoagulants while awaiting for diagnostic tests.[193]

Anti-D-dimer mAbs MA-15C5, MA-8D3 and TRF were developed by immunizing mice with purified D-dimer fragments.[171, 174] Iodine-123-MA-15C5 $(Fab')_2$ and Fab' fragments showed dissociation constants of 1 and 53 nM, respectively, towards human D-dimer while (intact) TRF displayed a dissociation constant of 0.6 nM towards human cross-linked fibrin.[172, 174] In rabbits, ^{123}I-MA-15C5 $(Fab')_2$ fragments enabled detection of VT within 4 h PI with a sensitivity of 77% and specificity of 87%.[172] Similarly, using scintigraphic imaging ^{131}I-TRF $(Fab')_2$ fragments allowed visualization of rabbit AT and VT.[174] In addition, thrombus uptake of ^{125}I-MA-15C5 and MA-8D3 Fab' fragments in rabbits was found to be independent of heparin treatment and clot age (up to 3 days).[171] In a clinical trial in 16 patients with deep and superficial VT, Ciavolella and coworkers showed 100% sensitivity at 3 h post ^{99m}Tc-TRF $(Fab')_2$ injection, compared with a 86% sensitivity for echo Doppler.[175] Technetium-99m-TRF $(Fab')_2$ was also injected in 8 patients scheduled for a revascularization procedure of the main carotid artery because of the presence of an uncomplicated atherosclerotic lesion.[176] Five out of eight patients showed increased tracer uptake in the plaque and it was speculated by the authors that this tracer might be useful for imaging insoluble fibrin depositions inside atherosclerotic plaques. Unfortunately, an increase in HAMA was observed in 41% (10/24) of patients.[175-176] This immunogenic response might be of major concern as it likely prohibits readministration of the mAb in patients, whereas thrombus imaging may need to be performed repeatedly to assess the course of therapy.

1.3.6.4 DD-3B6/22 anti-D-dimer mAb

Of particular interest is the development of anti-D-dimer mAb DD-3B6/22, which was obtained by immunizing mice with cross-linked fibrin lysate.[157] Intact DD-3B6/22 and the corresponding $F(ab')_2$ displayed dissociation constants of 0.3 and 1.6 nM, respectively, towards human D-Dimer.[158] DD-3B6/22 binds to human and baboon fibrin, but not to fibrin of dogs, pigs, rabbits and rats.[158-159] Iodine-131-labeled DD-3B6/22 intact mAb allowed imaging of human D-dimer coated sepharose beads and venous thrombi containing human fibrin in the jugular vein of rabbits.[158, 161] However, a relatively long

delay of ca. 20 h was required between mAb injection and scintigraphic imaging due to slow blood clearance of ^{131}I-DD-3B6/22 intact mAb. Iodine-131-labeled DD-3B6/22 F(ab')$_2$ fragments cleared faster from the circulation and therefore allowed detection of fibrin deposition in the rabbit jugular vein at an earlier time point (4 h PI).[158] In subsequent studies, DD-3B6/22 Fab' fragments were labeled with ^{99m}Tc. Technetium-99m-labeled DD-3B6/22 Fab' was stable for at least 24 h in an *in vitro* human plasma assay, it cleared rapidly from circulation and allowed imaging of D-dimer coated beads in rabbit jugular veins within 30 min PI.[162, 194] In addition, ^{99m}Tc-DD-3B6/22 Fab' was employed in a baboon model of acute and chronic (up to 29 days) VT.[159] Whole body scintigraphy of baboons showed that ^{99m}Tc-DD-3B6/22 Fab' is rapidly cleared via renal excretion with 40% of the injected dose present in the urine at 3 h PI, while little retention in other organs was observed. Technetium-99m-labeled DD-3B6/22 Fab' allowed imaging of 2.5 and 8 day old venous thrombi in baboons within 3 h PI with a sensitivity of 100% (6/6), whereas scintigraphy of 29 day old venous thrombi showed a decreased sensitivity of 33% (1/3).

To compare the effect of heparin treatment on anti-D-dimer and anti-β chain mAb thrombus uptake, Morris and coworkers injected ^{111}In-DD-3B6/22 intact mAb and anti-β chain ^{111}In-ZFB076.3 intact mAb into heparinized dogs with acute VT.[155] Fibrin imaging was performed up to 24 h PI and the sensitivity of ^{111}In-DD-3B6/22 was 100%, whereas sensitivity of anti-β chain ^{111}In-ZFB076.3 intact mAb was 60%. Thus, anti-D-dimer mAbs seem more suited for detection of VT in subjects undergoing heparin therapy than anti-β chain mAbs. This is likely due to heparin decreasing the number of accessible binding spots for anti-β chain mAbs, while not influencing the D-dimer epitope accessibility.

Safety and diagnostic accuracy of ^{99m}Tc-DD-3B6/22 Fab' were investigated in a clinical trial which enrolled 20 patients with confirmed acute DVT, as diagnosed using contrast venography or venous duplex scanning.[164] Nineteen patients were receiving heparin treatment during the study and 2 patients were also diagnosed with PE by angiography. The patients were injected with 600 MBq (0.5 mg) dose of labeled antibody, planar images of the lower limbs were recorded at 0, 2, 6 and 24 h PI and chest planar images were recorded at 6 and 24 h PI. Sensitivity of ^{99m}Tc-DD-3B6/22 Fab' scintigraphy for diagnosis of DVT was 100% (20/20) using images obtained at 6 h PI. In addition, 1 out of 2 PE was detected using chest scintigraphic images obtained at 6 h PI. A possible drawback of employing anti-D-dimer mAbs for diagnosis of thrombosis is that patients with thrombosis may display elevated plasma levels of D-dimer, possibly interfering with binding of the mAb to the D-dimer epitope present on the thrombus. Five patients had D-dimer plasma levels between 500 and 3000 ng/ml, whereas the normal upper limit is 320 ng/mL.[195] However, no qualitative differences in the images from these 5 patients were observed. These results were in concordance with previous preclinical studies. Baboons with acute VT displayed high D-dimer plasma levels of > 1500 ng/mL without adversely affecting scintigraphy, whereas a study in rabbits showed that plasma levels of D-dimer > 8000 ng/mL were required to inhibit thrombus binding.[159]

In addition to DVT, two of the patients enrolled in the trial had also malignant fibrous histiocytoma and squamous cell carcinoma, respectively, and both tumors were well visualized using ^{99m}Tc-DD-3B6/22

Fab' scintigraphy.[165] Figure 9 shows the ^{99m}Tc-DD-3B6/22 Fab' scintigraphic images obtained from the patient with malignant fibrous histiocytoma, displaying increased tracer uptake in the tumor lesion. One patient enrolled in the study displayed a mildly elevated HAMA response.

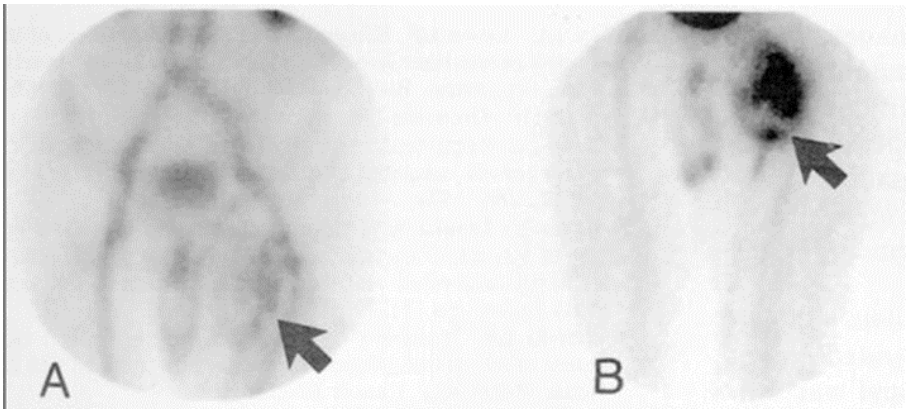

Figure 9. *^{99m}Tc-DD-3B6/22 scintigraphs of the proximal thighs obtained (A) immediately and (B) 6 h PI, displaying increased tracer uptake in a fibrous histiocytoma (arrows). Reprinted from Angelides and coworkers with permission from the publisher.[165]*

A significant obstacle in the development of anti-fibrin mAbs for noninvasive detection of fibrin deposition in patients has been the murine origin of the investigated mAbs, putting patients at risk for anti-mouse immune reactions, especially during repeated administration. A key advance for the field was the deimmunization of DD-3B6/22, with the deimmunized antibody fragment being designated as DD-3B6/22-80B3 (80B3).[192] The deimmunization procedure encompasses modification of potential T cell-stimulating epitopes by amino acid substitutions and subsequent insertion into a vector containing the constant regions of a human IgG1 subclass antibody. SPECT imaging of acute PE and VT in dogs 4 h PI of deimmunized ^{99m}Tc-80B3 Fab' showed a 100% sensitivity for PE and DVT displaying thrombi of mass 0.4 g or greater.[163] It was noted by the authors that SPECT imaging significantly increased the potential for detection of PE with respect to planar scintigraphy, which did not allow detection of PE. This was attributed to the inability of planar imaging to image small hotspots in regions such as the thorax, which contain a large blood pool fraction with accompanying high background signal.

Technetium-99m-labeled 80B3 Fab' (0.5-4 mg, 750 MBq) was injected in 32 healthy volunteers to evaluate the safety, pharmacokinetics and dosimetry.[168] No adverse effects related to mAb injection or human anti-human antibodies (HAHA) were detected. Technetium-99m-labeled 80B3 Fab' displayed a rapid plasma clearance ($t_{1/2,\alpha}$ = 1 h), via the renal pathway, and did not show high uptake in organs, except for kidney. The effective dose was calculated to be 9 mSv per 750 MBq. Thus, ^{99m}Tc-80B3 Fab' showed a favorable pharmacokinetic profile for a tracer that targets an intravascular epitope.

Subsequent phase I and II clinical trials were performed to evaluate the diagnostic performance of ^{99m}Tc-80B3 Fab' for detection of DVT and PE.[166-167, 169-170] Fifty-two patients suspected of acute PE were enrolled in a phase II clinical study to investigate the sensitivity and specificity of ^{99m}Tc-80B3 SPECT.[170] Patients underwent contrast enhanced thoracic CT, considered the golden standard, and thoracic SPECT

2.5 h PI of ^{99m}Tc-80B3 (0.5 mg, ca. 800 MBq). Figure 10 displays a typical example of an obtained thoracic SPECT image in a patient with acute PE, illustrating that ^{99m}Tc-80B3 yields clear embolus delineation. Compared to CT findings, ^{99m}Tc-80B3 SPECT showed 76% (16/21) sensitivity and a 90% (19/21) specificity. Four out of five false negative SPECT studies involved suspected PE in the (sub)segmental pulmonary arteries. However, as thoracic CT scanning is relatively prone to yield false-positive results in (sub)segmental pulmonary arteries, it seems probable that a part of the false-negative SPECT scans actually might have been true-negative.[170] Thus, the actual sensitivity of ^{99m}Tc-80B3 SPECT might be higher than the observed 76%.

A phase II study investigating the diagnostic accuracy of ^{99m}Tc-80B3 planar scintigraphy for DVT detection enrolled 94 patients with suspected DVT.[166] Contrast venography was performed and was considered the gold standard. For proximal DVT, combined analysis of 0.25 and 3 h PI images showed 84% (16/19) sensitivity and 98% (29/30) specificity. The accuracy for distal DVT was lower, and the authors speculated this might be due to lower thrombus burden in this subset of patients or due to the imaging protocol. Early images, considered to be blood pool images, were not completed until 45 min PI. At this point, a significant fraction of the tracer has either bound to its target or has been cleared via the kidneys. Thus, accuracy of analysis that compares early images to late specific tracer uptake images might have been diminished by classifying the signal in the early images as purely blood pool. Future studies should refine the image acquisition and analysis protocol to prevent this particular issue. Technetium-99m-labeled 80B3 Fab' (Thromboview®) is currently in the pipeline of AGEN Biomedical Ltd. as a diagnostic agent for detection of DVT and PE, however phase III clinical trials still have to be performed.

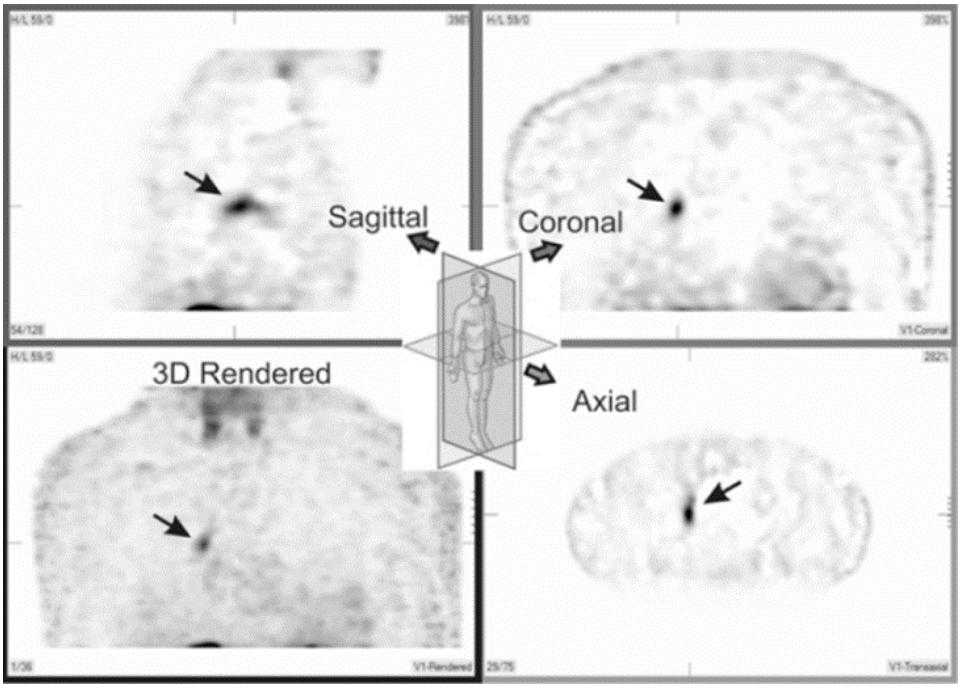

Figure 10. *^{99m}Tc-80B3 SPECT imaging of the thorax region in a patient with acute PE (2.5 h PI), showing focal uptake at the site of the embolus (arrows). Reprinted with permission of the American Thoracic Society.[170] Copyright © 2014 American Thoracic Society.*

1.3.7 Radiolabeled fibrin-binding peptides

Radiolabeled peptides have been investigated extensively as imaging tracers in the field of nuclear imaging.[196-198] Peptides display low immunogenicity and can be produced rather easily and inexpensively. In addition, because of their small size, most peptides are rapidly cleared from circulation and are able to swiftly penetrate tissues, thus allowing imaging procedures that yield more rapid results and higher target to background ratios with respect to, for instance, antibody-based nuclear imaging strategies. Several radiolabeled fibrin-binding peptides have been developed to visualize fibrin deposition in disease using nuclear imaging methods and these strategies will be discussed in the following sections.

1.3.7.1 Fibrin-binding domain (FBD) of fibronectin

Fibronectin is a 440 kDa protein that binds to several extracellular matrix components such as integrins, collagen and fibrin. The fibronectin FBD is situated at the N-terminus and is cross-linked to fibrin via the position 3 glutamine in a transglutaminase reaction under the action of activated factor 13 (FXIIIa). The entire FBD (31 kDa) consists of 259 amino acids which are paired in 10 disulfide bridges, yielding the so called five-finger regions. Using recombinant techniques, three FBD polypeptides have been produced: the entire five-finger FBD and the smaller three-finger (18 kDa) and two-finger region (12 kDa) FBDs.[199] Pharmacokinetic studies in rats using ^{125}I-FBD showed rapid clearance from circulation, with 31 kDa FBD showing a $t_{1/2,\alpha}$ of 30 min and 12 kDa FBD displaying even more swift elimination ($t_{1/2,\alpha}$ = 21 min). The 12 kDa and 31 kDa FBD peptides showed similar clot uptake in a vena cava thrombosis rat model and this uptake was not influenced by the presence of heparin. As 12 kDa FBD showed more rapid clearance with respect to 31 kDa FBD, it was concluded that 12 kDa FBD was the most promising candidate for detection of fibrin deposition. In a jugular vein thrombosis rabbit model, ^{111}In-FBD (12 kDa) showed thrombus to blood ratios of ca. 50 at 24 h PI, thus confirming the potential of FBD-based fibrin visualization.

Indium-111-labeled FBD (12 kDa) was investigated in a clinical trial enrolling 32 healthy control subjects and 30 patients with DVT, as confirmed by duplex ultrasound, contrast venography and/or impedance plethysmography.[200] Images were obtained at 18-24 h post ^{111}In-FBD administration and the sensitivity was found to be 73% (22/30), whereas the specificity was 94% (30/32). The somewhat low sensitivity was likely due to the fact that some patients in the study had clots that were likely more than one week old, whereas FBD binds mainly to fresh thrombi. Subsequent clinical studies employed ^{99m}Tc-labeled 12 kDa FBD. A phase I trial (10 healthy subjects) showed rapid blood clearance with 20% of the activity remaining in circulation after 30 min and less than 2% after 24 h.[197] Urinary excretion was 40% at 24 h. Nonspecific tracer accumulation was highest in kidney and no anti-FBD or anti-fibronectin antibodies were detected. In a phase II clinical trial, 41 patients with acute DVT (5 ± 4 days old) were injected with ^{99m}Tc-FBD (0.5-1 GBq, 20-40 nmol peptide) and imaged by planar scintigraphy at 0.5, 2 and 4-6 h PI.[197] The results were compared to ultrasound imaging and a D-dimer assay and ^{99m}Tc-FBD showed a sensitivity of 80-93%. Figure 11 displays typical examples of ^{99m}Tc-FBD scintigraphs obtained in patients with proven acute DVT of the right lower leg, illustrating the potential of ^{99m}Tc-FBD to visualize DVT.

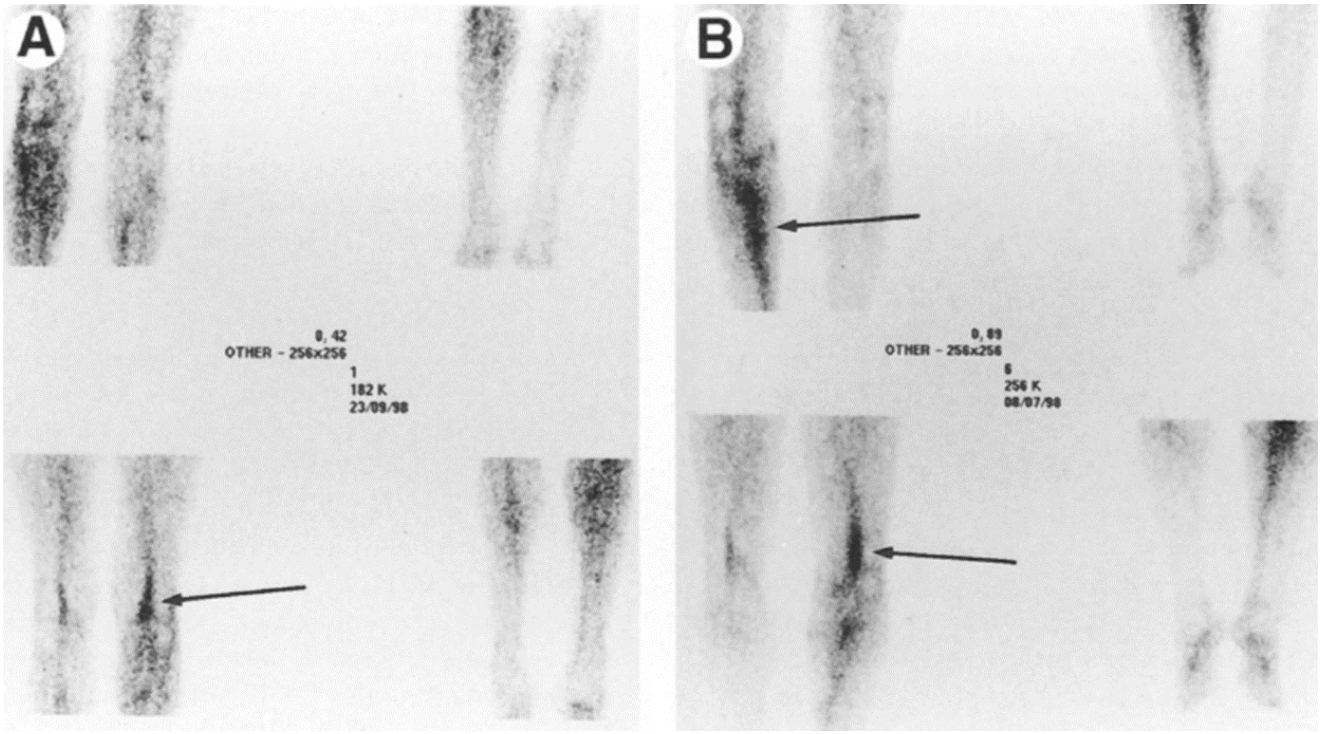

Figure 11. *^{99m}Tc-FBD scintigraphs of 2 patients (A,B) obtained 2 h post injection, showing acute DVT of the right lower leg (arrows). Upper row = anterior view; bottom row = posterior view. Reprinted from Taillefer et al. with permission from Elsevier.[197]*

1.3.7.2 α2-antiplasmin-based peptides

The glycoprotein α2-antiplasmin (α2-AP) is the main physiological inactivator of plasmin and is cross-linked to the α chain of fibrin under the action of FXIIIa.[7] Cross-linked α2-AP retains its full inhibitory activity and makes fibrin markedly resistant to plasmin-induced fibrinolysis.[6] Tung and coworkers pioneered the field of α2-AP-based imaging probes by employing the amino acid sequence N_{13}QEQVSPLTLLK$_{24}$, extracted from the N-terminus of α2-AP, as the functional template to develop a peptidic imaging probe that binds to fibrin under the action of FXIIIa.[201] Optical and MRI α2-AP-based probes were developed by conjugating the amino acid sequence to a dye (Alexa Fluor 680) or paramagnetic label (Gd-DOTA), respectively.

GE Healthcare Bio-Sciences (United Kingdom) subsequently reported on the development of NC100668, a ^{99m}Tc-labeled peptide containing the identical functional amino acid template (NQEQVSPLTLLK), as tracer for FXIIIa-mediated fibrin SPECT imaging in venous thromboembolism.[202-203] In an *in vitro* plasma clot binding study, ^{99m}Tc-NC100668 displayed significantly more thrombus uptake with respect to a negative control peptide and dansyl cadaverine, which is a known substrate of FXIIIa.[204] In addition, ^{99m}Tc-NC100668 was shown to be specific for plasma clots of rat, rabbit, dog and human origin. *In vivo* biodistribution studies in rats bearing 1 h old inferior vena cava thrombi showed rapid blood clearance, renal excretion and thrombus to blood and thrombus to muscle ratios of 9 and 31, respectively, at 1 h PI.[204] Additional studies in rats bearing vena cava thrombi showed that thrombus age (tested up to 4 h)

and heparin and thrombin inhibitor-based anticoagulation therapy did not influence ^{99m}Tc-NC100668 thrombus uptake, whereas tPA-based anticoagulation therapy decreased ^{99m}Tc-NC100668 uptake in clots by a factor of 3.[205] Studies in rats showed rapid radiotracer metabolism, with the major radio-metabolite being the ^{99m}Tc-chelate complex attached to glycine,[202, 206] which is unable to bind to fibrin. A phase I single ascending dose study in healthy volunteers showed rapid tracer clearance from circulation ($t_{1/2,\alpha}$ = 12 min), and the major metabolite in urine was identical to the major metabolite in rats.[207] Although the biodistribution results were promising, neither preclinical nor clinical imaging studies employing ^{99m}Tc-NC100668 have been reported. Hence, additional studies are required to properly gauge the potential of ^{99m}Tc-NC100668 to visualize pathological fibrin deposition.

Nahrendorf and colleagues developed ^{111}In- and ^{18}F-labeled versions of the NQEQVSPLTLLK-based probe to investigate the role of FXIIIa in myocardial healing in mice using SPECT and PET imaging, respectively.[208-210] FXIIIa was found to be critically important in murine myocardial healing, as FXIII-deficient mice all died within 5 days after myocardial infarction due to left ventricular rupture. In light of this review, which focuses on specific imaging of fibrin deposition, it is important to note that the authors of this study employed the ^{111}In- and ^{18}F-labeled α2-AP based probes to visualize cross-linking of extracellular matrix proteins, such as collagen, rather than fibrin deposition. Indeed, FXIIIa is also known to crosslink matrix proteins.[6] It is therefore important to recognize that both the α2-AP-based and the FBD-based tracers might not entirely be specific for fibrin imaging, but rather for FXIIIa-activity in a range of biological processes.

1.3.7.3 Fibrin-binding peptide TP850

During the clotting cascade, thrombin cleaves off fibrinopeptide A and B from the N-termini of the α and β fibrinogen chains, thereby exposing new amino acid sequences at the α and β chain N-termini. These newly exposed α chain N-termini bind subsequently to pre-existing binding pockets on the γ chain C-termini, inducing fibrin polymerization.[4] Thakur and coworkers developed the ^{99m}Tc-labeled fibrin-binding peptide TP850 (GPRPP-Aba-GG-[D]Ala-G),[211] which contains a ^{99m}Tc-chelating moiety (GG-[D]Ala-G) and a fibrin-binding sequence (GPRPP), which resembles the fibrinogen α chain N-terminus after thrombin cleavage (GPRV) and thus is able to bind to the γ-chain C-terminus of fibrinogen and fibrin.

In vitro fibrin-binding studies showed that TP850 binds to two sites per fibrin molecule and that it is able to bind to dog, rabbit and human derived fibrin.[211-212] Pharmacokinetic and biodistribution studies in healthy rabbits showed fast blood clearance ($t_{1/2,\alpha}$ = 4 min [20%]; $t_{1/2,\beta}$ = 13 min [80%]) and renal excretion, suggesting minimal binding of the tracer towards circulating fibrinogen. In rabbits having either acute jugular vein DVT or 24 h old PE, ^{99m}Tc-TP850 scintigraphy allowed delineation of all thrombi at 1.5-2 h PI, even though clot uptake (0.01-0.09% ID/g) and thrombus to blood ratios (1-12) were modest.[211] In subsequent studies in swine with acute and aged (up to 5 days) DVT and PE, ^{99m}Tc-TP850 scintigraphy visualized thrombi within 2 h PI (Fig. 12). However, thrombi that had fragmented into smaller pieces during the aging process were not detectable *in vivo*, and this was attributed to the small

size of the clots with respect to the resolution of the γ-camera. A wide range of thrombus to blood ratios was observed (0.4 – 155; 4 h PI).[212]

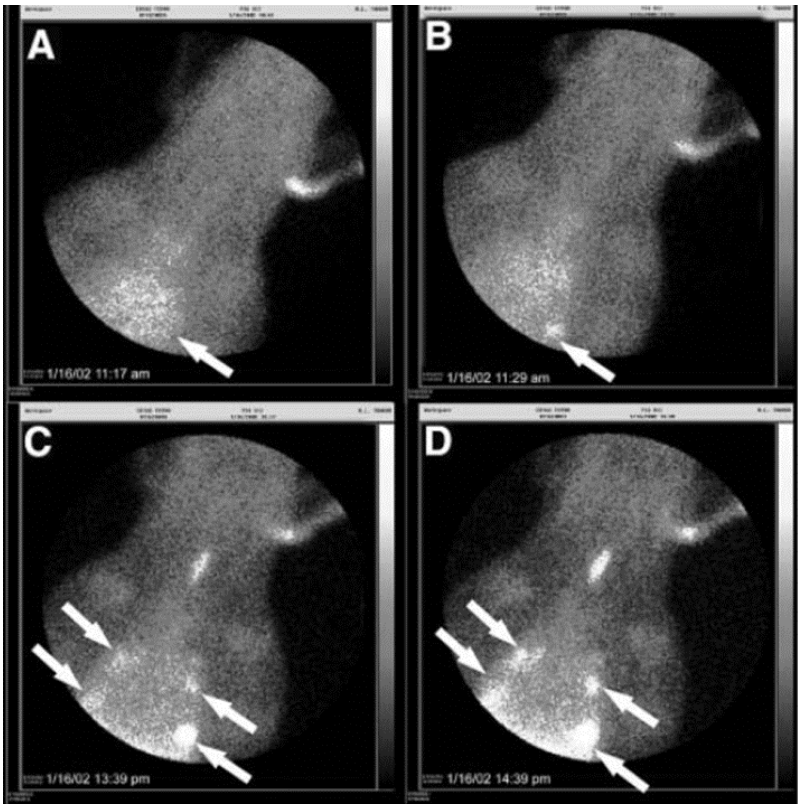

Figure 12. *Sequential ^{99m}Tc-TP850 scintigraphs of a swine with 1 day old pulmonary emboli. Images were obtained at (A) 45 min, (B) 1 h, (C) 3 h and (D) 4 h PI of ^{99m}Tc-TP850. Arrows indicate hotspots corresponding to the emboli. The other hotspots are the site of injection (ear) and the site of esophageal injury (due to ventilation tubing). These images illustrate that ^{99m}Tc-TP850-based delineation of emboli increased over time. This research was originally published in JNM.[212] © by the Society of Nuclear Medicine and Molecular Imaging, Inc.*

1.3.7.4 EP-2104R-based radiolabeled fibrin-binding peptides

EP-2104R (Fig. 13A) is a fibrin-specific, gadolinium-based peptidic MRI contrast agent developed by Epix Pharmaceuticals. The peptide contains a fibrin-binding, cyclic amino acid backbone (Y-dGlu-C-Hyp-3ClY-GLCYIQ), which was identified using phage display against human fibrin and further optimized for fibrin-binding purposes.[213] The fibrin-binding peptide sequence is conjugated on both the N-terminus and the C-terminus with 2 Gd-DOTA moieties to provide MRI contrast. EP-2104R displays binding to fibrin with a dissociation constant (K_d) of ca. 1 µM and has been extensively investigated for MRI visualization of fibrin deposition in preclinical models of thrombosis, atherosclerosis and cancer.[214-219] Furthermore, EP-2104R has been successfully employed in a phase II clinical study for MRI detection of arterial and venous thrombosis.[220-221] Figure 13B-C shows an example of EP-2104R-based molecular MR imaging of fibrin deposition in a patient with left ventricular thrombosis, displaying significant MR signal increase in the thrombus post-contrast injection.

More recently, Caravan and coworkers introduced the EP-2104R fibrin-binding peptide platform into the field of nuclear imaging. Their initial efforts encompassed construction of a bimodal fibrin-binding peptide for PET/MR imaging by partial removal of Gd from the DOTA-moieties of the EP-2104R peptide.

The “empty” DOTA-chelators (ca. 5% of all DOTA-moieties) were subsequently employed to radiolabel the peptide with ^{64}Cu, yielding a Gd and ^{64}Cu-labeled fibrin-binding peptide for PET/MR imaging of fibrin deposition.[222] In an elegant preclinical study, the ^{64}Cu and Gd-labeled EP-2104R peptide was shown to enable truly simultaneous MRI and PET visualization of a preformed carotid artery thrombus in rats within 1.5 h PI. Thrombus to contralateral carotid artery signal ratio was 1.9 ± 0.5 for PET imaging at 30-90 min PI and 1.7 ± 0.4 for MR images acquired at 10 min PI. Biodistribution (2 h PI) showed accumulation of Gd and ^{64}Cu in the thrombus and kidney, and low uptake in other organs, with exception of the liver, which showed significant accumulation of ^{64}Cu (1.1 ± 0.3% ID/g), but not of Gd (0.0 ± 0.0% ID/g). These data suggest that ^{64}Cu is released from the DOTA-chelator,[223] and subsequently is bound by liver proteins such as superoxide dismutase.[224]

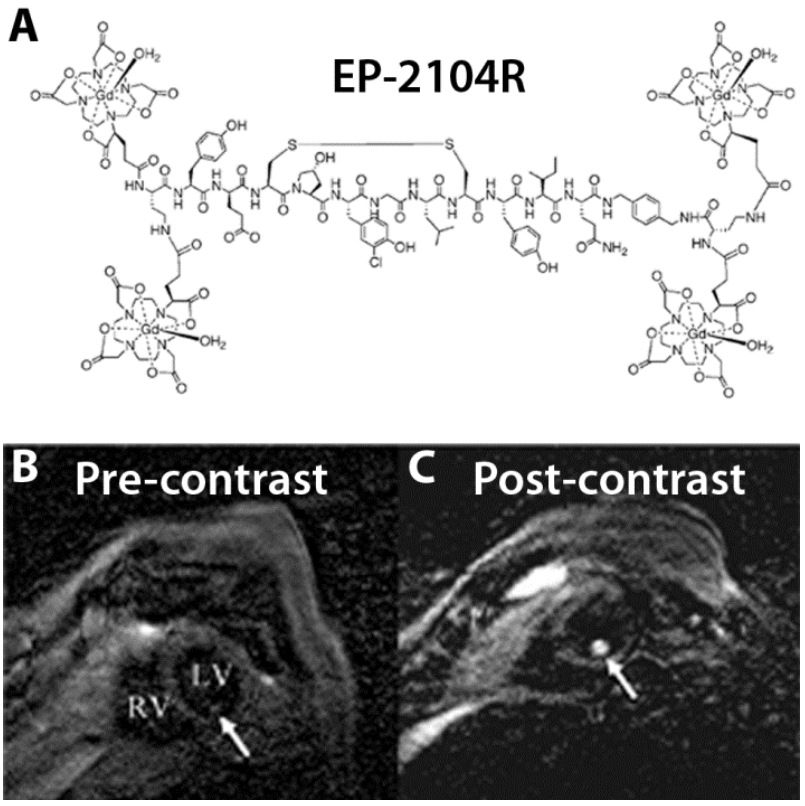

Figure 13. *(A) Structural formula of the fibrin-binding peptidic MRI contrast agent EP-2104R.Reprinted from Overoye-Chan and coworkers with permission from the American Chemical Society.[213] Copyright 2008 American Chemical Society. (B-C) Molecular MR imaging of fibrin deposition in a patient with left ventricular thrombus, displaying significant signal increase in the thrombus (arrows) post-contrast injection (2-6 h PI). LV = left ventricle; RV= right ventricle. Reprinted from Spuentrup et al. with kind permission from Springer Science and Business Media.[221]*

Subsequent studies focused on the synthesis and preclinical evaluation of monomodal, ^{64}Cu-labeled EP-2104R-like peptides for PET imaging of fibrin deposition. Ciesienski and coworkers developed three simplified versions of the EP-2104R peptide, designated as FBP1, FBP2 and FBP3.[225] These three peptides contain a fibrin-binding amino acid sequence similar (FBP1) or closely related to EP-2104R (FBP2-3) and a DOTA-moiety attached to both the N- and C-terminus of the peptide. The FBPs were radiolabeled with ^{64}Cu and subsequently injected in rats with acute carotid artery thrombosis. PET imaging of FBP1 and FBP2 showed marked PET signal in the thrombus area, illustrating the potential of FBP1 and FBP2 for PET imaging of fibrin deposition in disease. Biodistribution results at 2 h PI displayed

a moderate thrombus to blood ratio of 3 for both FBP1 and FBP2 and a low thrombus to blood ratio of 1 for FPB3. The latter finding was attributed to faster metabolism of FBP3. In addition, FBP1-3 showed high uptake in kidney and liver.

The relatively high level of activity in blood and liver due to release of ^{64}Cu from the DOTA-chelator increases radiation burden, lowers the thrombus to blood ratio and likely precludes visualization of fibrin deposition in a significant part of the abdomen using this radionuclide. In a quest to prevent ^{64}Cu transmetallation and its corresponding negative effect on the EP-2104R-based peptide biodistribution profile, the N- and C-terminus of the FBP2 fibrin-binding sequence were conjugated to pycup, a novel pyridine-containing, more stable chelator for ^{64}Cu-complexation, yielding a fibrin-binding peptide designated FBP12.[226] Copper-64-labeled FBP12 was then evaluated in an acute carotid thrombosis rat model. PET imaging (1 h PI) of ^{64}Cu-FBP12 allowed thrombus visualization and, in addition, uptake in lungs was visible. Biodistribution at 2 h PI showed a clot to blood ratio of 4 and a clot to contralateral artery ratio of 2. However, absolute uptake in lung (0.6 ± 0.3% ID/g), spleen (0.5 ± 0.1% ID/g), liver (2.5 ± 0.1% ID/g) and kidney (2.8 ± 0.1% ID/g) was higher than thrombus uptake (0.4 ± 0.1% ID/g). This increased uptake in lung and spleen was not observed in previous studies, and might be indicative of partial peptide aggregation at the time of injection. Metabolic studies showed that the ^{64}Cu-FBP12 was rapidly degraded *in vivo*, but that ^{64}Cu likely was still associated with the pycup-chelator. Therefore, unlike in previous studies, also the high ^{64}Cu-FBP12 liver uptake might be attributable to a fraction of aggregated peptides.

In order to further optimize the EP-2104R fibrin-binding peptide platform for PET imaging purposes, Caravan and coworkers focused on three other copper-avid chelators (CB-TE2A, NODAGA and NOTA) for ^{64}Cu-labeling of the FBP2 fibrin-binding sequence, yielding FBP7, FBP8 and FBP9, respectively.[227-228] Figure 14A shows the structural formulas of FBP8 and FBP9. Peptides FBP7-9 displayed dissociation constants of ca. 1 µM towards fibrin and showed high stability in serum *in vitro*. FBP7-9 allowed PET imaging of fibrin deposition in an acute carotid artery thrombosis rat model. Figure 14B-D shows typical examples of PET images acquired in rats using FBP8 and FBP9, clearly illustrating the potential of FBP8-9 for visualization of thrombosis. Biodistribution studies at 2 h PI showed absolute thrombus uptake of 0.5-0.8% ID/g and clot to blood ratios higher than 7 for peptides FBP7-9. In comparison to FBP12, peptides FBP7-9 showed significantly less uptake in lung (0.1-0.2% ID/g), liver (0.3-0.7% ID/g) and spleen (0.1-0.2% ID/g), whereas kidney uptake was similar. In addition, peptides FBP7-9 were metabolically stable *in vivo*, with ≥ 75% of the circulating dose existing as intact probe in plasma (tested up to 5 h PI). For these reasons, peptides FBP7-9 are more suitable options for clinical translation. In addition to studies in a carotid thrombosis rat model, FBP7 has also successfully been employed for thrombus detection and thrombolytic therapy monitoring using PET imaging in an embolic stroke rat model.[227]

The NODAGA- and NOTA-conjugated FBP2 fibrin-binding sequences have also been labeled with Al^{18}F, yielding radiolabeled peptides designated as FBP10 and FBP11, respectively (Fig. 14A).[228] Since the

peptides are rapidly cleared from circulation, labeling with the short-lived isotope ^{18}F is a feasible option for diagnostic purposes. Furthermore, the Al^{18}F strategy does allow the use of a "kit-like" formulation. *In vivo* PET imaging using FBP10 and FBP11 in rats with acute carotid artery thrombosis clearly visualized the thrombi (Fig. 14E-F). Biodistribution at 2 h PI showed an absolute thrombus uptake (0.4-0.6% ID/g) which was similar to that of the ^{64}Cu-labeled peptides FBP7-9. FBP10 exhibited low *in vivo* stability (<30% intact probe at 4 h PI) and high radioactivity uptake in bone (1.5% ID/g, Figure 14E), which indicates defluorination of the probe. In contrast, FBP11 showed high stability (>70% intact at 4 h PI) and displayed bone uptake which was 10-fold lower than for FBP10. This difference is likely due to higher stability of the Al^{18}F-NOTA complex (FBD11) compared to the Al^{18}F-NODAGA complex (FBD10). FBP11 is a promising candidate for clinical translation, as ^{18}F-chemistry is used routinely in clinical radiopharmacies and as FBP11 showed favorable imaging characteristics and biodistribution profiles, which were similar with respect to the ^{64}Cu-labeled peptides FBP7-9.

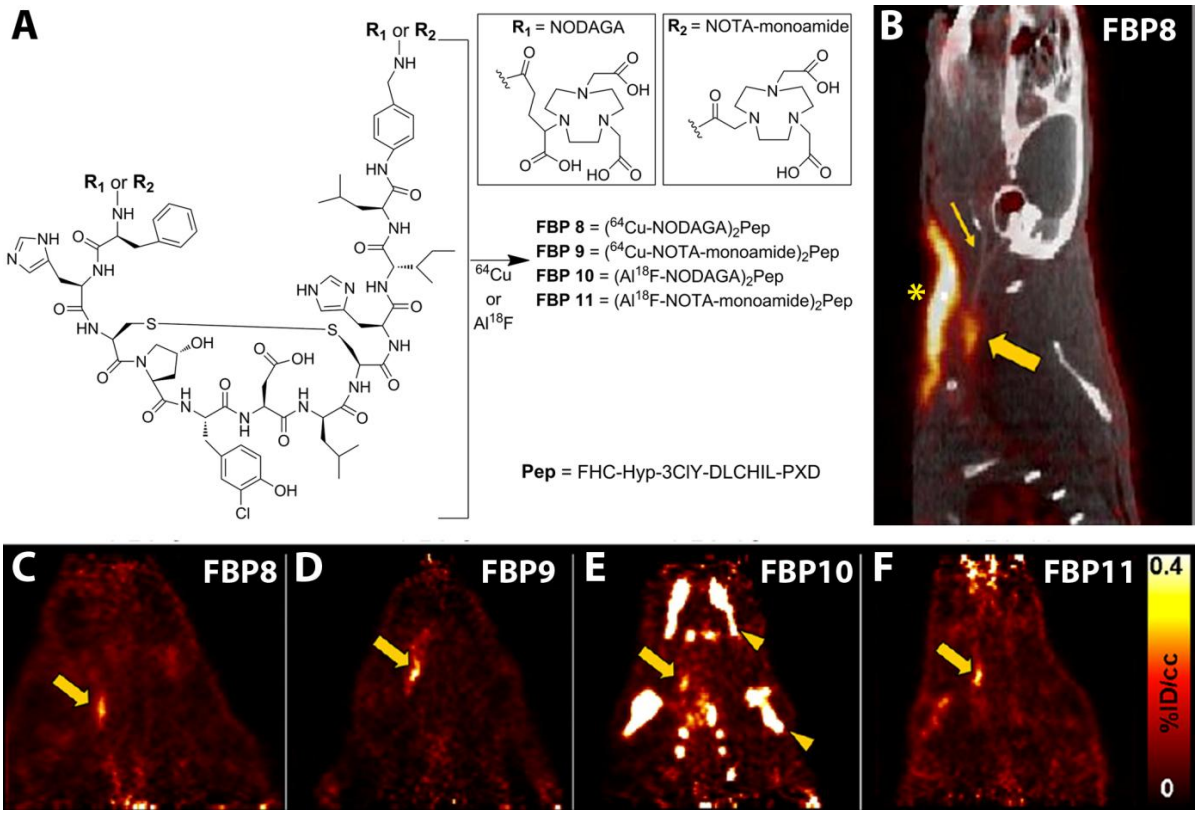

Figure 14. *(A) Structural formulas of fibrin-specific PET probes FBP8-11. (B) Typical PET/CT image obtained 30-90 min post injection of FBP8 in a rat with induced acute carotid artery thrombosis (sagittal view, head-neck area). Bold arrow indicates thrombus uptake of FBP8, thin arrow indicates carotid artery as visualized by CT angiography and * indicates FBP8 uptake in the surgical wound. (C-F) Coronal PET images (head-neck area) obtained 30-90 min post injection of FBP8-11 in rats with induced carotid artery thrombosis. Bold arrows indicate thrombus, arrowheads indicate bone uptake of FBP10. This research was originally published in JNM.*[228] *© by the Society of Nuclear Medicine and Molecular Imaging, Inc.*

1.4 Summary

To summarize, the field of fibrin nuclear imaging has evolved from employing radiolabeled proteins of the coagulation system and radiolabeled anti-fibrin antibodies to using radiolabeled fibrin-binding peptides. Fibrin-binding peptides display low immunogenicity, low costs of production, rapid blood clearance and high tissue penetration with respect to radiolabeled coagulation cascade proteins and antibodies against fibrin. Hence, radiolabeled fibrin-binding peptides have the highest potential to deliver value in routine clinical care of cardiovascular, oncological and neurological diseases.

1.5 Aim and outline thesis

The aim of this thesis was to develop novel small molecule and nanoparticulate probes for imaging of fibrin and to validate these novel probes in a preclinical setting. In the first part of this thesis, the development and preclinical assessment of ^{111}In-FibPep and ^{111}In-EPep, two fibrin-binding peptidic SPECT tracers, is presented. **Chapter 2** describes the synthesis and characterization of ^{111}In-FibPep and presents the preclinical evaluation of ^{111}In-FibPep in a carotid artery thrombosis mouse model. **Chapter 3** reports on the synthesis and characterization of ^{111}In-EPep. In addition, **Chapter 3** describes a head-to-head comparison of ^{111}In-FibPep and ^{111}In-EPep *in vivo* in a carotid artery thrombosis rat model. In **Chapter 4**, ^{111}In-EPep was evaluated for *in vivo* SPECT imaging of intratumoral fibrin deposition in tumor bearing mice.

The second part of the thesis comprises the development of novel fibrin-binding iron oxide nanoparticle micelles (ION-Micelles) for molecular magnetic particle imaging (MPI) and MRI of fibrin deposition. MPI is a relatively new imaging modality that could provide a radiation-free alternative for hot-spot based molecular imaging. **Chapter 5** reports on the synthesis and characterization of the ION-Micelles. In addition, **Chapter 5** describes the functionalization of the ION-Micelle nanoplatform with FibPep. The potential of these fibrin-binding FibPep-ION-Micelles for molecular MPI and MRI of fibrin deposition in thrombosis was subsequently evaluated *in vitro*. In **Chapter 6**, the potential of the FibPep-ION-Micelle nanoplatform for molecular MPI/MRI of fibrin deposition was evaluated *in vivo* in a carotid artery thrombosis mouse model.

The third part of this thesis entails a novel nanoparticulate platform for bimodal PET/MR imaging. PET/MRI is a powerful combination for molecular imaging purposes as it allows quantification and full body screening of probe uptake with PET and detailed characterization of this uptake at high resolution using MRI. **Chapter 7** describes the development of a ^{89}Zr- and Fe-labeled polymeric micelle nanoplatform (^{89}Zr/Fe-DFO-Micelles) for bimodal PET and T_1-weighted MR imaging. The ^{89}Zr/Fe-DFO-Micelles were characterized *in vitro* and evaluated *in vivo* using bimodal PET/MR imaging in tumor bearing mice. In addition, **Chapter 7** describes the functionalization of the ^{89}Zr/Fe-DFO-Micelle nanoplatform with FibPep, yielding fibrin-binding FibPep-^{89}Zr/Fe-DFO-Micelles. The potential of the FibPep-^{89}Zr/Fe-DFO-Micelles for bimodal PET/MR imaging of fibrin deposition was subsequently evaluated *in vitro*. Finally, a summarizing discussion of this thesis is presented in **Chapter 8**.

1.6 References

1. Laurens, N.; Koolwijk, P.; de Maat, M. P. Fibrin structure and wound healing. *J Thromb Haemost* **2006,** *4*, (5), 932-9.
2. Mosesson, M. W. Fibrinogen and fibrin structure and functions. *J Thromb Haemost* **2005,** *3*, (8), 1894-904.
3. Kamath, S.; Lip, G. Y. Fibrinogen: biochemistry, epidemiology and determinants. *QJM* **2003,** *96*, (10), 711-29.
4. Weisel, J. W. Fibrinogen and fibrin. *Adv Protein Chem* **2005,** *70*, 247-99.
5. Ariens, R. A. Fibrin(ogen) and thrombotic disease. *J Thromb Haemost* **2013,** *11 Suppl 1*, 294-305.
6. Muszbek, L.; Bereczky, Z.; Bagoly, Z.; Komaromi, I.; Katona, E. Factor XIII: a coagulation factor with multiple plasmatic and cellular functions. *Physiol Rev* **2011,** *91*, (3), 931-72.
7. Muszbek, L.; Yee, V. C.; Hevessy, Z. Blood coagulation factor XIII: structure and function. *Thromb Res* **1999,** *94*, (5), 271-305.
8. Marder, V. J.; Chute, D. J.; Starkman, S.; Abolian, A. M.; Kidwell, C.; Liebeskind, D.; Ovbiagele, B.; Vinuela, F.; Duckwiler, G.; Jahan, R.; Vespa, P. M.; Selco, S.; Rajajee, V.; Kim, D.; Sanossian, N.; Saver, J. L. Analysis of thrombi retrieved from cerebral arteries of patients with acute ischemic stroke. *Stroke* **2006,** *37*, (8), 2086-93.
9. Smith, E. B.; Thompson, W. D.; Crosbie, L.; Stirk, C. M. Fibrinogen/fibrin in atherogenesis. *Eur J Epidemiol* **1992,** *8 Suppl 1*, 83-7.
10. Bini, A.; Fenoglio, J. J., Jr.; Mesa-Tejada, R.; Kudryk, B.; Kaplan, K. L. Identification and distribution of fibrinogen, fibrin, and fibrin(ogen) degradation products in atherosclerosis. Use of monoclonal antibodies. *Arteriosclerosis* **1989,** *9*, (1), 109-21.
11. Sato, Y.; Hatakeyama, K.; Yamashita, A.; Marutsuka, K.; Sumiyoshi, A.; Asada, Y. Proportion of fibrin and platelets differs in thrombi on ruptured and eroded coronary atherosclerotic plaques in humans. *Heart* **2005,** *91*, (4), 526-30.
12. Congiu, T.; Schembri, L.; Tozzi, M.; Guasti, L.; Maio, R. C.; Cosentino, M.; Marino, F. Scanning electron microscopy examination of endothelium morphology in human carotid plaques. *Micron* **2010,** *41*, (5), 532-6.
13. Tavora, F.; Cresswell, N.; Li, L.; Ripple, M.; Burke, A. Immunolocalisation of fibrin in coronary atherosclerosis: implications for necrotic core development. *Pathology* **2010,** *42*, (1), 15-22.
14. Virmani, R.; Burke, A. P.; Farb, A.; Kolodgie, F. D. Pathology of the vulnerable plaque. *J Am Coll Cardiol* **2006,** *47*, (8 Suppl), C13-8.
15. Rickles, F. R.; Patierno, S.; Fernandez, P. M. Tissue factor, thrombin, and cancer. *Chest* **2003,** *124*, (3 Suppl), 58S-68S.
16. Palumbo, J. S.; Talmage, K. E.; Massari, J. V.; La Jeunesse, C. M.; Flick, M. J.; Kombrinck, K. W.; Jirouskova, M.; Degen, J. L. Platelets and fibrin(ogen) increase metastatic potential by impeding natural killer cell-mediated elimination of tumor cells. *Blood* **2005,** *105*, (1), 178-85.
17. Dvorak, H. F.; Nagy, J. A.; Berse, B.; Brown, L. F.; Yeo, K. T.; Yeo, T. K.; Dvorak, A. M.; van de Water, L.; Sioussat, T. M.; Senger, D. R. Vascular permeability factor, fibrin, and the pathogenesis of tumor stroma formation. *Ann N Y Acad Sci* **1992,** *667*, 101-11.
18. Costantini, V.; Zacharski, L. R. The role of fibrin in tumor metastasis. *Cancer Metastasis Rev* **1992,** *11*, (3-4), 283-90.
19. Paul, J.; Strickland, S.; Melchor, J. P. Fibrin deposition accelerates neurovascular damage and neuroinflammation in mouse models of Alzheimer's disease. *J Exp Med* **2007,** *204*, (8), 1999-2008.
20. La Corte, A. L.; Philippou H; Ariens, R. A., Role of fibrin structure in thrombosis and vascular disease. In *Advances in protein chemistry and structural biology*, Academic Press: 2011; Vol. 83, pp 75-127.
21. Pysz, M. A.; Gambhir, S. S.; Willmann, J. K. Molecular imaging: current status and emerging strategies. *Clin Radiol* **2010,** *65*, (7), 500-16.
22. Weissleder, R.; Mahmood, U. Molecular imaging. *Radiology* **2001,** *219*, (2), 316-33.
23. Ciesienski, K. L.; Caravan, P. Molecular MRI of Thrombosis. *Curr Cardiovasc Imaging Rep* **2010,** *4*, (1), 77-84.
24. Lu, Y.; Lorenzoni, A.; Fox, J. J.; Rademaker, J.; Vander Els, N.; Grewal, R. K.; Strauss, H. W.; Schoder, H. Noncontrast perfusion single-photon emission CT/CT scanning: a new test for the expedited, high-accuracy diagnosis of acute pulmonary embolism. *Chest* **2014,** *145*, (5), 1079-88.
25. Omran, H.; Jung, W.; Rabahieh, R.; Wirtz, P.; Becher, H.; Illien, S.; Schimpf, R.; Luderitz, B. Imaging of thrombi and assessment of left atrial appendage function: a prospective study comparing transthoracic and transoesophageal echocardiography. *Heart* **1999,** *81*, (2), 192-8.

26. Srichai, M. B.; Junor, C.; Rodriguez, L. L.; Stillman, A. E.; Grimm, R. A.; Lieber, M. L.; Weaver, J. A.; Smedira, N. G.; White, R. D. Clinical, imaging, and pathological characteristics of left ventricular thrombus: a comparison of contrast-enhanced magnetic resonance imaging, transthoracic echocardiography, and transesophageal echocardiography with surgical or pathological validation. *Am Heart J* **2006,** *152*, (1), 75-84.

27. Litmanovich, D.; Bankier, A. A.; Cantin, L.; Raptopoulos, V.; Boiselle, P. M. CT and MRI in diseases of the aorta. *AJR Am J Roentgenol* **2009,** *193*, (4), 928-40.

28. Markel, A.; Weich, Y.; Gaitini, D. Doppler ultrasound in the diagnosis of venous thrombosis. *Angiology* **1995,** *46*, (1), 65-73.

29. Kronzon, I.; Tunick, P. A. Aortic atherosclerotic disease and stroke. *Circulation* **2006,** *114*, (1), 63-75.

30. Clofent-Sanchez, G.; Jacobin-Valat, M. J.; Laroche-Traineau, J. The growing interest of fibrin imaging in atherosclerosis. *Atherosclerosis* **2012,** *222*, (1), 22-5.

31. Hanahan, D.; Weinberg, R. A. Hallmarks of cancer: the next generation. *Cell* **2011,** *144*, (5), 646-74.

32. Yasunaga, M.; Manabe, S.; Matsumura, Y. New concept of cytotoxic immunoconjugate therapy targeting cancer-induced fibrin clots. *Cancer Sci* **2011,** *102*, (7), 1396-402.

33. Hobbs, J. T.; Davies, J. W. Detection of venous thrombosis with 131 I-labelled fibrinogen in the rabbit. *Lancet* **1960,** *2*, (7142), 134-5.

34. Nanson, E. M.; Palko, P. D.; Dick, A. A.; Fedoruk, S. O. Early detection of deep venous thrombosis of the legs using I-131 tagged human fibrinogen: a clinical study. *Ann Surg* **1965,** *162*, (3), 438-45.

35. Atkins, P.; Hawkins, L. A. Detection of venous thrombosis in the legs. *Lancet* **1965,** *2*, (7424), 1217-9.

36. Kakkar, V. V.; Howe, C. T.; Nicolaides, A. N.; Renney, J. T.; Clarke, M. B. Deep vein thrombosis of the leg. Is there a "high risk" group? *Am J Surg* **1970,** *120*, (4), 527-30.

37. Kakkar, V. Diagnosis of Deep Vein-Thrombosis Using I-125 Fibrinogen Test. *Arch Surg-Chicago* **1972,** *104*, (2), 152-&.

38. Kakkar, V. V.; Howe, C. T.; Flanc, C.; Clarke, M. B. Natural history of postoperative deep-vein thrombosis. *Lancet* **1969,** *2*, (7614), 230-2.

39. Kakkar, V. V.; Flanc, C.; Howe, C. T.; O'Shea, M.; Flute, P. T. Treatment of deep vein thrombosis. A trial of heparin, streptokinase, and arvin. *Br Med J* **1969,** *1*, (5647), 806-10.

40. Kakkar, V. V.; Howe, C. T.; Laws, J. W.; Flanc, C. Late results of treatment of deep vein thrombosis. *Br Med J* **1969,** *1*, (5647), 810-1.

41. Kakkar, V. V. The problems of thrombosis in the deep veins of the leg. *Ann R Coll Surg Engl* **1969,** *45*, (5), 257-76.

42. Kakkar, V. V.; Field, E. S.; Nicolaides, A. N.; Flute, P. T. Low doses of heparin in prevention of deep-vein thrombosis. *Lancet* **1971,** *2*, (7726), 669-71.

43. Charkes, N. D.; Dugan, M. A.; Maier, W. P.; Soulen, R.; Escovitz, E.; Learner, N.; Dubin, R.; Kozar, J., 3rd. Scintigraphic detection of deep-vein thrombosis with 131I-fibrinogen. *J Nucl Med* **1974,** *15*, (12), 1163-6.

44. Denardo, S. J.; Denardo, G. L.; Obrien, T.; Peek, N. F.; Zielinsk.Fw; Jungerma.Ja. I-123 Fibrinogen Imaging of Thrombi in Dogs. *Journal of Nuclear Medicine* **1974,** *15*, (6), 487-487.

45. Denardo, S. J.; Denardo, G. L.; Carretta, R. F.; Jansholt, A. L.; Krohn, K. A.; Peek, N. F. Clinical Usefulness of Fibrinogen-I-123 (I-123-F) for Detection of Thrombophlebitis (Tp). *Journal of Nuclear Medicine* **1975,** *16*, (6), 524-524.

46. DeNardo, S. J.; DeNardo, G. L. Iodine-123-fibrinogen scintigraphy. *Semin Nucl Med* **1977,** *7*, (3), 245-51.

47. DeNardo, S. J.; Bogren, H. G.; DeNardo, G. L. Detection of thrombophlebitis in the lower extremities: a regional comparison of 123I fibrinogen scintigraphy and contrast venography. *AJR Am J Roentgenol* **1985,** *145*, (5), 1045-52.

48. Harwig, J. F.; Harwig, S. S.; Wells, L. D.; Welch, M. J. Preparation and in vitro properties of 99mTc-fibrinogen. *Int J Appl Radiat Isot* **1976,** *27*, (1), 5-13.

49. Knight, L. C.; Harwig, S. L.; Welch, M. J. In vitro stability and in vivo clearance of fibrinogen or serum albumin labeled with 77Br, 131I, or 125I by direct or indirect synthetic methods. *J Nucl Med* **1977,** *18*, (3), 282-8.

50. Ohmomo, Y.; Yokoyama, A.; Suzuki, J.; Tanaka, H.; Yamamoto, K.; Horiuchi, K.; Ishii, Y.; Torizuka, K. 67 Ga-labeled human fibrinogen: a new promising thrombus imaging agent. *Eur J Nucl Med* **1982,** *7*, (10), 458-61.

51. Hammond, J. D. S.; Verel, D. Observations on the Distribution and Biological Half-Life of Human Fibrinogen. *Brit J Haematol* **1959,** *5*, (4), 431-438.

52. Harwig, J. F.; Coleman, R. E.; Harwig, S. S.; Sherman, L. A.; Siegel, B. A.; Welch, M. J. Highly iodinated fibrinogen: a new thrombus-localizing agent. *J Nucl Med* **1975,** *16*, (8), 756-63.

53. Harwig, J. F.; Welch, M. J.; Coleman, R. E. Preparation and use of 123I-labeled highly iodinated fibrinogen for imaging deep-vein thrombi. *J Nucl Med* **1976,** *17*, (5), 397-400.

54. Sherman, L. A.; Harwig, S.; Lee, J. In vitro formation and i vivo clearance of fibrinogen: fibrin complexes. *J Lab Clin Med* **1975,** *86*, (1), 100-11.

55. Coleman, R. E.; Harwig, S. S.; Harwig, J. F.; Sherman, L. A.; Welch, M. J. Radioiodinated soluble canine fibrin. Preparation and evaluation as a thrombus localizing agent in the dog. *Circ Res* **1975,** *37*, (1), 35-40.

56. Coleman, R. E.; Harwig, S. S.; Harwig, J. F.; Siegel, B. A.; Welch, M. J. Fibrinogen uptake by thrombi: effect of thrombus age. *J Nucl Med* **1975,** *16*, (5), 370-3.

57. Mant, M. J.; O'Brien, B. D.; Russell, D. B. Diagnostic leg scanning for deep venous thrombosis in the recently heparinized patient. *Arch Intern Med* **1981,** *141*, (13), 1757-60.

58. Haines, S. T.; Bussey, H. I. Diagnosis of deep vein thrombosis. *Am J Health Syst Pharm* **1997,** *54*, (1), 66-74.

59. Matsuura, K.; Ichiya, Y.; Ayabe, Z.; Kuwabara, Y.; Otsuka, M.; Das Gunasekera, R. Clinical evaluation of Ga-67 DFO-DAS-fibrinogen scintigraphy. *Radiat Med* **1987,** *5*, (5), 183-5.

60. Mettinger, K. L.; Larsson, S.; Ericson, K.; Casseborn, S. Detection of atherosclerotic plaques in carotid arteries by the use of 123I-fibrinogen. *Lancet* **1978,** *1*, (8058), 242-4.

61. Olexa, S. A.; Budzynski, A. Z. Binding phenomena of isolated unique plasmic degradation products of human cross-linked fibrin. *J Biol Chem* **1979,** *254*, (11), 4925-32.

62. Olexa, S. A.; Budzynski, A. Z. Evidence for four different polymerization sites involved in human fibrin formation. *Proc Natl Acad Sci U S A* **1980,** *77*, (3), 1374-8.

63. Knight, L. C. Imaging thrombi with radiolabelled fragment E1. *Nucl Med Commun* **1988,** *9*, (10), 849-57.

64. Knight, L. C.; Olexa, S. A.; Malmud, L. S.; Budzynski, A. Z. Specific uptake of radioiodinated fragment E1 by venous thrombi in pigs. *J Clin Invest* **1983,** *72*, (6), 2007-13.

65. Knight, L. C.; Kollmann, M.; Maurer, A. H.; Budzynski, A. Z. Binding properties of 111In-diethylenetriaminepentaacetic acid (DTPA)-fragment E1,2, a fibrin-specific probe, are dependent on use of protecting complex during attachment of DTPA groups. *Biochim Biophys Acta* **1987,** *924*, (1), 45-53.

66. Knight, L. C.; Abrams, M. J.; Schwartz, D. A.; Hauser, M. M.; Kollman, M.; Gaul, F. E.; Rauh, D. A.; Maurer, A. H. Preparation and preliminary evaluation of technetium-99m-labeled fragment E1 for thrombus imaging. *J Nucl Med* **1992,** *33*, (5), 710-5.

67. Knight, L. C.; Maurer, A. H.; Robbins, P. S.; Malmud, L. S.; Budzynski, A. Z. Fragment E1 labeled with I-123 in the detection of venous thrombosis. *Radiology* **1985,** *156*, (2), 509-14.

68. Knight, L. C. Radiopharmaceuticals for thrombus detection. *Semin Nucl Med* **1990,** *20*, (1), 52-67.

69. Back, N.; Ambrus, J. L.; Mink, I. B. Distribution and fate of I-131-labeled components of the fibrinolysin system. *Circ Res* **1961,** *9*, 1208-16.

70. Tengborn, L.; Hedner, U.; Rohlin, M.; Stahlberg, F. Demonstration of 99mTc-labelled plasmin on the surface of ex vivo thrombi. *Thromb Res* **1982,** *28*, (6), 783-91.

71. Lucas, M. A.; Fretto, L. J.; McKee, P. A. The binding of human plasminogen to fibrin and fibrinogen. *J Biol Chem* **1983,** *258*, (7), 4249-56.

72. Ouchi, H.; Warren, R. Detection of intravascular thrombi by means of I-131-labeled plasmin. *Surgery* **1962,** *51*, 42-9.

73. Harwig, S. L.; Harwig, J. F.; Sherman, L. A.; Coleman, R. E.; Welch, M. J. Radioiodinated plasminogen: an imaging agent for pre-existing thrombi. *J Nucl Med* **1977,** *18*, (1), 42-5.

74. Persson, B. R.; Darte, L. Labeling plasmin with technetium-99m for scintigraphic localization of thrombi. *Int J Appl Radiat Isot* **1977,** *28*, (1-2), 97-104.

75. Deacon, J. M.; Ell, P. J.; Anderson, P.; Khan, O. Technetium 99m-plasmin: a new test for the detection of deep vein thrombosis. *Br J Radiol* **1980,** *53*, (631), 673-7.

76. Adolfsson, L.; Nordenfelt, I.; Olsson, H.; Torstensson, I. Diagnosis of deep vein thrombosis with 99Tcm-plasmin. *Acta Med Scand* **1982,** *211*, (5), 365-8.

77. Edenbrandt, C. M.; Nilsson, J.; Ohlin, P. Diagnosis of deep venous thrombosis by phlebography and 99Tcm-plasmin. *Acta Med Scand* **1982,** *211*, (1-2), 59-64.

78. Wallin, L.; Albrechtsson, U.; Fagher, B.; Lagerstedt, C.; Larusdottir, H.; Olsson, C. G.; Westling, H.; Oquist, B. Thermography in the diagnosis of deep venous thrombosis. A comparison with 99Tcm-plasmin test, clinical diagnosis and phlebography. *Acta Med Scand* **1983,** *214*, (1), 15-20.

79. Husted, S. E.; Nielsen, H. K.; Krusell, L.; Fasting, H.; Nielsen, B. O.; Pedersen, J. B.; Dalgaard, E.; Hansen, H. H. Deep vein thrombosis detection by 99mTc-plasmin test and phlebography. *Br J Surg* **1984,** *71*, (1), 65-6.

80. Lagerstedt, C.; Olsson, C. G.; Fagher, B.; Oqvist, B. 99mTc plasmin in 394 consecutive patients with suspected deep venous thrombosis. *Eur J Nucl Med* **1989,** *15*, (12), 771-5.

81. Dahlborn, M.; Ahlborg, G.; Soderborg, B.; Virgin, J.; Wilczek, B. Gamma camera detection of 99mTC-plasmin in the diagnosis of deep-vein thrombosis. *Eur J Nucl Med* **1984,** *9*, (11), 499-501.

82. Luckers, A. E.; Luth, W. J.; Teule, G. J.; Huijgens, P. C.; Heidendal, G. A. Diagnosis of deep venous thrombosis with 99mTc plasmin using the gamma camera. *Eur J Nucl Med* **1984,** *9*, (6), 282-3.

83. Overgaard, K. Thromboscintigraphy with 99Tcm-plasmin: a new diagnostic method in deep venous thrombosis of the legs. *Nucl Med Commun* **1984,** *5*, (2), 101-7.

84. Rawal, N.; Sjostrand, U.; Christoffersson, E.; Dahlstrom, B.; Arvill, A.; Rydman, H. Comparison of intramuscular and epidural morphine for postoperative analgesia in the grossly obese: influence on postoperative ambulation and pulmonary function. *Anesth Analg* **1984,** *63*, (6), 583-92.

85. Fasting, H.; Andersen, K.; Kraemmer Nielsen, H.; Husted, S. E.; Koopmann, H. D.; Simonsen, O.; Husegaard, H. C.; Vestergaard Madsen, J.; Pedersen, T. K. Prevention of postoperative deep venous thrombosis. Low-dose heparin versus graded pressure stockings. *Acta Chir Scand* **1985,** *151*, (3), 245-8.

86. Rasmussen, A.; Hansen, P. T.; Lindholt, J.; Poulsen, T. D.; Toftdahl, D. B.; Gram, J.; Toftgaard, C.; Jespersen, J. Venous thrombosis after abdominal surgery. A comparison between subcutaneous heparin and antithrombotic stockings, or both. *J Med* **1988,** *19*, (3-4), 193-201.

87. Christensen, S. W.; Wille-Jorgensen, P.; Bjerg-Nielsen, A.; Kjaer, L. Prevention of deep venous thrombosis following total hip replacement, using epidural analgesia. *Acta Orthop Belg* **1989,** *55*, (1), 58-61.

88. Wille-Jorgensen, P.; Christensen, S. W.; Bjerg-Nielsen, A.; Stadeager, C.; Kjaer, L. Prevention of thromboembolism following elective hip surgery. The value of regional anesthesia and graded compression stockings. *Clin Orthop Relat Res* **1989**, (247), 163-7.

89. Edenbrandt, C. M.; Dahlstrom, J. A.; Nilsson, J.; Ohlin, P. Comparison between 99Tcm-porcine plasmin and 99Tcm-labelled erythrocytes in diagnosis of deep vein thrombosis. *Clin Physiol* **1984,** *4*, (3), 243-52.

90. Stahlberg, F.; Andersson, L.; Edenbrandt, C. M.; Strand, S. E. Quantitative in vivo and in vitro comparison between radiolabelled colloids, biomolecules and blood cells in their ability to diagnose deep venous thrombosis. *Nucl Med Commun* **1984,** *5*, (12), 741-62.

91. Edenbrandt, C. M.; Nilsson, J.; Ohlin, P. Follow-up of circulatory changes secondary to deep venous thrombosis with special regards to radionuclide tests. *Clin Physiol* **1986,** *6*, (2), 153-61.

92. Collen, D.; Lijnen, H. R.; Todd, P. A.; Goa, K. L. Tissue-type plasminogen activator. A review of its pharmacology and therapeutic use as a thrombolytic agent. *Drugs* **1989,** *38*, (3), 346-88.

93. Hoylaerts, M.; Rijken, D. C.; Lijnen, H. R.; Collen, D. Kinetics of the activation of plasminogen by human tissue plasminogen activator. Role of fibrin. *J Biol Chem* **1982,** *257*, (6), 2912-9.

94. Melandri, G.; Vagnarelli, F.; Calabrese, D.; Semprini, F.; Nanni, S.; Branzi, A. Review of tenecteplase (TNKase) in the treatment of acute myocardial infarction. *Vasc Health Risk Manag* **2009,** *5*, (1), 249-56.

95. Kunadian, V.; Gibson, C. M. Thrombolytics and myocardial infarction. *Cardiovasc Ther* **2012,** *30*, (2), e81-8.

96. Bivard, A.; Lin, L.; Parsonsb, M. W. Review of Stroke Thrombolytics. *J Stroke* **2013,** *15*, (2), 90-98.

97. Hnatowich, D. J.; Virzi, F.; Doherty, P. W.; Wilson, J.; Rosa, J.; Ansell, J. E. Characterization of indium-111 labeled recombinant tissue plasminogen activator for the imaging of thrombi. *Eur J Nucl Med* **1987,** *13*, (9), 467-73.

98. Itoh, K.; Tsukamoto, E.; Nishibe, T.; Sakurama, S.; Ieko, M.; Tanabe, T.; Furudate, M. Tc-99m labeled tissue-type plasminogen activator: preparation, stability and preliminary imaging of thrombus-bearing rats. *Ann Nucl Med* **1991,** *5*, (2), 59-64.

99. Tsukamoto, E. In vivo distribution of Tc-99m labeled recombinant tissue-type plasminogen activator in control and thrombus-bearing rats. *Ann Nucl Med* **1992,** *6*, (3), 177-84.

100. Takahashi, A.; Itoh, K.; Tsukamoto, E.; Furudate, M.; Kamiyama, H.; Abe, H. Technetium-99m-labeled recombinant tissue plasminogen activator for the imaging of emboli in vivo. *Neurol Med Chir (Tokyo)* **1993,** *33*, (7), 415-9.

101. Itoh, K.; Ieko, M.; Hiraguchi, E.; Kitayama, H.; Tsukamoto, E. In vivo kinetics of 99mTc labeled recombinant tissue plasminogen activator in rabbits. *Ann Nucl Med* **1994,** *8*, (3), 193-9.

102. Uehara, A.; Isaka, Y.; Etani, H.; Kimura, K.; Yoneda, S.; Kamada, T.; Kozuka, T.; Nobuhara, M. Binding of 131I-labeled tissue-type plasminogen activator on de-endothelialized lesions in rabbits. *Nuklearmedizin* **1987,** *26*, (5), 224-8.

103. Fry, E. T.; Mack, D. L.; Monge, J. C.; Billadello, J. J.; Sobel, B. E. Labeling of human clots in vitro with an active-site mutant of t-PA. *J Nucl Med* **1990,** *31*, (2), 187-91.

104. Butler, S. P.; Kader, K. L.; Owen, J.; Wang, T. S.; Fawwaz, R. A.; Alderson, P. O. Rapid localization of indium-111-labeled inhibited recombinant tissue plasminogen activator in a rabbit thrombosis model. *J Nucl Med* **1991,** *32*, (3), 461-7.

105. Ord, J. M.; Hasapes, J.; Daugherty, A.; Thorpe, S. R.; Bergmann, S. R.; Sobel, B. E. Imaging of thrombi with tissue-type plasminogen activator rendered enzymatically inactive and conjugated to a residualizing label. *Circulation* **1992,** *85*, (1), 288-97.

106. De Bruyn, V. H.; Bergmann, S. R.; Keyt, B. A.; Sobel, B. E. Visualization of thrombi in pulmonary arteries with radiolabeled, enzymatically inactivated tissue-type plasminogen activator. *Circulation* **1995,** *92*, (5), 1320-5.

107. Butler, S. P.; Boyd, S. J.; Parkes, S. L.; Quinn, R. J. Technetium-99m-modified recombinant tissue plasminogen activator to detect deep venous thrombosis. *J Nucl Med* **1996,** *37*, (5), 744-8.

108. Butler, S. P.; Rahman, T.; Boyd, S. J.; Parkes, S. L.; Quinn, R. J. Detection of postoperative deep-venous thrombosis using technetium-99m-labeled tissue plasminogen activator. *J Nucl Med* **1997,** *38*, (2), 219-23.

109. Brighton, T.; Janssen, J.; Butler, S. P. Aging of acute deep vein thrombosis measured by radiolabeled 99mTc-rt-PA. *J Nucl Med* **2007,** *48*, (6), 873-8.

110. Spar, I. L.; Goodland, R. L.; Bale, W. F. Localization of I131 labeled antibody of rat fibrin in transplantable rat lymphosarcoma. *Proc Soc Exp Biol Med* **1959,** *100*, (2), 259-62.

111. Bale, W. F.; Spar, I. L.; Goodland, R. L. Experimental radiation therapy of tumors with I-131-carrying antibodies to fibrin. *Cancer Res* **1960,** *20*, 1488-94.

112. Spar, I. L.; Bale, W. F.; Goodland, R. L.; Casarett, G. W.; Michaelson, S. M. Distribution of injected I 131 labeled antibody to dog fibrin in tumor-bearing dogs. *UR Rep* **1960,** *UR-569*, 1-13.

113. Spar, I. L.; Bale, W. F.; Goodland, R. L.; Izzo, M. J. Preparation of Purified I-131-Labeled Antibody Which Reacts with Human Fibrin. Preliminary Tracer Studies on Tumor Patients. *Cancer Res* **1964,** *24*, 286-93.

114. McCardle, R. J.; Harper, P. V.; Spar, I. L.; Bale, W. F.; Andros, G.; Jiminez, F. Studies with iodine-131-labeled antibody to human fibrinogen for diagnosis and therapy of tumors. *J Nucl Med* **1966,** *7*, (11), 837-47.

115. Spar, I. L.; Bale, W. F.; Marrack, D.; Dewey, W. C.; McCardle, R. J.; Harper, P. V. 131-I-labeled antibodies to human fibrinogen. Diagnostic studies and therapeutic trials. *Cancer* **1967,** *20*, (5), 865-70.

116. Spar, I. L.; Goodland, R. L.; Schwartz, S. I. Detection of preformed venous thrombi in dogs by means of I-131-labeled antibodies to dog fibrinogen. *Circ Res* **1965,** *17*, (4), 322-9.

117. Kramer, R. S.; Ashburn, W. L.; Vasko, J. S.; Morrow, A. G. Detection of intracardiac thrombi using radio-iodinated antifibrinogen (RIAF) and precordial scanning: experimental and clinical studies. *Ann Surg* **1967,** *166*, (2), 173-82.

118. Spar, I. L.; Varon, M. I.; Goodland, R. L.; Schwartz, S. I. Isotopic detection of thrombi. *Arch Surg* **1966,** *92*, (5), 752-8.

119. Spar, I. L.; Perry, J. M.; Benz, L. L.; DeWeese, J. A.; Mahoney, E. B.; Izzo, M. J.; Schwartz, S. I.; Yu, P. N. Detection of left atrial thrombi. Scintillation scanning after administration of 131-I rabbit antibodies to human fibrinogen. *Am Heart J* **1969,** *78*, (6), 731-9.

120. Spar, I. L.; Goodland, R. L.; Desiderio, M. A. Immunological Removal of Circulating I-131-Labeled Rabbit Antibody to Rat Fibrinogen in Normal and Tumor-Bearing Rats. *J Nucl Med* **1964,** *5*, 428-43.

121. Bosnjakovic, V. B.; Jankovic, B. D.; Horvat, J.; Cvoric, J. Radiolabelled anti-human fibrin antibody: a new thrombus-detecting agent. *Lancet* **1977,** *1*, (8009), 452-4.
122. Bosnjakovic, V.; Jankovic, B. D.; Horvat, J.; Nastic-Miric, D.; Djukic, V.; Pavlovic, S. The validity of radiolabeled anti fibrin antibody for deep vein thrombosis imaging. *Eur J Nucl Med* **1988,** *14*, (9-10), 489-94.
123. Kohler, G.; Milstein, C. Continuous cultures of fused cells secreting antibody of predefined specificity. *Nature* **1975,** *256*, (5517), 495-7.
124. Scheefers-Borchel, U.; Muller-Berghaus, G.; Fuhge, P.; Eberle, R.; Heimburger, N. Discrimination between fibrin and fibrinogen by a monoclonal antibody against a synthetic peptide. *Proc Natl Acad Sci U S A* **1985,** *82*, (20), 7091-5.
125. Hui, K. Y.; Haber, E.; Matsueda, G. R. Monoclonal antibodies to a synthetic fibrin-like peptide bind to human fibrin but not fibrinogen. *Science* **1983,** *222*, (4628), 1129-32.
126. Morris, T. A.; Marsh, J. J.; Fagnani, R.; Hagan, M.; Moser, K. M. Degree of polymer organization decreases the binding of a monoclonal antibody raised against the beta-chain amino terminus of fibrin. *Thromb Haemost* **1997,** *77*, (4), 704-9.
127. Kudryk, B.; Rohoza, A.; Ahadi, M.; Chin, J.; Wiebe, M. E. Specificity of a monoclonal antibody for the NH2-terminal region of fibrin. *Mol Immunol* **1984,** *21*, (1), 89-94.
128. Rosebrough, S. F.; Kudryk, B.; Grossman, Z. D.; McAfee, J. G.; Subramanian, G.; Ritter-Hrncirik, C. A.; Witanowski, L. S.; Tillapaugh-Fay, G. Radioimmunoimaging of venous thrombi using iodine-131 monoclonal antibody. *Radiology* **1985,** *156*, (2), 515-7.
129. Cerqueira, M. D.; Stratton, J. R.; Vracko, R.; Schaible, T. F.; Ritchie, J. L. Noninvasive arterial thrombus imaging with 99mTc monoclonal antifibrin antibody. *Circulation* **1992,** *85*, (1), 298-304.
130. Knight, L. C.; Maurer, A. H.; Ammar, I. A.; Epps, L. A.; Dean, R. T.; Pak, K. Y.; Berger, H. J. Tc-99m antifibrin Fab' fragments for imaging venous thrombi: evaluation in a canine model. *Radiology* **1989,** *173*, (1), 163-9.
131. Rosebrough, S. F.; McAfee, J. G.; Grossman, Z. D.; Schemancik, L. A. Immunoreactivity of 111In and 131I fibrin-specific monoclonal antibody used for thrombus imaging. *J Immunol Methods* **1989,** *116*, (1), 123-9.
132. el Kouri, D.; Peltier, P.; Dupas, B.; Faivre, A.; Chaillou, P.; Moreau, A.; De Faucal, P.; Planchon, B. 99Tcm-labelled anti-fibrin Fab' fragment for evaluating the course of venous thrombosis in the rabbit. *Nucl Med Commun* **1994,** *15*, (1), 50-7.
133. Grossman, Z. D.; Rosebrough, S. F.; McAfee, J. G.; Subramanian, G.; Ritter-Hrncirik, C. A.; Witanowski, L. S.; Tillapaugh-Fay, G.; Urrutia, E. Imaging fresh venous thrombi in the dog with I-131 and In-111 labeled fibrin-specific monoclonal antibody and F(ab')2 fragments. *Radiographics* **1987,** *7*, (5), 913-21.
134. Rosebrough, S. F.; Grossman, Z. D.; McAfee, J. G.; Kudryk, B. J.; Subramanian, G.; Ritter-Hrncirik, C. A.; Witanowski, L. S.; Tillapaugh-Fay, G.; Urrutia, E. Aged venous thrombi: radioimmunoimaging with fibrin-specific monoclonal antibody. *Radiology* **1987,** *162*, (2), 575-7.
135. Rosebrough, S. F.; Grossman, Z. D.; McAfee, J. G.; Kudryk, B. J.; Subramanian, G.; Ritter-Hrncirik, C. A.; Witanowski, L. S.; Tillapaugh-Fay, G.; Urrutia, E.; Zapf-Longo, C. Thrombus imaging with indium-111 and iodine-131-labeled fibrin-specific monoclonal antibody and its F(ab')2 and Fab fragments. *J Nucl Med* **1988,** *29*, (7), 1212-22.
136. Rosebrough, S. F.; McAfee, J. G.; Grossman, Z. D.; Kudryk, B. J.; Ritter-Hrncirik, C. A.; Witanowski, L. S.; Maley, B. L.; Bertrand, E. A.; Gagne, G. M. Thrombus imaging: a comparison of radiolabeled GC4 and T2G1s fibrin-specific monoclonal antibodies. *J Nucl Med* **1990,** *31*, (6), 1048-54.
137. Hirano, T.; Tomiyoshi, K.; Watanabe, N.; Tateno, M.; Oriuch, N.; Inoue, T.; Endo, K. Technetium-99m-labeled anti-fibrin monoclonal antibody accumulation in an inflammatory focus. *J Nucl Med* **1992,** *33*, (6), 1181-2.
138. Manspeaker, P.; Weisman, H. F.; Schaible, T. F. Cardiovascular applications: current status of immunoscintigraphy in the detection of myocardial necrosis using antimyosin (R11D10) and deep venous thrombosis using antifibrin (T2G1s). *Semin Nucl Med* **1993,** *23*, (2), 133-47.
139. Stratton, J. R.; Cerqueira, M. D.; Dewhurst, T. A.; Kohler, T. R. Imaging arterial thrombosis: comparison of technetium-99m-labeled monoclonal antifibrin antibodies and indium-111-platelets. *J Nucl Med* **1994,** *35*, (11), 1731-7.
140. Matsueda, G. R.; Margolies, M. N. Structural basis for the species selectivity of a fibrin-specific monoclonal antibody. *Biochemistry* **1986,** *25*, (6), 1451-5.

141. Knight, L. C.; Maurer, A. H.; Ammar, I. A.; Shealy, D. J.; Mattis, J. A. Evaluation of indium-111-labeled anti-fibrin antibody for imaging vascular thrombi. *J Nucl Med* **1988,** *29*, (4), 494-502.

142. Kairemo, K.; Ljunggren, K.; Strand, S. E.; Hiltunen, J.; Penttila, P.; Nikula, T.; Laine, A.; Wahlstrom, T. Radioimmunotherapy with 90Y-labeled monoclonal antibodies in a nude mouse ovarian cancer model. *Acta Oncol* **1993,** *32*, (7-8), 801-5.

143. Kairemo, K. J.; Ljunggren, K.; Wahlstrom, T.; Stigbrand, T.; Strand, S. E. Correlation of beta-camera imaging and immunohistochemistry in radioimmunotherapy using 90Y-labeled monoclonal antibodies in ovarian cancer animal models. *Cell Biophys* **1994,** *24-25*, 293-300.

144. Alavi, A.; Palevsky, H. I.; Gupta, N.; Meranze, S.; Kelley, M. A.; Jatlow, A. D.; Schaible, T. F.; Brown, J.; Berger, H. J. Radiolabeled antifibrin antibody in the detection of venous thrombosis: preliminary results. *Radiology* **1990,** *175*, (1), 79-85.

145. Aronen, H. Diagnosis of deep venous thrombosis of the leg using immunoscintigraphy with 111In-labelled monoclonal antifibrin antibody fragments. *Acta Radiol* **1989,** *30*, (2), 159-62.

146. De Faucal, P.; Peltier, P.; Planchon, B.; Dupas, B.; Touze, M. D.; Baron, D.; Scaible, T.; Berger, H. J.; Chatal, J. F. Evaluation of indium-111-labeled antifibrin monoclonal antibody for the diagnosis of venous thrombotic disease. *J Nucl Med* **1991,** *32*, (5), 785-91.

147. Ferlin, G.; Zanco, P.; Lusiani, L.; Borsato, N. A new monoclonal antibody antifibrin: preliminary evaluation in the detection of venous thrombosis. *Int J Rad Appl Instrum B* **1989,** *16*, (2), 163-5.

148. Jung, M.; Kletter, K.; Dudczak, R.; Koppensteiner, R.; Minar, E.; Kahls, P.; Stumpflen, A.; Pokieser, P.; Ehringer, H. Deep vein thrombosis: scintigraphic diagnosis with In-111-labeled monoclonal antifibrin antibodies. *Radiology* **1989,** *173*, (2), 469-75.

149. Lusiani, L.; Zanco, P.; Visona, A.; Breggion, G.; Pagnan, A.; Ferlin, G. Immunoscintigraphic detection of venous thrombosis of the lower extremities by means of human antifibrin monoclonal antibodies labeled with 111In. *Angiology* **1989,** *40*, (7), 671-7.

150. Vorne, M. S.; Honkanen, T. T.; Lantto, T. J.; Laitinen, R. O.; Karppinen, K. J.; Jauhola, S. V. Thrombus imaging with 99mTc-HMPAO-labeled platelets and 111In-labeled monoclonal antifibrin antibodies. *Acta Radiol* **1993,** *34*, (1), 59-63.

151. Kanke, M.; Matsueda, G. R.; Strauss, H. W.; Yasuda, T.; Liau, C. S.; Khaw, B. A. Localization and visualization of pulmonary emboli with radiolabeled fibrin-specific monoclonal antibody. *J Nucl Med* **1991,** *32*, (6), 1254-60.

152. Hui, K. Y.; Haber, E.; Matsueda, G. R. Immunodetection of human fibrin using monoclonal antibody-64C5 in an extracorporeal chicken model. *Thromb Haemost* **1985,** *54*, (2), 524-7.

153. Morris, T. A.; Marsh, J. J.; Konopka, R.; Pedersen, C. A.; Chiles, P. G.; Fagnani, R.; Hagan, M.; Moser, K. M. Antibodies against the fibrin beta-chain amino-terminus detect active canine venous thrombi. *Circulation* **1997,** *96*, (9), 3173-9.

154. Morris, T. A.; Marsh, J. J.; Konopka, R.; Pedersen, C. A.; Chiles, P. G. Anti-thrombotic efficacies of enoxaparin, dalteparin, and unfractionated heparin in venous thrombo-embolism. *Thromb Res* **2000,** *100*, (3), 185-94.

155. Morris, T. A.; Marsh, J. J.; Konopka, R.; Pedersen, C. A.; Chiles, P. G. Improved imaging of deep venous thrombi during anticoagulation using radiolabelled anti-D-dimer antibodies. *Nucl Med Commun* **2004,** *25*, (9), 917-22.

156. Hisada, Y.; Yasunaga, M.; Hanaoka, S.; Saijou, S.; Sugino, T.; Tsuji, A.; Saga, T.; Tsumoto, K.; Manabe, S.; Kuroda, J.; Kuratsu, J.; Matsumura, Y. Discovery of an uncovered region in fibrin clots and its clinical significance. *Sci Rep* **2013,** *3*, 2604.

157. Rylatt, D. B.; Blake, A. S.; Cottis, L. E.; Massingham, D. A.; Fletcher, W. A.; Masci, P. P.; Whitaker, A. N.; Elms, M.; Bunce, I.; Webber, A. J.; et al. An immunoassay for human D dimer using monoclonal antibodies. *Thromb Res* **1983,** *31*, (6), 767-78.

158. Walker, K. Z.; Milner, L. J.; Bautovich, G. J.; Borham, P.; Wood, A. K.; Rylatt, D. B.; Martin, P.; Bundesen, P. G.; Boniface, G. R. Detection of experimental thrombi in rabbits with an 131I-labelled fibrin-specific monoclonal antibody. *Eur J Nucl Med* **1990,** *16*, (11), 787-94.

159. Walker, K. Z.; Boniface, G. R.; Phippard, A. F.; Harewood, W.; Bautovich, G. J.; Bundesen, P. G. Preclinical evaluation of 99m technetium-labeled DD-3B6/22 Fab' for thrombus detection. *Thromb Res* **1991,** *64*, (6), 691-701.

160. Walker, K. Z.; Khafagi, F.; Bautovich, G. J.; Boniface, G. R.; Bundesen, P. G.; Rylatt, D. B. Anti-fibrin monoclonal antibodies for radioimmunodetection: preliminary assessment in a rat model system. *Thromb Res* **1988,** *52*, (4), 269-78.

161. Tymkewycz, P. M.; Creighton, L. J.; Gascoine, P. S.; Zanelli, G. D.; Webbon, P. M.; Gaffney, P. J. Imaging of human thrombi in the rabbit jugular vein: I: Comparison of two fibrin-specific monoclonal antibodies. *Thromb Res* **1989,** *54*, (5), 411-21.

162. Lee, F. T.; Milner, L. J.; Boniface, G. R.; Bautovich, G. J.; Weedon, A. R.; Bundesen, P. G.; Rylatt, D. B.; Walker, K. Z. Evaluation of thrombus detection in a rabbit model using a technetium-99m-labelled anti-fibrin monoclonal antibody. *Immunol Cell Biol* **1992,** *70 (Pt 3)*, 173-9.

163. Morris, T. A.; Marsh, J. J.; Chiles, P. G.; Konopka, R. G.; Pedersen, C. A.; Schmidt, P. F.; Gerometta, M. Single photon emission computed tomography of pulmonary emboli and venous thrombi using anti-D-dimer. *Am J Respir Crit Care Med* **2004,** *169*, (9), 987-93.

164. Bautovich, G.; Angelides, S.; Lee, F. T.; Greenough, R.; Bundesen, P.; Murray, P.; Schmidt, P.; Waugh, R.; Harris, J.; Cameron, K.; et al. Detection of deep venous thrombi and pulmonary embolus with technetium-99m-DD-3B6/22 anti-fibrin monoclonal antibody Fab' fragment. *J Nucl Med* **1994,** *35*, (2), 195-202.

165. Angelides, S.; Lee, F. T.; Basten, A.; Lambrecht, R. M.; Walker, K. Z.; Bundesen, P. G.; Bautovich, G. J. Detection of malignant tumors using Tc-99m labeled Fab' fragments from a monoclonal antibody with specificity for D-dimer of cross-linked fibrin. *Clin Nucl Med* **1996,** *21*, (3), 242-4.

166. Douketis, J. D.; Ginsberg, J. S.; Haley, S.; Julian, J.; Dwyer, M.; Levine, M.; Eisenberg, P. R.; Smart, R.; Tsui, W.; White, R. H.; Morris, T. A.; Kaatz, S.; Comp, P. C.; Crowther, M. A.; Kearon, C.; Kassis, J.; Bates, S. M.; Schulman, S.; Desjardins, L.; Taillefer, R.; Begelman, S. M.; Gerometta, M. Accuracy and safety of (99m)Tc-labeled anti-D-dimer (DI-80B3) Fab' fragments (ThromboView(R)) in the diagnosis of deep vein thrombosis: a phase II study. *Thromb Res* **2012,** *130*, (3), 381-9.

167. Macfarlane, D.; Socrates, A.; Eisenberg, P.; Larcos, G.; Roach, P.; Gerometta, M.; Smart, R.; Tsui, W.; Scott, A. M. Imaging of deep venous thrombosis in patients using a radiolabelled anti-D-dimer Fab' fragment (99mTc-DI-DD3B6/22-80B3): results of a phase I trial. *Eur J Nucl Med Mol Imaging* **2009,** *36*, (2), 250-9.

168. Macfarlane, D. J.; Smart, R. C.; Tsui, W. W.; Gerometta, M.; Eisenberg, P. R.; Scott, A. M. Safety, pharmacokinetic and dosimetry evaluation of the proposed thrombus imaging agent 99mTc-DI-DD-3B6/22-80B3 Fab'. *Eur J Nucl Med Mol Imaging* **2006,** *33*, (6), 648-56.

169. Morris, T. A.; Gerometta, M.; Smart, R. C.; Eisenberg, P.; Roach, P. J.; Tsui, W. W.; Better, N.; Taubman, K. L.; Unger, S. A.; Macfarlane, D. Pulmonary emboli imaging with (99m)Tc-labelled anti-D-dimer (DI-80B3) Fab' followed by SPECT. *Heart Lung Circ* **2011,** *20*, (8), 503-11.

170. Morris, T. A.; Gerometta, M.; Yusen, R. D.; White, R. H.; Douketis, J. D.; Kaatz, S.; Smart, R. C.; Macfarlane, D.; Ginsberg, J. S. Detection of pulmonary emboli with 99mTc-labeled anti-D-dimer (DI-80B3)Fab' fragments (ThromboView). *Am J Respir Crit Care Med* **2011,** *184*, (6), 708-14.

171. Holvoet, P.; Stassen, J. M.; Hashimoto, Y.; Spriggs, D.; Devos, P.; Collen, D. Binding properties of monoclonal antibodies against human fragment D-dimer of cross-linked fibrin to human plasma clots in an in vivo model in rabbits. *Thromb Haemost* **1989,** *61*, (2), 307-13.

172. Hashimoto, Y.; Stassen, J. M.; Leclef, B.; De Roo, M.; Vandecruys, A.; Melin, J.; Verhoeven-Mester, D.; Trouet, A.; Collen, D. Thrombus imaging with an I-123-labeled F(ab')2 fragment of an anti-human fibrin monoclonal antibody in a rabbit model. *Radiology* **1989,** *171*, (1), 223-6.

173. Greco, C.; Di Loreto, M.; Ciavolella, M.; Banci, M.; Taurino, M.; Cerquetani, E.; Chiavarelli, R.; Naro, F.; Cusella-De Angelis, G.; Mele, A.; et al. Immunodetection of human atherosclerotic plaque with 125I-labeled monoclonal antifibrin antibodies. *Atherosclerosis* **1993,** *100*, (2), 133-9.

174. Scopinaro, F.; Di Loreto, M.; Banci, M.; Schillaci, O.; Di Macio, L.; de Santis, R.; Anastasi, A. M.; Ciancarella, W.; Centi Colella, A.; Mele, A. Anti D dimer monoclonal antibodies: a possible scintigraphic agent for immunodetection of thrombi. *Nucl Med Commun* **1992,** *13*, (10), 723-9.

175. Ciavolella, M.; Tavolaro, R.; Di Loreto, M.; La Torre, F.; Nicolai, A.; Schillaci, O.; Ierardi, M.; Scopinaro, F. Immunoscintigraphy of venous thrombi: clinical effectiveness of a new antifibrin D-dimer monoclonal antibody. *Angiology* **1999,** *50*, (2), 103-9.

176. Ciavolella, M.; Tavolaro, R.; Taurino, M.; Di Loreto, M.; Greco, C.; Sbarigia, E.; Casini, A.; Speziale, F.; Scopinaro, F. Immunoscintigraphy of atherosclerotic uncomplicated lesions in vivo with a monoclonal antibody against D-dimers of insoluble fibrin. *Atherosclerosis* **1999,** *143*, (1), 171-5.

177. Wasser, M. N.; Cleyndert, P.; Camps, J. A.; Feitsma, R. I.; Nieuwenhuizen, W.; Pauwels, E. K. An in vitro model for the scintigraphic detection of thrombi using a 99Tcm-labelled antifibrin monoclonal antibody. *Nucl Med Commun* **1989,** *10*, (9), 653-9.

178. Wasser, M. N.; Koppert, P. W.; Arndt, J. W.; Emeis, J. J.; Feitsma, R. I.; Pauwels, E. K.; Nieuwenhuizen, W. An antifibrin monoclonal antibody useful in immunoscintigraphic detection of thrombi. *Blood* **1989,** *74*, (2), 708-14.

179. Wasser, M. N.; Pauwels, E. K.; Nieuwenhuizen, W. Thrombus detection using a Tc-99m labeled antifibrin monoclonal antibody (MoAb). Experiments in vitro and in animals. *Thromb Res Suppl* **1990,** *10*, 91-104.

180. Gargan, P. E.; Ploplis, V. A.; Scheu, J. D. A fibrin specific monoclonal antibody which interferes with the fibrinolytic effect of tissue plasminogen activator. *Thromb Haemost* **1988,** *59*, (3), 426-31.

181. Houranieh, A.; Statland, B. E.; Davis, G. L.; Ito, R. K.; Relias, V.; Kudryk, B.; Yunis, E. J. Monoclonal antibody to human cross-linked fibrin. *Hybridoma* **1988,** *7*, (1), 55-68.

182. Raut, S.; Gaffney, P. J. Evaluation of the fibrin binding profile of two anti-fibrin monoclonal antibodies. *Thromb Haemost* **1996,** *76*, (1), 56-64.

183. Tymkewycz, P. M.; Creighton Kempsford, L. J.; Gaffney, P. J. Generation and partial characterization of five monoclonal antibodies with high affinities for fibrin. *Blood Coagul Fibrinolysis* **1993,** *4*, (2), 211-21.

184. Edgell, T.; McEvoy, F.; Webbon, P.; Gaffney, P. J. Monoclonal antibodies to human fibrin: interaction with other animal fibrins. *Thromb Haemost* **1996,** *75*, (4), 595-9.

185. Gargan, P. E.; Gaffney, P. J.; Pleasants, J. M.; Ploplis, V. A. A Monoclonal-Antibody Which Recognizes An Epitopic Region Unique To The Intact Fibrin Polymeric Structure. *Fibrinolysis* **1993,** *7*, 275-283.

186. Line, B. R.; Weber, P. B.; Lukasiewicz, R.; Dansereau, R. N. Reduction of background activity through radiolabeling of antifibrin Fab' with 99mTc-dextran. *J Nucl Med* **2000,** *41*, (7), 1264-70.

187. Line, B. R.; Keenan, J. F.; Lukasiewicz, R. L.; Dansereau, R. N.; Tublin, M. E.; Williams, L. M.; Gargan, P. E. Cardiopulmonary thromboembolism detected by Tc-99m MH-1 antifibrin antibody. *Clin Nucl Med* **1997,** *22*, (6), 376-9.

188. Gaffney, P. J.; Creighton, L. J.; Perry, M. J.; Callus, M.; Thorpe, R.; Spitz, M. Monoclonal antibodies to crosslinked fibrin degradation products (XL-FDP). I. Characterization and preliminary evaluation in plasma. *Br J Haematol* **1988,** *68*, (1), 83-90.

189. Liau, C. S.; Su, C. T. Imaging of experimental arterial thrombi with iodine-131-labeled fibrin-specific monoclonal antibody. *Taiwan Yi Xue Hui Za Zhi* **1989,** *88*, (3), 209-12.

190. Xia, L. J.; Li, P. X.; Zhao, Y. M.; Wang, Q. C.; Xi, X. D.; Ruan, C. G. Antifibrin monoclonal antibodies for the detection of venous thrombosis. *Chin Med J (Engl)* **1994,** *107*, (7), 483-6.

191. Ruan, C.; Wang, Q.; He, G.; Wu, J. Radioimmunoimaging of arterial and venous thrombi in canine model using 99mTc labeled monoclonal antifibrin antibody. *Chin Med J (Engl)* **1997,** *110*, (1), 69-72.

192. Morris, T. A. SPECT imaging of pulmonary emboli with radiolabeled thrombus-specific imaging agents. *Semin Nucl Med* **2010,** *40*, (6), 474-9.

193. Buller, H. R.; Agnelli, G.; Hull, R. D.; Hyers, T. M.; Prins, M. H.; Raskob, G. E. Antithrombotic therapy for venous thromboembolic disease: the Seventh ACCP Conference on Antithrombotic and Thrombolytic Therapy. *Chest* **2004,** *126*, (3 Suppl), 401S-428S.

194. Lee, F. T.; Boniface, G. R.; Lambrecht, R. M.; Rylatt, D. B.; Bundesen, P. G. Technetium-99 m labelling of DD-3B6/22 antifibrin monoclonal antibody fragment Fab' for thrombus imaging. *Immunol Cell Biol* **1993,** *71 (Pt 2)*, 117-24.

195. Hillyard, C. J.; Blake, A. S.; Wilson, K.; Rylatt, D. B.; Miles, S.; Bunch, R.; Elms, M. J.; Barnes, A.; Bundesen, P. G. A latex agglutination assay for D dimer: evaluation and application to the diagnosis of thrombotic disease. *Clin Chem* **1987,** *33*, (10), 1837-40.

196. Knight, L. C. Non-oncologic applications of radiolabeled peptides in nuclear medicine. *Q J Nucl Med* **2003,** *47*, (4), 279-91.

197. Taillefer, R. Radiolabeled peptides in the detection of deep venous thrombosis. *Semin Nucl Med* **2001,** *31*, (2), 102-23.

198. Weiner, R. E.; Thakur, M. L. Radiolabeled peptides in diagnosis and therapy. *Semin Nucl Med* **2001,** *31*, (4), 296-311.

199. Ezov, N.; Nimrod, A.; Parizada, B.; Werber, M. M.; Goldlust, A.; Greenstein, L. A.; Vogel, T.; Drizlich, N.; Levanon, A.; Reich, S.; Gorecki, M.; Panet, A. Recombinant polypeptides derived from the fibrin binding domain of fibronectin are potential agents for the imaging of blood clots. *Thromb Haemost* **1997,** *77*, (4), 796-803.

200. Rosenthall, L.; Leclerc, J. A new thrombus imaging agent. Human recombinant fibrin binding domain labeled with In-111. *Clin Nucl Med* **1995,** *20*, (5), 398-402.

201. Tung, C. H.; Ho, N. H.; Zeng, Q.; Tang, Y.; Jaffer, F. A.; Reed, G. L.; Weissleder, R. Novel factor XIII probes for blood coagulation imaging. *Chembiochem* **2003,** *4*, (9), 897-9.

202. Skotland, T.; Hustvedt, S. O.; Oulie, I.; Jacobsen, P. B.; Friisk, G. A.; Langoy, A. S.; Uran, S.; Sandosham, J.; Cuthbertson, A.; Toft, K. G. Nc100668, a new tracer for imaging of venous thromboembolism: disposition and metabolism in rats. *Drug Metab Dispos* **2006,** *34*, (1), 111-20.

203. Toft, K. G.; Oulie, I.; Skotland, T. Quantification of NC100668, a new tracer for imaging of venous thromboembolism, in human plasma using reversed-phase liquid chromatography coupled with electrospray ionization ion-trap mass spectrometry. *J Chromatogr B Analyt Technol Biomed Life Sci* **2005,** *829*, (1-2), 91-6.

204. Edwards, D.; Lewis, J.; Battle, M.; Lear, R.; Farrar, G.; Barnett, D. J.; Godden, V.; Oliveira, A.; Coombes, C.; Ahlstrom, H. (99m)Tc-NC100668, a new tracer for imaging venous thromboemboli: pre-clinical biodistribution and incorporation into plasma clots in vivo and in vitro. *Eur J Nucl Med Mol Imaging* **2006,** *33*, (11), 1258-65.

205. Edwards, D.; Lewis, J.; Battle, M.; Lear, R.; Farrar, G.; Jon Barnett, D.; Godden, V.; Oliveira, A.; Coombes, C.; Ahlstrom, H. 99mTc-NC100668, an agent for imaging venous thromboembolism: The effect of anticoagulant or thrombolytic therapy on the uptake and retention of radioactivity in blood clots in vivo. *Nucl Med Commun* **2007,** *28*, (1), 55-62.

206. Edwards, D.; Battle, M.; Lear, R.; Farrar, G.; Barnett, D. J.; Godden, V.; Coombes, C.; Oliveira, A.; Ahlstrom, H. The in vivo and in vitro metabolic profile of 99mTc-NC100668, a new tracer for imaging venous thromboembolism: identification and biodistribution of the principal radiolabeled metabolite. *Drug Metab Dispos* **2006,** *34*, (7), 1128-35.

207. Toft, K. G.; Johnson, J. A.; Oulie, I.; Skotland, T. NC100668, a new tracer tested for imaging of venous thromboembolism: pharmacokinetics and metabolism in humans. *Drug Metab Dispos* **2007,** *35*, (11), 1979-84.

208. Majmudar, M. D.; Keliher, E. J.; Heidt, T.; Leuschner, F.; Truelove, J.; Sena, B. F.; Gorbatov, R.; Iwamoto, Y.; Dutta, P.; Wojtkiewicz, G.; Courties, G.; Sebas, M.; Borodovsky, A.; Fitzgerald, K.; Nolte, M. W.; Dickneite, G.; Chen, J. W.; Anderson, D. G.; Swirski, F. K.; Weissleder, R.; Nahrendorf, M. Monocyte-directed RNAi targeting CCR2 improves infarct healing in atherosclerosis-prone mice. *Circulation* **2013,** *127*, (20), 2038-46.

209. Nahrendorf, M.; Aikawa, E.; Figueiredo, J. L.; Stangenberg, L.; van den Borne, S. W.; Blankesteijn, W. M.; Sosnovik, D. E.; Jaffer, F. A.; Tung, C. H.; Weissleder, R. Transglutaminase activity in acute infarcts predicts healing outcome and left ventricular remodelling: implications for FXIII therapy and antithrombin use in myocardial infarction. *Eur Heart J* **2008,** *29*, (4), 445-54.

210. Nahrendorf, M.; Hu, K.; Frantz, S.; Jaffer, F. A.; Tung, C. H.; Hiller, K. H.; Voll, S.; Nordbeck, P.; Sosnovik, D.; Gattenlohner, S.; Novikov, M.; Dickneite, G.; Reed, G. L.; Jakob, P.; Rosenzweig, A.; Bauer, W. R.; Weissleder, R.; Ertl, G. Factor XIII deficiency causes cardiac rupture, impairs wound healing, and aggravates cardiac remodeling in mice with myocardial infarction. *Circulation* **2006,** *113*, (9), 1196-202.

211. Thakur, M. L.; Pallela, V. R.; Consigny, P. M.; Rao, P. S.; Vessileva-Belnikolovska, D.; Shi, R. Imaging vascular thrombosis with 99mTc-labeled fibrin alpha-chain peptide. *J Nucl Med* **2000,** *41*, (1), 161-8.

212. Aruva, M. R.; Daviau, J.; Sharma, S. S.; Thakur, M. L. Imaging thromboembolism with fibrin-avid 99mTc-peptide: evaluation in swine. *J Nucl Med* **2006,** *47*, (1), 155-62.

213. Overoye-Chan, K.; Koerner, S.; Looby, R. J.; Kolodziej, A. F.; Zech, S. G.; Deng, Q.; Chasse, J. M.; McMurry, T. J.; Caravan, P. EP-2104R: a fibrin-specific gadolinium-Based MRI contrast agent for detection of thrombus. *J Am Chem Soc* **2008,** *130*, (18), 6025-39.

214. Makowski, M. R.; Forbes, S. C.; Blume, U.; Warley, A.; Jansen, C. H.; Schuster, A.; Wiethoff, A. J.; Botnar, R. M. In vivo assessment of intraplaque and endothelial fibrin in ApoE(-/-) mice by molecular MRI. *Atherosclerosis* **2012,** *222*, (1), 43-9.

215. Sirol, M.; Fuster, V.; Badimon, J. J.; Fallon, J. T.; Moreno, P. R.; Toussaint, J. F.; Fayad, Z. A. Chronic thrombus detection with in vivo magnetic resonance imaging and a fibrin-targeted contrast agent. *Circulation* **2005,** *112*, (11), 1594-600.

216. Spuentrup, E.; Buecker, A.; Katoh, M.; Wiethoff, A. J.; Parsons, E. C., Jr.; Botnar, R. M.; Weisskoff, R. M.; Graham, P. B.; Manning, W. J.; Gunther, R. W. Molecular magnetic resonance imaging of coronary thrombosis and pulmonary emboli with a novel fibrin-targeted contrast agent. *Circulation* **2005,** *111*, (11), 1377-82.

217. Spuentrup, E.; Katoh, M.; Buecker, A.; Fausten, B.; Wiethoff, A. J.; Wildberger, J. E.; Haage, P.; Parsons, E. C., Jr.; Botnar, R. M.; Graham, P. B.; Vettelschoss, M.; Gunther, R. W. Molecular MR imaging of human thrombi in a swine model of pulmonary embolism using a fibrin-specific contrast agent. *Invest Radiol* **2007,** *42*, (8), 586-95.

218. Spuentrup, E.; Katoh, M.; Wiethoff, A. J.; Parsons, E. C., Jr.; Botnar, R. M.; Mahnken, A. H.; Gunther, R. W.; Buecker, A. Molecular magnetic resonance imaging of pulmonary emboli with a fibrin-specific contrast agent. *Am J Respir Crit Care Med* **2005,** *172*, (4), 494-500.

219. Uppal, R.; Medarova, Z.; Farrar, C. T.; Dai, G.; Moore, A.; Caravan, P. Molecular imaging of fibrin in a breast cancer xenograft mouse model. *Invest Radiol* **2012,** *47*, (10), 553-8.

220. Vymazal, J.; Spuentrup, E.; Cardenas-Molina, G.; Wiethoff, A. J.; Hartmann, M. G.; Caravan, P.; Parsons, E. C., Jr. Thrombus imaging with fibrin-specific gadolinium-based MR contrast agent EP-2104R: results of a phase II clinical study of feasibility. *Invest Radiol* **2009,** *44*, (11), 697-704.

221. Spuentrup, E.; Botnar, R. M.; Wiethoff, A. J.; Ibrahim, T.; Kelle, S.; Katoh, M.; Ozgun, M.; Nagel, E.; Vymazal, J.; Graham, P. B.; Gunther, R. W.; Maintz, D. MR imaging of thrombi using EP-2104R, a fibrin-specific contrast agent: initial results in patients. *Eur Radiol* **2008,** *18*, (9), 1995-2005.

222. Uppal, R.; Catana, C.; Ay, I.; Benner, T.; Sorensen, A. G.; Caravan, P. Bimodal thrombus imaging: simultaneous PET/MR imaging with a fibrin-targeted dual PET/MR probe--feasibility study in rat model. *Radiology* **2011,** *258*, (3), 812-20.

223. Boswell, C. A.; Sun, X.; Niu, W.; Weisman, G. R.; Wong, E. H.; Rheingold, A. L.; Anderson, C. J. Comparative in vivo stability of copper-64-labeled cross-bridged and conventional tetraazamacrocyclic complexes. *J Med Chem* **2004,** *47*, (6), 1465-74.

224. Bass, L. A.; Wang, M.; Welch, M. J.; Anderson, C. J. In vivo transchelation of copper-64 from TETA-octreotide to superoxide dismutase in rat liver. *Bioconjug Chem* **2000,** *11*, (4), 527-32.

225. Ciesienski, K. L.; Yang, Y.; Ay, I.; Chonde, D. B.; Loving, G. S.; Rietz, T. A.; Catana, C.; Caravan, P. Fibrin-targeted PET probes for the detection of thrombi. *Mol Pharm* **2013,** *10*, (3), 1100-10.

226. Boros, E.; Rybak-Akimova, E.; Holland, J. P.; Rietz, T.; Rotile, N.; Blasi, F.; Day, H.; Latifi, R.; Caravan, P. Pycup-A Bifunctional, Cage-like Ligand for (64)Cu Radiolabeling. *Mol Pharm* **2014,** *11*, (2), 617-29.

227. Ay, I.; Blasi, F.; Rietz, T. A.; Rotile, N. J.; Kura, S.; Brownell, A. L.; Day, H.; Oliveira, B. L.; Looby, R. J.; Caravan, P. In vivo molecular imaging of thrombosis and thrombolysis using a fibrin-binding positron emission tomographic probe. *Circ Cardiovasc Imaging* **2014,** *7*, (4), 697-705.

228. Blasi, F.; Oliveira, B. L.; Rietz, T. A.; Rotile, N. J.; Day, H.; Looby, R. J.; Ay, I.; Caravan, P. Effect of Chelate Type and Radioisotope on the Imaging Efficacy of 4 Fibrin-Specific PET Probes. *J Nucl Med* **2014,** *55*, (7), 1157-1163.

Chapter 2

SPECT imaging of fibrin using fibrin-binding peptides

Abstract

Noninvasive detection of fibrin *in vivo* using diagnostic imaging modalities may improve clinical decision making on possible therapeutic options in atherosclerosis, cancer and thrombus-related pathologies such as pulmonary embolism and deep venous thrombosis. The aim of this study was to assess the potential of a novel ^{111}In-labeled fibrin-binding peptide (FibPep) to visualize thrombi in mice noninvasively using single-photon emission computed tomography (SPECT). FibPep and a negative control peptide (NCFibPep) were synthesized and their fibrin-binding properties were assessed *in vitro*. FibPep showed enhanced binding compared to NCFibPep to both fibrin and blood clots. FibPep bound to fibrin with a dissociation constant (K_d) of 0.8 μM, whereas NCFibPep displayed at least a 100-fold lower affinity towards fibrin. A $FeCl_3$-injury carotid artery thrombosis mouse model was used to evaluate the peptides *in vivo*. FibPep and NCFibPep displayed rapid blood clearance and were eliminated via the renal pathway. *In vivo* SPECT imaging using FibPep allowed clear visualization of thrombi. *Ex vivo* biodistribution showed significantly increased uptake of FibPep in the thrombus-containing carotid in comparison to the non-injured carotid (5.7 ± 0.7 and 0.6 ± 0.4% injected dose per gram (% ID/g), respectively; $p < 0.01$; n=4), whereas non-specific NCFibPep did not (0.4 ± 0.2 and 0.3 ± 0.0% ID/g, respectively; n=4). In conclusion, FibPep displayed high affinity towards fibrin *in vitro*, rapid blood clearance *in vivo* and allowed sensitive detection of thrombi using SPECT imaging. Therefore, this particular imaging approach may provide a new tool to diagnose and monitor diseases such as atherosclerosis and cancer.

This chapter is based on:

Starmans, L. W.; van Duijnhoven, S. M.; Rossin, R.; Aime, S.; Daemen, M. J.; Nicolay, K.; Grull, H. SPECT imaging of fibrin using fibrin-binding peptides. *Contrast Media Mol Imaging* **2013,** *8*, (3), 229-37.

2.1 Introduction

Thrombosis is the underlying pathology in a number of cardiovascular diseases, such as heart attack, deep venous thrombosis, pulmonary embolism and ischemic stroke.[1] These cardiovascular diseases represent a major cause of mortality in society and therefore development of thrombus-specific detection, characterization and treatment methodologies are of paramount importance in clinical practice. Currently, detection of (intravascular) thrombi is mostly pursued using indirect imaging modalities such as computed tomography angiography, ultrasound and ventilation/perfusion scintigraphy.[2, 3] Molecular imaging with nuclear techniques presents an alternative way to visualize thrombi in a more specific fashion, at a higher sensitivity and with lower limitations with respect to thrombus-location in the body.

A suitable target for molecular imaging of thrombi is fibrin, which is the major constituent of a thrombus and has the advantage that it is virtually absent in non-pathological situations, thus providing a beneficial target-to-background ratio. In addition to molecular imaging of intravascular thrombi, fibrin-targeted probes may allow assessment of atherosclerotic plaque vulnerability, as microthrombi on the surface of plaques are direct indicators of microfissures in the fibrous cap,[4] and as fibrin is present in plaques displaying intraplaque hemorrhage, a process associated with plaque destabilization.[5] Molecular imaging of cancer is another field in which fibrin-targeted probes might be of value, as fibrin deposition is associated with a variety of malignant tumors, including breast, lung, brain and prostate.[6] Fibrin has a pivotal role in tumor stroma formation and deposition of fibrin has been shown to facilitate tumor angiogenesis and metastasis.[6-8] The presence of fibrin in tumor stroma can also be exploited to facilitate cancer treatment, as fibrin-targeted monoclonal antibodies were recently shown to be successful vehicles for directing cytotoxic immunoconjugates to solid tumors.[9] Hence, fibrin-targeted probes seem promising for diagnostic and therapeutic applications in a variety of thrombus-related cardiovascular pathologies and cancer.

Strategies employing ^{99m}Tc-labeled fibrin-targeted antibody fragments and linear peptides have been investigated to image deep venous thrombosis and pulmonary embolism in preclinical and clinical studies in the past 15 years.[10-13] Recently, the cyclic fibrin-binding peptide EP-2104R, containing the fibrin-binding motif Y-dGlu-C-Hyp-3CLY-GLCYIQ and 4 Gd-DOTA moieties, was successfully used for magnetic resonance imaging (MRI) of fibrin in both preclinical and clinical studies.[14-18] For detection of minute fibrin deposits, however, highly sensitive nuclear imaging using radiolabeled cyclic fibrin-binding peptides might be a more suitable option. In addition, targeted MRI-probes labeled with Gd will likely have to overcome safety issues concerning nephrogenic systemic fibrosis,[19] and therefore their nuclear counterparts might be more readily translatable in the clinic. Here we describe a proof-of-concept study in which an ^{111}In-labeled DOTA-conjugated fibrin-binding peptide (FibPep; Fig. 1A), containing the cyclic fibrin-binding motif RWQPCPAESWT-Cha-CWDP,[20] was developed to visualize fibrin noninvasively using single-photon emission computed tomography (SPECT). *In vitro* fibrin and blood clot binding of FibPep was assessed in comparison to a scrambled, linear control probe (NCFibPep; Fig. 1B). Then, we evaluated the potential of FibPep for SPECT imaging of fibrin in a preclinical study using a well-

established $FeCl_3$-induced carotid injury thrombosis model in mice.[21-24] Blood kinetic and biodistribution profiles of FibPep and NCFibPep were also obtained and, finally, *in vivo* SPECT/CT imaging was performed.

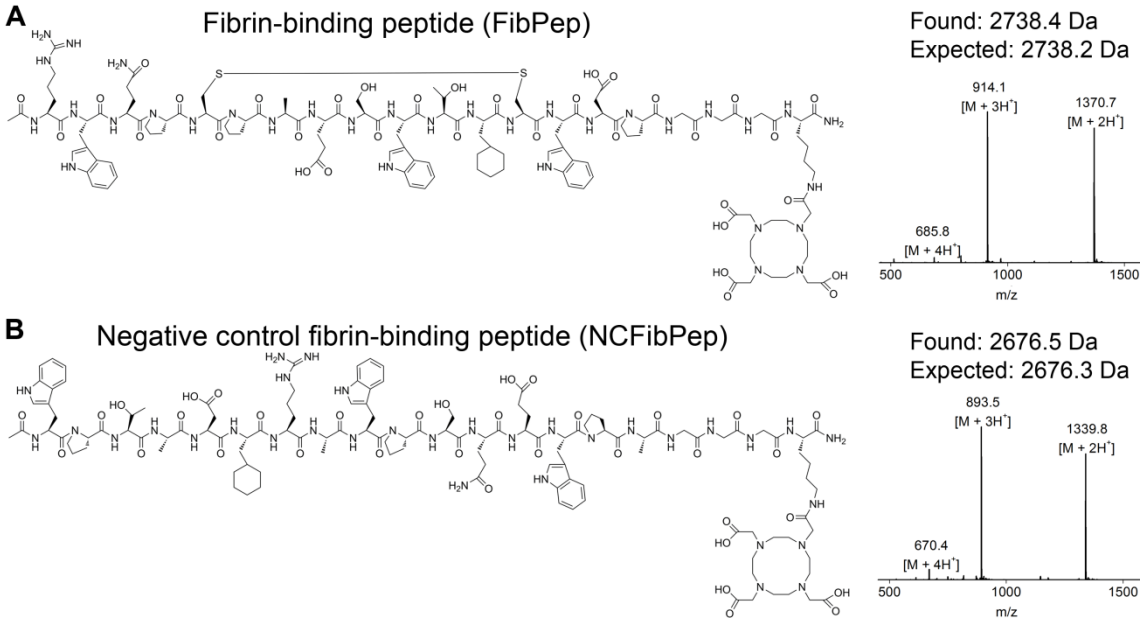

Figure 1. *Structural formulas and corresponding mass spectra of (A) FibPep and (B) NCFibPep.*

2.2 Results and Discussion

2.2.1 Synthesis and in vitro validation of the peptide probes

The synthesized peptides were analyzed using LC-MS and the found masses were in agreement with the expected ones (Fig. 1). Radiolabeling with ^{111}In resulted in ≥ 95% yield and radiochemical purity for both peptides (Fig. S1). *In vitro* binding studies showed significantly higher binding to fibrin for FibPep with respect to NCFibPep and free ^{111}In (85.8 ± 3.8, 1.2 ± 2.5 and 2.1 ± 4.2% dose, respectively; $p < 0.01$; Fig. 2A). In addition, FibPep exhibited significantly higher binding to blood clots than NCFibPep and free ^{111}In (32.2 ± 7.1, 5.1 ± 1.7 and 1.0 ± 0.7% dose, respectively; $p < 0.01$; Fig. 2B). To investigate the fibrin-binding properties of the probes in more detail, the affinity towards fibrin was analyzed in a microtiter-plate equilibrium binding assay.[25, 26] FibPep bound with good affinity to fibrin (K_d= 0.8 ± 0.1 µM, Fig. 2C) and the number of binding sites per fibrin molecule was 2.8 ± 0.1. In comparison, NCFibPep bound at least 100-fold weaker to fibrin (Fig. 2C).

2.2.2 Blood kinetic and biodistribution profiles

Figure 3A shows the blood kinetics of ^{111}In-labeled FibPep and NCFibPep in mice. Both peptides exhibited biphasic elimination from circulation. FibPep showed an α half-life of 1 min (58%) and a β half-life of 16 min, resulting in less than 1% ID/g in blood 90 min post injection (PI). After 4 h, only 0.1% ID/g was still present in the blood pool, corresponding to less than 0.3% of total injected dose. NCFibPep showed similar elimination kinetics (α half-life = 2 min (55%); β half-life = 20 min). The calculated volumes of distribution (V_D) were 0.20 ± 0.05 and 0.17 ± 0.01 L/kg for FibPep and NCFibPep,

respectively, suggesting rapid distribution of the peptides throughout the extra-vascular space without cell membrane crossing.[27] The biodistribution profiles of the probes 4 h PI showed low uptake in the majority of the considered organs (< 1.4% ID/g; Fig. 3B) and higher uptake in kidneys (7.1 ± 0.9 and 12.9 ± 4.2% ID/g for FibPep and NCFibPep, respectively; p = 0.07).

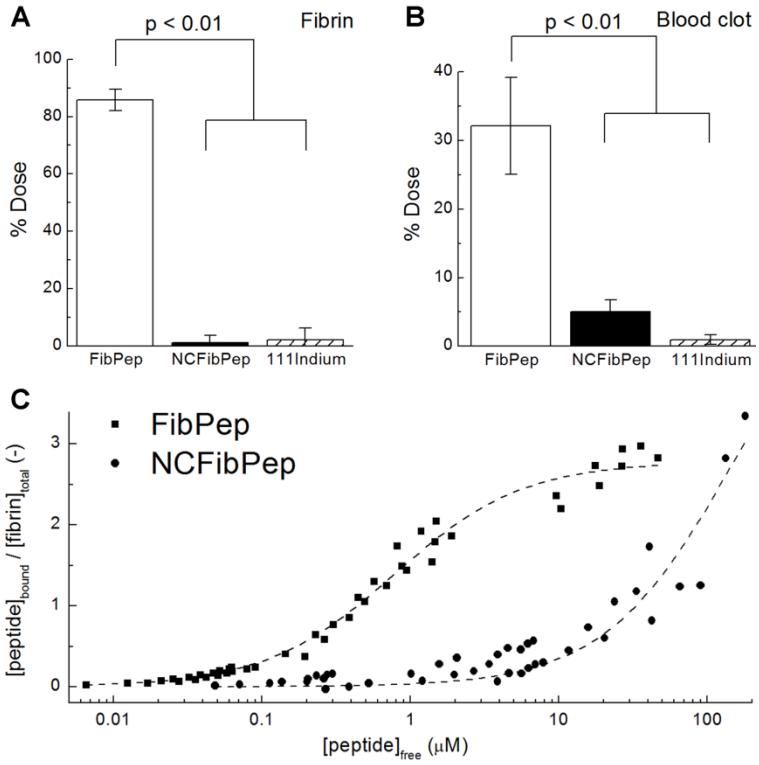

Figure 2. *Binding of ^{111}In-labeled FibPep (empty bars), NCFibPep (solid bars) and $^{111}InCl_3$ (dashed bars) to (A) fibrin and (B) blood clots. Data are the mean % dose ± SD (n=4). (C) FibPep and NCFibPep fibrin affinity curves, dashed lines plotted as described in the text.*

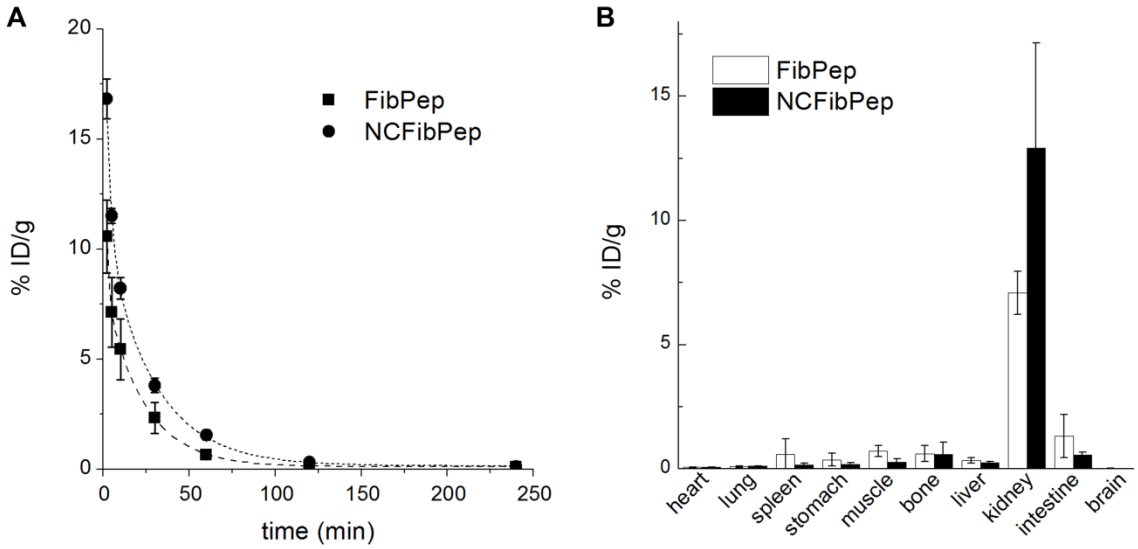

Figure 3. *(A) blood kinetic and (B) biodistribution profiles of FibPep and NCFibPep 4 h post injection. Data are the mean % ID/g ± SD (n=4). Plotted dashed lines are the corresponding bi-exponential elimination fits.*

2.2.3 In vivo SPECT studies

In vivo SPECT was performed starting 90 minutes PI with a total scan time of approximately 1.6 h. Subsequently, the mice were euthanized and overnight post-mortem SPECT scans were performed. In mice injected with ^{111}In-labeled FibPep, a high SPECT signal was observed in the thrombus-containing carotid for both *in vivo* and post-mortem SPECT scans, whereas this was not the case in the mice that received NCFibPep (Fig. 4). The surgical wound bed was visible in both groups of mice, most likely due to FibPep binding to clotted blood at the wound site and to non-specific deposition of both tracers in the surgical wound bed, possibly due to edema formation and deposition of fluid on the skin around the surgical wound.[24] Besides these focal uptakes, only kidney and bladder were visible in the post-mortem full body scans (Fig. 5) suggesting renal elimination of both radiolabeled peptides. Quantification of the signal in VOIs drawn over the injured carotids showed a significantly higher uptake of FibPep with respect to NCFibPep ($p < 0.02$), suggesting specific binding to fibrin (Fig. 6). FibPep uptake in the blood clot was 9-to-14 times higher than that in muscle while the carotid-to-muscle ratio was lower (2-to-4) in mice injected with NCFibPep (Fig. S2A). Similar differences of the uptake ratios between the two tracers were observed using the contralateral area as normalization region (Fig. S2B).

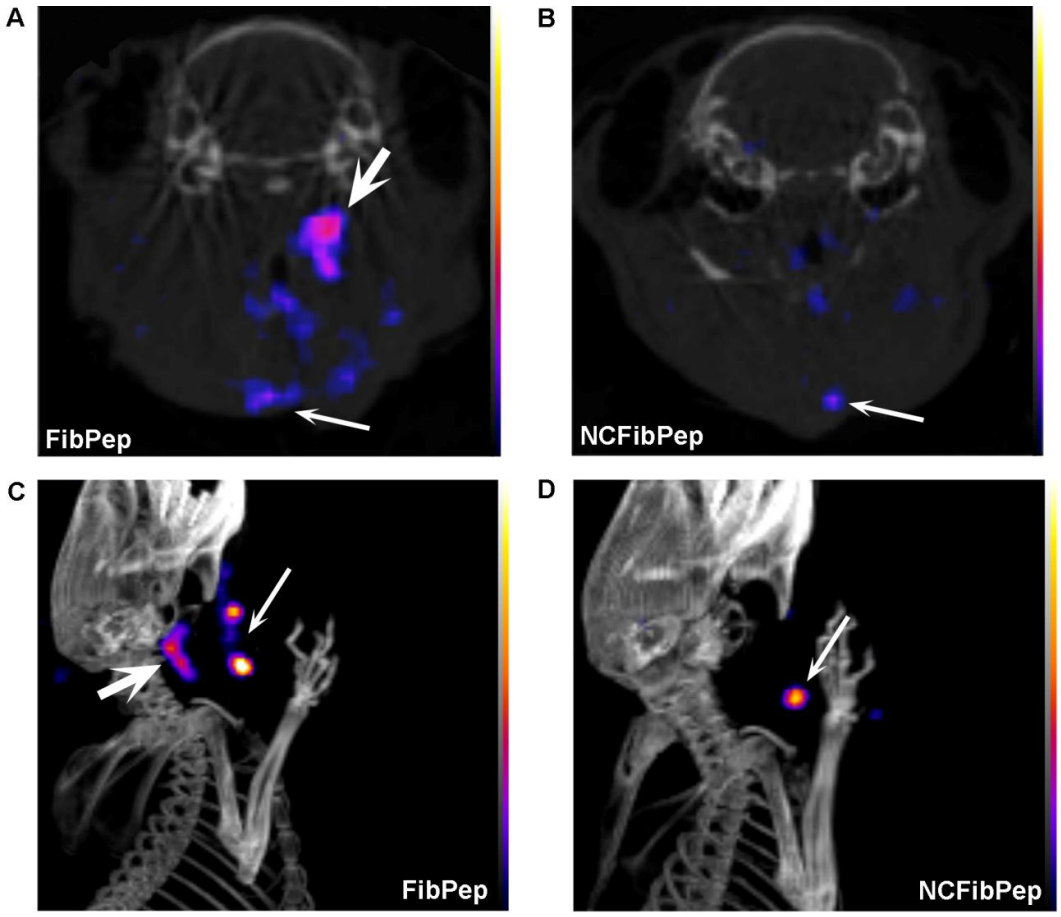

Figure 4. *SPECT/CT imaging using FibPep and NCFibPep. SPECT/CT images (transversal slices, 90 min post injection) of live mice injected with (A) FibPep and (B) NCFibPep. Post-mortem maximum intensity projection of the neck area of mice injected with (C) FibPep and (D) NCFibPep. Bold arrow = thrombus; thin arrow = surgical wound area.*

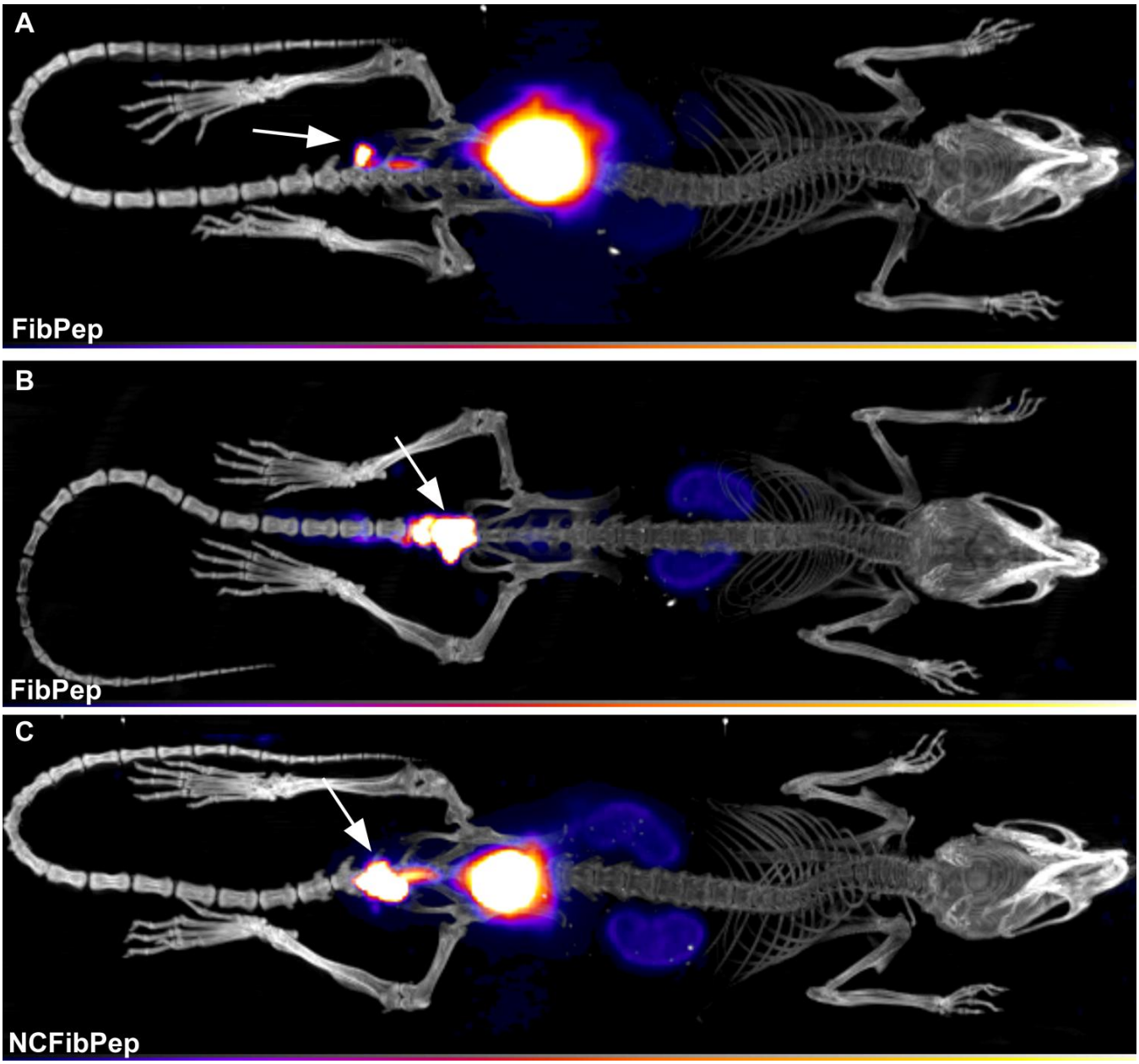

Figure 5. *Post-mortem whole body SPECT/CT images (maximum intensity projections) of mice injected with ^{111}In-labeled FibPep (A, B) and NCFibPep (C) showing high uptake in kidney and high activity in the urine. In (B) the bladder was emptied before the post-mortem SPECT scan to highlight the uptake in kidney. All images are on the same color scale. Arrows: urine contamination on the skin.*

These *in vivo* findings were confirmed by *ex vivo* γ-counting of the harvested tissues (Fig. 7). FibPep accumulated significantly more in the injured carotid than in the non-injured one and in muscle (5.7 ± 0.7, 0.6 ± 0.4 and 0.2 ± 0.2% ID/g, respectively; $p < 0.01$). NCFibPep uptake was significantly lower than that of FibPep in the injured carotid and no major differences were observed among the carotids and muscle in mice treated with the control peptide (0.4 ± 0.2% ID/g in injured carotid, 0.3 ± 0.0 in control carotid and 0.1 ± 0.1% ID/g in muscle; $p < 0.01$ with respect to FibPep injured carotid uptake). Hematoxylin and eosin stained histological sections confirmed the presence of thrombus in the injured carotid (Fig. 8).

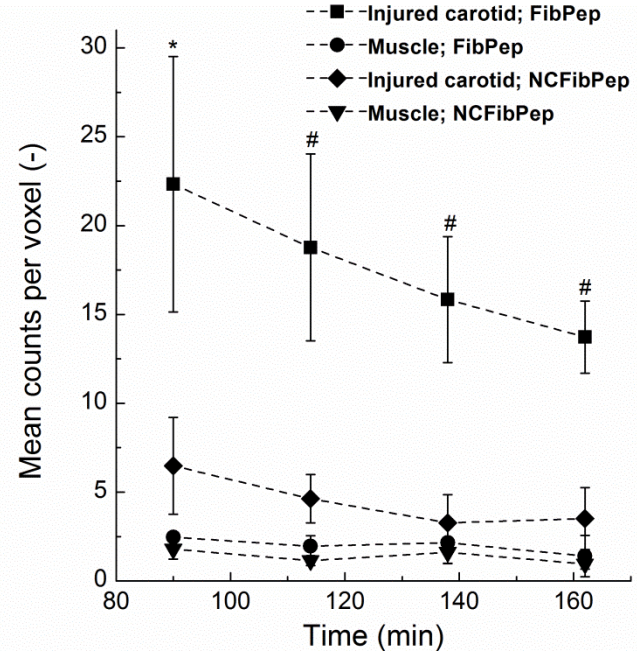

Figure 6. *Analysis of in vivo SPECT scans. Mean count per voxel in injured carotid and muscle area plotted against the time post injection of FibPep and NCFibPep. Data are the mean counts/voxel ± SD (n=4). * p < 0.02; # p < 0.01 for FibPep treated carotid vs. NCFibPep treated carotid and muscle (both probes).*

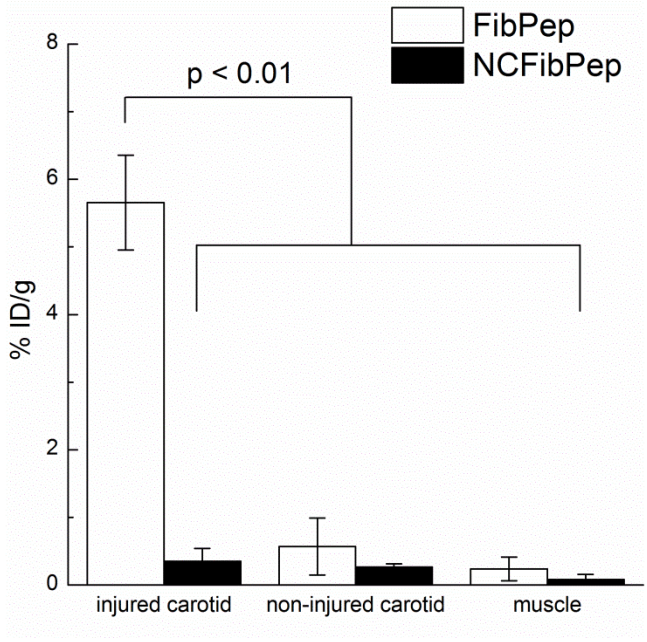

Figure 7. *Post-SPECT ex vivo quantification of FibPep (empty bars) and NCFipPep (solid bars) uptake in the injured carotid, non-injured carotid and muscle ca. 3.5 h post injection. Data are the mean % ID/g ± SD (n=4).*

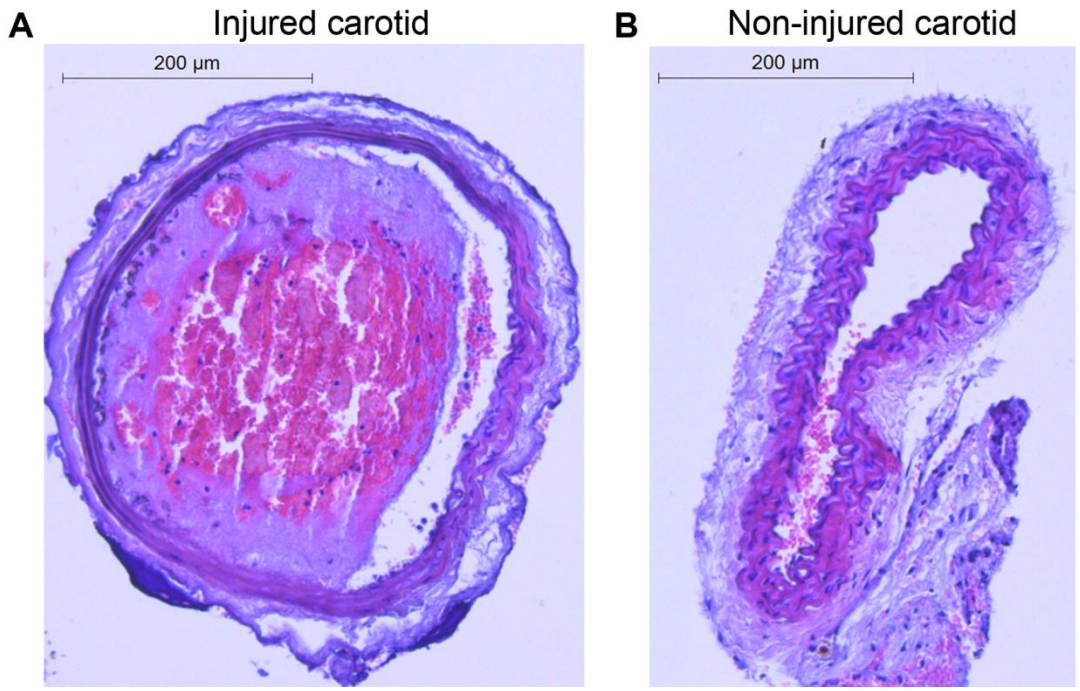

Figure 8. *Hematoxylin and eosin stained transversal histological sections of the (A) injured carotid artery and (B) the non-injured, contralateral carotid artery showing wall-adherent thrombosis for the injured carotid and not for the non-injured carotid.*

2.2.4 General discussion

The present study demonstrates the feasibility of highly sensitive noninvasive SPECT imaging of fibrin with the fibrin-binding peptide FibPep. Previous studies investigating EP-2104R, a paramagnetic labeled fibrin-binding peptide, have shown that this compound holds potential to visualize fibrin deposition using MRI in preclinical models of pulmonary embolism, atherosclerosis, coronary and carotid artery thrombosis, as well as in patients.[14-18, 28] In a phase II clinical trial, EP-2014R allowed the detection of thrombi which were not readily visible in pre-contrast MRI screening and enhanced signal intensity of thrombi that were already detected on pre-contrast scans. However, 71% of the thrombi located in the venous system remained undetected. This relatively high number of false negatives can probably be attributed to lack of sensitivity of molecular MRI. In a subsequent preclinical study, part of the Gd in the DOTA-chelator of EP-2104R was replaced with the positron-emitter ^{64}Cu for multi-modal PET/MR imaging and the obtained hybrid tracer was evaluated in rats injected with preformed thrombi.[29] In this model, T1-weighed molecular MRI was able to distinguish the occluded carotid artery 10 min after contrast agent injection, while the focal uptake of ^{64}Cu was clearly visible in PET images acquired 30-90 min PI. Such an approach might allow for more sensitive detection of fibrin deposition and also could eliminate the need for a baseline MR examination, which would eradicate issues with respect to co-registration of pre- and post-contrast images, complex workflow and patient compliance.

With these promising preclinical and clinical results in mind, we set out to evaluate the cyclic fibrin-binding amino acid sequence RWQPCPAESWT-Cha-CWDP, previously identified via phage-display using

fibrinogen-binder depleted libraries and subsequently optimized for fibrin-binding,[20, 30] for highly sensitive fibrin detection using nuclear imaging. For this purpose, the fibrin-binding sequence was linked to a DOTA chelator, yielding FibPep (Fig. 1), which could be readily labeled with ^{111}In. FibPep exhibited a good affinity towards fibrin (K_d = 0.8 μM) in an *in vitro* microtiter-plate equilibrium binding assay as opposed to the scrambled, linear peptide NCFibPep (K_d > 100 μM) which was used as negative control. The affinity of FibPep was slightly improved with respect to that of EP-2104R (K_d = 1.8 μM),[25] however the low micromolar affinity was not expected to be a major problem *in vivo* due to the high abundance of fibrin on clots.

The pharmacokinetics, biodistribution and *in vivo* fibrin targeting capabilities of the candidate tracer were evaluated in a mouse carotid injury model. Notably, FibPep cleared rapidly from the circulation, which is key to detect intra-vascular targets, as high blood levels of radioactivity might obscure thrombus-specific signal. Therefore, in this proof-of-concept study a 90 min delay after tracer injection was chosen for SPECT imaging to ensure sufficiently low FibPep blood levels. FibPep exhibited also a favorable biodistribution with low uptake (<1.3% ID/g) in most considered non-target tissues. Only kidney retained a significant amount of radioactivity 4 h PI (7.1 ± 0.9% ID/g), probably due to the negative charge of FibPep. However, this value is lower than that of other radiopeptides used in the clinic, such as ^{111}In-DOTATOC,[31] and therefore it is not expected to raise dosimetry concerns. The rapid blood clearance and low retention in most organs in conjunction with the finding that FibPep is able to extravasate supports the hypothesis that FibPep will likely be able to visualize its fibrin-target in most parts of the body within a useful time-frame.

Subsequently, *in vivo* SPECT imaging using the fibrin specific and non-specific peptides was performed to gauge the potential of FibPep for *in vivo* detection of fibrin deposition. FibPep allowed clear visualization of the small (~ 1 mm^3) thrombi generated in mice while the injured carotids of the mice injected with NCFibPep could not be distinguished from the surrounding tissues. Quantitative analysis of SPECT data was performed by drawing volumes of interest on the SPECT images, as the carotids were not visible on the CT scans. In the live mice the clot-to-muscle and clot-to-background (contra-lateral area) ratio did not change significantly during the assessed time-frame (90-162 min PI, Fig. S2) suggesting that less than 90 min elapse between injection and imaging might be feasible with short-lived radionuclides. However, the mean counts per voxel in the injured carotid area exhibited a declining trend during the assessed time frame for FibPep (Fig. 6), with an approximately 2 h half-life at the clot site. This half-life is ca.7-times longer than that of FibPep in circulation, suggesting specific FibPep retention in the clot.

Selecting small volumes of interest based on SPECT images is an inherently biased process. Therefore, in future studies we are planning to administer a long-circulating CT contrast agent to the mice in addition to FibPep,[32] which should allow clear visualization of the arteries by CT and better quantification of the SPECT data in the co-registered images. Also, the dosage and specific activity of the tracer were not optimized in this proof-of-concept study and, therefore, it is plausible that the pharmacokinetics,

targeting-efficiency and time between injection and detection can be further improved by optimizing these parameters. A limitation of the employed scrambled negative control peptide NCFibPep is the fact that the peptide has a linear structure, whereas FibPep is cyclic. Even though FibPep and NCFibPep are very similar in chemical nature, and have similar blood kinetic and biodistribution profiles, the current study set-up does not allow to investigate whether part of the binding property of the peptide is actually due to the cyclic nature of the peptide, and not because of the specific amino acid sequence. Interestingly, Uppal and co-workers showed recently that for the EP-2104R peptide, linearization of the peptide obliterates any specificity towards fibrin.[33] It is not unlikely that a linearized, non-scrambled version of FibPep also has virtually no affinity towards fibrin.

The presented results show promise for FibPep as a SPECT-agent for thrombus-detection and provide a solid foundation for further exploration of the potential of FibPep in animal models of e.g. atherosclerosis and cancer. Employing SPECT as imaging modality for detection of fibrin deposition is especially of interest for future applications concerning the evaluation of atherosclerotic plaque vulnerability and cancer, as multi-isotope SPECT imaging allows simultaneous assessment of multiple biomarkers,[34, 35] which is vital for obtaining reliable and robust read-outs of complex pathological systems such as tumors and atherosclerotic lesions. Furthermore, the use of DOTA allows a rapid translation of this SPECT tracer into a PET tracer, e.g. by using ^{68}Ga- or Al^{18}F-labeling approaches.[36, 37] FibPep does not contain Gd^{3+} ions and therefore avoids the risk of inducing nephrogenic systemic fibrosis, which is linked to extended retention of Gd in the body in combination with less stable Gd-chelates.[19, 38] Thanks to the high sensitivity of nuclear imaging, radiotracers can be administered at very low doses, reducing the risk of toxicity or pharmacological effects. Thus nuclear probes like FibPep may have to overcome lower hurdles for clinical translation and commercialization compared to MRI probes.

2.3 Conclusions

The present proof-of-concept study demonstrates the ability of ^{111}In-labeled FibPep to noninvasively image minute thrombi *in vivo* using SPECT. If further successfully validated and translated, this particular imaging approach may provide a new tool to diagnose and monitor atherosclerosis, cancer and thrombus-related pathologies such as pulmonary embolism and deep venous thrombosis.

2.4 Experimental

2.4.1 Synthesis of the peptide probes

9-fluorenylmethyloxycarbonyl–protected L-amino acids and Rink amide resin were purchased from either Novabiochem(Merck) or Bachem. The fibrin-binding peptide Ac-RWQPCPAESWT-Cha-CWDPGGGK-NH_2 and a scrambled negative control Ac-WPTAD-Cha-RAWPSQEWPAGGGK-NH_2 with C-A substitutions were synthesized on 4-methylbenzhydrylamine hydrochloride salt rink amide resin by the use of standard 9-fluorenylmethyloxycarbonyl solid-phase peptide synthesis. The fibrin-binding peptide contains the fibrin-binding motif RWQPCPAESWT-Cha-CWDP, which was previously identified via phage-display using fibrinogen-binder depleted libraries and subsequently optimized for fibrin-binding.[20, 30] The peptides were cleaved from the resin with a trifluoroacetic acid : triisopropylsilane :

H_2O : ethanedithiol (90.5:5:2.5:2 v/v) mixture for 3 h and purified by preparative reversed-phase high-pressure liquid chromatography (RP-HPLC) using an Agilent 1200 apparatus equipped with a C_{18} Zorbax column (150 x 21.2 mm; 5.0 µm particle size). The peptide Ac-RWQPCPAESWT-Cha-CWDPGGGK-NH_2 was cyclisized via the formation of a disulfide bond between the cysteine residues in dimethylsulfoxide:H_2O (9:1 v/v) for 5 days with the pH set to 8 using N-methyl-D-glucamine (Sigma Aldrich),[20] and subsequently purified using preparative RP-HPLC. Next, the peptides were functionalized at the lysine ε-amino group with 1,4,7,10-tetraazacyclododecane-1,4,7,10-tetraacetic acid (DOTA) by mixing the peptides and a 7-fold excess of DOTA-NHS ester (Macrocyclics) in dimethylformamide containing 3.6% (v/v) triethylamine at room temperature overnight. Finally, the peptides were purified using preparative RP-HPLC, yielding the DOTA-functionalized fibrin-binding peptide (FibPep) and negative control (NCFibPep) (Fig. 1). The peptide structures were analyzed by liquid chromatography–mass spectrometry (LC-MS) on an Agilent 1200 apparatus, equipped with a C_8 Eclipse plus column (100 x 2.1 mm; 3.5 µm particle size) and an electrospray mass spectrometer (time-of-flight LC-MS model 6210; Agilent Technologies).

2.4.2 Radiolabeling

$^{111}InCl_3$ (PerkinElmer) was mixed with FibPep or NCFibPep in ammonium acetate buffer (0.2-0.25M, pH 6, 35-200 µL) and shaken (350 rpm) for 60 min at 75 °C. For *in vivo* experiments the mixture was subsequently diluted with saline and challenged with an equivalent dose of diethylene triamine pentaacetic acid (DTPA; Sigma-Aldrich).

The ^{111}In-labeling yield was determined using radio thin-layer chromatography (TLC) and the radiochemical purity was determined by radio-HPLC. TLC was performed on instant TLC silica gel strips (Varian Inc.) eluted with 200 mM ethylenediaminetetetraacetic acid (EDTA) in saline. The strips were imaged on a phosphor imager (FLA-7000; Fujifilm) and the labeling yields were quantified with AIDA Image Analyzer software. Analytical radio-HPLC was performed on an Agilent 1100 system equipped with a C_{18} Eclipse XBD column (150 x 4.6 mm; 5 µm particle size) and a Gabi radioactive detector (Raytest). The radiolabeled peptides did not undergo any purification procedures prior to use.

2.4.3 In vitro fibrin and blood clot binding assays

2.4.3.1 Fibrin binding: fibrin coated tubes were prepared by adding 4 µL of 100 U/mL human thrombin (Sigma Aldrich) in ultrapure water (Millipore) to 200 µL of 2.9 mg/mL human fibrinogen (Sigma Aldrich) in HEPES buffered saline (HBS, pH 7.4) and incubated overnight at 37 °C. Prior to further use, the tubes were rinsed with HBS. ^{111}In-labeled FibPep, NCFibpep or $^{111}InCl_3$ (0.75 ± 0.10 MBq, 2 nmol peptide, n=4 per probe) were diluted with HBS to a total volume of 150 µL, added to the tubes and incubated for 2 h at 37 °C. Subsequently, the solution was removed and the fibrin clot was washed 3x with HBS. The fibrin-bound radioactivity was measured using a dose calibrator (VDC-405; Veenstra Instruments) and expressed as % dose.

2.4.3.2 Blood clot binding: blood clots were prepared by incubating a mixture of 5 µL human tissue factor (Dade Behring), 6 µL of 1 M $CaCl_2$ in ultrapure water and 400 µL of citrated human blood plasma (Sanquin) for 30 min at 37 °C. Subsequently, the blood clots were washed 3x with HBS. Next, ^{111}In-labeled FibPep, NCFibPep or $^{111}InCl_3$ (0.76 ± 0.17 MBq, 2 nmol peptide, n=4 per probe) were diluted with HBS to a total volume of 450 µL, added to the blood clots and incubated for 30 min at 37 °C. After incubation, the solution was removed and the blood clots were washed 3x with HBS. The clot-bound radioactivity was measured and expressed as % dose.

2.4.3.3 Fibrin binding affinity assay: human fibrinogen (Sigma-Aldrich) was dissolved in HBS pH 7.4 (2.5 mg/mL fibrinogen) and $CaCl_2$ was added to a final concentration of 7 mM. The fibrinogen solution (50 µL) was dispensed into a 96-well polystyrene microplate (Nunc). 50 µL of human thrombin (2 U/mL; Sigma-Aldrich) was added to the wells to induce the clotting of fibrinogen and then the plates were dried at 37 °C overnight, yielding a thin fibrin-layer. Subsequently, the plates were sealed and stored at -20 °C until further use. The assayed solutions ranged from 0.1 to 80 µM and from 0.1 to 200 µM peptide for FibPep and NCFibPep, respectively. 100 µL of ^{111}In-labeled FibPep or NCFibPep (5-45 kBq / nmol peptide) in HBS pH 7.4 was added to the wells and the microplate was shaken at 500 rpm and room temperature for 2 h. After incubation, the solution was removed and the radioactivity was measured in a γ–counter (Wizard 1480; PerkinElmer) along with standards to determine the concentration of free peptide. The fibrin-bound peptide concentration was calculated by subtraction ($[peptide_{bound}] = [peptide_{total}] - [peptide_{free}]$). Data were fit using Origin software to a model of N equivalent binding sites with the dissociation constant K_d (µM) given by $\frac{[\mathrm{peptide_{bound}}]}{[\mathrm{fibrin_{total}}]} = \frac{\mathrm{N} \times [\mathrm{peptide_{free}}]}{[\mathrm{peptide_{free}}] + \mathrm{K_d}}$, according to Overoye-Chan and co-workers.[25] Total fibrin concentration was estimated to be 3.7 µM by calculating the concentration of polymerized fibrinogen monomer using a molecular weight of 340 kD for fibrinogen.

2.4.4 In vivo experiment

All animal procedures were approved by the ethical review committee of Maastricht University (The Netherlands) and were performed according to the principles of laboratory animal care and the Dutch national law "Wet op Dierproeven" (Stb 1985, 336).[39] For *in vivo* thrombus formation a well-established $FeCl_3$ induced carotid artery thrombosis model in mice was used.[21-24] C57BL/6 mice (23 ± 3 g body weight; Charles River Laboratories) were housed under standard conditions and acclimatized for at least 1 wk. Food and water were freely available. 30 min prior to surgery, the mice were subcutaneously injected with buprenorphine hydrochloride (0.1 mg/kg; Schering-Plough). The mice were anesthetized with isoflurane and a segment of the right carotid artery was exposed through an incision of the skin and blunt dissection of the fascia over the vessel. Wall-adherent thrombus formation in the right carotid artery was induced by applying a small piece of cleaning cloth soaked in 10% $FeCl_3$ on the carotid. After 5 min, the cloth was removed, the carotid was washed with saline and the skin was closed with a suture.

2.4.5 Blood kinetics and biodistribution

The mice were allowed to recover from anesthesia after the surgery. 1 h post-thrombus formation, ^{111}In-labeled FibPep or NCFibPep (15 nmol, 100 µL, 1.13 ± 0.09 MBq, n=4 per probe) was injected into the tail vein of the mice. At selected time points post injection (PI; 2, 5, 10, 30, 60 and 120 min), blood samples (25 ± 4 µL) were withdrawn from the vena saphena, weighed, and diluted to 1 mL with water. The mice were euthanized 4 h PI using pentobarbital (Alfasan). A blood sample and tissues of interest were collected, weighed and subsequently 1 mL water was added. The radioactivity in the blood samples and organs was measured in a γ–counter along with standards to determine the % injected dose per gram (% ID/g). The probe concentration at time t=0 (C_0) was calculated by fitting the blood kinetic curves to a bi-exponential decay function using Origin software. The volume of distribution (V_D) was calculated as V_D [L/Kg] = injected dose / (weight animal × C_0).

2.4.6 SPECT studies

For SPECT studies, a cannula filled with ~100 µL saline containing 50 U heparin / mL was connected to the tail vein after the surgical procedure to allow injection of the peptides subsequent to acquisition of the CT-scans, without being required to reposition the animals. The mice were positioned into the SPECT scanner and were kept continuously under anesthesia using isoflurane at 37 °C. Scans were performed using a dedicated high resolution small animal SPECT/CT system (NanoSPECT/CT, Bioscan) equipped with 4 detector heads and converging 9-pinhole collimators (pinhole diameter: 1 mm). First, a CT scan of the head-neck region was acquired for detailed anatomical information. Images were acquired over 12 min with 360 projections (exposure time per projection: 2000 ms; peak tube voltage: 45 kV; tube current: 177 mA; field of view: 35 mm). 1 h post-thrombus formation, ^{111}In-labeled FibPep or NCFibPep (15 nmol, 100 µL, 37.5 ± 1.6 MBq, n=4 per probe) was injected together with the saline already present in the cannula. Next, SPECT imaging was performed on the same area, starting at 90 min PI (120 sec/projection; 24 projections/scan; 4 scans total). The total scan time was approximately 1.6 h. Photopeaks for ^{111}In were set to 171 keV (15% FW) and 245 keV (20% FW) for all scans. After the last scan, the mice were euthanized using pentobarbital and post-mortem whole-body CT (settings as above, field of view: 120-130 mm) and SPECT (1 scan; 36 projections, 900 sec per projection) were performed overnight. Finally, the carotids and other tissues of interest were harvested and weighed. Subsequently, 1 mL water was added and the radioactivity was measured in a γ–counter along with standards to determine the % ID/g.

SPECT and CT images were reconstructed using the InVivoScope software (Bioscan) to an isotropic voxel size of 300 µm (SPECT) and 200 µm (CT). The SPECT data were quantitatively evaluated by drawing a volume of interest (VOI) around the hot spot in the injured carotid area. To measure the background signal, VOI's of similar size were placed in the muscle (front limb) and contra-laterally of the injured carotid using the trachea as reference point. The mean size of the VOIs was 1.0 ± 0.1 mm^3.

2.4.7 Histology

The injured as well as the contralateral arteries were fixed in 4% formaldehyde and subsequently embedded in paraffin. The arteries were cut in transversal sections of 5µm and the sections were stained with hematoxylin and eosin.

2.4.8 Statistical analysis

All data represent the mean value ± SD. For differences between multiple groups, data sets were tested using 1-way ANOVA followed by a post-hoc Tukey HSD test for multiple comparisons. For differences between 2 groups, data sets were compared using either a paired or an unpaired 2-tailed *t*-test (not assuming equal variances). For all statistical analysis, differences with $p < 0.05$ were considered significant.

2.5 Acknowledgements

We thank Maarten Merkx (Eindhoven University of Technology) for support with the peptide synthesis, Hugo Knobel and René Beerends (Philips Research) for LC-MS measurements, Iris Verel (Philips Research) and Tilman Hackeng (Maastricht University) for valuable discussions, Katia Donato and Suzanne Kivits (Philips Research), Caren van Kammen, Melanie Blonk and Carlijn van Helvert (Maastricht University) for their excellent support with the *in vivo* experiments. This research was supported by the Center for Translational Molecular Medicine and the Netherlands Heart Foundation (PARISK, grant 01C-202).

2.6 References

1. Turpie, A. G.; Esmon, C. Venous and arterial thrombosis--pathogenesis and the rationale for anticoagulation. *Thromb Haemost* **2011,** *105*, (4), 586-96.

2. Burns, S. K.; Haramati, L. B. Diagnostic imaging and risk stratification of patients with acute pulmonary embolism. *Cardiol Rev* **2012,** *20*, (1), 15-24.

3. Elliott, C. G.; Lovelace, T. D.; Brown, L. M.; Adams, D. Diagnosis: imaging techniques. *Clin Chest Med* **2010,** *31*, (4), 641-57.

4. Constantinides, P. Cause of thrombosis in human atherosclerotic arteries. *Am J Cardiol* **1990,** *66*, (16), 37G-40G.

5. Kolodgie, F. D.; Gold, H. K.; Burke, A. P.; Fowler, D. R.; Kruth, H. S.; Weber, D. K.; Farb, A.; Guerrero, L. J.; Hayase, M.; Kutys, R.; Narula, J.; Finn, A. V.; Virmani, R. Intraplaque hemorrhage and progression of coronary atheroma. *N Engl J Med* **2003,** *349*, (24), 2316-25.

6. Rickles, F. R.; Patierno, S.; Fernandez, P. M. Tissue factor, thrombin, and cancer. *Chest* **2003,** *124*, (3 Suppl), 58S-68S.

7. Dvorak, H. F.; Nagy, J. A.; Berse, B.; Brown, L. F.; Yeo, K. T.; Yeo, T. K.; Dvorak, A. M.; van de Water, L.; Sioussat, T. M.; Senger, D. R. Vascular permeability factor, fibrin, and the pathogenesis of tumor stroma formation. *Ann N Y Acad Sci* **1992,** *667*, 101-11.

8. Palumbo, J. S.; Talmage, K. E.; Massari, J. V.; La Jeunesse, C. M.; Flick, M. J.; Kombrinck, K. W.; Jirouskova, M.; Degen, J. L. Platelets and fibrin(ogen) increase metastatic potential by impeding natural killer cell-mediated elimination of tumor cells. *Blood* **2005,** *105*, (1), 178-85.

9. Yasunaga, M.; Manabe, S.; Matsumura, Y. New concept of cytotoxic immunoconjugate therapy targeting cancer-induced fibrin clots. *Cancer Sci* **2011,** *102*, (7), 1396-402.

10. Morris, T. A.; Marsh, J. J.; Chiles, P. G.; Konopka, R. G.; Pedersen, C. A.; Schmidt, P. F.; Gerometta, M. Single photon emission computed tomography of pulmonary emboli and venous thrombi using anti-D-dimer. *Am J Respir Crit Care Med* **2004,** *169*, (9), 987-93.

11. Morris, T. A.; Gerometta, M.; Smart, R. C.; Eisenberg, P.; Roach, P. J.; Tsui, W. W.; Better, N.; Taubman, K. L.; Unger, S. A.; Macfarlane, D. Pulmonary emboli imaging with (99m)Tc-labelled anti-D-dimer (DI-80B3) Fab' followed by SPECT. *Heart Lung Circ* **2011,** *20*, (8), 503-11.

12. Thakur, M. L.; Pallela, V. R.; Consigny, P. M.; Rao, P. S.; Vessileva-Belnikolovska, D.; Shi, R. Imaging vascular thrombosis with 99mTc-labeled fibrin alpha-chain peptide. *J Nucl Med* **2000,** *41*, (1), 161-8.

13. Aruva, M. R.; Daviau, J.; Sharma, S. S.; Thakur, M. L. Imaging Thromboembolism with Fibrin-Avid 99mTc-Peptide: Evaluation in Swine. *J Nucl Med* **2006,** *47*, (1), 155-162.

14. Spuentrup, E.; Botnar, R. M.; Wiethoff, A. J.; Ibrahim, T.; Kelle, S.; Katoh, M.; Ozgun, M.; Nagel, E.; Vymazal, J.; Graham, P. B.; Gunther, R. W.; Maintz, D. MR imaging of thrombi using EP-2104R, a fibrin-specific contrast agent: initial results in patients. *Eur Radiol* **2008,** *18*, (9), 1995-2005.

15. Sirol, M.; Fuster, V.; Badimon, J. J.; Fallon, J. T.; Moreno, P. R.; Toussaint, J. F.; Fayad, Z. A. Chronic thrombus detection with in vivo magnetic resonance imaging and a fibrin-targeted contrast agent. *Circulation* **2005,** *112*, (11), 1594-600.

16. Botnar, R. M.; Perez, A. S.; Witte, S.; Wiethoff, A. J.; Laredo, J.; Hamilton, J.; Quist, W.; Parsons, E. C., Jr.; Vaidya, A.; Kolodziej, A.; Barrett, J. A.; Graham, P. B.; Weisskoff, R. M.; Manning, W. J.; Johnstone, M. T. In vivo molecular imaging of acute and subacute thrombosis using a fibrin-binding magnetic resonance imaging contrast agent. *Circulation* **2004,** *109*, (16), 2023-9.

17. Vymazal, J.; Spuentrup, E.; Cardenas-Molina, G.; Wiethoff, A. J.; Hartmann, M. G.; Caravan, P.; Parsons, E. C., Jr. Thrombus imaging with fibrin-specific gadolinium-based MR contrast agent EP-2104R: results of a phase II clinical study of feasibility. *Invest Radiol* **2009,** *44*, (11), 697-704.

18. Spuentrup, E.; Buecker, A.; Katoh, M.; Wiethoff, A. J.; Parsons, E. C., Jr.; Botnar, R. M.; Weisskoff, R. M.; Graham, P. B.; Manning, W. J.; Gunther, R. W. Molecular magnetic resonance imaging of coronary thrombosis and pulmonary emboli with a novel fibrin-targeted contrast agent. *Circulation* **2005,** *111*, (11), 1377-82.

19. Kribben, A.; Witzke, O.; Hillen, U.; Barkhausen, J.; Daul, A. E.; Erbel, R. Nephrogenic Systemic Fibrosis: Pathogenesis, Diagnosis, and Therapy. *Journal of the American College of Cardiology* **2009,** *53*, (18), 1621-1628.

20. Marinelli, E.; Ramalingam, K.; Swenson, R.; Song, B.; Lattuada, L.; Uggeri, F.; Lorusso, V.; Aime, S.; Morosini, P.; Chaabane, L. Fibrin Binding Peptide Conjugates for Diagnostic and Therapeutic Applications. WO 2008/071679 A1, 2008.

21. Sachs, U. J. H.; Nieswandt, B. In Vivo Thrombus Formation in Murine Models. *Circ Res* **2007,** *100*, (7), 979-991.

22. von zur Muhlen, C.; von Elverfeldt, D.; Moeller, J. A.; Choudhury, R. P.; Paul, D.; Hagemeyer, C. E.; Olschewski, M.; Becker, A.; Neudorfer, I.; Bassler, N.; Schwarz, M.; Bode, C.; Peter, K. Magnetic Resonance Imaging Contrast Agent Targeted Toward Activated Platelets Allows In Vivo Detection of Thrombosis and Monitoring of Thrombolysis. *Circulation* **2008,** *118*, (3), 258-267.

23. Miserus, R. J.; Herias, M. V.; Prinzen, L.; Lobbes, M. B.; Van Suylen, R. J.; Dirksen, A.; Hackeng, T. M.; Heemskerk, J. W.; van Engelshoven, J. M.; Daemen, M. J.; van Zandvoort, M. A.; Heeneman, S.; Kooi, M. E. Molecular MRI of early thrombus formation using a bimodal alpha2-antiplasmin-based contrast agent. *JACC Cardiovasc Imaging* **2009,** *2*, (8), 987-96.

24. Heidt, T.; Deininger, F.; Peter, K.; Goldschmidt, J.; Pethe, A.; Hagemeyer, C. E.; Neudorfer, I.; Zirlik, A.; Weber, W. A.; Bode, C.; Meyer, P. T.; Behe, M.; von zur Mühlen, C. Activated Platelets in Carotid Artery Thrombosis in Mice Can Be Selectively Targeted with a Radiolabeled Single-Chain Antibody. *PLoS ONE* **2011,** *6*, (3), e18446.

25. Overoye-Chan, K.; Koerner, S.; Looby, R. J.; Kolodziej, A. F.; Zech, S. G.; Deng, Q.; Chasse, J. M.; McMurry, T. J.; Caravan, P. EP-2104R: a fibrin-specific gadolinium-Based MRI contrast agent for detection of thrombus. *J Am Chem Soc* **2008,** *130*, (18), 6025-39.

26. Kolodziej, A. F.; Nair, S. A.; Graham, P.; McMurry, T. J.; Ladner, R. C.; Wescott, C.; Sexton, D. J.; Caravan, P. Fibrin specific peptides derived by phage display: characterization of peptides and conjugates for imaging. *Bioconjug Chem* **2012,** *23*, (3), 548-56.

27. Smith, D. A.; Waterbeemd, H. v. d.; Walker, D. K., *Pharmacokinetics and metabolism in drug design*. 2nd ed.; Wiley-VCH: Weinheim, 2006.

28. Makowski, M. R.; Forbes, S. C.; Blume, U.; Warley, A.; Jansen, C. H.; Schuster, A.; Wiethoff, A. J.; Botnar, R. M. In vivo assessment of intraplaque and endothelial fibrin in ApoE(-/-) mice by molecular MRI. *Atherosclerosis* **2012,** *222*, (1), 43-9.

29. Uppal, R.; Catana, C.; Ay, I.; Benner, T.; Sorensen, A. G.; Caravan, P. Bimodal thrombus imaging: simultaneous PET/MR imaging with a fibrin-targeted dual PET/MR probe--feasibility study in rat model. *Radiology* **2011,** *258*, (3), 812-20.

30. Wescot, C. R.; Beltzer, J. P.; Sato, A. K. Fibrin Binding Moieties Useful as Imaging Agents. WO 02/055544 A2, 2002.

31. Eisenwiener, K. P.; Prata, M. I.; Buschmann, I.; Zhang, H. W.; Santos, A. C.; Wenger, S.; Reubi, J. C.; Macke, H. R. NODAGATOC, a new chelator-coupled somatostatin analogue labeled with [67/68Ga] and [111In] for SPECT, PET, and targeted therapeutic applications of somatostatin receptor (hsst2) expressing tumors. *Bioconjug Chem* **2002,** *13*, (3), 530-41.

32. de Vries, A.; Custers, E.; Lub, J.; van den Bosch, S.; Nicolay, K.; Grull, H. Block-copolymer-stabilized iodinated emulsions for use as CT contrast agents. *Biomaterials* **2010,** *31*, (25), 6537-44.

33. Uppal, R.; Medarova, Z.; Farrar, C. T.; Dai, G.; Moore, A.; Caravan, P. Molecular imaging of fibrin in a breast cancer xenograft mouse model. *Invest Radiol* **2012,** *47*, (10), 553-8.

34. Heiba, S. I.; Kolker, D.; Mocherla, B.; Kapoor, K.; Jiang, M.; Son, H.; Rangaswamy, B.; Kostakoglu, L.; Savitch, I.; DaCosta, M.; Machac, J. The optimized evaluation of diabetic foot infection by dual isotope SPECT/CT imaging protocol. *J Foot Ankle Surg* **2010,** *49*, (6), 529-36.

35. Hsieh, P. C.; Lee, I. H.; Yeh, T. L.; Chen, K. C.; Huang, H. C.; Chen, P. S.; Yang, Y. K.; Yao, W. J.; Lu, R. B.; Chiu, N. T. Distribution volume ratio of serotonin and dopamine transporters in euthymic patients with a history of major depression - a dual-isotope SPECT study. *Psychiatry Res* **2010,** *184*, (3), 157-61.

36. Breeman, W. A. P.; de Blois, E.; Sze Chan, H.; Konijnenberg, M.; Kwekkeboom, D. J.; Krenning, E. P. 68Ga-labeled DOTA-Peptides and 68Ga-labeled Radiopharmaceuticals for Positron Emission Tomography: Current Status of Research, Clinical Applications, and Future Perspectives. *Seminars in Nuclear Medicine* **2011,** *41*, (4), 314-321.

37. McBride, W. J.; D'Souza, C. A.; Sharkey, R. M.; Karacay, H.; Rossi, E. A.; Chang, C.-H.; Goldenberg, D. M. Improved 18F Labeling of Peptides with a Fluoride-Aluminum-Chelate Complex. *Bioconjugate Chemistry* **2010,** *21*, (7), 1331-1340.

38. Morcos, S. K. Nephrogenic systemic fibrosis following the administration of extracellular gadolinium based contrast agents: is the stability of the contrast agent molecule an important factor in the pathogenesis of this condition? *Br J Radiol* **2007,** *80*, (950), 73-6.

39. Institute of Laboratory Animal Resources (U.S.). Committee on Care and Use of Laboratory Animals., Guide for the care and use of laboratory animals. In *NIH publication*, U.S. Dept. of Health and Human Services, Public Health Service: Bethesda, Md., 1985.

2.7 Supplementary Information

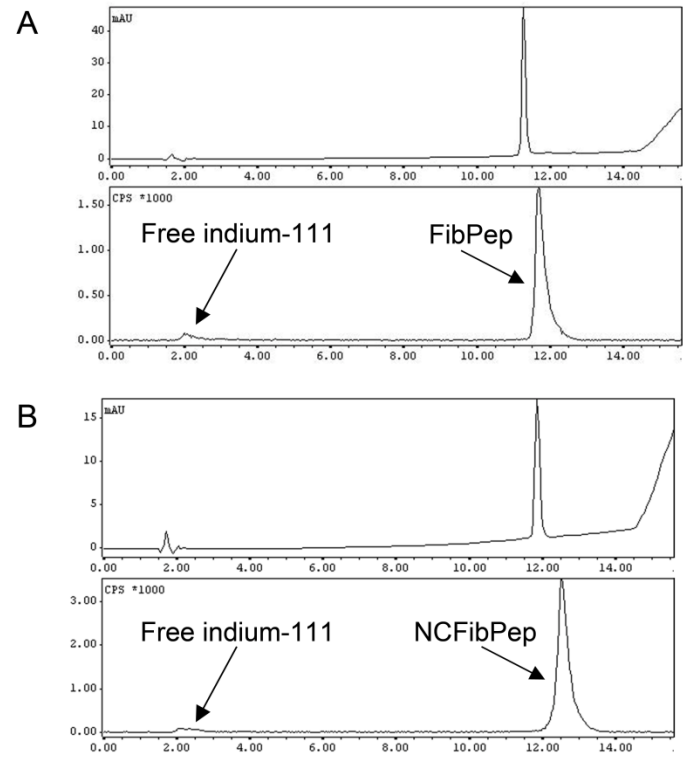

Figure S1. *Typical HPLC chromatograms of (A) ^{111}In-FibPep and (B) ^{111}In-NCFibPep labeling mixtures. The upper panels show the UV profiles (254 nm) and the lower panels show the radioactivity profiles. Typical radiochemical purities of ^{111}In-labeled FibPep and NCFibPep were ≥ 95%.*

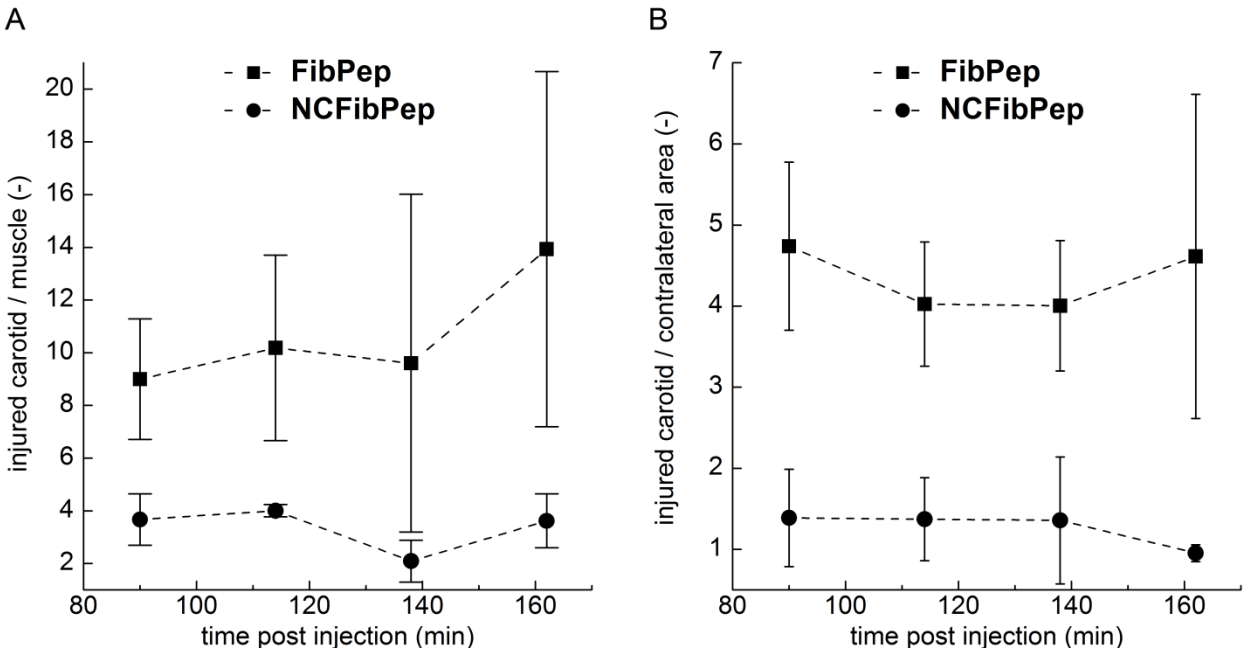

Figure S2. *Quantitative SPECT data 90, 114, 138 and 162 min post injection of ^{111}In-labeled FibPep and NCFibPep. The data are expressed as the ratio between the injured carotid and (A) muscle or (B) the contra-lateral area (mean ± SD, n=4).*

Chapter 3

Evaluation of ^{111}In-labeled EPep and FibPep as tracers for fibrin SPECT imaging

Abstract

Fibrin targeting is an attractive strategy for nuclear imaging of thrombosis, atherosclerosis and cancer. Recently, FibPep, an ^{111}In-labeled fibrin-binding peptide, was established as a tracer for fibrin SPECT imaging and was reported to allow sensitive detection of minute thrombi in mice using SPECT. In this study, we developed EPep, a novel ^{111}In-labeled fibrin-binding peptide containing the fibrin-binding domain of the clinically verified EP-2104R peptide, and sought to compare the potential of EPep and FibPep as tracers for fibrin SPECT imaging. *In vitro,* both EPep and FibPep showed high stability in serum, but were less stable in liver and kidney homogenate assays. Both peptide probes displayed comparable affinities toward human and mouse derived fibrin ($K_d \approx 1$ μM), and similarly to FibPep, EPep showed fast blood clearance, low nontarget uptake and high thrombus uptake (6.8 ± 1.2% ID/g) in a mouse carotid artery thrombosis model. Furthermore, EPep showed a similar affinity toward rat derived fibrin ($K_d \approx 1$ μM), displayed high thrombus uptake in a rat carotid artery thrombosis model (0.74 ± 0.39% ID/g), and allowed sensitive detection of thrombosis in rats using SPECT. In contrast, FibPep displayed a significantly lower affinity toward rat derived fibrin ($K_d \approx 14$ μM), low uptake in rat thrombi (0.06 ± 0.02% ID/g) and did not allow clear visualization of carotid artery thrombosis in rats using SPECT. These results were confirmed *ex vivo* by autoradiography, which showed a 7-fold higher ratio of activity in the thrombus over the contralateral carotid artery for EPep in comparison to FibPep. These findings suggest that the FibPep binding fibrin epitope is not fully homologous between humans and rats, and that preclinical rat models of disease should not be employed to gauge the clinical potential of FibPep. In conclusion, both peptides showed approximately similar metabolic stability and affinity toward human and mouse derived fibrin, and displayed high thrombus uptake in a mouse carotid artery thrombosis model. Therefore, both EPep and FibPep are promising fibrin targeted tracers for translation into clinical settings to serve as novel tools for molecular imaging of fibrin.

This chapter is based on:
Starmans, L. W.; van Duijnhoven, S. M.; Rossin, R.; Berben, M.; Aime, S.; Daemen, M. J.; Nicolay, K.; Grull, H. Evaluation of ^{111}In-labeled EPep and FibPep as tracers for fibrin SPECT imaging. *Mol Pharm* **2013,** *10*, (11), 4309-21.

3.1 Introduction

Fibrin is a key protein in hemostasis and is formed by thrombin-induced fibrinopeptide removal in the central region of fibrinogen and subsequent fibrinogen polymerization.[1, 2] Fibrin is a major component of thrombi, which are the underlying cause in a range of diseases, such as heart attack, stroke, deep venous thrombosis and pulmonary embolism, affecting millions of patients worldwide.[3, 4] Visualization of fibrin using nuclear imaging techniques might allow detection of thrombosis with higher sensitivity and with fewer limitations with respect to thrombus location in the body in comparison to currently employed imaging techniques in thrombosis diagnostics, such as ultrasound, computed tomography (CT) angiography, and ventilation/perfusion scintigraphy.[5, 6] Employing fibrin as target for nuclear imaging of thrombosis offers the advantage of high sensitivity and specificity, as it is present in high concentrations in arterial, venous, acute and aged thrombi and is virtually absent in nonpathological situations. In addition to sensitive detection of thrombosis, nuclear tracers targeting fibrin may allow assessment of atherosclerosis as increased fibrin deposition in atherosclerotic plaques correlates with progression of atherosclerotic disease.[7, 8] Furthermore, fibrin deposition is associated with plaque erosion and with the necrotic core and dysfunctional endothelium of atherosclerotic plaques.[8-10] Oncology is another field of interest for fibrin imaging, as fibrin deposition is associated with a variety of malignant tumors.[11] Fibrin plays a pivotal role in tumor stroma formation, and deposition of fibrin has been associated with tumor angiogenesis and metastasis.[11-13] Hence, nuclear imaging of fibrin may improve diagnosis and clinical decision-making on therapeutic options in cancer, atherosclerosis and thrombus-related pathologies such as for instance deep venous thrombosis and pulmonary embolism.

Different strategies have been pursued to investigate the potential of fibrin molecular imaging, including fibrin-binding peptide- or antibody-conjugated nanoparticles for ultrasound imaging, magnetic resonance imaging (MRI), CT, and fluorescence imaging,[14-19] as well as radiolabeled fibrin-targeted antibodies, antibody fragments, and small peptides for single photon emission computed tomography (SPECT) of fibrin.[20-25] An advantage of employing peptide-based strategies is that the small size of peptides might increase penetration in tumor stroma, atherosclerotic plaques and thrombi. In addition, peptides often display more advantageous pharmacokinetics and lower cost of production with respect to nanoparticles and antibodies. Of particular interest is the work performed with the fibrin-binding EP-2104R peptide, which contains four gadolinium(III) 1,4,7,10-tetraazacyclododecane-1,4,7,10-tetraacetic acid (DOTA) moieties and shows binding to fibrin with a dissociation constant (K_d) of approximately 1 μM.[26] EP-2104R was successfully employed in multiple preclinical MRI studies for visualization of thrombosis, atherosclerosis and fibrin deposition in cancer.[27-32] In clinical phase 2 studies, EP-2104R allowed enhanced detection of thrombi located in the heart and in the arterial and venous system.[33, 34]

Recently, we established the ^{111}In-labeled fibrin-binding peptide FibPep for nuclear imaging of fibrin and successfully demonstrated sensitive detection of minute thrombi in mice using SPECT.[35] FibPep showed affinity toward human derived fibrin ($K_d \approx 1$ μM) similar to that of EP-2104R and displayed rapid blood clearance, low uptake in nontarget organs and high uptake in thrombi in a carotid artery

thrombosis mouse model. In addition, FibPep-conjugated iron oxide nanoparticle-micelles displayed high potency for detection of thrombi using MRI and magnetic particle imaging (MPI).[36] In this study, we developed a novel ^{111}In-labeled fibrin-binding peptide, EPep, based on the clinically proven EP-2104R fibrin-binding motif Y-dGlu-C-Hyp-3ClY-GLCYIQ (Fig. 1A). Similarly to FibPep (Fig. 1B), EPep consists of a cyclic fibrin-binding domain which is linked via a glycine linker to a DOTA chelator. Here, we sought to compare the potential of EPep and FibPep for fibrin SPECT imaging. NCFibPep (Fig. 1C),[35] which is a scrambled and linearized version of FibPep, was employed as negative control. We investigated the metabolic stability and fibrin-binding capabilities of the peptides *in vitro* and employed a carotid thrombosis model in mice and rats to assess blood kinetics, biodistribution and thrombus uptake of the probes *in vivo.* Finally, *ex vivo* autoradiography and histology were performed to corroborate the *in vivo* findings.

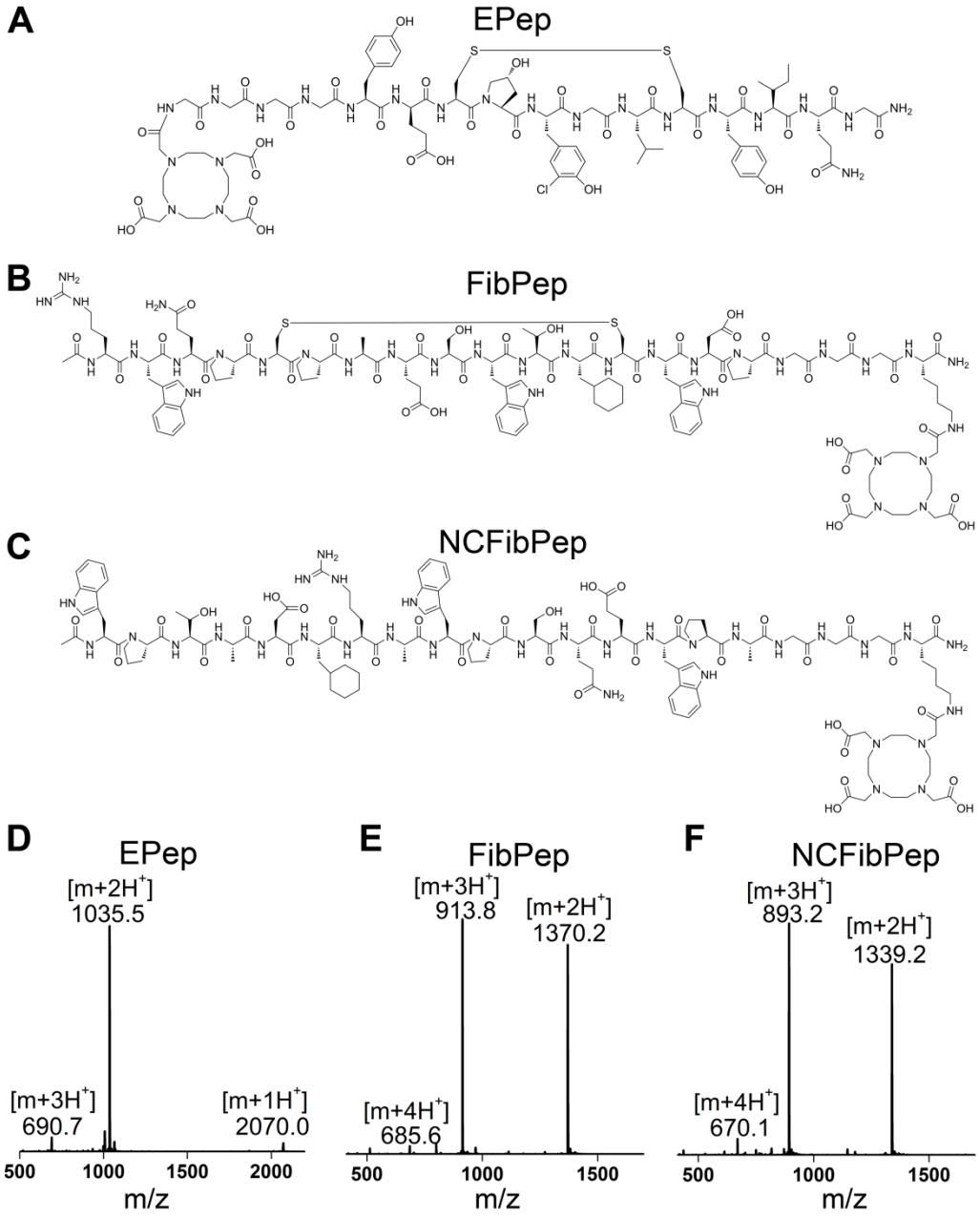

Figure 1.
Structural formulas and corresponding mass spectra of (A,D) EPep, (B,E) FibPep and (C,F) NCFibPep.

3.2 Materials and methods

3.2.1 Materials

Amino acids and Rink amide resin were purchased from Novabiochem, Bachem and Anaspec. DOTA-NHS ester was obtained from Macrocyclics and $^{111}InCl_3$ was purchased from PerkinElmer. All chemicals were used without additional purification. Human, mouse and rat serum were obtained from Innovative Research and human plasma and blood were purchased from Sanquin. Thrombin and human, mouse and rat-derived fibrinogen were purchased from Sigma-Aldrich.

3.2.2 Peptide probe synthesis

EPep ([DOTA]GGGGY-dGlu-C-Hyp-3ClY-GLCYIQG-NH_2) comprises the fibrin-binding amino acid sequence of the EP-2104R peptide (Y-dGlu-C-Hyp-3ClY-GLCYIQ)[26] linked to a DOTA-chelator via a glycine linker. The amino acid sequence GGGG-Y-dGlu-C-Hyp-3ClY-GLCYIQG-NH_2 was synthesized on 4-methylbenzydrylamine hydrochloride salt Rink amide resin using standard 9-fluorenylmethyloxycarbonyl (Fmoc) solid phase peptide synthesis. The peptide was cleaved from the resin with a trifluoroacetic acid (TFA) : triisopropylsilane : H_2O : ethanedithiol (90.5:5:2.5:2 v/v) mixture for 3 h and subsequently purified by preparative reversed-phase high-pressure liquid chromatography (RP-HPLC) using an Agilent 1200 apparatus and a C_{18} Zorbax column (150 × 21.2 mm; 5.0 µm particle size). Next, a disulfide bond between the cysteine residues was formed by dissolving the purified amino acid sequence GGGG-Y-dGlu-C-Hyp-3ClY-GLCYIQG-NH_2 in water : dimethylsulfoxide : acetonitrile (75:15:10 v/v) in a concentration of approximately 2.5 mg peptide per mL and stirring the obtained solution at room temperature (RT) for 5 days. Subsequently, the cyclic peptide was purified using preparative RP-HPLC. DOTA-functionalization on the N-terminal amine was achieved by mixing the cyclic amino acid sequence GGGG-Y-dGlu-C-Hyp-3ClY-GLCYIQG-NH_2 and a 7-fold excess of DOTA-NHS ester in dimethylformamide containing 3% (v/v) triethylamine (peptide concentration ≈ 35 mg/mL) at RT overnight. Finally, the peptides were purified using preparative RP-HPLC, yielding the DOTA-functionalized EPep (Fig. 1A). FibPep (Ac-RWQPCPAESWT-Cha-CWDPGGGK[DOTA]-NH_2; Fig. 1B) and negative control NCFibPep (Ac-WPTAD-Cha-RAWPSQEWPAGGGK[DOTA]-NH_2; Fig. 1C) were synthesized according to a previously published protocol.[35] FibPep and NCFibPep were dissolved in ultrapure water for further analysis and experiments, and EPep was dissolved in ultrapure water containing 20 mM NaOH. The obtained peptide solutions were examined using a LC-MS Agilent 1200 apparatus, equipped with a C_8 Eclipse plus column (100 × 2.1 mm, 3.5 µm particle size) and an electrospray mass spectrometer (time-of-flight LC-MS model 6210; Agilent Technologies).

3.2.3 Radiolabeling

Solutions of (NC)FibPep in ammonium acetate buffer (0.2 M, pH 6) or EPep in ammonium acetate buffer (0.25 M, pH 7.5) were mixed with $^{111}InCl_3$ and shaken (350 rpm) at 80 °C for 60 min. For *in vivo* experiments and *in vitro* stability assays, the (NC)FibPep labeling mix was diluted in saline, and the EPep labeling mix was diluted in saline containing 10 mM NaOH. The obtained solutions were challenged with a 1- to 2-fold equivalent dose of diethylenetriaminepentaacetic acid. The radiochemical purity was determined by radio-HPLC and the labeling yield was determined using radio thin layer chromatography

(TLC). Analytical radio-HPLC was performed on an Agilent 1100 system equipped with a C_{18} Eclipse XBD column (150 × 4.6 mm; 5 µm particle size) and a Gabi radioactive detector (Raytest) using a flow of 1 mL/min and H_2O + 0.1% TFA as mobile phase A and acetonitrile + 0.1% TFA as mobile phase B with a gradient of 2.5 min 5% B, 10 min to 55% B and 3.5 min at 95% B. TLC was performed on instant TLC silica gel strips (Varian Inc.) eluted with saline containing 200 mM ethylenediaminetetraacetic acid. The strips were imaged on a phosphor imager (FLA-7000; Fujifilm), and the labeling yields were quantified using AIDA Image Analyzer software. The radiolabeled peptides did not undergo any purification prior to use.

3.2.4 In vitro stability

3.2.4.1 Serum assays: 50 µL of EPep, FibPep or NCFibpep solution (1.7 ± 0.1 MBq, 3.75 nmol peptide, n=3 per probe) was incubated with 200 µL mouse (non-Swiss albino from C57BL/6 background), rat (Wistar) or human serum at 37 °C for 90 min. Immediately after incubation, 250 µL ice-cold acetonitrile was added and the samples were centrifuged (16.1k rcf) for 6 min. Subsequently, the supernatant was separated from the protein pellet and the radioactivity of the pellet and supernatant was measured using a dose calibrator (VDC-405; Veenstra Instruments). The supernatants were diluted by a factor of 2 using ultrapure water and subsequently analyzed by radio-HPLC, using a flow of 1 mL/min with a gradient of 2.5 min 5% B, 5 min to 37% B, 6 min to 43% B and 3.5 min at 95% B. The results were expressed as % intact parent compound.

3.2.4.2 Tissue homogenate assays: rat (Sprague Dawley) and mouse (C57BL/6) liver and kidneys were excised and immediately stored at -80 °C until further use. Prior to the experiments, seven weight equivalents of HEPES buffered saline (HBS, pH 7.4) was added to the liver/kidneys and the tissues were homogenized using a Qiagen TissueLyser (25 Hz, 15-25 min, 6 °C). Subsequently, 50 µL of EPep, FibPep or NCFibpep solution (1.8 ± 0.1 MBq, 3.75 nmol peptide, n=3 per probe) was incubated with 200 µL liver and kidney homogenates at 37 °C for 10 min. Acetonitrile precipitation and subsequent supernatant radio-HPLC analysis was performed as described above.

3.2.5 In vitro fibrin and blood clot binding

3.2.5.1 Blood clot binding: Blood clots were prepared using citrated human plasma according to a previously published protocol.[35] 50 µL of the EPep, FibPep or NCFibPep solution (0.76 ± 0.14 MBq, 2 nmol peptide, n=4 per probe) and 400 µL HBS were added to the blood clots and incubated at 37 °C for 30 min. After incubation, the solution was removed and the blood clots were washed 3 times with HBS. The clot-bound radioactivity was measured using a dose calibrator and expressed as % dose.

3.2.5.2 Fibrin-binding: human derived fibrin coated tubes were prepared according to a previously published protocol.[35] 50 µL of EPep, FibPep or NCFibpep solution (0.83 ± 0.10 MBq, 2 nmol peptide, n=4 per probe) and 100 µL HBS or heparinized human blood were added to the tubes and incubated at 37 °C for 2 h. Subsequently, the solution was removed and the fibrin clot was washed 3 times with HBS. The fibrin bound radioactivity was measured using a dose calibrator and expressed as % dose.

3.2.5.3 Fibrin-binding affinity assay: human, rat and mouse derived fibrinogen was dissolved in HBS (2.5 mg fibrinogen/mL) and $CaCl_2$ was added to a final concentration of 7 mM. The fibrinogen solution (50 µL) was dispensed into a 96-well polystyrene microplate (Nunc). 50 µL of human thrombin (2 U/mL) was added to the wells to induce the clotting of fibrinogen and then the plates were dried at 37 °C overnight, yielding a thin fibrin layer. Subsequently, the plates were sealed and stored at -20 °C until further use.

The assayed solutions ranged from 0.1 to 40 µM peptide (23-33 kBq/nmol peptide), 0.1 to 60 µM peptide (16-55 kBq/nmol peptide) and 0.1 to 400 µM peptide (3-38 kBq/nmol peptide) for EPep, FibPep and NCFibPep, respectively. 100 µL of ^{111}In-labeled peptides in HBS was added to the wells and the microplate was shaken at 500 rpm and RT for 2 h. Total fibrin concentration was estimated to be 3.7 µM by calculating the concentration of polymerized fibrinogen monomer using a molecular weight of 340 kDa for fibrinogen. After incubation, the solution was removed and the radioactivity was measured in a γ–counter (Wizard 1480; PerkinElmer) along with standards to determine the concentration of free peptide. The fibrin-bound peptide concentration was calculated and the data were fit as described previously.[35]

3.2.6 Animal model

For *in vivo* thrombus formation a well established $FeCl_3$ induced carotid artery thrombosis model was used.[35, 37-40] Sprague-Dawley rats (176 ± 19 g body weight; Charles River Laboratories) and C57BL/6 mice (25 ± 1 g body weight; Charles River Laboratories) were housed under standard conditions and acclimatized for at least one week. Food and water were freely available. The animals were subcutaneously injected with buprenorphine hydrochloride (Schering-Plough; 0.1 and 0.05 mg/kg for mice and rats, respectively) 30 min prior to surgery. The animals were anesthetized using isoflurane and a segment of the right carotid artery was exposed through incision of the skin and blunt dissection of the fascia over the vessel. Wall-adherent thrombus formation in the right carotid artery was induced by applying a small piece of cleaning cloth soaked in 10% $FeCl_3$ on the carotid. After 5 min, the cloth was removed, the carotid was washed with saline and the skin was closed with a suture. All animal procedures were approved by the ethical review committee of Maastricht University (The Netherlands) and were performed according to the Dutch national law and the guidelines set by the institutional animal care committee, accredited by the national department of health.

3.2.7 Blood kinetics and biodistribution

The animals were allowed to recover from anesthesia after surgery. In the carotid thrombosis mouse model, EPep (15 nmol, 100 µL, 1.2 ± 0.0 MBq, blood kinetics: n=3, biodistribution: n=4) was injected via the tail vein 1 h post thrombus induction. In the carotid thrombosis rat model, EPep, FibPep or NCFibPep (15 nmol, 200 µL, 2.7 ± 0.2 MBq, blood kinetics: n=3, biodistribution: n=5) was injected via the tail vein 30 min post thrombus induction. Additionally, a group of rats was intravenously injected with a 5-fold increased dose of FibPep (75 nmol, 200 µL, 3.7 ± 1.1 MBq, biodistribution: n=3).

At selected time points post injection (2, 5, 10, 30, 60 and 120 min), blood samples were withdrawn from the vena saphena, weighed, and diluted with water to a volume of 1 mL. The animals were euthanized 4 h post injection by intraperitoneal injection of pentobarbital (Alfasan). Urine was analyzed using a radio-HPLC protocol as described in the radiolabeling section. Tissues of interest, including a blood sample, were harvested, weighed, and subsequently 1 mL water was added. The radioactivity in the collected blood samples and organs was measured in a γ–counter along with standards to determine the % injected dose per gram (% ID/g).

3.2.7 SPECT imaging and ex vivo autoradiography

The rats were allowed to recover from anesthesia after surgery. EPep, FibPep or NCFibPep (15 nmol, 200 µL, 38 ± 2 MBq, n=4 per group) were injected via the tail vein 30 min post thrombus formation. Approximately 2 h post injection, the rats were anesthetized using isoflurane and were positioned in a dedicated high-resolution small-animal SPECT/CT scanner (NanoSPECT/CT, Bioscan) equipped with four detector heads and converging nine-pinhole collimators (pinhole diameter 2.5 mm). Subsequently, a CT scan of the rat head-neck area was performed to provide anatomical information. Images were acquired over 12 min with 360 projections (exposure time per projection: 2 s, peak tube voltage: 45 kV; tube current: 177 mA; field of view: 37 mm). 2.5 h post injection, a SPECT scan of the head-neck area was acquired (300 s per projection; 24 projections per scan; 1 h total scan time). ^{111}Indium photopeaks were set to 171 keV (20% FW) and 245 keV (15% FW). After acquiring the *in vivo* SPECT scan, the rats were euthanized using pentobarbital (intravenous injection). Subsequently, post mortem whole body CT (settings as above, field of view: 166-202 mm, 60-80 min total scan time) and SPECT (100 s per projection, 24 projection per scan, 70-80 min total scan time) were performed to visualize the biodistribution of the tracers over the entire body. SPECT and CT images were reconstructed using InVivoScope (Bioscan) to an isotropic voxel size of 600 µm (SPECT) and 200 µm (CT). The *in vivo* SPECT data were quantitatively evaluated by drawing a volume of interest around the hot spot in the injured carotid area. To measure background signal, volumes of interest were placed contralaterally of the injured carotid using the trachea as a reference point. The mean size of the volumes of interest was 6 ± 2 mm^3. The recorded counts in the volumes of interest were converted to Becquerel using a quantification factor that was calculated using a known amount of ^{111}In. The results were then expressed as percent injected dose per volume (% ID/cm^3) for both the injured carotid and the noninjured, contralateral carotid area.

Subsequent to the post-mortem SPECT/CT scans, the carotid arteries were excised and a photostimulable phosphor plate was placed on top of the excised arteries for approximately 24 h. The exposed plates were scanned using a phosphor imager. The acquired images were quantitatively analyzed by drawing regions of interest in the thrombus containing area and in the contralateral carotid using AIDA image analyzer software.

3.2.8 Histology

The carotid arteries were fixed in 4% formaldehyde and subsequently embedded in paraffin. Transversal sections of 5 µm were stained with hematoxylin and eosin.

3.2.9 Statistical analysis

Data represent the mean value ± standard deviation (SD), unless noted otherwise. For differences between more than two groups, a 1-way ANOVA with a *post-hoc* Tukey honestly significant difference test was used. For differences between two paired groups, data sets were compared using a paired, two-tailed *t*-test. For analysis of the rat biodistribution, a Kruskal-Wallis test was performed. For all statistical analysis, values of $p < 0.05$ were considered significant.

3.3 Results

3.3.1 Synthesis and radiolabeling peptide probes

The fibrin-binding probes EPep and FibPep, as well as the negative control peptide NCFibPep were synthesized using standard Fmoc solid phase peptide synthesis. LC-MS analysis of the synthesized peptides (Fig. 1D-F) showed exact masses (2069.0, 2738.4 and 2676.5 Da for EPep, FibPep and NCFibPep, respectively) that matched well with the expected exact masses (2068.8, 2738.2 and 2676.3 Da for EPep, FibPep and NCFibPep, respectively). Radiolabeling with ^{111}In resulted in ≥ 95% yield and radiochemical purity for FibPep and NCFibPep, whereas radiolabeling of EPep resulted in ≥ 93% yield and radiochemical purity.

3.3.2 In vitro stability assays

In vitro stability of EPep, FibPep and NCFibPep was assayed in serum and in kidney and liver homogenates. After incubation in serum or tissue homogenate, proteins were precipitated and the supernatant was analyzed using radio-HPLC. The radioactivity recovery (parent compounds and metabolites) in the supernatant was 93 ± 2, 91 ± 2 and 92 ± 3% for EPep, FibPep and NCFibPep, respectively. Figure 2 shows the chromatograms after 90 min of incubation in mouse, rat and human serum. EPep and FibPep were stable in serum (89-100 and 95-100% intact parent compound, respectively), whereas NCFibPep displayed lower stability (15-55% intact parent compound). Chromatograms obtained after 10 min of incubation in mouse and rat tissue homogenates (Fig. 3) show that EPep and FibPep were moderately stable in liver homogenates (63-74 and 57-89% intact parent compound, respectively) and were rapidly degraded in kidney homogenates (17-46 and 6-14% intact parent compound, respectively). NCFibPep was not stable in liver and kidney homogenate (≤18 and 1% intact parent compound, respectively).

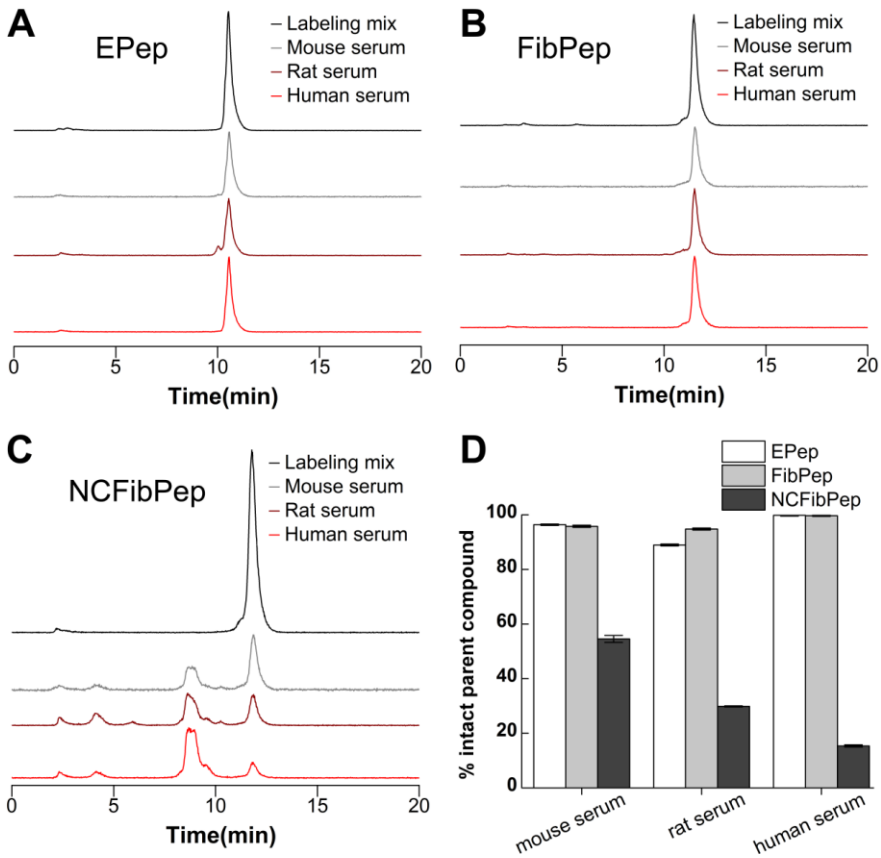

Figure 2. *Serum stability assay. Typical chromatograms of (A) EPep, (B) FibPep and (C) NCFibPep prior to incubation and after 90 min of incubation in mouse, rat or human serum. (D) Percentage intact peptide probes after 90 min of serum incubation as derived from the chromatograms. Data expressed as mean percentage intact parent compound ± SD (n=3).*

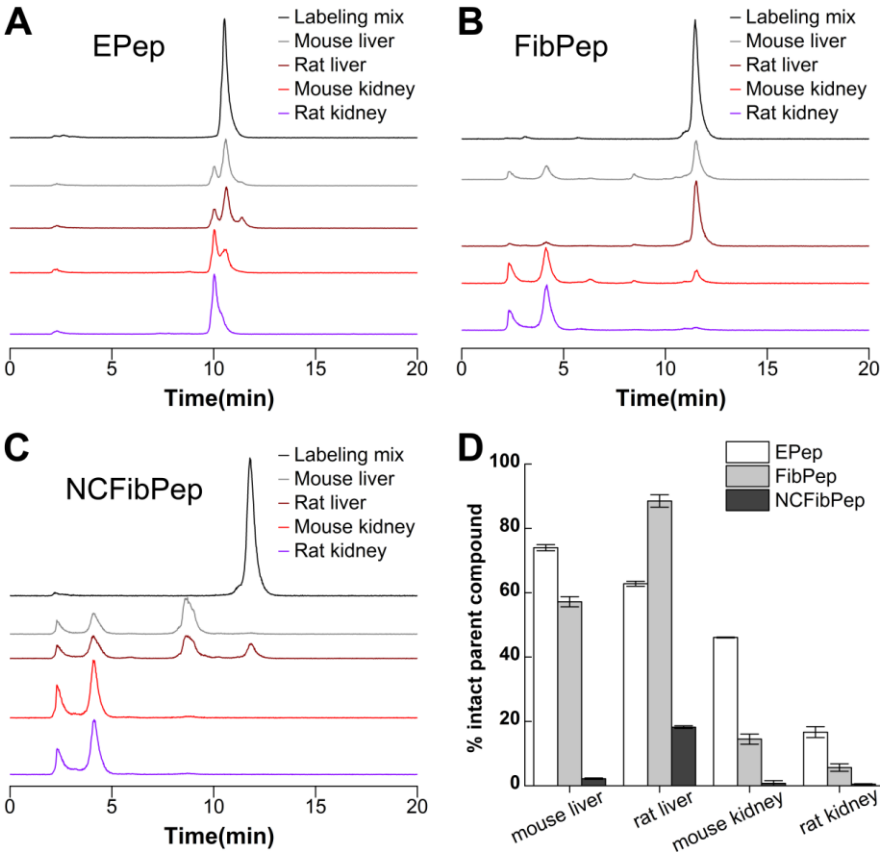

Figure 3. *Tissue homogenate stability assay. Typical chromatograms of (A) EPep, (B) FibPep and (C) NCFibPep prior to incubation and after 10 min of incubation in mouse and rat kidney/liver tissue homogenates. (D) Percentage intact peptide probes after 10 min of tissue homogenate incubation as derived from the chromatograms. Data expressed as mean percentage intact parent compound ± SD (n=3).*

3.3.3 In vitro fibrin and blood clot binding

In vitro binding studies showed no significant difference between EPep and FibPep with respect to binding to blood clots derived from citrated human plasma (29.8 ± 3.1 and 35.3 ± 3.8% dose, respectively, Fig. 4A), whereas NCFibPep showed significantly lower clot association (4.2 ± 1.8% dose, $p < 0.001$). Figure 4B shows *in vitro* binding of the peptide probes toward human derived fibrin in either HBS or human blood. In HBS, EPep showed significantly lower fibrin-binding in comparison to FibPep (75.5 ± 2.0 and 88.5 ± 1.3% dose, respectively, $p < 0.001$), whereas both EPep and FibPep showed significantly higher fibrin-binding in comparison to NCFibPep (1.2 ± 2.4% dose, $p < 0.001$). Incubation of the samples in blood instead of HBS led to similar results (77.5 ± 5.1, 89.9 ± 1.3 and 2.2 ± 0.9% dose for EPep, FibPep and NCFibPep, respectively, $p>0.05$ in comparison to samples incubated in HBS).

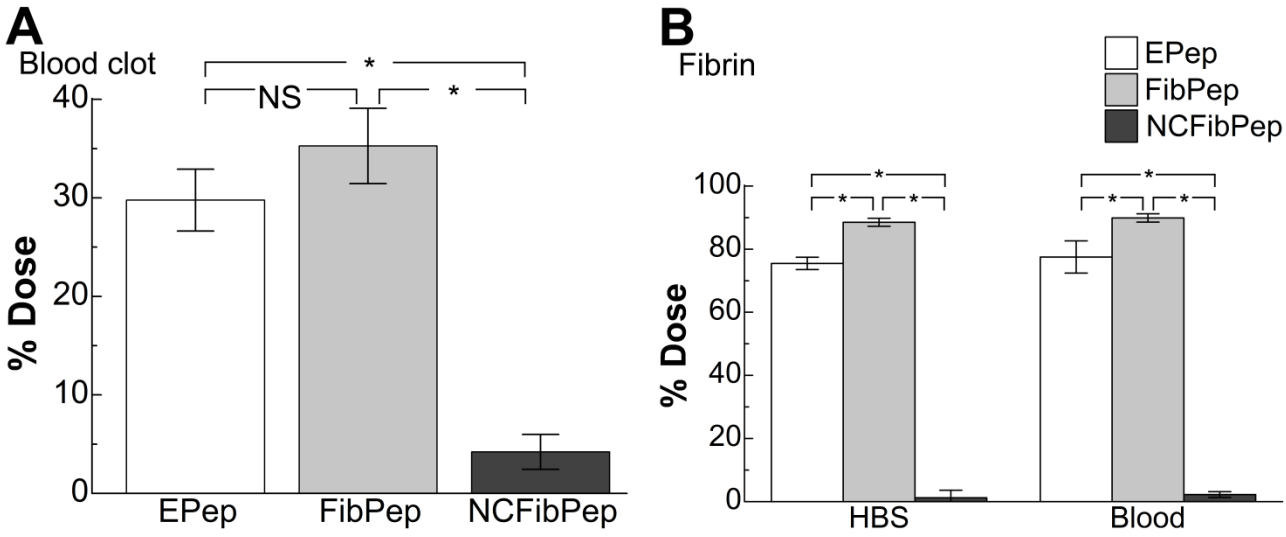

Figure 4. *Binding of EPep, FibPep and NCFibPep to (A) human plasma derived blood clots in HBS and (B) human derived fibrin in either HBS or human blood. Data is expressed as mean percentage dose ± SD (n=4). *p < 0.01; NS = not significant.*

The probe affinities toward human, mouse and rat derived fibrin were analyzed in a microtiter-plate equilibrium binding assay.[26, 35] The determined dissociation constants and number of binding sites per fibrin molecule are shown in Table 1. EPep bound to human, mouse and rat derived fibrin with a dissociation constant (K_d) of approximately 1 µM and displayed ca. 2 binding sites per fibrin molecule (Fig. 5A). FibPep bound in a similar fashion to human and mouse derived fibrin (Fig. 5B), whereas binding toward rat derived fibrin was much weaker (K_d = 14 µM). NCFibPep bound approximately 100-fold more weakly to human, mouse and rat derived fibrin in comparison to EPep and seemingly displayed a higher number of binding sites (Fig. 5C). This is likely due to a small fraction of nonspecific retention in the microtiter plates which becomes relevant in the fitting procedure for samples incubated with high concentrations of tracer, as was the case for NCFibPep.

Table 1. *Dissociation constant (K_d) values and number of binding sites per fibrin molecule (# binding sites) ± standard error for EPep, FibPep and NCFibPep as obtained from the fits of the binding curves (Fig. 5) which were fitted as described in a previously published protocol.*[35]

	Human derived fibrin		Mouse derived fibrin		Rat derived fibrin	
Tracer	**K_d (µM)**	**# binding sites**	**K_d (µM)**	**# binding sites**	**K_d (µM)**	**# binding sites**
EPep	0.9 ± 0.1	2.0 ± 0.0	1.4 ± 0.1	2.2 ± 0.1	1.2 ± 0.1	2.2 ± 0.0
FibPep	0.6 ± 0.0	2.8 ± 0.0	0.8 ± 0.1	2.3 ± 0.0	14 ± 2	2.0 ± 0.1
NCFibPep	98 ± 21	4.8 ± 0.5	146 ± 61	7.5 ± 1.9	77 ± 20	5.6 ± 0.7

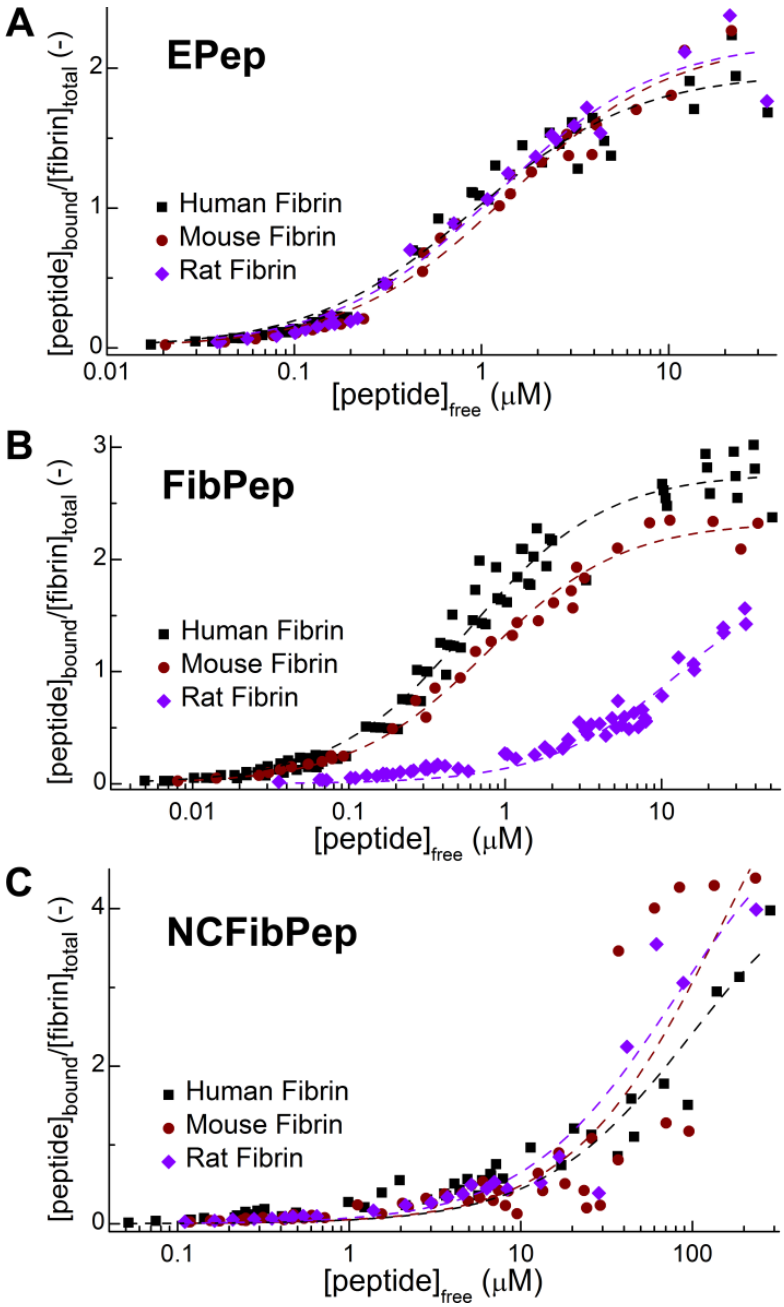

Figure 5. *(A) EPep, (B) FibPep and (C) NCFibPep fibrin-binding curves for human, mouse and rat derived fibrin. Dashed lines plotted as described in a previously published protocol.*[35]

3.3.4 Blood kinetic, biodistribution and histology

The blood kinetic and biodistribution profiles of EPep, FibPep and NCFibPep were investigated in a carotid artery thrombosis rat model. In addition, EPep was also evaluated in a carotid artery thrombosis mouse model for comparison with previously published data on FibPep in the same model.[35] Figure 6 summarizes the obtained blood kinetic and biodistribution profiles of EPep in mice. EPep displayed a biphasic elimination from circulation (Fig. 6A), with an α half-life of 1.0 ± 0.3 min (46%) and a β half-life of 15.3 ± 0.7 min. The biodistribution in mice 4 h post injection showed significant higher uptake of EPep in the injured carotid in comparison to the noninjured, contralateral carotid artery (6.8 ± 1.2 and 0.2 ± 0.1% ID/g, respectively, $p < 0.01$, Fig. 6B). In addition, EPep displayed low retention in nontarget organs (<0.4% ID/g), with exception of the kidneys (8.8 ± 1.8% ID/g).

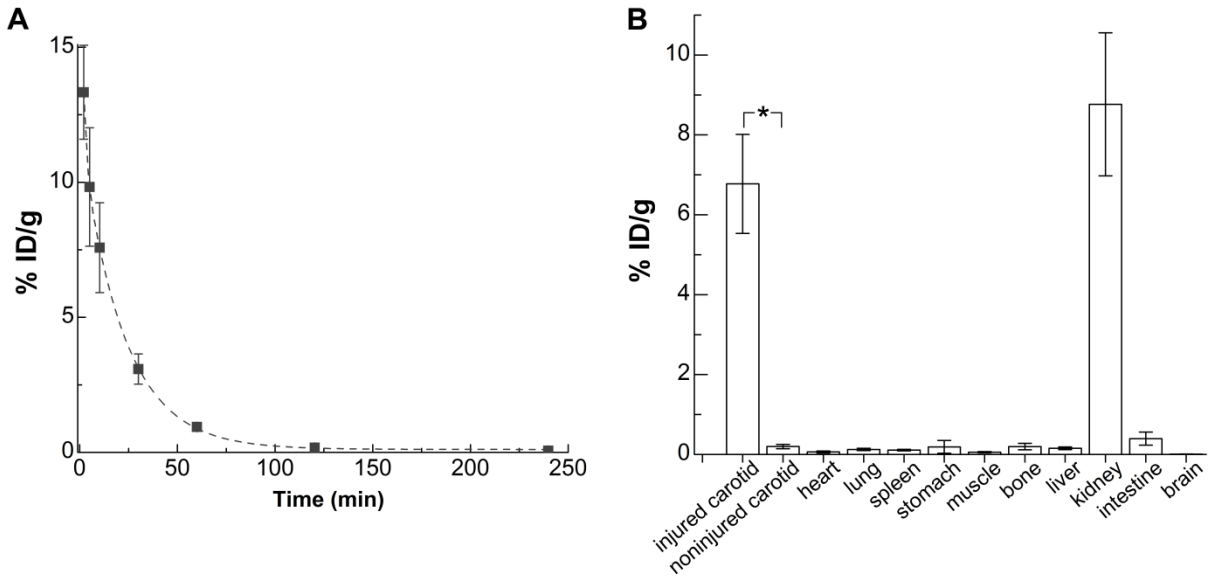

Figure 6. *(A) Blood kinetic (n=3) and (B) biodistribution profiles (4 h post injection; n=4) of EPep in mice. Data are the mean percentage injected dose per gram ± SD. Plotted dashed line is the corresponding bi-exponential elimination fit. *p < 0.01.*

Figure 7A shows the blood kinetic profiles of EPep, FibPep and NCFibPep in rats. All peptide probes were eliminated from the circulation in a biphasic fashion. EPep displayed an α half-life of 1.4 ± 0.5 (56%) min and a β half-life of 25.0 ± 3.2 min. FibPep and NCFibPep had similar elimination kinetics, showing an a α half-life of 2.0 ± 1.0 (54%) and 1.1 ± 0.4 (60%) min and a β half-life of 23.3 ± 3.0 min and 21.9 ± 0.6 min, respectively. Figure 7B shows the biodistribution profiles of EPep, FibPep and NCFibPep in rats 4 h post injection. A group that received a 5-fold increased dose of FibPep was also included. EPep showed significantly higher uptake in the thrombus containing, injured carotid with respect to FibPep and NCFibPep (0.74 ± 0.39, 0.06 ± 0.02 and 0.04 ± 0.01% ID/g, respectively, $p < 0.01$). A 5-fold increase in dose for FibPep did not significantly improve the uptake in the injured carotid (0.09 ± 0.03% ID/g). The retention in nontarget tissues was similar for all probes, with low uptake in most of the assessed organs and higher levels of activity in the kidneys. The only exception was an increased liver uptake of FibPep with respect to EPep and NCFibPep. Urine was collected from the rats 4 h post injection and analyzed using radio-HPLC (Fig. 8A-B). All probes were metabolized, with EPep still

showing a minor percentage of intact parent compound (12 ± 4%), whereas virtually no intact probe (<1%) was measured in the urine of rats that received FibPep and NCFibPep.

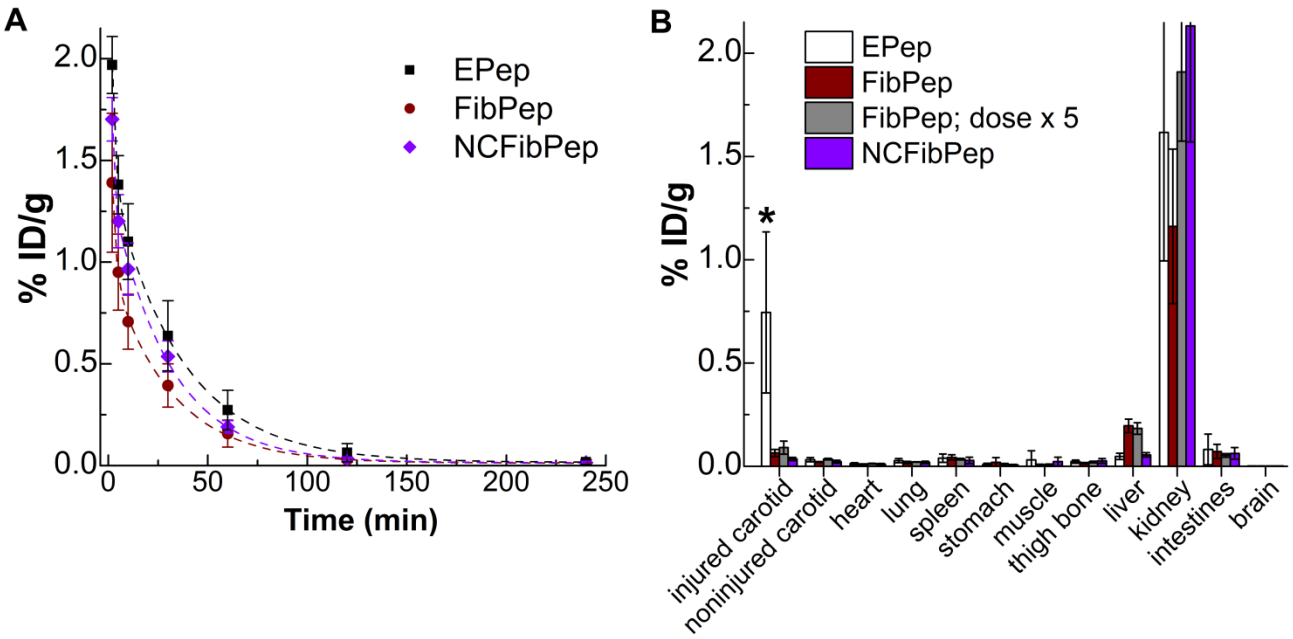

Figure 7. *(A) Blood kinetic (n=3) and (B) biodistribution profiles (4 h post injection) in rats injected with EPep, FibPep and NCFibPep (n=5) and FibPep injected with a 5-fold increased dose (n=3). Plotted dashed lines are the corresponding bi-exponential elimination fits and data is expressed as the mean percentage injected dose per gram ± SD. *p < 0.01 vs FibPep and NCFibPep injured carotid.*

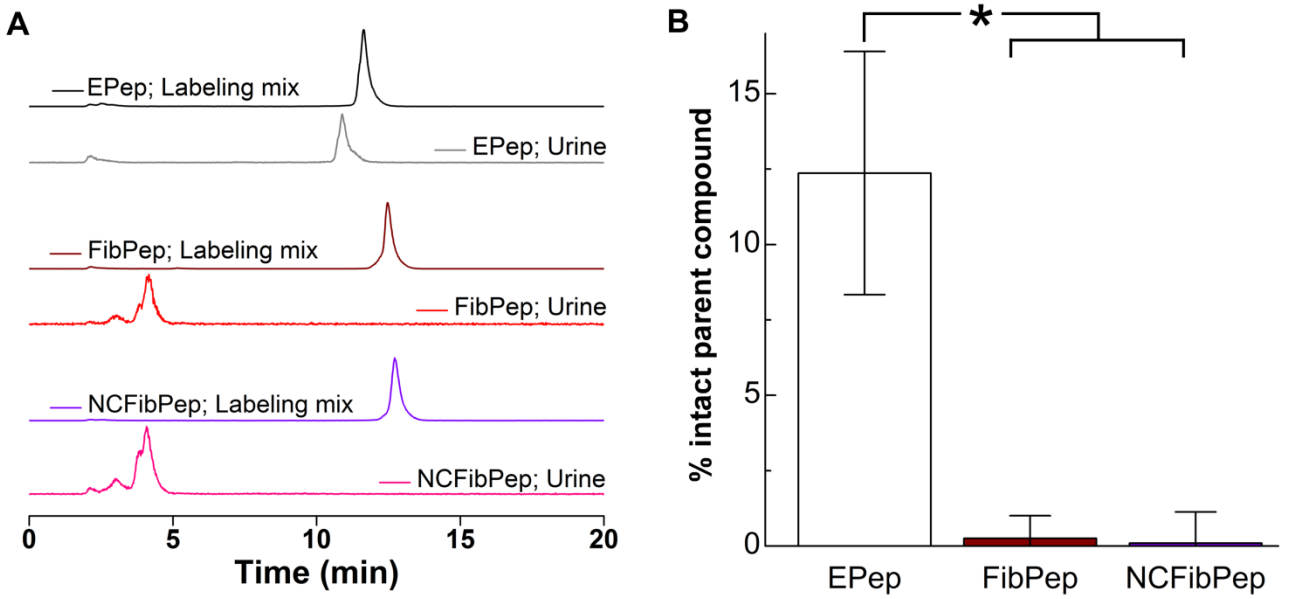

Figure 8. *(A) Typical chromatograms of EPep, FibPep and NCFibPep prior to injection and in urine which was collected 4 h post injection. (B) Stability of the peptide probes in urine 4 h post injection as derived from the chromatograms. Data expressed as mean percentage intact parent compound ± SD (n=3). *p < 0.01.*

3.3.5 SPECT imaging and ex vivo autoradiography

In vivo SPECT imaging of the head-neck area of live rats with carotid artery thrombosis was performed starting 2.5 h post tracer injection with a total scan time of 1 h. Subsequently, the rats were euthanized and a post-mortem full body SPECT/CT scan was performed. Next, the injured and contralateral carotids were excised and evaluated by autoradiography.

In vivo SPECT imaging showed high signal at the thrombus site for EPep, whereas FibPep and NCFibPep did not allow clear visualization of the thrombus-containing carotid (Fig. 9). Quantitative analysis of the *in vivo* SPECT images showed significantly higher signal in the injured carotid area for EPep (0.25 ± 0.04% ID/cm^3) with respect to FibPep and NCFibPep (0.06 ± 0.02 and 0.04 ± 0.01% ID/cm^3, respectively, $p < 0.01$, Fig. 10), and to the contralateral areas (0.01 ± 0.01; 0.01 ± 0.00 ad 0.01 ± 0.01% ID/cm^3, respectively, $p < 0.01$). Post-mortem full body SPECT/CT scans showed mainly bladder (radioactive urine) and kidney uptake for all probes (Fig. 11). Figure 12 displays photo- and autoradiographs of the excised carotids. The injured carotids show noticeable increased tracer accumulation at the thrombus site for rats injected with EPep and, to a lesser extent, for rats injected with FibPep, whereas uptake in the noninjured carotids was low and homogeneous for all tracers. The thrombus-to-contralateral carotid signal ratio from autoradiography measurements for rats injected with EPep (31.7 ± 16.0) was significantly higher than that for rats injected with FibPep and NCFibPep (4.7 ± 1.1 and 1.7 ± 0.1, respectively, $p < 0.01$, Fig. 12G). Histological sections stained with hematoxylin and eosin confirmed the presence of thrombus in the injured rat carotid artery (Fig. 12H-I).

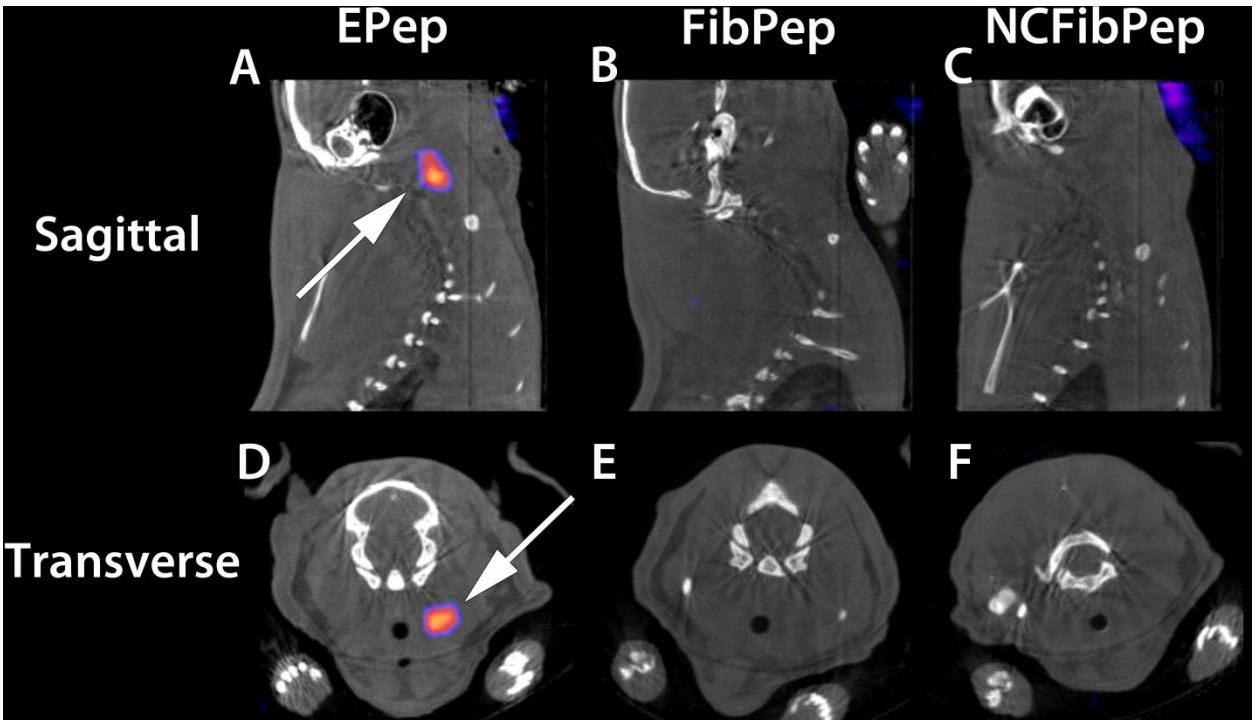

Figure 9. *In vivo SPECT/CT imaging of the head/neck area using (A,D) EPep, (B,E) FibPep and (C,F) NCFibPep in a carotid thrombosis rat model (3 h post injection; sagittal and transverse slices). Arrows: increased uptake of tracer in the induced thrombus. All images are displayed using the same color scale.*

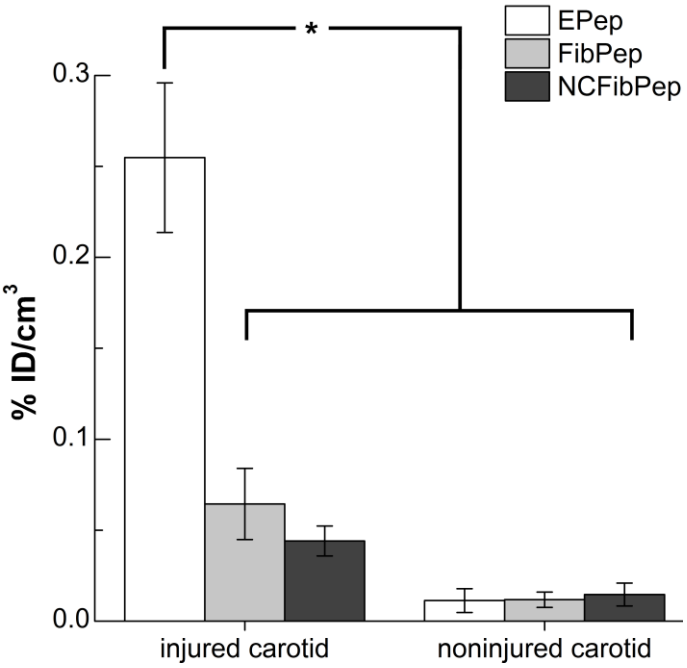

Figure 10. *Quantitative analysis of the in vivo SPECT scans (3 h post injection). Percentage injected dose per cm^3 of EPep, FibPep and NCFibPep in volumes of interest of the injured carotid and contralateral area. Data is expressed as mean percentage injected dose per cm^3 ± SD (n=4). *p < 0.01.*

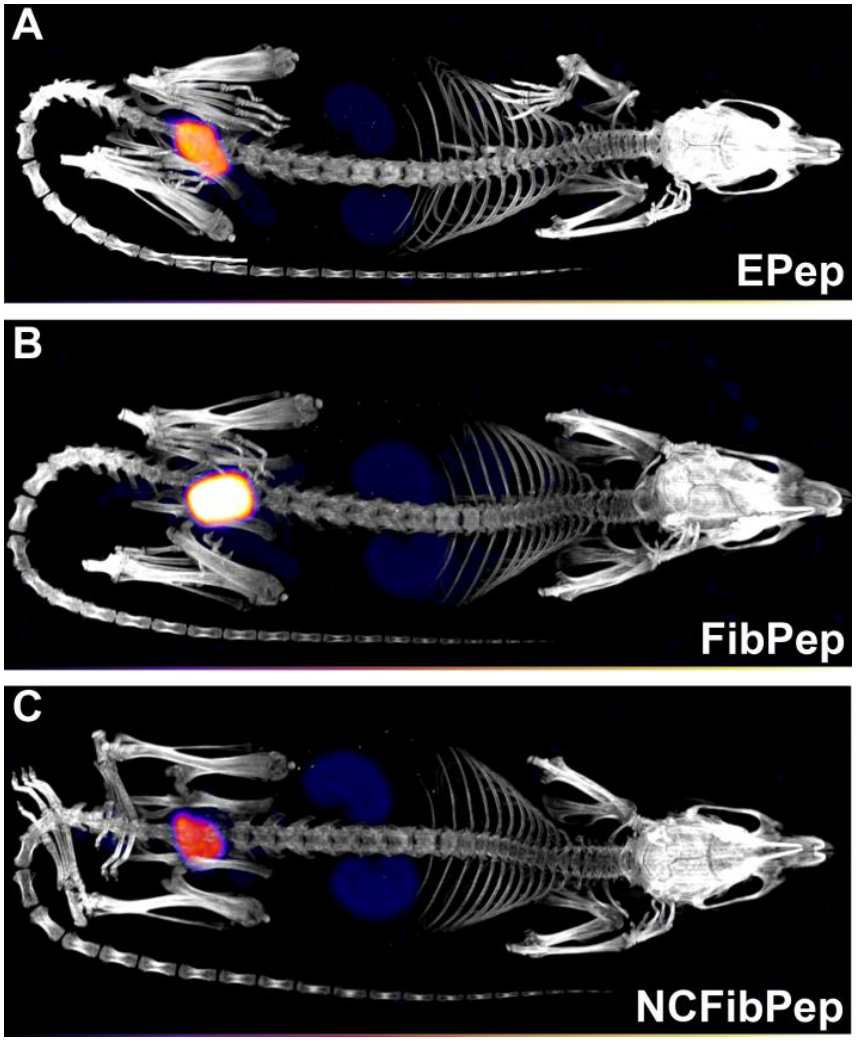

Figure 11. *Post-mortem whole body SPECT/CT imaging of rats injected with (A) EPep, (B) FibPep and (C) NCFibPep showing uptake in kidneys and high activity in the urine (3.5 h post injection; maximum intensity projections). All images are displayed using the same color scale.*

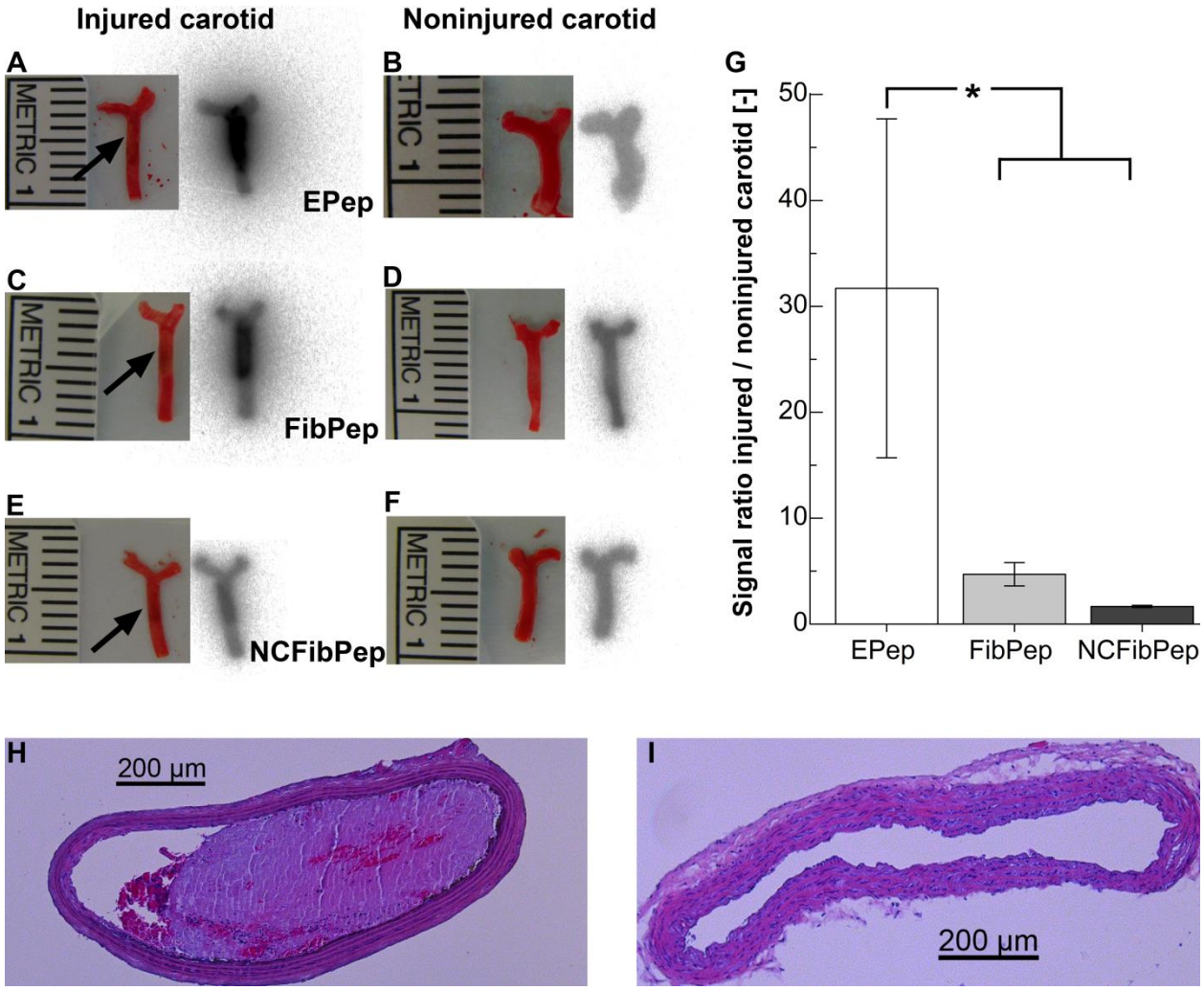

Figure 12. *Representative photo- and autoradiographs of excised injured and contralateral, noninjured carotid arteries post SPECT imaging of rats injected with (A,B) EPep, (C,D) FibPep and (E,F) NCFibPep. Arrows: site of thrombus induced by $FeCl_3$-injury. (G) Quantitative analysis of the autoradiographs using regions of interest drawn in the thrombus and the contralateral artery. Data is expressed as signal ratio of injured over noninjured carotid ± SD (n=4). *p < 0.01. (H,I) Hematoxylin and eosin stained transversal histological section of the (H) injured carotid and (I) noninjured, contralateral carotid artery showing thrombosis in the injured carotid and not in the contralateral carotid.*

3.4 Discussion

Fibrin is a promising and frequently employed target for molecular imaging,[15, 19-21, 23, 24, 28, 29] as it is involved in thrombosis, atherosclerosis and tumor metastasis and angiogenesis.[7, 8, 11-13] In previous work, we established ^{111}In-labeled FibPep as a tracer for fibrin SPECT imaging and successfully showed detection of carotid thrombosis in mice using FibPep.[35] In this study, we developed EPep, a novel ^{111}In-labeled fibrin-binding peptide containing the fibrin-binding domain of the clinically verified EP-2104R peptide, and sought to compare the potential of EPep and FibPep as tracers for fibrin SPECT imaging. As a negative control, NCFibPep, a scrambled and linearized version of FibPep, was employed in the study.

In vitro stability assays in serum showed high stability for both EPep and FibPep while NCFibPep displayed noticeable lower stability. Cyclization of peptides is known to decrease proteolytic degradation,[41] and thus the relative low stability of NCFibPep might be due to the linear nature of the peptide. Small molecules such as peptides are often able to distribute throughout the extravascular space and therefore may encounter proteolytic enzymes in kidney and liver, which are not taken into consideration when using serum stability assays to predict *in vivo* metabolism.[41, 42] Therefore, to account for the influence of these organs on the systemic metabolism, additional *in vitro* stability assays were performed in kidney and liver homogenates. EPep and FibPep were moderately stable in liver homogenates but were rapidly degraded in kidney homogenates after 10 min. NCFibPep showed virtually complete degradation in both liver and kidney homogenates. It should, however, be noted that many of the proteolytic enzymes active in the homogenates are located in the cytosole under physiological conditions. Thus, *in vivo* the tracers will likely be digested in lower rates than in the tissue homogenate assays.[41] In fact, the time window prior to degradation seems nevertheless sufficient to allow effective targeting of fibrin *in vivo*, as FibPep showed high clot association in a carotid thrombosis mouse model.[35]

FibPep and EPep displayed roughly similar binding to blood clots derived from human plasma and fibrin clots derived from human fibrinogen *in vitro*, with FibPep showing approximately 15-20% more binding than EPep. A similar experiment performed using human whole blood as incubation medium instead of HBS did not show any significant differences in EPep and FibPep binding to human derived fibrin clots in comparison to the experiments performed using HBS. This proves that both peptides have a high degree of specificity for fibrin over plasma proteins such as serum albumin and fibrinogen and confirms that, similar to serum, both peptides are not significantly metabolized in human whole blood *in vitro*. EPep showed similar affinity (K_d ≈ 1 µM) and number of binding sites (ca. 2 binding sites per fibrin molecule) for human, mouse and rat derived fibrin in a microtiter-plate equilibrium binding assay. These values correspond well to the values reported for EP-2104R (K_d ≈1.5 µM and approximately 2 binding sites per fibrin molecule),[26] indicating that EPep binds in a fashion similar to EP-2104R toward fibrin of different origin. FibPep showed affinity for human and mouse derived fibrin (K_d ≈ 0.7 µM) and number of binding sites (≈2.5) comparable to those of EPep, which is in accordance with the similar clot uptake values found *in vitro* for EPep and FibPep in the human derived blood and fibrin clot binding tests. Interestingly, however, the affinity of FibPep toward rat derived fibrin was considerably lower (K_d = 14 µM). Fibrin(ogen) is known to be only partially homologous in different species,[43, 44] and for multiple monoclonal antibodies against human fibrin(ogen) it has been shown that they are unable to cross-react with fibrin(ogen) derived from other species.[45-48] In a similar fashion, we hypothesize that the FibPep binding fibrin epitope is not entirely homologous between humans and rats. Our results also suggest that FibPep and EPep bind to different epitopes on the fibrin molecule, as, contrary to FibPep, EPep does not show a significant difference in binding between human and rat derived fibrin. Since the fibrin-binding amino acid sequences of both EPep and FibPep were derived by phage display against human fibrin using fibrinogen binder depleted libraries,[49-51] the exact binding epitopes of EPep and FibPep are likely surfaces exposed by fibrin polymerization induced domain movements or new surfaces

formed by interdomain contact present in fibrin but absent in fibrinogen.[51] This study did not attempt to elucidate the exact EPep and FibPep binding epitopes, and thus similarly to the fibrin-binding peptide families recently published by Kolodziej and coworkers,[51] which includes the amino acid sequence on which the EP-2104R peptide was based, the exact binding sites on the fibrin molecule remain unidentified for both EPep and FibPep.

The pharmacokinetics, biodistribution and *in vivo* fibrin targeting capabilities of EPep were evaluated in a $FeCl_3$-induced carotid injury mouse model in order to allow comparison to recently published data for FibPep in the same mouse model.[35] EPep cleared rapidly from the circulation, resembling closely the FibPep blood kinetic profile in mice.[35] In addition, the uptake in the injured carotid 4 h post injection was similar for EPep (6.8 ± 1.2% ID/g) and FibPep (5.7 ± 0.7% ID/g)[35] and comparable behaviors were observed in nontarget organs. These findings, combined with the *in vitro* stability and binding assays, suggest that both EPep and FibPep are equally suitable for fibrin SPECT imaging in preclinical mouse models of disease.

To investigate potential consequences of the reduced affinity of FibPep toward rat derived fibrin, the two ^{111}In-labeled fibrin-binding peptides were evaluated also in a rat carotid injury model. In rats, both peptides showed fast clearance from the circulation. EPep showed high uptake in the injured carotid, whereas FibPep showed only marginally increased uptake when compared to the negative control NCFibPep. This is in contrast with the high thrombus uptake found for FibPep in a mouse carotid thrombosis model.[35] As the amount of injected peptide (15 nmol per animal) was identical for rats and mice, the dose of peptides in rats (mol/kg) was approximately 8-fold smaller than in mice. However, injection of a 5-fold higher FibPep amount (75 nmol per animal) did not significantly increase uptake in the injured carotid in rats. Therefore, the different dose used in mice and rats did not contribute to the reduced FibPep thrombus uptake in rats. Overall, our findings suggest that the reduced affinity of FibPep toward rat derived fibrin significantly decreases *in vivo* thrombus association of FibPep in rats.

The uptake of EPep and FibPep in most nontarget organs in rats was similar to that found in mice. Only exception was the liver uptake, which showed approximately a 10-fold higher FibPep uptake to most other nontarget rat organs, whereas uptake in mouse liver was not increased.[35] This suggests that FibPep might be metabolized in different fashions or rates *in vivo* in mice and rats. Interestingly, this might correspond well to the findings of the *in vitro* mouse and rat kidney/liver homogenate stability assays, where, only in rat liver homogenates, FibPep was more stable than EPep. Radio-HPLC analysis of rat urine collected 4 h post injection showed that for EPep only a minor fraction was still intact, whereas FibPep was virtually completely metabolized. These results correspond well to the *in vitro* rat kidney homogenate assay.

In vivo SPECT imaging 3 h post injection showed a clear uptake of radioactivity in the carotid thrombus of the rats injected with EPep, whereas in the carotid thrombus of the rats injected with FibPep no uptake was visible. *Ex vivo* autoradiography displayed a 32-fold increase in signal in the thrombus over

the contralateral carotid for EPep, whereas FibPep only showed a 5-fold increase. These results indicate that EPep is a promising tracer for fibrin SPECT imaging in preclinical rat models of disease, and that although FibPep still showed an increased uptake in the rat thrombus over the contralateral vessel, the amount of additional uptake is insufficient for FibPep to allow thrombus detection using fibrin SPECT imaging in rat carotid thrombosis model. The results of this study demonstrate that when animal models are being employed to gauge the clinical potential of novel imaging tracers, it is critically important to verify the binding characteristics of the tracer not only against its human derived target but also against the target obtained from the animal species to be employed in the preclinical studies.
Overall, based on the data presented in this study, both peptides seem equally promising for molecular imaging of fibrin using SPECT in clinical settings, as both peptides show similar affinities toward human fibrin, similar stability in human serum and roughly comparable stability in rat and mouse tissue homogenates. A potential area of improvement for both EPep and FibPep is reducing the rate of metabolism of the peptides *in vivo*, since both probes are metabolized rapidly in kidney and liver homogenate assays and, in addition, are also mainly found back in urine as metabolized species. Judicious modification of the peptides by for instance replacing potentially labile amino acids with their D-amino acid counterparts, or attaching at both the C- and N-termini a DOTA-chelator may decrease metabolism of the peptides.[41, 52] Naturally, any change in peptide structure may affect fibrin affinity and/or blood kinetic and biodistribution profiles, and therefore modified versions of EPep and FibPep should be carefully re-evaluated with respect to these properties.

Multiple other approaches for nuclear imaging of fibrin deposition have been reported in the past decades.[20-25] In a very promising, recent and also similar effort, Caravan and coworkers successfully employed the EP-2104R peptide and subsequently simplified versions of the same peptide for PET imaging of thrombi using ^{64}Cu–DOTA labeling.[53, 54] The affinity of these peptides toward human fibrin is roughly similar to that of EPep and FibPep and experiments in rats showed that these tracers are also found back in urine for a significant part as metabolized species. The main advantage of employing PET over SPECT imaging is the higher spatial resolution in clinical settings. However, the ^{64}Cu-DOTA isotope-chelator complex is known to release ^{64}Cu,[55] which subsequently accumulates in the liver by binding to superoxide dismutase.[56] This leads to increased radiation exposure and also to high PET signal in the liver area,[53, 54] which hampers the ability to image fibrin in a major part in the abdomen and possibly also in the heart and coronaries. Our approach is not hampered by high liver uptake and furthermore SPECT allows multi-isotope imaging,[57-59] enabling the simultaneous assessment of multiple biomarkers, which could be vital for obtaining reliable and robust read-outs of complex pathologies such as cancer and atherosclerosis. In addition, the availability of SPECT-CT systems allows combining fibrin SPECT imaging with anatomical CT or with contrast enhanced CT-based strategies, such as for instance CT angiography using iodinated contrast agents,[60] and acute thrombus imaging, employing (nontargeted) gold nanoparticles that become trapped in newly formed blood clots.[61]

In conclusion, we assessed the potential of two ^{111}In-labeled fibrin-binding peptides, EPep and FibPep, for SPECT imaging of fibrin. Affinities toward human and mouse derived fibrin were similar for EPep and

FibPep, and EPep displayed similar thrombus uptake in comparison to FibPep in mice. Thus, both peptides are equally promising for translation into clinical settings and may provide a new tool to diagnose and monitor diseases such as atherosclerosis, cancer, deep venous thrombosis and pulmonary embolism.

3.5 Acknowledgements

The authors thank Hugo Knobel and Jeroen van den Berg (Philips Research) for LC-MS measurements and Iris Verel, Katia Donato, Suzanne Kivits (Philips Research), Caren van Kammen, Melanie Blonk, Marleen Hendriks and Carlijn van Helvert (Maastricht University) for their excellent support with the *in vivo* experiments. This research was supported by the Center for Translational Molecular Medicine and the Netherlands Heart Foundation (PARISK, grant 01C-202).

3.6 References

1. Weisel, J. W. Fibrinogen and fibrin. *Adv Protein Chem* **2005,** *70*, 247-99.
2. Mosesson, M. W. Fibrinogen and fibrin structure and functions. *Journal of Thrombosis and Haemostasis* **2005,** *3*, (8), 1894-1904.
3. Go, A. S.; Mozaffarian, D.; Roger, V. L.; Benjamin, E. J.; Berry, J. D.; Borden, W. B.; Bravata, D. M.; Dai, S.; Ford, E. S.; Fox, C. S.; Franco, S.; Fullerton, H. J.; Gillespie, C.; Hailpern, S. M.; Heit, J. A.; Howard, V. J.; Huffman, M. D.; Kissela, B. M.; Kittner, S. J.; Lackland, D. T.; Lichtman, J. H.; Lisabeth, L. D.; Magid, D.; Marcus, G. M.; Marelli, A.; Matchar, D. B.; McGuire, D. K.; Mohler, E. R.; Moy, C. S.; Mussolino, M. E.; Nichol, G.; Paynter, N. P.; Schreiner, P. J.; Sorlie, P. D.; Stein, J.; Turan, T. N.; Virani, S. S.; Wong, N. D.; Woo, D.; Turner, M. B. Executive summary: heart disease and stroke statistics--2013 update: a report from the American Heart Association. *Circulation* **2013,** *127*, (1), 143-52.
4. Alwan, A.; Armstrong, T.; Bettcher, D.; Branca, F.; Chisholm, D.; Ezzati, M.; Garfield, R.; MacLean, D.; Mathers, C.; Mendis, S.; Poznyak, V.; Riley, L.; Tang, K. C.; Wild, C., Global status report on noncommunicable diseases 2010. World Health Organization: 2011.
5. Burns, S. K.; Haramati, L. B. Diagnostic imaging and risk stratification of patients with acute pulmonary embolism. *Cardiol Rev* **2012,** *20*, (1), 15-24.
6. Elliott, C. G.; Lovelace, T. D.; Brown, L. M.; Adams, D. Diagnosis: imaging techniques. *Clin Chest Med* **2010,** *31*, (4), 641-57.
7. Bini, A.; Fenoglio, J. J., Jr.; Mesa-Tejada, R.; Kudryk, B.; Kaplan, K. L. Identification and distribution of fibrinogen, fibrin, and fibrin(ogen) degradation products in atherosclerosis. Use of monoclonal antibodies. *Arteriosclerosis* **1989,** *9*, (1), 109-21.
8. Tavora, F.; Cresswell, N.; Li, L.; Ripple, M.; Burke, A. Immunolocalisation of fibrin in coronary atherosclerosis: implications for necrotic core development. *Pathology* **2010,** *42*, (1), 15-22.
9. Congiu, T.; Schembri, L.; Tozzi, M.; Guasti, L.; Maio, R. C.; Cosentino, M.; Marino, F. Scanning electron microscopy examination of endothelium morphology in human carotid plaques. *Micron* **2010,** *41*, (5), 532-6.
10. Sato, Y.; Hatakeyama, K.; Yamashita, A.; Marutsuka, K.; Sumiyoshi, A.; Asada, Y. Proportion of fibrin and platelets differs in thrombi on ruptured and eroded coronary atherosclerotic plaques in humans. *Heart* **2005,** *91*, (4), 526-30.
11. Rickles, F. R.; Patierno, S.; Fernandez, P. M. Tissue factor, thrombin, and cancer. *Chest* **2003,** *124*, (3 Suppl), 58S-68S.
12. Dvorak, H. F.; Nagy, J. A.; Berse, B.; Brown, L. F.; Yeo, K. T.; Yeo, T. K.; Dvorak, A. M.; van de Water, L.; Sioussat, T. M.; Senger, D. R. Vascular permeability factor, fibrin, and the pathogenesis of tumor stroma formation. *Ann N Y Acad Sci* **1992,** *667*, 101-11.

13. Palumbo, J. S.; Talmage, K. E.; Massari, J. V.; La Jeunesse, C. M.; Flick, M. J.; Kombrinck, K. W.; Jirouskova, M.; Degen, J. L. Platelets and fibrin(ogen) increase metastatic potential by impeding natural killer cell-mediated elimination of tumor cells. *Blood* **2005,** *105*, (1), 178-85.

14. Lanza, G. M.; Wallace, K. D.; Scott, M. J.; Cacheris, W. P.; Abendschein, D. R.; Christy, D. H.; Sharkey, A. M.; Miller, J. G.; Gaffney, P. J.; Wickline, S. A. A novel site-targeted ultrasonic contrast agent with broad biomedical application. *Circulation* **1996,** *94*, (12), 3334-40.

15. Flacke, S.; Fischer, S.; Scott, M. J.; Fuhrhop, R. J.; Allen, J. S.; McLean, M.; Winter, P.; Sicard, G. A.; Gaffney, P. J.; Wickline, S. A.; Lanza, G. M. Novel MRI contrast agent for molecular imaging of fibrin: implications for detecting vulnerable plaques. *Circulation* **2001,** *104*, (11), 1280-5.

16. Pan, D.; Senpan, A.; Caruthers, S. D.; Williams, T. A.; Scott, M. J.; Gaffney, P. J.; Wickline, S. A.; Lanza, G. M. Sensitive and efficient detection of thrombus with fibrin-specific manganese nanocolloids. *Chem Commun (Camb)* **2009**, (22), 3234-6.

17. Pan, D.; Roessl, E.; Schlomka, J. P.; Caruthers, S. D.; Senpan, A.; Scott, M. J.; Allen, J. S.; Zhang, H.; Hu, G.; Gaffney, P. J.; Choi, E. T.; Rasche, V.; Wickline, S. A.; Proksa, R.; Lanza, G. M. Computed tomography in color: NanoK-enhanced spectral CT molecular imaging. *Angew Chem Int Ed Engl* **2010,** *49*, (50), 9635-9.

18. Pan, D.; Caruthers, S. D.; Senpan, A.; Yalaz, C.; Stacy, A. J.; Hu, G.; Marsh, J. N.; Gaffney, P. J.; Wickline, S. A.; Lanza, G. M. Synthesis of NanoQ, a copper-based contrast agent for high-resolution magnetic resonance imaging characterization of human thrombus. *J Am Chem Soc* **2011,** *133*, (24), 9168-71.

19. McCarthy, J. R.; Patel, P.; Botnaru, I.; Haghayeghi, P.; Weissleder, R.; Jaffer, F. A. Multimodal nanoagents for the detection of intravascular thrombi. *Bioconjug Chem* **2009,** *20*, (6), 1251-5.

20. Bosnjakovic, V. B.; Jankovic, B. D.; Horvat, J.; Cvoric, J. Radiolabelled anti-human fibrin antibody: a new thrombus-detecting agent. *Lancet* **1977,** *1*, (8009), 452-4.

21. Rosebrough, S. F.; Kudryk, B.; Grossman, Z. D.; McAfee, J. G.; Subramanian, G.; Ritter-Hrncirik, C. A.; Witanowski, L. S.; Tillapaugh-Fay, G. Radioimmunoimaging of venous thrombi using iodine-131 monoclonal antibody. *Radiology* **1985,** *156*, (2), 515-7.

22. Thakur, M. L.; Pallela, V. R.; Consigny, P. M.; Rao, P. S.; Vessileva-Belnikolovska, D.; Shi, R. Imaging vascular thrombosis with 99mTc-labeled fibrin alpha-chain peptide. *J Nucl Med* **2000,** *41*, (1), 161-8.

23. Aruva, M. R.; Daviau, J.; Sharma, S. S.; Thakur, M. L. Imaging Thromboembolism with Fibrin-Avid 99mTc-Peptide: Evaluation in Swine. *J Nucl Med* **2006,** *47*, (1), 155-162.

24. Morris, T. A.; Gerometta, M.; Smart, R. C.; Eisenberg, P.; Roach, P. J.; Tsui, W. W.; Better, N.; Taubman, K. L.; Unger, S. A.; Macfarlane, D. Pulmonary Emboli Imaging with 99mTc-labelled Anti-D-dimer (DI-80B3) Fab' Followed by SPECT. *Heart, Lung and Circulation* **2011,** *20*, (8), 503-511.

25. Douketis, J. D.; Ginsberg, J. S.; Haley, S.; Julian, J.; Dwyer, M.; Levine, M.; Eisenberg, P. R.; Smart, R.; Tsui, W.; White, R. H.; Morris, T. A.; Kaatz, S.; Comp, P. C.; Crowther, M. A.; Kearon, C.; Kassis, J.; Bates, S. M.; Schulman, S.; Desjardins, L.; Taillefer, R.; Begelman, S. M.; Gerometta, M. Accuracy and safety of 99mTc-labeled anti-D-dimer (DI-80B3) Fab' fragments (ThromboView®) in the diagnosis of deep vein thrombosis: A phase II study. *Thrombosis Research* **2012,** *130*, (3), 381-389.

26. Overoye-Chan, K.; Koerner, S.; Looby, R. J.; Kolodziej, A. F.; Zech, S. G.; Deng, Q.; Chasse, J. M.; McMurry, T. J.; Caravan, P. EP-2104R: a fibrin-specific gadolinium-Based MRI contrast agent for detection of thrombus. *J Am Chem Soc* **2008,** *130*, (18), 6025-39.

27. Sirol, M.; Fuster, V.; Badimon, J. J.; Fallon, J. T.; Moreno, P. R.; Toussaint, J. F.; Fayad, Z. A. Chronic thrombus detection with in vivo magnetic resonance imaging and a fibrin-targeted contrast agent. *Circulation* **2005,** *112*, (11), 1594-600.

28. Uppal, R.; Medarova, Z.; Farrar, C. T.; Dai, G.; Moore, A.; Caravan, P. Molecular imaging of fibrin in a breast cancer xenograft mouse model. *Invest Radiol* **2012,** *47*, (10), 553-8.

29. Makowski, M. R.; Forbes, S. C.; Blume, U.; Warley, A.; Jansen, C. H.; Schuster, A.; Wiethoff, A. J.; Botnar, R. M. In vivo assessment of intraplaque and endothelial fibrin in ApoE(-/-) mice by molecular MRI. *Atherosclerosis* **2012,** *222*, (1), 43-9.

30. Spuentrup, E.; Katoh, M.; Wiethoff, A. J.; Parsons, E. C., Jr.; Botnar, R. M.; Mahnken, A. H.; Gunther, R. W.; Buecker, A. Molecular magnetic resonance imaging of pulmonary emboli with a fibrin-specific contrast agent. *Am J Respir Crit Care Med* **2005,** *172*, (4), 494-500.

31. Spuentrup, E.; Katoh, M.; Buecker, A.; Fausten, B.; Wiethoff, A. J.; Wildberger, J. E.; Haage, P.; Parsons, E. C., Jr.; Botnar, R. M.; Graham, P. B.; Vettelschoss, M.; Gunther, R. W. Molecular MR imaging of human thrombi in a swine model of pulmonary embolism using a fibrin-specific contrast agent. *Invest Radiol* **2007,** *42*, (8), 586-95.

32. Spuentrup, E.; Buecker, A.; Katoh, M.; Wiethoff, A. J.; Parsons, E. C., Jr.; Botnar, R. M.; Weisskoff, R. M.; Graham, P. B.; Manning, W. J.; Gunther, R. W. Molecular magnetic resonance imaging of coronary thrombosis and pulmonary emboli with a novel fibrin-targeted contrast agent. *Circulation* **2005,** *111*, (11), 1377-82.

33. Vymazal, J.; Spuentrup, E.; Cardenas-Molina, G.; Wiethoff, A. J.; Hartmann, M. G.; Caravan, P.; Parsons, E. C., Jr. Thrombus imaging with fibrin-specific gadolinium-based MR contrast agent EP-2104R: results of a phase II clinical study of feasibility. *Invest Radiol* **2009,** *44*, (11), 697-704.

34. Spuentrup, E.; Botnar, R. M.; Wiethoff, A. J.; Ibrahim, T.; Kelle, S.; Katoh, M.; Ozgun, M.; Nagel, E.; Vymazal, J.; Graham, P. B.; Gunther, R. W.; Maintz, D. MR imaging of thrombi using EP-2104R, a fibrin-specific contrast agent: initial results in patients. *Eur Radiol* **2008,** *18*, (9), 1995-2005.

35. Starmans, L. W.; van Duijnhoven, S. M.; Rossin, R.; Aime, S.; Daemen, M. J.; Nicolay, K.; Grull, H. SPECT imaging of fibrin using fibrin-binding peptides. *Contrast Media Mol Imaging* **2013,** *8*, (3), 229-37.

36. Starmans, L. W.; Burdinski, D.; Haex, N. P.; Moonen, R. P.; Strijkers, G. J.; Nicolay, K.; Grull, H. Iron oxide nanoparticle-micelles (ION-micelles) for sensitive (molecular) magnetic particle imaging and magnetic resonance imaging. *PLoS ONE* **2013,** *8*, (2), e57335.

37. Sachs, U. J. H.; Nieswandt, B. In Vivo Thrombus Formation in Murine Models. *Circ Res* **2007,** *100*, (7), 979-991.

38. von zur Muhlen, C.; von Elverfeldt, D.; Moeller, J. A.; Choudhury, R. P.; Paul, D.; Hagemeyer, C. E.; Olschewski, M.; Becker, A.; Neudorfer, I.; Bassler, N.; Schwarz, M.; Bode, C.; Peter, K. Magnetic Resonance Imaging Contrast Agent Targeted Toward Activated Platelets Allows In Vivo Detection of Thrombosis and Monitoring of Thrombolysis. *Circulation* **2008,** *118*, (3), 258-267.

39. Miserus, R. J.; Herias, M. V.; Prinzen, L.; Lobbes, M. B.; Van Suylen, R. J.; Dirksen, A.; Hackeng, T. M.; Heemskerk, J. W.; van Engelshoven, J. M.; Daemen, M. J.; van Zandvoort, M. A.; Heeneman, S.; Kooi, M. E. Molecular MRI of early thrombus formation using a bimodal alpha2-antiplasmin-based contrast agent. *JACC Cardiovasc Imaging* **2009,** *2*, (8), 987-96.

40. Heidt, T.; Deininger, F.; Peter, K.; Goldschmidt, J.; Pethe, A.; Hagemeyer, C. E.; Neudorfer, I.; Zirlik, A.; Weber, W. A.; Bode, C.; Meyer, P. T.; Behe, M.; von zur Mühlen, C. Activated Platelets in Carotid Artery Thrombosis in Mice Can Be Selectively Targeted with a Radiolabeled Single-Chain Antibody. *PLoS ONE* **2011,** *6*, (3), e18446.

41. Werle, M.; Bernkop-Schnürch, A. Strategies to improve plasma half life time of peptide and protein drugs. *Amino Acids* **2006,** *30*, (4), 351-367.

42. Ocak, M.; Helbok, A.; von Guggenberg, E.; Ozsoy, Y.; Kabasakal, L.; Kremser, L.; Decristoforo, C. Influence of biological assay conditions on stability assessment of radiometal-labelled peptides exemplified using a 177Lu-DOTA-minigastrin derivative. *Nuclear Medicine and Biology* **2011,** *38*, (2), 171-179.

43. Murakawa, M.; Okamura, T.; Kamura, T.; Shibuya, T.; Harada, M.; Niho, Y. Diversity of primary structures of the carboxy-terminal regions of mammalian fibrinogen A alpha-chains. Characterization of the partial nucleotide and deduced amino acid sequences in five mammalian species; rhesus monkey, pig, dog, mouse and Syrian hamster. *Thromb Haemost* **1993,** *69*, (4), 351-60.

44. Gorodetsky, R.; Vexler, A.; Shamir, M.; An, J.; Levdansky, L.; Shimeliovich, I.; Marx, G. New cell attachment peptide sequences from conserved epitopes in the carboxy termini of fibrinogen. *Exp Cell Res* **2003,** *287*, (1), 116-29.

45. Courtney, M. A.; Bunce, L. A.; Neroni, L. A.; Simpson-Haidaris, P. J. Cloning of the complete coding sequence of rat fibrinogen B beta chain cDNA: interspecies conservation of fibrin beta 15-42 primary structure. *Blood Coagul Fibrinolysis* **1994,** *5*, (4), 487-96.

46. Edgell, T.; McEvoy, F.; Webbon, P.; Gaffney, P. J. Monoclonal antibodies to human fibrin: interaction with other animal fibrins. *Thromb Haemost* **1996,** *75*, (4), 595-9.

47. Matsueda, G. R.; Margolies, M. N. Structural basis for the species selectivity of a fibrin-specific monoclonal antibody. *Biochemistry* **1986,** *25*, (6), 1451-5.

48. Walker, K. Z.; Khafagi, F.; Bautovich, G. J.; Boniface, G. R.; Bundesen, P. G.; Rylatt, D. B. Anti-fibrin monoclonal antibodies for radioimmunodetection: preliminary assessment in a rat model system. *Thromb Res* **1988,** *52*, (4), 269-78.

49. Wescot, C. R.; Beltzer, J. P.; Sato, A. K. Fibrin Binding Moieties Useful as Imaging Agents. WO 02/055544 A2, 2002.

50. Marinelli, E.; Ramalingam, K.; Swenson, R.; Song, B.; Lattuada, L.; Uggeri, F.; Lorusso, V.; Aime, S.; Morosini, P.; Chaabane, L. Fibrin Binding Peptide Conjugates for Diagnostic and Therapeutic Applications. WO 2008/071679 A1, 2008.

51. Kolodziej, A. F.; Nair, S. A.; Graham, P.; McMurry, T. J.; Ladner, R. C.; Wescott, C.; Sexton, D. J.; Caravan, P. Fibrin specific peptides derived by phage display: characterization of peptides and conjugates for imaging. *Bioconjug Chem* **2012,** *23*, (3), 548-56.

52. Zhang, Z.; Kolodziej, A. F.; Qi, J.; Nair, S. A.; Wang, X.; Case, A. W.; Greenfield, M. T.; Graham, P. B.; McMurry, T. J.; Caravan, P. Effect of Peptide-Chelate Architecture on Metabolic Stability of Peptide-based MRI Contrast Agents. *New J Chem* **2010,** *2010*, (34), 611-616.

53. Ciesienski, K. L.; Yang, Y.; Ay, I.; Chonde, D. B.; Loving, G. S.; Rietz, T. A.; Catana, C.; Caravan, P. Fibrin-targeted PET probes for the detection of thrombi. *Mol Pharm* **2013,** *10*, (3), 1100-10.

54. Uppal, R.; Catana, C.; Ay, I.; Benner, T.; Sorensen, A. G.; Caravan, P. Bimodal thrombus imaging: simultaneous PET/MR imaging with a fibrin-targeted dual PET/MR probe--feasibility study in rat model. *Radiology* **2011,** *258*, (3), 812-20.

55. Boswell, C. A.; Sun, X.; Niu, W.; Weisman, G. R.; Wong, E. H.; Rheingold, A. L.; Anderson, C. J. Comparative in vivo stability of copper-64-labeled cross-bridged and conventional tetraazamacrocyclic complexes. *J Med Chem* **2004,** *47*, (6), 1465-74.

56. Bass, L. A.; Wang, M.; Welch, M. J.; Anderson, C. J. In vivo transchelation of copper-64 from TETA-octreotide to superoxide dismutase in rat liver. *Bioconjug Chem* **2000,** *11*, (4), 527-32.

57. Hijnen, N. M.; de Vries, A.; Nicolay, K.; Grull, H. Dual-isotope 111In/177Lu SPECT imaging as a tool in molecular imaging tracer design. *Contrast Media Mol Imaging* **2012,** *7*, (2), 214-22.

58. Heiba, S. I.; Kolker, D.; Mocherla, B.; Kapoor, K.; Jiang, M.; Son, H.; Rangaswamy, B.; Kostakoglu, L.; Savitch, I.; DaCosta, M.; Machac, J. The optimized evaluation of diabetic foot infection by dual isotope SPECT/CT imaging protocol. *J Foot Ankle Surg* **2010,** *49*, (6), 529-36.

59. Durack, J. C.; Hope, T. A.; Seo, Y.; Saeed, M.; He, J.; Wilson, M. W.; Kerlan, R. K., Jr.; Ring, E. J. Intravenous vasopressin for the prevention of nontarget gastrointestinal embolization during liver-directed cancer treatment: experimental study in a porcine model. *J Vasc Interv Radiol* **2012,** *23*, (11), 1505-12.

60. de Vries, A.; Custers, E.; Lub, J.; van den Bosch, S.; Nicolay, K.; Grull, H. Block-copolymer-stabilized iodinated emulsions for use as CT contrast agents. *Biomaterials* **2010,** *31*, (25), 6537-44.

61. Kim, D. E.; Kim, J. Y.; Sun, I. C.; Schellingerhout, D.; Lee, S. K.; Ahn, C. H.; Kwon, I. C.; Kim, K. Hyperacute direct thrombus imaging using computed tomography and gold nanoparticles. *Ann Neurol* **2013,** *73*, (5), 617-25.

Chapter 4

Noninvasive visualization of tumoral fibrin deposition using a peptidic fibrin-binding SPECT tracer

Abstract

Fibrin deposition plays an important role in the formation of mature tumor stroma and provides a facilitating scaffold for tumor angiogenesis and intratumoral growth factor storage. The aim of this study was to investigate the potential of the ^{111}In-labeled fibrin-binding peptide EPep for SPECT imaging of intratumoral fibrin deposition. EPep and negative control NCEPep were synthesized, radiolabeled with ^{111}In and characterized *in vitro*. *In vivo* SPECT images and *ex vivo* biodistribution profiles were obtained in a fibrin-rich BT-20 breast cancer mouse model. In addition, BT-20 tumor sections were subjected to autoradiography and histology. Furthermore, *ex vivo* biodistribution profiles were obtained in a fibrin-poor MDA-MD-231 breast cancer mouse model. EPep and NCEPep were both highly stable *in vitro* in human and mouse serum (≥ 97% stability after 3 h). *In vitro,* ^{111}In-labeled EPep displayed significantly more binding than NCEPep towards human derived fibrin (66.6 ± 1.4 and 3.2 ± 1.3% dose per clot, respectively) and mouse derived fibrin (74.2 ± 2.4 and 7.8 ± 3.0% dose per clot, respectively). SPECT/CT images displayed marked SPECT signal in tumor area for BT-20 tumor bearing mice injected with EPep, but not for mice injected with NCEPep. *Ex vivo* biodistribution profiles of BT-20 tumor bearing mice 3 h post tracer injection showed significantly higher tumor uptake for EPep with respect to NCEPep (0.39 ± 0.14 and 0.11 ± 0.03% ID/g, respectively), whereas uptake in other organs was similar for EPep and NCEPep. *Ex vivo* autoradiography of BT-20 tumor sections displayed high signal for EPep and this signal co-localized with intratumoral fibrin deposits. Histological evaluation of MDA-MB-231 tumor sections displayed dense cell mass, no significant tumor stroma and only minute fibrin deposits. *Ex vivo* biodistribution profiles in MDA-MB-231 tumor bearing mice 3 h post injection showed EPep tumor uptake (0.14 ± 0.04% ID/g) which was significantly lower with respect to EPep BT-20 tumor uptake, indicating fibrin-specificity of EPep tumoral uptake. In conclusion, this work demonstrates the potential of EPep SPECT imaging for specific visualization of tumoral fibrin deposition.

This chapter is based on:
Starmans, L. W.; van Mourik, T.; Rossin, R.; Verel, I.; Nicolay, K.; Grull, H. Noninvasive visualization of tumoral fibrin deposition using a peptidic fibrin-binding single photon emission computed tomography tracer. *Under review.*

4.1 Introduction

The global demography shows a steady increase in aging population, which presents perhaps one of the most pressing challenges for humanity in the 21st century. The prevalence of age related diseases will continue to rise, with cancer predicted to be an increasingly key cause of morbidity and mortality in the next few decades.[1] Consequently, major efforts are being devoted to the development of new medical imaging methodologies in oncology care. Molecular imaging methodologies which visualize biological hallmarks of cancer,[2] such as angiogenesis and metastatic potency, hold promise to emerge at center stage for initial diagnosis, staging and characterization of cancer and for predicting and monitoring treatment response.[3]

Fibrin represents a suitable target that allows molecular imaging strategies to assess several critical biological hallmarks of cancer. Fibrin deposition plays an important role in the formation of mature tumor stroma and provides a facilitating scaffold for tumor angiogenesis and intratumoral growth factor storage.[4, 5] In addition, fibrin deposits are known to protect cancer cells from natural killer cell-mediated elimination.[6] Recently, we have developed strategies for molecular imaging of fibrin deposition using fibrin-binding peptides as targeting moieties.[7-9] One such promising strategy was to radiolabel the small fibrin-binding peptide EPep (DOTA-GGGGY-dGlu-C-Hyp-3ClY-GLCYIQG-NH_2) with ^{111}In to yield a fibrin single photon emission computed tomography (SPECT) tracer. ^{111}In-EPep displays a 900 nM dissociation constant (K_d) towards human fibrin and was shown to be highly effective in detecting fibrin deposition in a rat carotid artery thrombosis model using SPECT imaging.[9] An advantage of employing peptide-based tracers for nuclear imaging in oncology is their low molecular weight, which allows rapid extravasation and potent tissue penetration.[10] Therefore, fibrin-binding peptide-based tracers should be able to effectively infiltrate tumor stroma and bind to fibrin.

In this study, we investigated the potential of ^{111}In-labeled EPep to visualize fibrin deposition in a fibrin-rich BT-20 breast cancer mouse model using SPECT imaging. NCEPep, which is a scrambled version of EPep, was employed as negative control. To corroborate the *in vivo* SPECT findings, *ex vivo* biodistribution profiles were obtained and histology and high resolution autoradiography were performed on BT-20 tumor sections. In addition, biodistribution profiles were obtained in a MDA-MD-231 breast cancer mouse model, which displayed little tumor stroma and only minor fibrin deposits with respect to the more fibrin-rich BT-20 tumor model.

4.2 Materials and Methods

4.2.1 Peptide probe synthesis

EPep ([DOTA]GGGGY-dGlu-C-Hyp-3ClY-GLCYIQG-NH_2, Fig. 1A) was synthesized according to a previously published protocol.[9] The scrambled peptide NCEPep ([DOTA]GGGG-3CLY-LCI-dGlu-QYCG-Hyp-Y-G-NH_2) was synthesized in similar fashion to EPep and employed as negative control. The obtained peptides were analyzed with a LC-MS Agilent 1200 apparatus which was equipped with a C_8 Eclipse plus column (100 × 2.1 mm, 3.5 µm particle size) and an electrospray mass spectrometer (time-of-flight, LC-MS model 6210, Agilent Technologies, Santa Clara, CA, USA).

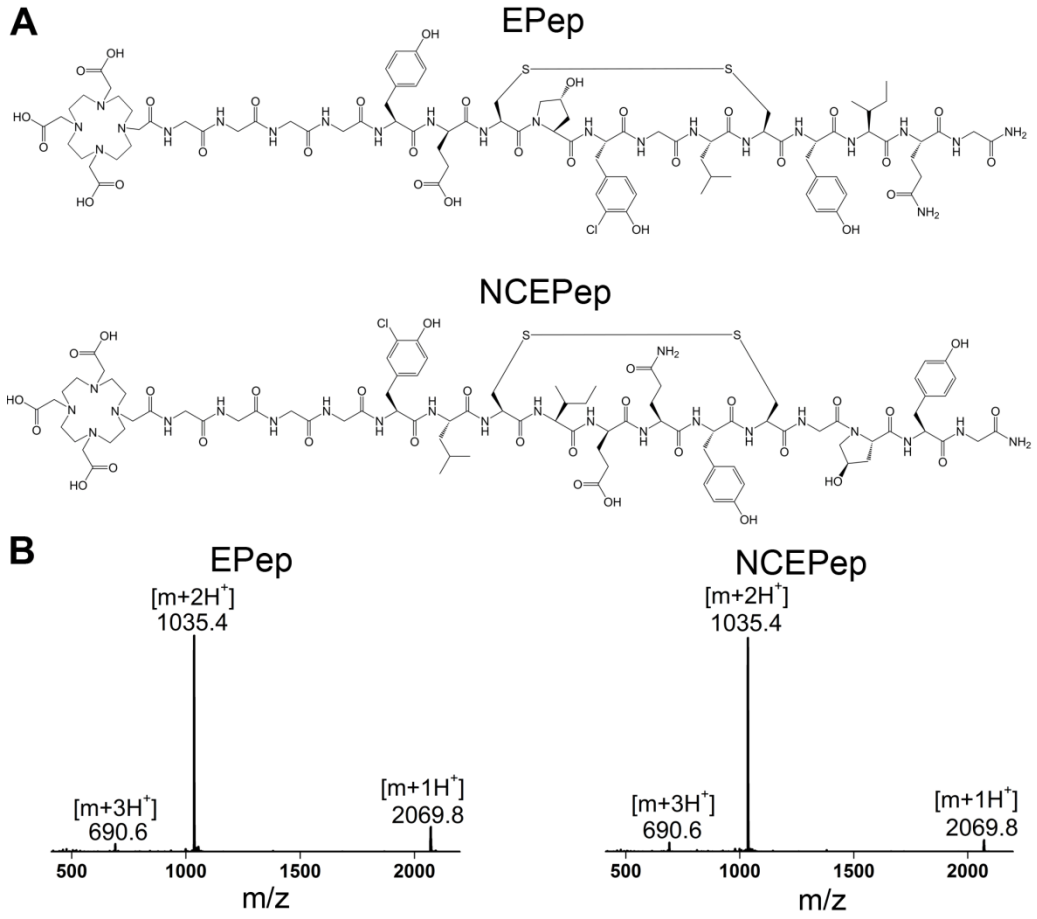

Figure 1. *Structural formulas (A) and corresponding mass spectra (B) of EPep and NCEPep.*

4.2.2 Radiolabeling

The peptides were radiolabeled with $^{111}InCl_3$ (Perkin Elmer, Boston, MA, USA and Mallinckrodt Pharmaceuticals, Zaltbommel, the Netherlands) in ammonium acetate buffer (0.25 M, pH 7.5) at 80 °C for 45 min. Subsequently, the labeling mixtures were diluted in saline containing 10-25 mM NaOH and challenged with an equivalent dose of diethylenetriaminepentaacetic acid (DTPA). Radiochemical purity was determined by radio-HPLC according to a previously published protocol.[9] The radiolabeled peptides showed > 95% radiochemical purity and were used without further purification.

4.2.3 In vitro serum stability

200 µL of ^{111}In-EPep/NCEPep solution (4 MBq, 15 nmol peptide, n=3 per group) was incubated with 800 µL of mouse serum (non-Swiss albino from C57BL/6; Innovative Research Inc., Novi, MI, USA) or human serum (Innovative Research Inc.) for up to 24 h. At 1, 3, 8 and 24 h time points, 200 µL was taken from each solution and was added to 200 µL of ice-cold acetonitrile. Subsequently, samples were centrifuged at 16.1k rcf for 6 min and the supernatant was separated from the pellet. Next, the supernatant and pellet radioactivity was measured using a dose calibrator (VDC-405, Veenstra Instruments, Joure, The Netherlands) and the radioactivity recovery (parent compound + metabolites) in the supernatant was calculated. The radioactivity recovery in the supernatant was 92 ± 2 and 90 ± 1% for EPep and NCEPep,

respectively. An equivalent amount of ultrapure water was then added to the supernatant and this mixture was analyzed by radio-HPLC.[9] The results were expressed as percentage intact parent compound.

4.2.4 In vitro fibrin-binding assay

Fibrin was prepared by adding 4 µL of 100 U/mL human thrombin (Sigma-Aldrich, Saint Louis, MO, USA) in ultrapure water to 200 µL of 2.9 mg/mL human or mouse fibrinogen (Sigma-Aldrich) in HEPES buffered saline (HBS, pH 7.4) and incubated at 37 °C overnight. Subsequently, the samples were sealed and stored at -80 °C until further use. Prior to use, the fibrin clots were thawed and rinsed once with HBS. Next, ^{111}In-labeled EPep or NCEPep (50 µL, 0.96 ± 0.03 MBq, 2 nmol peptide, n=5 per group) and 100 µL of HEPES Buffered Saline (HBS, pH 7.4) were mixed with the fibrin clots at 37 °C for two h. Subsequently, the clots were washed three times with HBS and the fibrin bound radioactivity was measured using a dose calibrator and expressed as percentage dose.

4.2.5 Cell culture

BT-20 and MDA-MB-231 cells were obtained from the America Type Culture Collection (ATCC, Manassas, VA, USA). BT-20 cells were cultured under standard conditions in Minimal Essential Medium Eagle (MEM; Sigma-Aldrich) supplemented with L-glutamine (2 mM, ThermoFisher Scientific (TFS), Waltham, MA, USA), penicillin (100 U/mL, TFS), streptomycin (100 µg/mL, TFS) and 10% heat inactivated fetal bovine serum (TFS). MDA-MB-231 cells were cultured in Dulbecco's Modified Eagle Medium (TFS) supplemented with Glutamax (2 mM, TFS), penicillin (100 U/mL), streptomycin (100 µg/mL) and 10% heat inactivated fetal bovine serum.

4.2.6 Animal model

All animal procedures were approved by the Maastricht University ethical review committee and were performed according to the Dutch national law and the institutional animal care committee guidelines. Five-to-nine week old female BALB/c nude mice (Charles River, Burlington, MA, USA) were housed under standard conditions and acclimatized for at least one week. Food and water were freely available. Tumors were grown on the hind leg of the mice by a subcutaneous/intramuscular injection of BT-20 cells (11×10^6 cells in 100 µL L-glutamine supplemented MEM, n=12) or MDA-MB-231 cells (5×10^6 cells in 100 µL sterile phosphate buffered saline (PBS), pH 7.4, n=9). Tumor size was monitored twice a week, and animals were typically used for experiments when the tumor size was at least 5 mm^3 (3-7 weeks).

4.2.7 In vivo SPECT/CT imaging

Six BT-20 tumor bearing mice were imaged by SPECT/CT. Mice were injected with ^{111}In-labeled EPep (15 nmol, 130 µL, 22 ± 4 MBq, n=3) or NCEPep (15 nmol, 130 µL, 19 ± 1 MBq, n=3). Approximately 1.5 h post injection, the mice were anesthetized using isoflurane and were positioned in a dedicated small-animal SPECT/CT scanner (NanoSPECT/CT, TriFoil Imaging, Chatsworth, CA, USA) equipped with four detector heads and converging nine-pinhole collimators (diameter 1.3 mm). First, a CT scan of the lower

mouse body was performed. CT scan parameters were: 12 min scan time, 360 projections, 2 seconds per projection, 45 kV peak tube voltage, 177 mA tube current and 37 mm field of view. From 2 to 3 h post injection a SPECT scan of the lower mouse body was acquired. SPECT scan parameters were: 300 seconds per projection, 60 min scan time, 24 projections, 171 keV (20% window) and 245 keV (15% window) ^{111}In-photopeaks.

SPECT and CT images were reconstructed using InVivoScope software (TriFoil Imaging) to an isotropic voxel size of 300 µm (SPECT) and 100 µm (CT). Images show CT data in gray scale and SPECT signal in color (purple to yellow) scale. SPECT data were evaluated by placing a volume of interest in the tumor SPECT hot spot area. As background signal, volumes of interest were drawn in the muscle of the non-tumor bearing limb. The recorded counts in the volumes of interest were converted to Bq using a quantification factor obtained by scanning a known amount of ^{111}In using identical scan parameters. Results were expressed as percentage injected dose per volume (% ID/cm^3) for both the tumor and the contralateral muscle area. Subsequent to the *in vivo* SPECT scans, mice were euthanized by cervical dislocation and the tumor and other tissues were harvested and weighed. Radioactivity was measured in a γ-counter (Wizard 1480, PerkinElmer, Waltham, MA, USA) along with standards to determine the percentage injected dose per gram (% ID/g). Tumors were subsequently embedded in Shandon cryomatrix (TFS), snap frozen in methylbutane (ca. -40 °C) and stored at -80 °C. Prior to use, the tumor was cut in 10 µm slices.

4.2.8 Biodistribution

Six BT-20 tumor bearing mice were injected with ^{111}In-labeled EPep or NCEPep (15 nmol, 100 µL, 2-21 MBq, n=3 per group) and nine MDA-MB-231 tumor bearing mice were injected with EPep or NCEPep (15 nmol, 100 µL, 2-27 MBq, n=4-5 per group). Mice were euthanized by cervical dislocation at 3 h post injection and the tumor and other tissues were harvested and weighed. Radioactivity was measured in a γ-counter along with standards to determine the percentage injected dose per gram. Tumors were subsequently fixed in 4% formaldehyde, embedded in paraffin and cut in 5 µm sections. The biodistribution data of mice in the SPECT group were combined with the "biodistribution-only" data obtained from BT-20 bearing mice, yielding biodistribution profiles with 6 animals for both EPep and NCEPep.

4.2.9 Histology and ex vivo autoradiography

Paraffin and cryo sections were stained with hematoxylin and eosin (H&E). Prior to H&E-staining, cryo sections were fixed in 4% formaldehyde for 10 min. In addition, paraffin sections were stained according to the Carstairs method, which displays fibrin in bright red, platelets in gray blue to navy, collagen in bright blue, muscle in red and red blood cells in clear yellow.[11] Anti-fibrin(ogen) fluorescence immunohistochemistry was performed on cryo sections according to a modified protocol from Zhang and coworkers.[12] Sections were fixed in ice-cold acetone for 5 min, air-dried and subsequently washed three times with PBS. Next, nonspecific binding was minimized by pre-incubation with 20% goat serum

in PBS containing 1% bovine serum albumin (BSA) at room temperature (RT) for 15 min. Primary incubation was performed at RT for 90 min using rabbit polyclonal anti-fibrin(ogen) antibody (Ab34269, Abcam, Cambridge, UK; diluted 1:100 in PBS with 1% BSA) and slides were subsequently washed three times with PBS. Secondary incubation was performed at RT for 60 min using anti-rabbit IgG conjugated to Alexa Fluor 488 (ab150077, Abcam, diluted 1:100 in PBS with 1% BSA and 5% goat serum). Slides were subsequently washed three times with PBS. Finally, sections were stained with DAPI (TFS, diluted 1:100.000 in PBS) at RT for 10 min, washed three times with PBS and mounted using Fluoromount (Sigma-Aldrich). Fluorescence images were acquired with a fluorescence microscope (DM6000 B, Leica, Wetzlar, Germany) using the Leica L5 and the R/G/B filter cubes. Negative control experiments, performed by incubation of rabbit serum instead of primary antibody, did not show focal anti-fibrin(ogen) fluorescence signal.

Autoradiographs of tumor cryo sections were obtained using a ^{d}FINE BetaImager (Biospace Lab, Paris, France). Ca. 2-3 days post-euthanasia, the samples were covered with scintillating foil and were scanned for 5 h per sample. The images were analyzed using M3Vision software (Biospace Lab). The radioactivity distribution maps (blue to red scale) were co-registered with photographs of the tumor sections (gray scale).

4.2.10 Statistical Analysis

Data represent the mean value ± standard deviation (SD). For differences between 2 groups, data sets were compared using unpaired 2-sided *t*-test (not assuming equal variances). Values with $p < 0.05$ were considered significant.

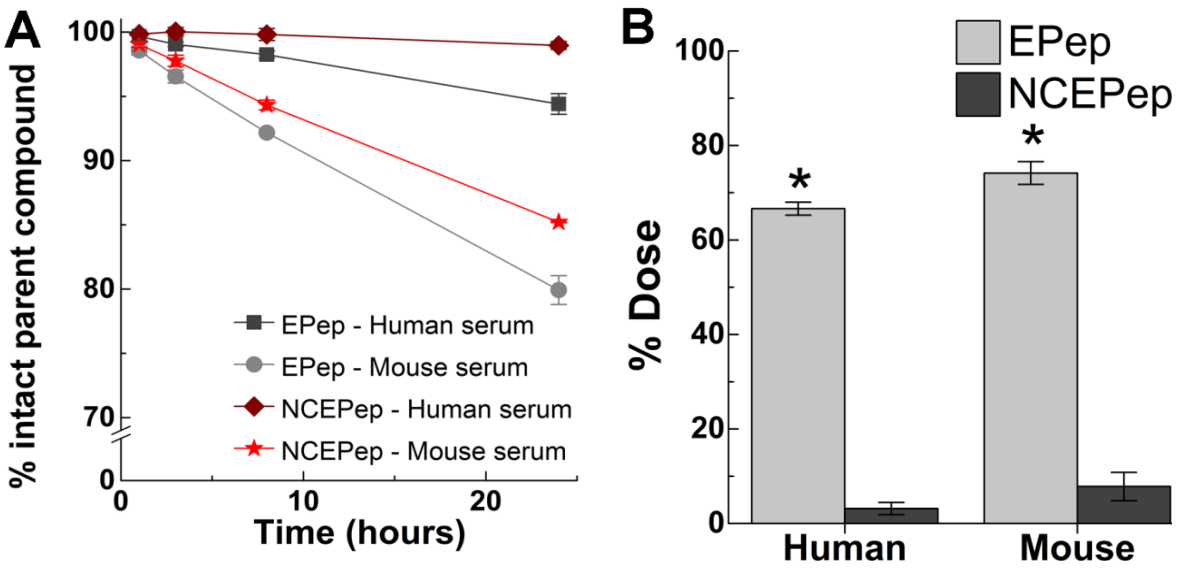

Figure 2. *(A) Serum stability assay. Percentage intact peptide probes after incubation in human and mouse serum for 1, 3, 8 and 24 h. Data is expressed as mean percentage intact parent compound ± SD (n=3). (B) Binding of EPep and NCEPep to human and mouse derived fibrin. Data is expressed as mean percentage dose ± SD (n=5).*

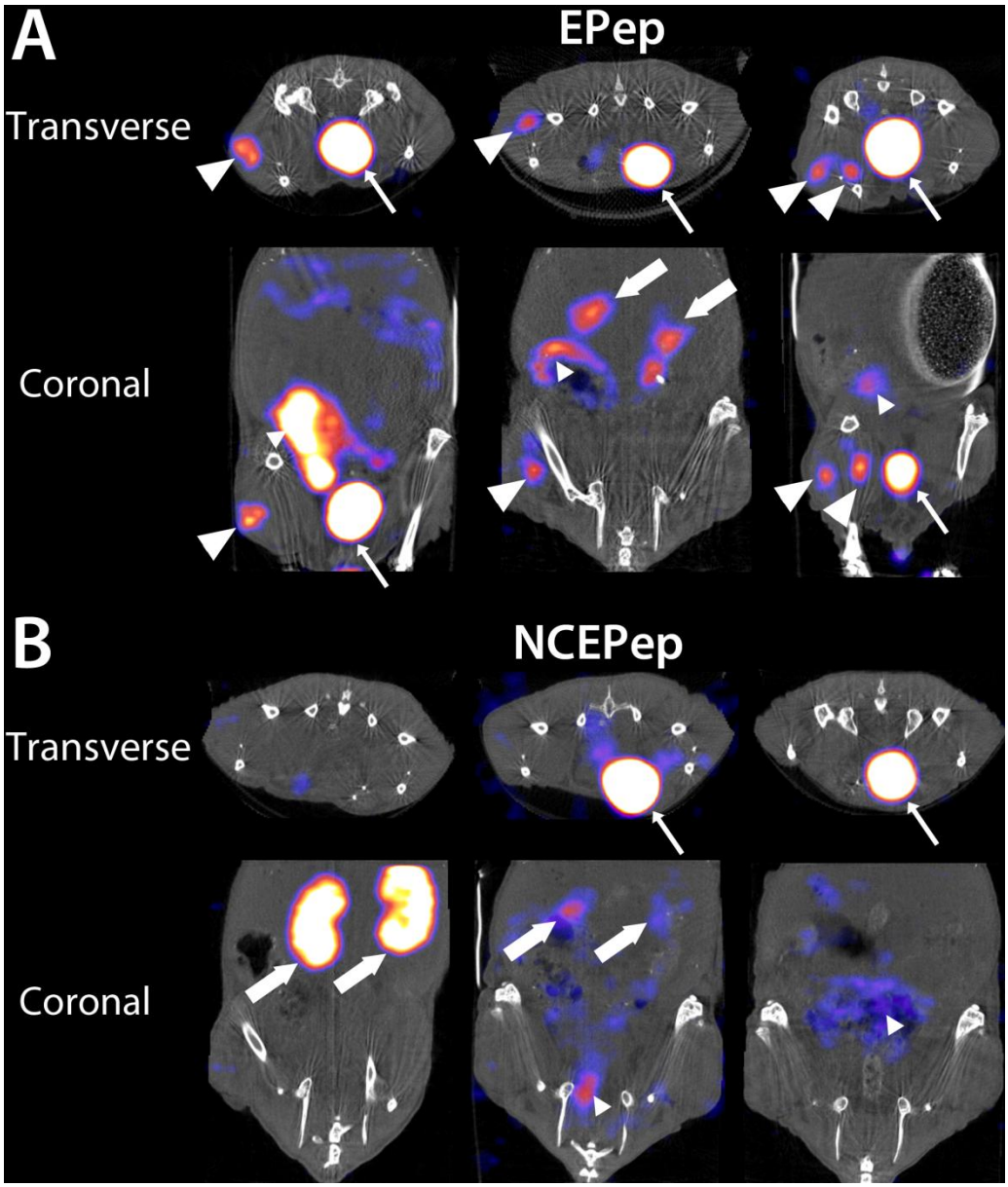

Figure 3. *In vivo SPECT/CT images of BT-20 tumor-bearing mice after injection of (A) EPep and (B) NCEPep (2-3 h post injection, transverse and coronal slices, n=3 per group). Large arrowhead indicates intratumoral fibrin deposition, small arrowhead designates intestinal uptake, bold arrow indicates kidney and thin arrow indicates urine in bladder. All images are displayed in identical color scale.*

4.3 Results

4.3.1 Synthesis and radiolabeling

The fibrin-binding peptide EPep and negative control NCEPep (Fig. 1A) were synthesized using Fmoc solid phase peptide synthesis. LC-MS analysis of the purified peptides (Fig. 1B) displayed exact molecular masses (2068.8 Da for both EPep and NCEPep) which matched exactly the expected values. Radiolabeling of EPep and NCEPep with ^{111}In resulted in > 95% radiochemical purity.

4.3.2 In vitro serum stability and fibrin binding

In vitro stability of EPep and NCEPep was assayed in human and mouse serum. ^{111}In-labeled EPep and NCEPep were incubated in serum for up to 24 h and, subsequently, proteins were precipitated by acetonitrile and the supernatant was analyzed using radio-HPLC. EPep and NCEPep were both highly stable in human and mouse serum (Fig. 2A), with ≥ 97% stability after 3 h of incubation and ≥ 80% stability after 24 h of serum incubation. *In vitro* fibrin-binding studies (Fig. 2B) showed significantly higher binding for ^{111}In-EPep with respect to the negative control NCEPep towards human derived fibrin (66.6 ± 1.4 and 3.2 ± 1.3% dose, respectively, $p < 0.001$) and mouse derived fibrin (74.2 ± 2.4 and 7.8± 3.0% dose, respectively, $p < 0.001$).

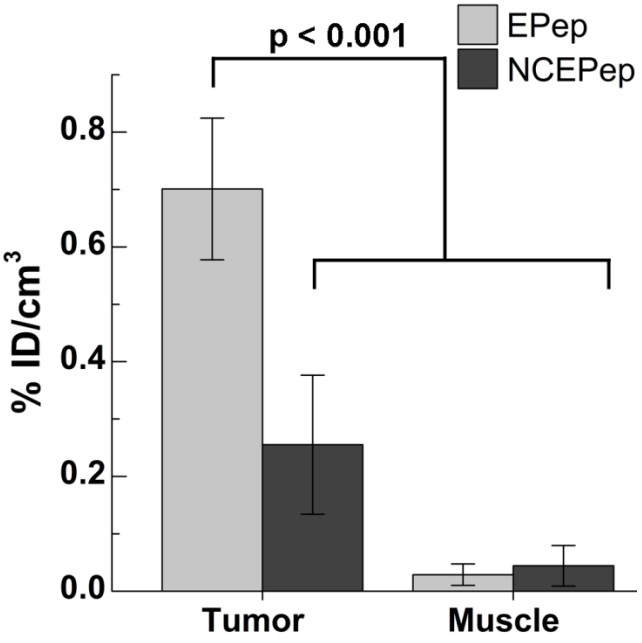

Figure 4. *Quantitative analysis of the in vivo SPECT scans (2-3 h post injection) for EPep and NCEPep using volumes of interest drawn in tumor (BT-20) and contralateral muscle areas. Data is expressed as mean percentage injected dose/cm^3 ± SD (n=3).*

4.3.3 In vivo SPECT/CT imaging of intratumoral fibrin deposition in BT-20 xenografts

In vivo SPECT/CT imaging of the lower body of BT-20 tumor bearing mice was performed 2 h post tracer injection with a total scan time of 1 h. In the obtained images, the tumors of the mice injected with ^{111}In-EPep was clearly visible, contrary to the mice injected with negative control NCEPep (Fig. 3). Quantitative analysis of the SPECT data (Fig. 4) confirmed significantly higher tumor uptake for ^{111}In-EPep with respect to ^{111}In-NCEPep (0.70 ± 0.12 and 0.26 ± 0.12% ID/cm^3, respectively, $p < 0.001$). Also, the EPep tumor uptake was significantly higher than both EPep and NCPep contralateral muscle signal (0.03 ± 0.02 and 0.04 ± 0.04, respectively, $p < 0.001$). Beside tumor, the SPECT scans showed intestinal and kidney uptake and excretion into urine for both EPep and NCEPep.

The *ex vivo* biodistribution profiles in BT-20 tumor bearing mice 3 h post tracer injection showed significant higher tumor uptake for ^{111}In-EPep with respect to the negative control peptide (0.39 ± 0.14 and 0.11 ± 0.03% ID/g, respectively, $p < 0.01$, Fig. 5), whereas uptake in other organs was similar for EPep and NCEPep. Uptake in most non-target organs was low (≤ 0.09% ID/g), with exception of intestine (0.16 ± 0.11 and 0.22 ± 0.25% ID/g for EPep and NCEPep, respectively) and kidney uptake (3.51

± 0.25 and 3.58 ± 0.66% ID/g for EPep and NCEPep, respectively). In BT-20 tumor bearing mice injected with ^{111}In-EPep, the tumor to organ ratios at 3 h post injection were high: ≥ 19 for blood, heart, muscle, brain and bone, and ≥ 4 for all other organs except kidney (Table 1). In mice injected with ^{111}In-NCPep, the tumor to organ ratios were ca. 3-6 fold lower than in mice which received EPep.

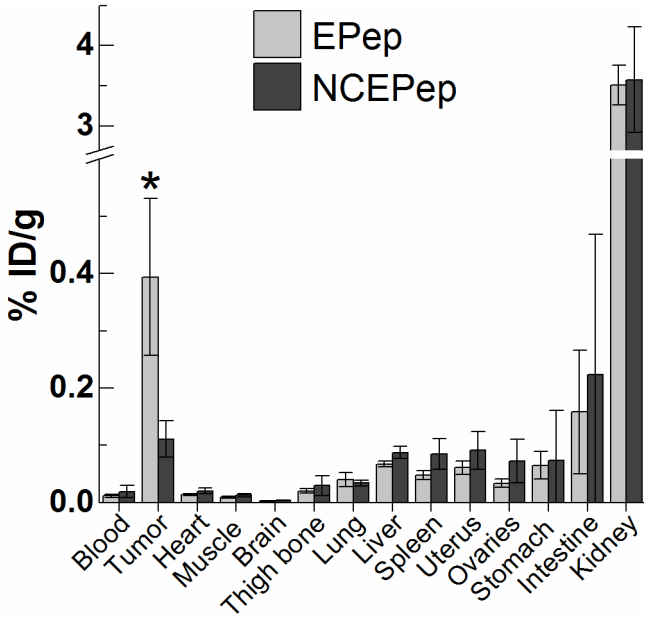

Figure 5. *Biodistribution profiles for EPep and NCEPep at 3 h post injection (n=6 per group) in mice bearing BT-20 tumors. Data are the mean percentage injected dose per gram ± SD. *p < 0.01 vs NCEPep tumor.*

Table 1. *Tumor to organ ratios of EPep and NCEpep in BT-20 tumor bearing mice at 3 h post injection (n=6 per group).*

Organ	EPep Tumor : organ ratio	NCEPep Tumor : organ ratio
Blood	33.4 ± 8.8	7.5 ± 4.8
Heart	27.6 ± 10.8	5.7 ± 2.0
Muscle	42.2 ± 15.3	8.9 ± 3.1
Brain	127.1 ± 44.9	34.5 ± 11.2
Thigh bone	19.0 ± 6.7	4.5 ± 2.1
Lung	9.9 ± 4.3	3.3 ± 1.0
Liver	5.7 ± 2.4	1.3 ± 0.3
Spleen	8.0 ± 2.7	1.4 ± 0.5
Uterus	6.4 ± 1.3	1.3 ± 0.6
Ovaries	12.3 ± 6.0	1.8 ± 0.8
Stomach	6.4 ± 2.5	3.2 ± 2.0
Intestine	4.3 ± 4.6	0.8 ± 0.4
Kidney	0.11 ± 0.04	0.03 ± 0.01

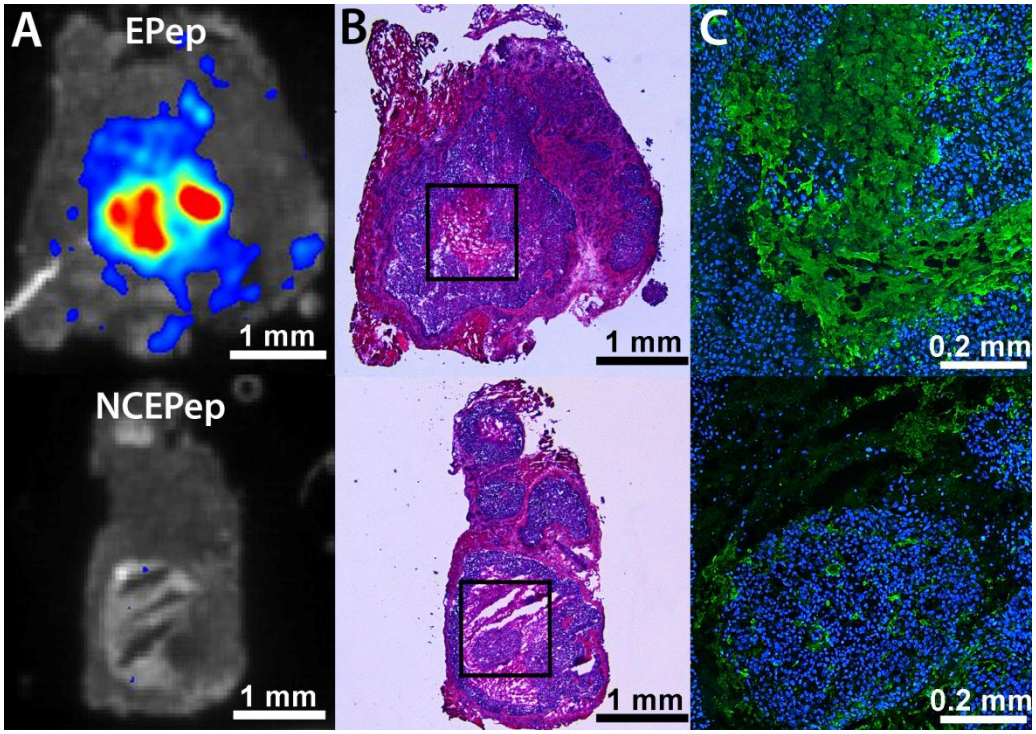

Figure 6. *(A) Autoradiographic, (B) hematoxylin and eosin stained and (C) anti-fibrin(ogen) immunofluorescence images of BT-20 tumor sections of mice injected with EPep (upper row) and NCEPep (bottom row). Autoradiographic images are displayed in identical color scales. Location of the higher magnification anti-fibrin(ogen) immunofluorescence images is indicated by the black square in the hematoxylin and eosin stained images. Immunofluorescence images show anti-fibrin(ogen) staining in green and DAPI in blue, and are displayed in identical color scales.*

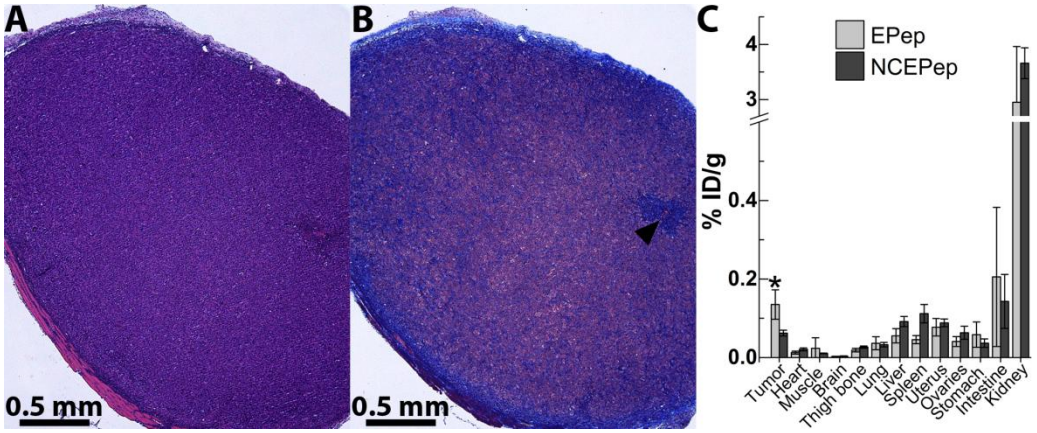

Figure 7. *(A) Hematoxylin and eosin stained and (B) Carstairs stained MDA tumor sections. Arrowhead indicates (minor) site of intratumoral fibrin deposition. (C) Biodistribution profiles for EPep and NCEPep at 3 h post injection (n=4-5 per group) in mice bearing MDA tumors. Data are the mean percentage injected dose per gram ± SD. *p < 0.05 vs NCEPep tumor.*

Ex vivo autoradiography of BT-20 tumor sections showed high uptake of ^{111}In-EPep (Fig. 6A) and the signal co-localized well with intratumoral fibrin deposits (Fig. 6B-C). BT-20 tumor slices from mice injected with negative control NCEPep did not show high tumor signal in autoradiography (Fig. 6A), while the presence of intratumoral fibrin deposits was confirmed by immunohistochemistry (Fig. 6B-C).

4.3.4 Biodistribution in MDA-MB-231 xenografts

Histological evaluation of MDA-MB-231 tumor sections showed dense cell mass, no significant tumor stroma and only minute fibrin deposits (Fig. 7A-B). The *ex vivo* biodistribution profiles in MDA-MB-231 tumor bearing mice 3 h post tracer injection (Fig. 7C) showed ^{111}In-EPep tumor uptake (0.14 ± 0.04% ID/g) which was significantly lower than in BT-20 tumors ($p < 0.01$). ^{111}In-EPep uptake in MDA-MB-231 tumors was, however, significantly higher with respect to the negative control peptide (0.06 ± 0.01% ID/g, $p < 0.05$). Beside tumor, all other organs showed similar uptake of EPep and NCEPep with respect to the BT-20 tumor bearing mice. Table 2 shows the tumor to organ ratios in MDA-MB-231 bearing mice injected with ^{111}In-labeled EPep and NCEPep at 3 h post injection. These ratios are ca. 2.8 and 1.8 fold lower than those in the BT-20 model, respectively.

Table 2. *Tumor to organ ratios of EPep and NCEPep in MDA-MB-231 tumor bearing mice at 3 h post injection (n=4-5 per group).*

Organ	**EPep** **Tumor : organ ratio**	**NCEPep** **Tumor : organ ratio**
Heart	10. 7 ± 0.6	3.0 ± 0.4
Muscle	11.5 ± 6.7	5.9 ± 1.1
Brain	51.9 ± 6.9	17.1 ± 1.5
Thigh bone	7.1 ± 0.6	2.4 ± 0.2
Lung	4.0 ± 1.0	1.9 ± 0.3
Liver	2.5 ± 0.3	0.7 ± 0.1
Spleen	2.9 ± 0.3	0.6 ± 0.1
Uterus	1.9 ± 0.8	0.7 ± 0.1
Ovaries	3.3 ± 0.5	1.0 ± 0.3
Stomach	3.8 ± 3. 6	1.8 ± 0.3
Intestine	1.2 ± 1.0	0.5 ± 0.2
Kidney	0.05 ± 0.01	0.02 ± 0.00

4.4 Discussion

The aim of this study was to gauge the potential of the ^{111}In-labeled fibrin-binding peptide EPep for SPECT imaging of intratumoral fibrin deposition. EPep consists of the fibrin-binding motif Y-dGlu-C-Hyp-3ClY-GLCYIQ,[13] displays a dissociation constant towards human fibrin of 900 nM, is highly stable in serum *in vitro* and showed rapid blood clearance and low retention in non-target organs in preclinical studies in mice and rats.[9] Furthermore, we previously demonstrated the potential of EPep for highly sensitive, noninvasive visualization of fibrin deposition in a carotid thrombosis rat model using SPECT imaging.[9] As fibrin deposition plays an important role in tumor angiogenesis and stroma formation,[4, 5] we hypothesized that EPep might be of value in the characterization of tumor lesions with respect to angiogenesis and metastatic potential. To assess the suitability of EPep-based SPECT detection of intratumoral fibrin deposition, we performed *in vivo* SPECT/CT imaging experiments in BT-20 tumor bearing mice at 2 to 3 h post ^{111}In-EPep injection. In these mice the images showed marked signal in the tumor area, and *ex vivo* biodistribution at 3 h post injection showed favorable tumor to organ ratios of ≥ 19 for organs such as blood, heart, muscle, brain and bone.

Tumor lesions are known to exhibit increased nonspecific retention of molecules, and consequently, this challenges the assessment of novel tracers for specific visualization of expressed epitopes in tumors.[14] In order to adequately test the specificity of EPep-based visualization of fibrin deposition in tumors, we developed a scrambled version of EPep, NCEPep, which showed similar stability in serum *in vitro* and displayed similar uptake in non-target organs *in vivo* with respect to EPep, therefore displaying ideal properties as a negative control tracer. The scrambled peptide was unable to bind significantly to fibrin *in vitro* and displayed significantly lower uptake in the tumor lesions *in vivo* with respect to EPep, suggesting that EPep deposition in tumor lesions is fibrin-specific. *Ex vivo* autoradiography and anti-fibrin(ogen) immunohistochemistry of BT-20 tumor sections showed ^{111}In-EPep accumulation in fibrin-rich tumor areas, further corroborating specificity. Finally, EPep uptake in MDA-MB-231 tumor bearing mice was investigated. MDA-MD-231 tumors showed little tumor stroma and only minor fibrin deposits. In concordance, ^{111}In-EPep accumulation was significantly lower with respect to the BT-20 tumor model, which exhibited higher levels of fibrin deposition. Taken together, these data prove fibrin-specific uptake of EPep within the tumor lesions. Blocking studies to further demonstrate specificity were not attempted, as fibrin is, in comparison to for instance cell membrane receptor-based epitopes, an abundant target and therefore not particularly suitable for blocking purposes.

Nuclear imaging of fibrin deposition in tumor lesions has been a topic of interest for over half a century. In the 1960's, Spar and colleagues initiated the exploration of ^{131}I-labeled polyclonal antibodies reactive towards fibrin(ogen) for detection of fibrin deposition in tumors using scintigraphic methods.[15-19] More recently, fibrin specific monoclonal antibodies have been employed for visualization of tumoral fibrin deposition. Hisada and coworkers developed an ^{89}Zr-labeled monoclonal antibody specific for the fibrin Bβ chain and showed that this antibody allowed visualization of tumoral fibrin deposition in a spontaneous skin cancer mouse model at 5 days post injection using positron emission tomography

(PET).[20] Furthermore, Angelides and colleagues showed that ^{99m}Tc-DD-3B6/22, a monoclonal antibody Fab' fragment specific for the D-dimer region of fibrin, allowed visualization of two malignant tumors at 6-24 h post injection using scintigraphic methods in a phase II clinical study in patients with pulmonary embolism and deep venous thrombosis.[21]

Owing to their smaller size, peptide-based tracers such as EPep are rapidly cleared from the blood and are able to swiftly penetrate tumor tissue, thus allowing imaging procedures which yield more rapid results and higher target to background ratios with respect to anti-fibrin antibody-based nuclear imaging strategies. In addition, peptide-based tracers display low immunogenicity and can be produced rather inexpensively. Taken together, peptide-based fibrin-binding tracers such as ^{111}In-labeled EPep hold promise for clinical translation of molecular imaging of tumoral fibrin deposition. To the best of our knowledge, this study is the first to report on nuclear imaging of tumoral fibrin deposition using a radiolabeled peptide-based tracer.

4.5 Conclusions

In conclusion, EPep produced high contrast SPECT images of BT-20 tumors in mice within 2-3 h post injection and the areas of high ^{111}In uptake correlated well with areas of high fibrin deposition. Therefore, this work paves the way for the use of EPep SPECT for fibrin imaging in oncology care.

4.6 Acknowledgments

The authors would like to thank Hugo Knobel and Jeroen van den Berg for LC-MS measurements, Freek Hoeben and Henk Janssen for peptide synthesis and Monique Berben, Caren van Kammen, Carlijn van Helvert and Marije Janssen for their support with *in vivo* experiments. This work was supported by the Center for Translational Molecular Medicine and The Netherlands Heart Foundation (PARISK, Grant 01C-202).

4.7 References

1. Alwan, A.; Armstrong, T.; Bettcher, D.; Branca, F.; Chisholm, D.; Ezzati, M.; Garfield, R.; Maclean, D.; Mathers, C.; Mendis, S.; Poznyak, V.; Riley, L.; Tang, K. C.; Wild, C. Global status report on noncommunicable disease 2010. *World Health Organization* **2010**.

2. Hanahan, D.; Weinberg, R. A. Hallmarks of cancer: the next generation. *Cell* **2011,** *144*, (5), 646-74.

3. Gambhir, S. S. Introduction. *Journal of Nuclear Medicine* **2008,** *49*, (Suppl 2), 1S-4S.

4. Dvorak, H. F.; Nagy, J. A.; Berse, B.; Brown, L. F.; Yeo, K. T.; Yeo, T. K.; Dvorak, A. M.; van de Water, L.; Sioussat, T. M.; Senger, D. R. Vascular permeability factor, fibrin, and the pathogenesis of tumor stroma formation. *Ann N Y Acad Sci* **1992,** *667*, 101-11.

5. Rickles, F. R.; Patierno, S.; Fernandez, P. M. Tissue factor, thrombin, and cancer. *Chest* **2003,** *124*, (3 Suppl), 58S-68S.

6. Palumbo, J. S.; Talmage, K. E.; Massari, J. V.; La Jeunesse, C. M.; Flick, M. J.; Kombrinck, K. W.; Jirouskova, M.; Degen, J. L. Platelets and fibrin(ogen) increase metastatic potential by impeding natural killer cell-mediated elimination of tumor cells. *Blood* **2005,** *105*, (1), 178-85.

7. Starmans, L. W.; Burdinski, D.; Haex, N. P.; Moonen, R. P.; Strijkers, G. J.; Nicolay, K.; Grull, H. Iron oxide nanoparticle-micelles (ION-micelles) for sensitive (molecular) magnetic particle imaging and magnetic resonance imaging. *PLoS One* **2013,** *8*, (2), e57335.

8. Starmans, L. W.; van Duijnhoven, S. M.; Rossin, R.; Aime, S.; Daemen, M. J.; Nicolay, K.; Grull, H. SPECT imaging of fibrin using fibrin-binding peptides. *Contrast Media Mol Imaging* **2013,** *8*, (3), 229-37.

9. Starmans, L. W.; van Duijnhoven, S. M.; Rossin, R.; Berben, M.; Aime, S.; Daemen, M. J.; Nicolay, K.; Grull, H. Evaluation of 111In-labeled EPep and FibPep as tracers for fibrin SPECT imaging. *Mol Pharm* **2013,** *10*, (11), 4309-21.

10. Weiner, R. E.; Thakur, M. L. Radiolabeled peptides in diagnosis and therapy. *Semin Nucl Med* **2001,** *31*, (4), 296-311.

11. Carstairs, K. C. The identification of platelets and platelet antigens in histological sections. *J Pathol Bacteriol* **1965,** *90*, (1), 225-31.

12. Zhang, Y.; Fan, S.; Yao, Y.; Ding, J.; Wang, Y.; Zhao, Z.; Liao, L.; Li, P.; Zang, F.; Teng, G. J. In vivo near-infrared imaging of fibrin deposition in thromboembolic stroke in mice. *PLoS One* **2012,** *7*, (1), e30262.

13. Overoye-Chan, K.; Koerner, S.; Looby, R. J.; Kolodziej, A. F.; Zech, S. G.; Deng, Q.; Chasse, J. M.; McMurry, T. J.; Caravan, P. EP-2104R: a fibrin-specific gadolinium-Based MRI contrast agent for detection of thrombus. *J Am Chem Soc* **2008,** *130*, (18), 6025-39.

14. Uppal, R.; Medarova, Z.; Farrar, C. T.; Dai, G.; Moore, A.; Caravan, P. Molecular imaging of fibrin in a breast cancer xenograft mouse model. *Invest Radiol* **2012,** *47*, (10), 553-8.

15. Spar, I. L.; Goodland, R. L.; Bale, W. F. Localization of I131 labeled antibody of rat fibrin in transplantable rat lymphosarcoma. *Proc Soc Exp Biol Med* **1959,** *100*, (2), 259-62.

16. Spar, I. L.; Bale, W. F.; Goodland, R. L.; Casarett, G. W.; Michaelson, S. M. Distribution of injected I 131 labeled antibody to dog fibrin in tumor-bearing dogs. *UR Rep* **1960,** *UR-569*, 1-13.

17. Spar, I. L.; Bale, W. F.; Goodland, R. L.; Izzo, M. J. Preparation of Purified I-131-Labeled Antibody Which Reacts with Human Fibrin. Preliminary Tracer Studies on Tumor Patients. *Cancer Res* **1964,** *24*, 286-93.

18. McCardle, R. J.; Harper, P. V.; Spar, I. L.; Bale, W. F.; Andros, G.; Jiminez, F. Studies with iodine-131-labeled antibody to human fibrinogen for diagnosis and therapy of tumors. *J Nucl Med* **1966,** *7*, (11), 837-47.

19. Spar, I. L.; Bale, W. F.; Marrack, D.; Dewey, W. C.; McCardle, R. J.; Harper, P. V. 131-I-labeled antibodies to human fibrinogen. Diagnostic studies and therapeutic trials. *Cancer* **1967,** *20*, (5), 865-70.

20. Hisada, Y.; Yasunaga, M.; Hanaoka, S.; Saijou, S.; Sugino, T.; Tsuji, A.; Saga, T.; Tsumoto, K.; Manabe, S.; Kuroda, J.; Kuratsu, J.; Matsumura, Y. Discovery of an uncovered region in fibrin clots and its clinical significance. *Sci Rep* **2013,** *3*, 2604.

21. Angelides, S.; Lee, F. T.; Basten, A.; Lambrecht, R. M.; Walker, K. Z.; Bundesen, P. G.; Bautovich, G. J. Detection of malignant tumors using Tc-99m labeled Fab' fragments from a monoclonal antibody with specificity for D-dimer of cross-linked fibrin. *Clin Nucl Med* **1996,** *21*, (3), 242-4.

Chapter 5

Iron oxide nanoparticle-micelles (ION-Micelles) for sensitive (molecular) MPI and MRI

Abstract

Iron oxide nanoparticles (IONs) are a promising nanoplatform for contrast-enhanced MRI. Recently, magnetic particle imaging (MPI) was introduced as a new imaging modality, which is able to directly visualize magnetic particles and could serve as a more sensitive and quantitative alternative to MRI. However, MPI requires magnetic particles with specific magnetic properties for optimal use. Current commercially available iron oxide formulations perform suboptimal in MPI, which is triggering research into optimized synthesis strategies. Most synthesis procedures aim at size control of iron oxide nanoparticles rather than control over the magnetic properties. In this study, we report on the synthesis, characterization and application of a novel ION platform for sensitive MPI and MRI. IONs were synthesized using a thermal-decomposition method and subsequently phase-transferred by encapsulation into lipidic micelles (ION-Micelles). Next, the material and magnetic properties of the ION-Micelles were analyzed. Most notably, vibrating sample magnetometry measurements showed that the effective magnetic core size of the IONs is 16 nm. In addition, magnetic particle spectrometry (MPS) measurements were performed. MPS is essentially zero-dimensional MPI and therefore allows to probe the potential of iron oxide formulations for MPI. ION-Micelles induced up to 200 times higher signal in MPS measurements than commercially available iron oxide formulations (Endorem, Resovist and Sinerem) and thus likely allow for significantly more sensitive MPI. In addition, the potential of the ION-Micelle platform for molecular MPI and MRI was showcased by MPS and MRI measurements of fibrin-binding peptide functionalized ION-Micelles (FibPep-ION-Micelles) bound to blood clots. The presented data underlines the potential of the ION-Micelle nanoplatform for sensitive (molecular) MPI and warrants further investigation of the FibPep-ION-Micelle platform for *in vivo*, noninvasive imaging of fibrin in preclinical disease models of thrombus-related pathologies and atherosclerosis.

This chapter is based on:
Starmans, L. W.; Burdinski, D.; Haex, N. P.; Moonen, R. P.; Strijkers, G. J.; Nicolay, K.; Grull, H. Iron oxide nanoparticle-micelles (ION-micelles) for sensitive (molecular) magnetic particle imaging and magnetic resonance imaging. *PLoS One* **2013,** *8*, (2), e57335.

5.1 Introduction

Cancer is one of the leading causes of death in the western world with a still increasing prevalence due to the aging society. As survival rates strongly increase with earlier diagnosis, much effort is devoted to improve the sensitivity and specificity of imaging methods such as PET, SPECT, CT, and MRI to detect smaller lesions. MRI offers superb contrast for soft tissue at high resolution and is often the modality of choice to characterize malignant tissue. However, MRI suffers from low sensitivity, which triggered the development of disease specific contrast agents. Especially iron oxide nanoparticles (IONs) have been investigated extensively as contrast agents for magnetic resonance imaging (MRI) during the past few decades.[1-5] Commonly referred to as negative contrast agents, IONs predominantly generate signal voids in MR images due to their high transversal relaxivity. They generally display good biocompatibility profiles, lack non-endogenous elements (unlike Gd^{3+}-based MR contrast agents), contain a high payload per nanoparticle and can be functionalized with binding molecules, such as antibodies and peptides, which are typically linked covalently to their surface. Therefore, IONs are a promising and frequently employed nanoplatform for molecular and cellular MR imaging.[6-13] A drawback of ION-based contrast-enhanced MRI is that it is often necessary to acquire both pre- and post-contrast enhanced images, which could lead to problems with respect to image co-registration and patient compliance. In addition, negative contrast ION-MRI is relatively prone to yield ambiguous information as signal voids, which may also be caused by imaging artifacts, might disguise morphology in the area of interest.

Recently, magnetic particle imaging (MPI) was introduced as a new imaging modality that is able to directly visualize magnetic particles rather than their effect on proton relaxation that is the basis of MRI detection.[14] In MPI, IONs are magnetized by a radiofrequency magnetic field and their time-varying, non-linear magnetization induces a time-dependent voltage in a receiver coil. The non-linearity of the magnetization response induces higher harmonics, the intensity of which directly corresponds to the respective ION concentration. This technique allows for radiation-free, hotspot-like imaging and should provide a more sensitive and quantitative alternative for molecular and cellular MRI.[15] A promising preclinical *in vivo* proof of concept MPI study using Resovist has already been reported.[16] Besides considerable efforts to improve MPI scanner design and image processing, optimization of IONs for MPI is critical for applications of MPI beyond proof-of-principal preclinical studies. Although it was immediately recognized by the inventers of MPI that the properties of the IONs are crucial for MPI,[14] relatively limited effort has been devoted to the synthesis of iron oxide nanoparticles for MPI purposes.[17-19] Commercially available contrast agents that are currently being employed for MPI studies are not optimized for MPI and thus prevent current MPI studies from reaching optimal resolution and sensitivity. For example, only 3% of the particles in Resovist, a commercially available contrast agent used in most MPI studies, have an appropriate particle diameter to be able to contribute significantly to the MPI signal.[14] Resovist contains iron oxide nanoparticles with an average nanocrystal size of 4-6 nm,[20, 21] whereas larger-sized iron oxide nanocrystal cores that display steeper magnetization curves would be more beneficial for MPI purposes. Simulation studies suggested that using monodisperse iron oxide nanocrystal cores with a size of 30 nm could increase the obtained MPS signal by a factor of about 30.[14]

Several different procedures were published in the recent years that allow a size controlled synthesis of particles in the size range between 5-25 nm, often based on a thermal decomposition of an iron-based precursor.[22-24] Usually, particles are obtained with a magnetically active crystalline core surrounded by an amorphous layer of iron oxides (Fig. 1). An analysis of the magnetic properties reveals that most particles show a smaller size of the magnetic active core with a high polydispersity compared to the geometrical size obtained e.g. with TEM.[25] Consequently, these particles will likely show a poor performance in MPI. Hence, synthesis procedures should be optimized to yield iron oxide nanoparticles with a well defined crystal core-size large enough to allow for more sensitive MPI. Naturally, these particles will also show improved magnetic properties in MR imaging.

In this study, we developed a novel iron oxide nanoparticle-micelle platform (ION-Micelle), containing iron oxide nanocrystals cores of 25 nm, for (molecular) MPI and MRI purposes. The synthesized ION-Micelles were characterized using (cryo) transmission electron microscopy (cryo-TEM), dynamic light scattering (DLS) and vibrating sample magnetometry (VSM). The effective magnetic core size of the ION-Micelles was derived from the VSM measurements. In addition, their potency for MPI and MRI was assessed using magnetic particle spectrometry (MPS)[26] and proton relaxometry, respectively. Furthermore, as a showcase for the suitability of the presented ION-Micelle platform for molecular MPI and MRI, the ION-Micelles were functionalized with a fibrin-binding peptide (FibPep) and *in vitro* blood clot binding was assessed using MPS and MRI.

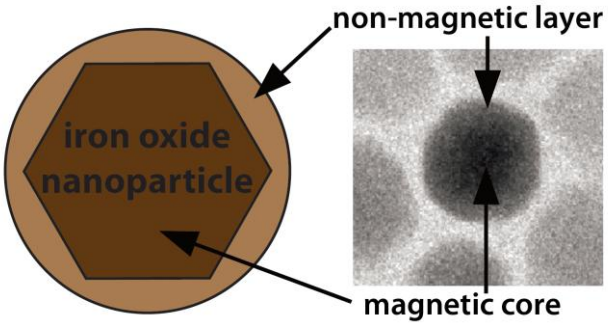

Figure 1. *Schematic overview and TEM-micrograph of an ION displaying a magnetic core and a non-magnetic layer.*

5.2 Materials and Methods

5.2.1 Materials

All materials were purchased from Sigma-Aldrich unless otherwise specified. 1,2-distearoyl-*sn*-glycero-3-phosphoethanolamine-N-[methoxy(polyethyleneglycol)-2000] (PEG2000–DSPE) was obtained from Lipoid and 1,2-distearoyl-sn-glycero-3-phosphoethanolamine-N-[maleimide(polyethyleneglycol)-2000] (Mal–PEG2000–DSPE) was obtained from Avanti Polar Lipids. 9-fluorenylmethyloxycarbonyl–protected amino acids and Rink amide resin were purchased from either Novabiochem(Merck) or Bachem and succinimidyl acetylthioacetate (SATA) was obtained from Invitrogen. Human tissue factor was purchased from Dade Behring and citrated human blood plasma was obtained from Sanquin. Resovist was purchased from Bayer Schering Pharma and Endorem and Sinerem were obtained from Guerbet.

5.2.2 Iron oxide nanoparticle (ION) synthesis

IONs were obtained through a method based on thermal decomposition of FeO(OH) in the presence of oleic acid, which was developed by Yu and coworkers[22] and subsequently optimized for our purposes.[27] In short, FeO(OH) (0.10 g, 1.13 mmol) was grounded using mortar and pestle and subsequently mixed with oleic acid (3.80 g, 13.5 mmol) and eicosane (0.60 g, 2.12 mmol). The mixture was heated to 360 °C under vigorously magnetic stirring at a constant ramping rate of 3.3 °C/min and then kept at this temperature for 2 h. During the reaction, the color of the mixture changed from red/brownish to black. After the reaction, the sample was cooled down and 10 mL of hexane was added to the mixture. The sample was precipitated using 20 mL of acetone and centrifuged at 4671 g during 30 minutes at RT. The iron oxide particles were redispersed using 10 mL of hexane and 20 µL oleic acid. The precipitation-redispersion procedure was repeated twice.

5.2.3 Iron oxide nanoparticle–micelle (ION-Micelle) synthesis

IONs were phase-transferred by encapsulation of IONs into lipidic micelles according to a similar procedure used to phase-transfer quantum dots.[28, 29] In a typical phase-transfer procedure, PEG2000-DSPE (0.20 g, 71.3 µmol) was dissolved in 4 mL chloroform and 1 mL IONs in hexane (6 mg Fe) was added. A ~40-fold excess of lipids required to entirely cover the surface of all IONs with a lipid monolayer was used. This suspension was injected into stirred, deionized water at 80 °C with an injection-speed of 6 mL/hr. Upon evaporation of the organic solvents, the IONs were encapsulated in the core of phospholipidic micelles, creating iron oxide nanoparticles-micelles (ION-Micelles). Next, phospholipid micelles without nanocrystals were removed by ultracentrifugation (42875 g; RT; 15 min) using an Optima™ L-90K ultracentrifuge equipped with a type 70.1 TI rotor (Beckman Coulter). After ultracentrifugation, the supernatant containing the empty lipidic micelles was carefully aspirated and discarded. The pellet, containing the ION-Micelles, was redispersed in HBS (10 mM HEPES, 137 mM NaCl, pH 7.4) by gently shaking. This ultracentrifugation procedure was repeated one more time.

5.2.4 Nanoparticle characterization

IONs were characterized by transmission electron microscopy (TEM) and electron diffraction using a FEI Tecnai 20, type Sphera TEM instrument operating at 200 kV. Cryogenic-TEM (cryo-TEM) of ION-Micelles was performed using a Gatan cryoholder at approximately -170 °C. Sample vitrification was carried out using an automated vitrification robot (FEI Vitrobot Mark III). The hydrodynamic size of the ION-Micelles in HBS was determined with dynamic light scattering (DLS) on a Zetasizer Nano-S (Malvern) using intensity- and number-weighted particle size distributions. In addition, the hydrodynamic particle size of three commercially available iron oxide compounds (Endorem, Resovist and Sinerem) was analyzed using DLS.

Magnetization curves were obtained from ION-Micelles in HBS using a vibrating sample magnetometer (ADE Technologies). The magnetic field was varied in the range between -20 and 20 kOe. Tubes solely filled with HBS were used to correct for the diamagnetic contribution of the solvent. Effective magnetic core sizes of the ION-Micelles were determined as described by Luigjes and coworkers.[25] In short, the

magnetic dipole moment distribution of the ION-micelles was calculated by fitting the magnetization curves assuming a log-normal distribution of the magnetic dipole moments. Subsequently, a volume-weighted effective magnetic core size distribution was derived from the calculated magnetic dipole moments, assuming spherical particles and a theoretical bulk magnetization of magnetite (~90 Am^2/kg). The volume-weighted effective magnetic core size distribution was converted to a number-weighted size distribution to allow for a more reasonable comparison between the obtained (volume-weighted) effective magnetic core size distribution and the (number-weighted) nanoparticle size distribution derived from TEM measurements.

Magnetic particle spectrometry was performed with a dedicated magnetic spectrometer (Philips),[17, 26] which is essentially a zero-dimensional version of an MPI scanner. Signal was obtained over 30 s upon application of an oscillating magnetic field with an amplitude of 10 mT at 25 kHz. As a reference, MPS measurements were also performed using Endorem, Resovist and Sinerem. Longitudinal and transverse proton relaxivities ($mM^{-1}s^{-1}$) of the ION-Micelles were determined using a Minispec MQ60 Spectrometer (1.41 T; 37°C; Bruker). Iron concentrations were determined using inductively coupled plasma atomic emission spectrometry (ICP-AES).

5.2.5 Peptide synthesis

Peptide Ac-RWQPCPAESWT-Cha-CWDPGGGK-NH_2, containing the fibrin-binding motif RWQPCPAESWT-Cha-CWDP (previously identified via phage-display using fibrinogen-binder depleted libraries and subsequently optimized for fibrin-binding),[30, 31] and a scrambled negative control Ac-WPTAD-Cha-RAWPSQEWPAGGGK-NH_2 with C-A substitutions were synthesized on 4-methylbenzhydrylamine hydrochloride salt (MBHA) rink amide resin by the use of standard 9-fluorenylmethyloxycarbonyl solid-phase peptide synthesis.[32] The peptides were cleaved from resin by trifluoroacetic acid : triisopropylsilane : H_2O : ethanedithiol (90.5:5:2.5:2 v/v%) for 3 h and purified by preparative reversed-phase high-pressure liquid chromatography (RP-HPLC) using an Agilent 1200 apparatus, equipped with a C18 Zorbax column (length x internal diameter = 150 x 21.2 mm; particle size, 5.0 µm). Peptide Ac-RWQPCPAESWT-Cha-CWDPGGGK-NH2 was cyclisized (formation of a disulfide bond between both cysteine residues) by dimethylsulfoxide:H_2O (9:1 v/v%) for 5 days with the pH set to 8 using n-methyl-d-glucamine,[31] and subsequently purified using preparative RP-HPLC. Next, the peptides were functionalized at the lysine ε-amino group with a SATA group by mixing the peptides and a 10 fold excess of SATA in dimethylformamide containing 3.6 v/v% triethylamine at room-temperature overnight. Subsequently, the peptides were purified using preparative RP-HPLC, yielding the SATA-functionalized fibrin-binding peptide (FibPep) and negative control (NCFibPep) (Fig. S1). Peptide structures were analyzed by liquid chromatography–mass spectrometry (LC-MS) on an Agilent 1200 apparatus, equipped with a C8 Eclipse plus column (100 x 2.1 mm; particle size, 3.5 µm) and an electrospray mass spectrometer (Agilent Technologies model 6210, time-of-flight LC-MS).

5.2.6 Fibrin-binding peptide functionalized ION-Micelle (FibPep-ION-Micelle) and negative control fibrin-binding peptide functionalized ION-Micelle (NCFibPep-ION-Micelle) synthesis

To create fibrin-binding FibPep-ION-Micelles, the phase-transfer procedure was slightly modified. In a typical phase-transfer procedure, PEG2000-DSPE (0.525 g, 187.1 µmol) and MAL-PEG2000-DSPE (0.061 g, 20.7 µmol) were dissolved in chloroform (4 mL) and IONs in hexane (2 mL; 12 mg Fe) were added. ION-Micelles were formed and subsequently separated from empty micelles using the previously described injection and ultracentrifugation procedure. After ultracentrifugation, the ION-Micelle pellets were redispersed in HBS (pH 6.7) and the ultracentrifugation procedure was repeated one more time. In parallel to the phase-transfer procedure, the SATA-groups of the fibrin-binding peptides were deacetylated at RT for 1 hr using a hydroxylamine containing buffer (Fig. S1). Subsequently, fibrin-binding peptide functionalized ION-Micelles (FibPep-ION-Micelles) were created by coupling the deacetylated fibrin-binding peptides (200 nmol peptide) to the distal end of the MAL-PEG2000-DSPE lipids overnight at 4 °C, using half of the obtained ION-Micelle suspension. Negative control fibrin-binding peptide functionalized micelles (NCFibPep-ION-Micelles) were obtained by conjugating NCFibPep to the remaining half of the ION-Micelle suspension in a similar fashion. Next, the FibPep/NCFibPep-ION-Micelles were prepared for *in vitro* application by removing any precipitation/large aggregates using centrifugation (500 g; 5 min) and subsequently changing the buffer to HBS (pH 7.4) using centrifugation-filtration (Vivaspin 50k MWCO, 6 mL; Sartorius Stedim Biotech).

5.2.7 Blood clot assay

Blood clots were prepared by incubating a mixture of 1.3 µL human tissue factor, 1.5 µL of 1 M $CaCl_2$ in ultrapure water and 100 µL of citrated human blood plasma for 30 minutes at 37 °C. Subsequently, the blood clots were washed 3x with HBS. Next, 15 µl of FibPep-ION-Micelles or NCFibPep-ION-Micelles (8 µg Fe per sample; n=4 per group) and 30 µl HBS were added to the blood clots and incubated for 1 h at RT. Subsequently, the solution was removed and the blood clot was washed 3x with HBS. The clots were then photographed and subjected to MPS and MRI measurements. MR imaging was performed on a 9.4 T preclinical scanner (Bruker BioSpin) using a 35 mm birdcage transceiver volume coil. Sagittal T_1-weighted images were acquired using a FLASH sequence with the following settings: TE 3.2 ms, TR 90 ms, 40° flip angle, 6 averages, FOV 25 x 20 mm^2, matrix 500 x 400, pixel dimensions 0.05 x 0.05 mm^2 and a slice thickness of 0.5 mm. Transversal slices were obtained using a TE of 3.6 ms, FOV of 50 x 20 mm^2 and a matrix of 1000 x 400. Signal to noise ratio of the blood clots in the transversal scans were calculated by drawing a region of interest (ROI) around each vial and subsequently dividing the mean MR signal in the ROI by 0.8 x mean MR noise level. Iron content of the clots was determined using ICP-AES.

5.2.8 Statistical analysis

For differences between 2 groups, data sets were compared using unpaired 2-sided *t*-test (not assuming equal variances). Values of $p < 0.05$ were considered significant.

5.3 Results and Discussion

Iron oxide nanoparticles (IONs) were synthesized by heating a mixture of FeO(OH), oleic acid and eicosane to 360 °C for 2 h (Fig. 2A-B) as described by Burdinski and coworkers.[27] IONs were subsequently purified by precipitation and re-dispersion of the nanoparticles, using acetone and hexane respectively. Figure 3A shows a TEM image of the obtained IONs. The nanoparticles were relatively monodisperse, with an average size of 24.9 ± 1.9 nm (calculated from 400 nanoparticles; Fig. 3B). Occasionally, a minor fraction of much smaller IONs was observed as well (arrows; inset Fig. 3A). The diameter of the synthesized IONs was approximately a factor 5 larger compared with Endorem, Resovist and Sinerem (Table 1), which were used as benchmark iron oxide formulations in this study. Figure 3C displays a selected area electron diffraction (SAED) pattern acquired from the synthesized IONs. The measured lattice spacings based on the rings in the diffraction patterns match well with the known lattice spacings of magnetite (Table 2).

Table 1. *Physical characteristics and relaxivities. Relaxometric measurements were performed at 1.41 T and 37 °C.*

Compound	**Diameter iron oxide core (nm)**	**Hydrodynamic diameter*** **(nm)**	**r_1 ($mM^{-1}s^{-1}$)**	**r_2 ($mM^{-1}s^{-1}$)**	**r_2/r_1**
ION-Micelle	25	61	6.7	253	37.7
Endorem	4-6 [33]	116	8.5	80	9.4
Resovist	4-6 [20, 21]	62	9.9	119	12.0
Sinerem	4-6 [33]	32	9.5	67	7.1

r_1: longitudinal relaxivity; r_2: transversal relaxivity; *Z-average

Table 2. *Calculated atomic lattice spacing d (Å) corresponding to diffraction pattern in Fig. 3C compared to standard atomic spacing for bulk magnetite (Fe_3O_4) along with their respective hkl indices from the PDF database.*

d	4.87	2.95	2.51	2.07	1.70	1.60	1.47	1.31	1.27	1.20
Fe_3O_4	4.86	2.97	2.53	2.10	1.71	1.62	1.48	1.33	1.28	1.21
Ring	1	2	3	4	5	6	7	8	9	10
hkl index	111	220	311	400	422	511	440	620	533	444

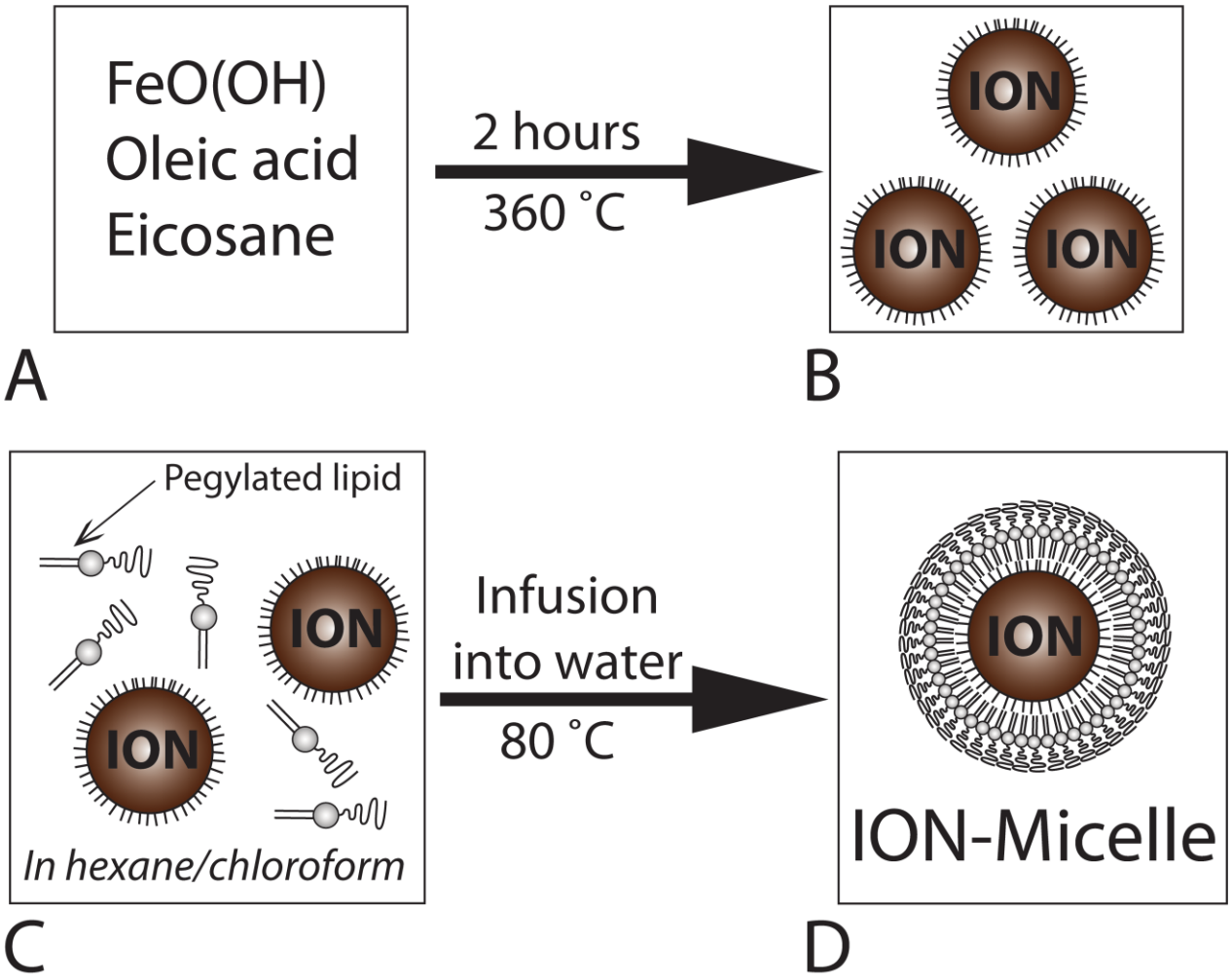

Figure 2. *Schematic overview of the (A-B) iron oxide nanoparticles and (C-D) ION-Micelle synthesis.*

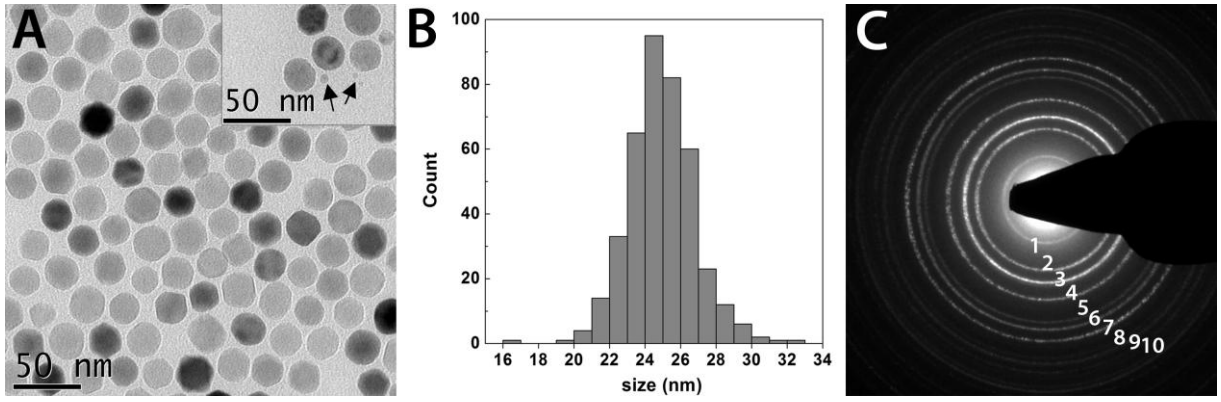

Figure 3. *Transmission electron microscopy analysis of the IONs. (A) Typical TEM micrograph of the IONs; inset shows occasional presence of a subset of particles with a smaller diameter (arrows). (B) Size distribution profile of the IONs obtained from TEM analysis of 400 nanoparticles. (C) Selected area electron diffraction (SAED) pattern acquired from IONs.*

Water-soluble ION-Micelles were formed by infusing a hexane/chloroform mixture containing IONs and 1,2-Distearoyl-*sn*-glycero-3-phosphoethanolamine-N-[methoxy(polyethyleneglycol)-2000] (PEG2000–DSPE) lipids into ultrapure water at 80 °C (Fig. 2C-D). ION-Micelles were separated from micelles not containing an iron oxide core using ultracentrifugation and subsequently the ION-Micelles were redispersed in HEPES-buffered saline (HBS) at pH 7.4. The dispersion state of the ION-Micelles in HBS was studied using cryogenic-TEM (cryo-TEM) and dynamic light scattering (DLS). Figure 4A-B shows typical high-resolution cryo-TEM images of ION-Micelles. The ION-Micelles were mostly dispersed in HBS as single particles or as small aggregates of nanoparticles. Occasionally, also larger, worm-like aggregates were observed (Fig. 4C). Other lipidic structures, such as liposomes and (empty) micelles, were not observed. Figure 4D shows the ION-Micelle hydrodynamic size-distribution obtained from an intensity-weighted analysis of the time correlation function measured with DLS. One dominant peak was observed at 47 nm for the ION micelles. The minor peak at larger sizes was indicative of a small fraction of aggregated nanoparticles, which matches well with the cryo-TEM findings (Fig. 4A-C). This peak disappeared in the number-weighted analysis (Fig. 4E), implying that the relative contribution of the larger sized aggregates to the overall size-distribution was negligible. The hydrodynamic diameter of the ION-Micelles obtained using number-weighted analysis was 38 nm, which corresponds well with the nanoparticles core size-measurements (25 nm, Fig. 3B). The apparent increase of the hydrodynamic size as determined by DLS compared to the nanoparticles core size measured by TEM is caused by the (hydrated) PEG2000-DSPE coating of the particles and the fact that a fraction of the particles contains multiple iron oxide cores. The hydrodynamic diameter of the ION-Micelles was similar to Resovist, approximately a factor two larger than Sinerem and a factor two smaller than Endorem (Table 1). The magnetic properties of the ION-Micelles were analyzed using a vibrating sample magnetometer (VSM). The ION-Micelles behaved superparamagnetically at room-temperature (RT), as the magnetization curve had no hysteresis (Fig. 5A). The saturation magnetization of the ION-Micelles was found to be 82 $Am^2/kg\ Fe_3O_4$, which is relatively close to the saturation magnetization of bulk magnetite (~90 $Am^2/kg\ Fe_3O_4$ at RT).

It has been recognized that the usual assumption that uniform size and shape guarantee well-defined magnetic properties is often in stark contrast with reality. For instance, Luigjes and coworkers showed that two formulations of iron oxide nanoparticles, both with a 20 nm size on TEM, displayed significantly different effective magnetic core sizes (16 and 6 nm), which were calculated from the magnetization curves.[25] As the magnetic properties of the nanoparticles are likely the sole critical factor for MPI-purposes, we calculated the effective magnetic core size distribution of our ION-Micelles as described by Luigjes *et al*.[25] Figure 5B shows the obtained number-weighted magnetic core size distribution, which displayed a maximum at 16 nm. The fact that the effective magnetic core size of the ION-Micelles is already larger than the average size of an entire iron oxide core in Resovist (4-6 nm), suggests that the ION-Micelles will allow for significantly more sensitive MPI.

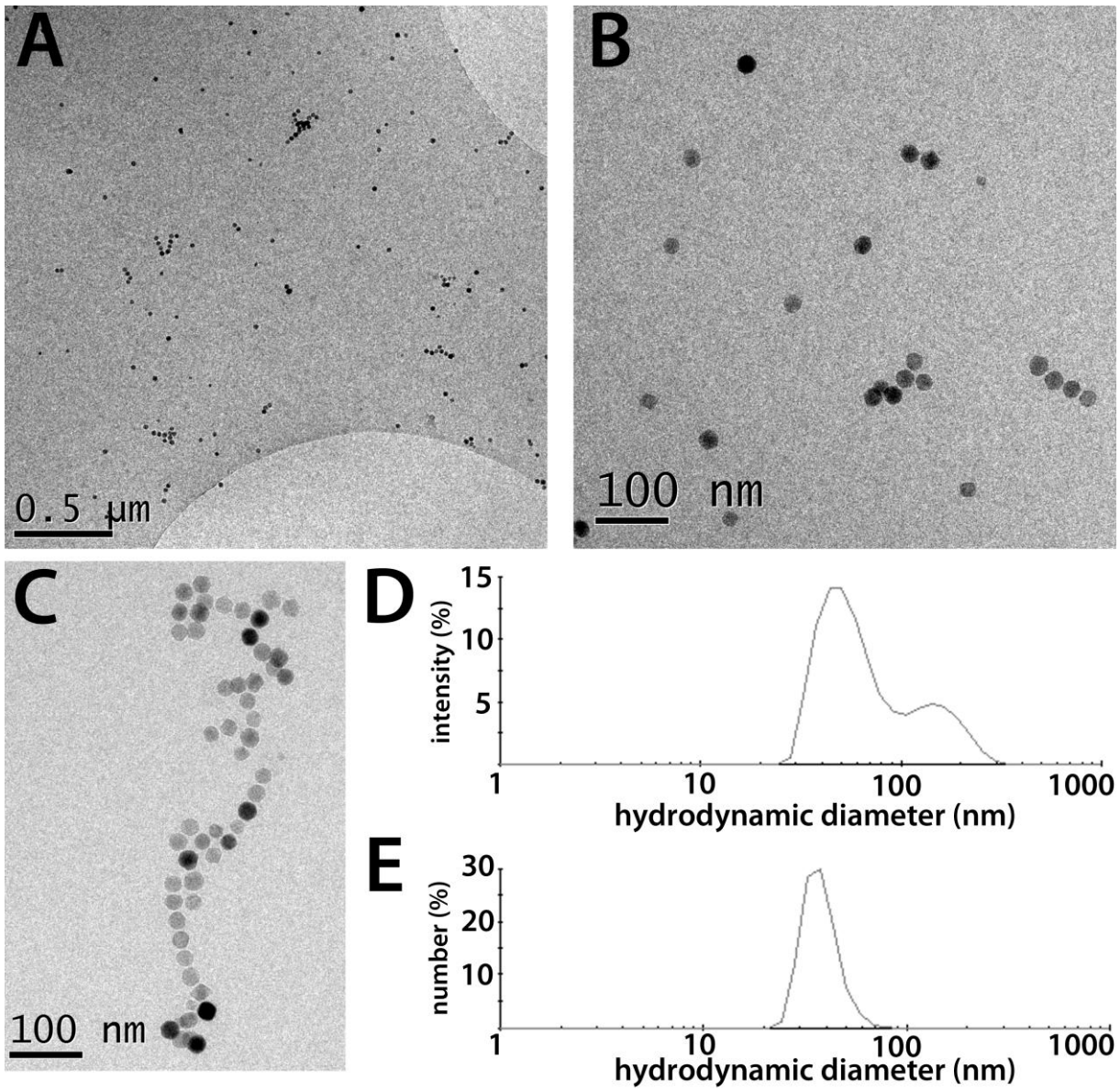

Figure 4. *Cryo-TEM and DLS analysis of the ION-Micelles in HEPES buffered saline (HBS). (A,B) Typical Cryo-TEM micrographs of the ION-Micelles showing that the ION-Micelles are mostly dispersed as single particles or as small aggregates of particles in HBS. (C) Occasionally, larger ION-Micelle aggregates were observed. (D) Typical intensity-weighted and (E) number-weighted size-distribution profiles of the ION-Micelles obtained by dynamic light scattering measurements.*

Magnetic particle spectrometry (MPS) measurements were performed to further evaluate the potential of the ION-Micelle nanoplatform for MPI. MPS is essentially zero-dimensional MPI and therefore allows to probe the suitability of iron oxide nanoparticles for MPI purposes.[26] In addition to the ION-Micelles, also three commercially available iron oxide formulations (Endorem, Resovist and Sinerem) were measured as a benchmark. MPS measurements were performed using a dedicated magnetic particle spectrometer and each sample was acquired over thirty seconds upon application of an oscillating magnetic field with an amplitude of 10 mT at 25 kHz and RT. ION-Micelles generated increased MPS signals in comparison to the commercially available iron oxide nanoparticles over the entire frequency

range (Fig. 5C). For the lower frequencies (<0.5 MHz), the ION-Micelles generated 4-6 times more signal per gram iron than Resovist, which was the best performing benchmark formulation with respect to inducing an MPS signal. At higher frequencies (>1 MHz), the improvement in ION-Micelle MPS signal compared to that of the other preparations was even more profound: the ION-Micelles generated an MPS signal per gram iron that was more than a factor 200 higher than that of the commercially available iron oxides. Similar results were obtained for samples that were diluted in whole blood (Fig. S2). These findings support the hypothesis that the ION-Micelle nanoplatform will allow significantly more sensitive MPI than Resovist, Endorem and Sinerem. In addition to MPI, iron oxides are frequently employed for CA-MRI purposes. To evaluate the potential of the ION-Micelle nanoplatform for CA-MRI, proton relaxometry measurements were performed. The ION-Micelles displayed a longitudinal relaxivity r_1 of 6.7 $mM^{-1}s^{-1}$ and a transversal relaxivity r_2 of 253 $mM^{-1}s^{-1}$ (Table 1). Both the transversal relaxivity and the ratio of transversal/longitudinal relaxivity of the ION-Micelles were much higher than the corresponding values found for all tested commercially available iron oxide compounds. Thus, the ION-Micelles allow for more sensitive MR imaging than the three benchmark formulations.

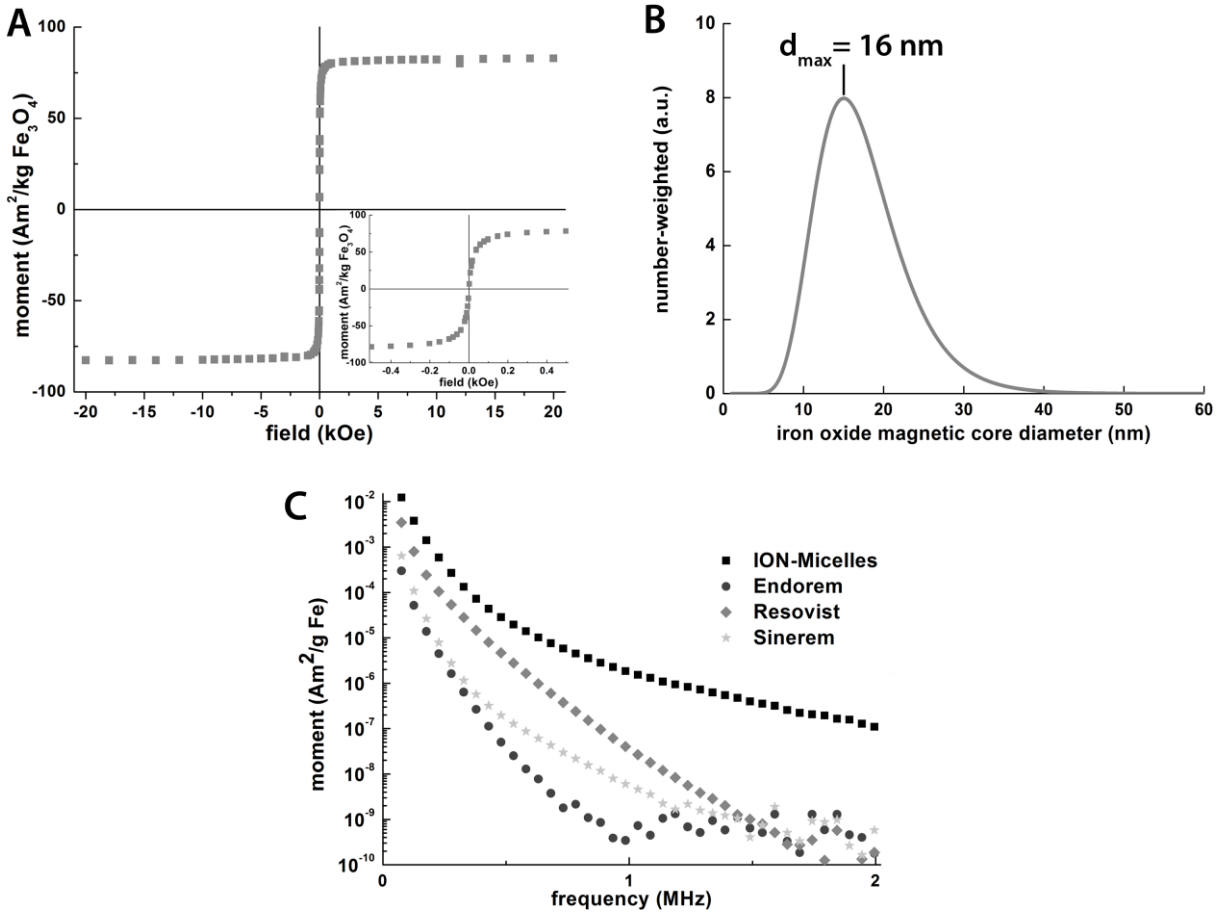

Figure 5. *Analysis of ION-Micelles magnetic properties. (A) Magnetization curve of the ION-Micelles at room temperature. Inset: zoomed-in view around zero field. (B) Number-weighted particle size distribution of the ION-Micelles calculated from the magnetization curve. d_{max} is the diameter corresponding to the maximum of the peak. (C) MPS experimental data of the ION-Micelles, Endorem, Resovist and Sinerem plotted as magnetic moment (normalized for iron content) versus frequency.*

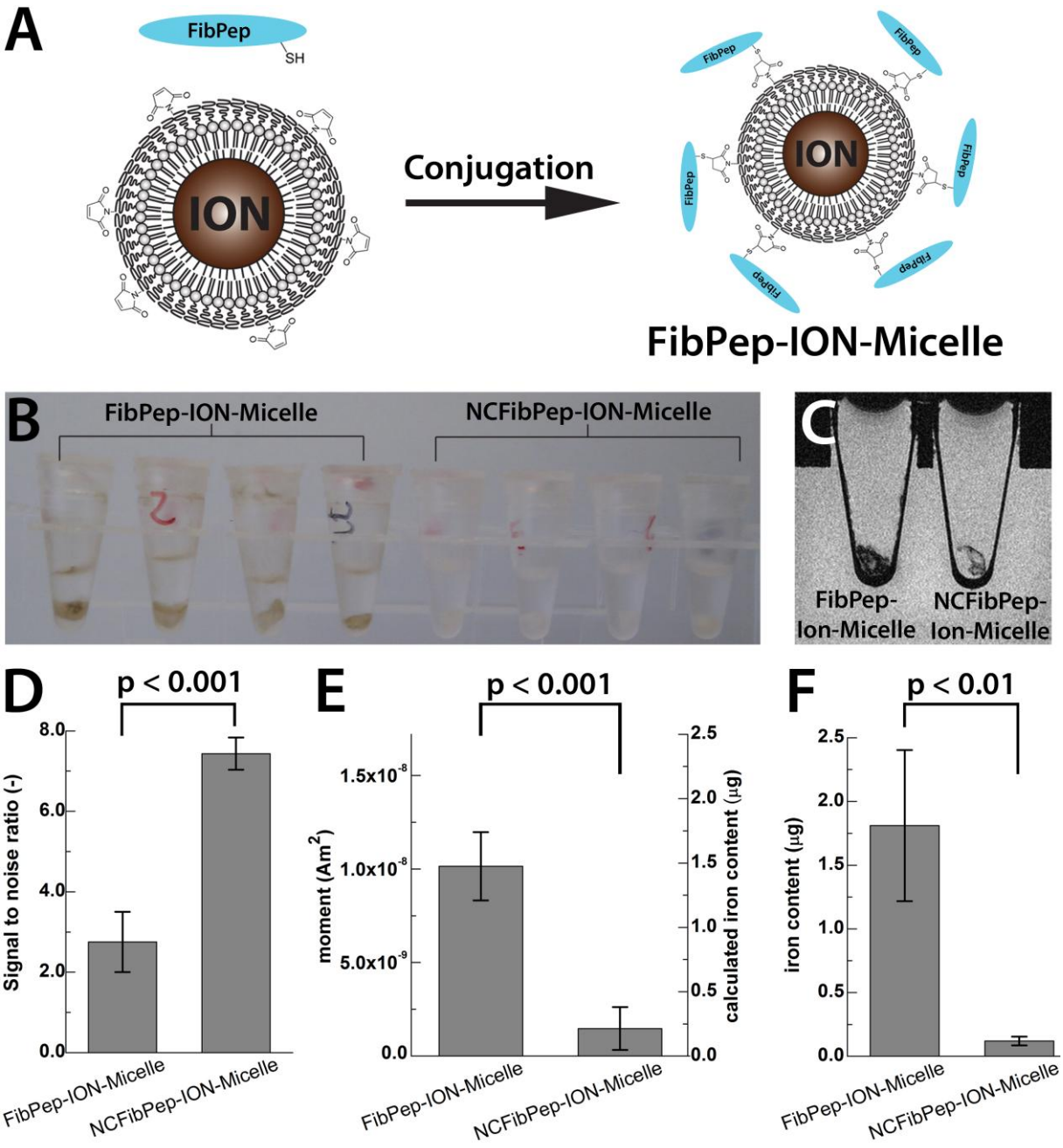

Figure 6. *In vitro blood clot binding test using FibPep-ION-Micelles and negative control NCFibPep-ION-Micelles. (A) Schematic overview of fibrin-binding peptides (FibPep) conjugation to the ION-Micelles. (B) Photograph and (C) sagittal MR image of blood clots incubated with either FibPep-ION-Micelles (left) or NCFibPep-ION-Micelles (right). (D) MR signal to noise ratio of the (NC)FibPep-ION-Micelles incubated clots. (E) Third harmonic (76 kHz) MPS signal amplitude and estimated iron content of blood clots incubated with (NC)FibPep-ION-Micelles. Estimated iron content was calculated using the third harmonic MPS signal and a previously defined conversion factor for this particular batch IONs of 6.87 mAm^2/g Fe. (F) Iron content of blood clots incubated with (NC)FibPep-ION-Micelles. Data represents mean ± standard deviation (n=4).*

A proof of concept, *in vitro* blood clot-targeting experiment was performed using fibrin-targeted ION-Micelles to evaluate the suitability of the ION-Micelle nanoplatform for molecular MPI and MRI. Fibrin is a major component of blood clots and plays an important role in thrombi-related pathologies such as deep venous thrombosis, pulmonary embolism and atherosclerosis. Because of the high potency of the ION-Micelle nanoplatform to generate contrast in MPI and MRI, a fibrin-targeted ION-Micelle nanoplatform was envisioned to be suitable for noninvasive detection of thrombi using MPI and/or MRI. To this aim, ION-Micelles were modified with fibrin-binding peptides (FibPeps), which were directly linked to the lipid coating of the nanoparticles. FibPep is a peptide constituted of a fibrin-binding motif (RWQPCPAESWT-Cha-CWDP),[30, 31] which is coupled to an n-succinimidyl-s-acetylthioacetate (SATA) group via a glycine linker (Fig. S1A-B). To facilitate conjugation of FibPep to the nanoplatform, the coating of the ION-Micelles was adapted by exchanging 10% of the PEG2000-DSPE lipids with maleimide-functionalized PEG2000-DSPE lipids during the phase-transfer process. Prior to conjugation of the fibrin-binding peptides to the ION-Micelles, the SATA group of the peptides was deacetylated to provide a functional thiol group (Fig. S1C). Subsequently, the deacetylated fibrin-binding peptides were conjugated to the ION-Micelles using standard maleimide-thiol chemistry, forming a covalent thioether linkage between the lipidic coating of the nanoparticles and the fibrin-binding peptides (FibPep-ION-Micelles, Fig. 6A). As a negative control, a scrambled peptide with C-A substitutions (NCFibPep, Fig. S1D-F) was synthesized and coupled to the thiol-modified ION-Micelles, to obtain non-targeting NCFibPep-ION-Micelles.

Blood clots were prepared by incubating a mixture of human tissue factor, calcium chloride and citrated human blood plasma for 30 minutes at 37 °C. Next, blood clots were incubated with HBS containing either FibPep-ION-Micelles or NCFibPep-ION-Micelles for 1 h (n=4 per preparation). Subsequently, the solution (containing unbound ION-Micelles) was carefully removed and the clots were washed three times with HBS. Thereafter, clots were subjected to MRI and MPS measurements. A photograph of the clots after the incubation and washing procedure is shown in Fig. 6B. The clots incubated with FibPep-ION-Micelles had obtained a brownish color, whereas the clots incubated with the NCFibPep-ION-Micelles had remained white. This is a strong indication that the (brownish-colored) FibPep-ION-Micelles bound specifically to the clots. MRI measurements showed clear signal voids for these clots that were incubated with FibPep-ION-Micelles, whereas those clots that were incubated with NCFibPep-ION-Micelles did not (Fig. 6C and Fig. S3A). The signal to noise ratio (SNR) of the clots incubated with FibPep-ION-Micelles was significantly lower than the NCFibPep-ION-Micelles incubated clots SNR (2.75 ± 0.75 and 7.43 ± 0.40, respectively; $p < 0.001$; Fig. 6D). MPS measurements displayed increased signal amplitudes for the FibPep-ION-Micelles incubated clots in comparison to the NCFibPep-ION-Micelles incubated clots throughout the whole frequency spectrum up to ~750 kHz (Fig. S3B). Above ~750 kHz, the signal dropped into noise level for both the FibPep-ION-Micelles as well as the NCFibPep-ION-Micelles incubated clots. Specific analysis of the third harmonic (72.6 kHz), which is the harmonic with the highest signal amplitude, showed a seven-fold increase in signal for the FibPep-ION-Micelles incubated clots in comparison to the NCFibPep-ION-Micelles incubated clots (10.1 ± 1.8 and 1.5 ± 1.1 nAm^2 at 76 kHz, respectively; $p < 0.001$; Fig. 6E). The estimated iron content was

calculated to be 1.48 ± 0.27 and 0.21 ± 0.17 µg Fe for FibPep-ION-Micelles and NCFibPep-ION-Micelles incubated clots, respectively, using the third harmonic MPS signal and a previously determined conversion factor of 6.87 mAm^2/g Fe for this particular batch of IONs. Thus, the targeting of the FibPep-ION-Micelles to the clots could be detected using MRI and MPS. To validate whether the FibPep-ION-Micelles indeed bound significantly more to the clots than the NCFibPep-ION-Micelles, the clots were analyzed for iron content using inductively coupled plasma atomic emission spectrometry (ICP-AES). ICP-AES measurements showed that the FibPep-ION-Micelles incubated clots contained significantly more iron than the NCFibPep-ION-Micelles (1.81 ± 0.59 and 0.12 ± 0.03 µg Fe, respectively; $p < 0.01$; Fig. 6F). The ICP-AES results match well with the estimated iron content that was calculated from the MPS signal. Hence, these results show that the FibPep-ION-Micelles can selectively bind to blood clots and that this targeting can be visualized using MRI and quantified using MPS. These findings therefore underline the potential of the ION-Micelle nanoplatform for molecular MPI and MRI and encourage future assessment of the FibPep-ION-Micelle nanoplatform for noninvasive detection of thrombi *in vivo* using MRI and MPI.

5.4 Conclusions

Currently, MPI research is mainly being performed employing commercially available iron oxide formulations which were developed for contrast-enhanced MRI. However, these iron oxide formulations contain nanocrystals of which the size is too small and disperse to induce efficiently MPI signal. Therefore, iron oxide formulations optimized for MPI are likely critical in the fruition of MPI as established imaging modality. In this work, we have presented ION-Micelles as a novel nanoplatform, consisting of 25 nm sized iron oxide nanocrystals encapsulated in lipidic micelles, for sensitive application in (molecular) MPI and MRI. The ION-Micelles iron oxide nanocrystals displayed a narrow size-distribution, high saturation magnetization and an effective magnetic core size of 16 nm. In addition, ION-Micelles had a higher potency to generate contrast in MPI and MRI than commercially available iron-oxide formulations (Endorem, Resovist, Sinerem). Thus, ION-Micelles allow for more sensitive MPI and MRI than the currently available iron oxide formulations. Furthermore, the potential of the ION-Micelle platform for molecular MPI and/or MRI was illustrated by an *in vitro* blood clot-targeting experiment using ION-Micelles which were functionalized with fibrin-binding peptides. The fibrin-targeted ION-Micelles (FibPep-ION-Micelles) bound specifically to the blood clots and this could be detected by MPS and MRI. Overall, these findings underline the potential of the ION-Micelle nanoplatform for (molecular) MPI and MRI and warrant further investigation of the FibPep-ION-Micelle platform for *in vivo*, noninvasive imaging of fibrin in preclinical disease models of thrombus-related pathologies and atherosclerosis.

5.5 Acknowledgements

The authors would like to thank Sander van Duijnhoven for assistance with the solid-phase peptide synthesis, Paul Bomans for support with the cryo-TEM measurements, Peter Pasmans and Peter Graat for assistance with the VSM measurements, Jeanette Smulders for the ICP-AES measurements and Hugo Knobel and Jeroen van den Berg for assistance with the LC-MS measurements.This research was supported by the Center for Translational Molecular Medicine and the Netherlands Heart Foundation (PARISK, grant 01C-202).

5.6 References

1. Corot, C.; Robert, P.; Idée, J.; Port, M. Recent Advances in Iron Oxide Nanocrystal Technology for Medical Imaging. *Advanced Drug Delivery Reviews* **2006,** *58*, (14), 1471-1504.

2. Gupta, A. K.; Gupta, M. Synthesis and surface engineering of iron oxide nanoparticles for biomedical applications. *Biomaterials* **2005,** *26*, (18), 3995-4021.

3. Mendonca Dias, M. H.; Lauterbur, P. C. Ferromagnetic Particles As Contrast Agents for Magnetic Resonance Imaging of Liver and Spleen. *Magn Reson Med* **1986,** *3*, (2), 328-30.

4. Pankhurst, Q. A.; Connolly, J.; Jones, S. K.; Dobson, J. Applications of Magnetic Nanoparticles in Biomedicine. *Journal of Physics D: Applied Physics* **2003,** *36*, (13), R167-R181.

5. Xu, C.; Sun, S. Superparamagnetic nanoparticles as targeted probes for diagnostic and therapeutic applications. *Dalton Trans* **2009,** *29*, (29), 5583-91.

6. Berman, S. C.; Galpoththawela, C.; Gilad, A. A.; Bulte, J. W.; Walczak, P. Long-Term MR Cell Tracking of Neural Stem Cells Grafted in Immunocompetent Versus Immunodeficient Mice Reveals Distinct Differences in Contrast Between Live and Dead Cells. *Magn Reson Med* **2011,** *65*, (2), 564-74.

7. Briley-Saebo, K. C.; Cho, Y. S.; Shaw, P. X.; Ryu, S. K.; Mani, V.; Dickson, S.; Izadmehr, E.; Green, S.; Fayad, Z. A.; Tsimikas, S. Targeted iron oxide particles for in vivo magnetic resonance detection of atherosclerotic lesions with antibodies directed to oxidation-specific epitopes. *J Am Coll Cardiol* **2011,** *57*, (3), 337-47.

8. Dash, R.; Chung, J.; Chan, T.; Yamada, M.; Barral, J.; Nishimura, D.; Yang, P. C.; Simpson, P. C. A Molecular MRI Probe to Detect Treatment of Cardiac Apoptosis in Vivo. *Magn Reson Med* **2011,** *66*, (4), 1152-62.

9. Jayapaul, J.; Hodenius, M.; Arns, S.; Lederle, W.; Lammers, T.; Comba, P.; Kiessling, F.; Gaetjens, J. FMN-coated fluorescent iron oxide nanoparticles for RCP-mediated targeting and labeling of metabolically active cancer and endothelial cells. *Biomaterials* **2011,** *32*, (25), 5863-71.

10. McAteer, M. A.; Schneider, J. E.; Ali, Z. A.; Warrick, N.; Bursill, C. A.; von zur Muhlen, C.; Greaves, D. R.; Neubauer, S.; Channon, K. M.; Choudhury, R. P. Magnetic Resonance Imaging of Endothelial Adhesion Molecules in Mouse Atherosclerosis Using Dual-Targeted Microparticles of Iron Oxide. *Arterioscler Thromb Vasc Biol* **2008,** *28*, (1), 77-83.

11. Muja, N.; Cohen, M. E.; Zhang, J.; Kim, H.; Gilad, A. A.; Walczak, P.; Ben-Hur, T.; Bulte, J. W. Neural Precursors Exhibit Distinctly Different Patterns of Cell Migration Upon Transplantation During Either the Acute or Chronic Phase of EAE: a Serial MR Imaging Study. *Magn Reson Med* **2011,** *65*, (6), 1738-49.

12. Radermacher, K. A.; Beghein, N.; Boutry, S.; Laurent, S.; Vander Elst, L.; Muller, R. N.; Jordan, B. F.; Gallez, B. In Vivo Detection of Inflammation Using Pegylated Iron Oxide Particles Targeted at E-selectin: a Multimodal Approach Using MR Imaging and EPR Spectroscopy. *Invest Radiol* **2009,** *44*, (7), 398-404.

13. von zur Muhlen, C.; von Elverfeldt, D.; Moeller, J. A.; Choudhury, R. P.; Paul, D.; Hagemeyer, C. E.; Olschewski, M.; Becker, A.; Neudorfer, I.; Bassler, N.; Schwarz, M.; Bode, C.; Peter, K. Magnetic Resonance Imaging Contrast Agent Targeted Toward Activated Platelets Allows In Vivo Detection of Thrombosis and Monitoring of Thrombolysis. *Circulation* **2008,** *118*, (3), 258-267.

14. Gleich, B.; Weizenecker, J. Tomographic Imaging Using the Nonlinear Response of Magnetic Particles. *Nature* **2005,** *435*, (7046), 1214-7.

15. Weizenecker, J.; Borgert, J.; Gleich, B. A Simulation Study on the Resolution and Sensitivity of Magnetic Particle Imaging. *Phys Med Biol* **2007,** *52*, (21), 6363-74.

16. Weizenecker, J.; Gleich, B.; Rahmer, J.; Dahnke, H.; Borgert, J. Three-Dimensional Real-Time In Vivo Magnetic Particle Imaging. *Phys Med Biol* **2009,** *54*, (5), L1-L10.

17. Markov, D. E.; Boeve, H.; Gleich, B.; Borgert, J.; Antonelli, A.; Sfara, C.; Magnani, M. Human Erythrocytes as Nanoparticle Carriers for Magnetic Particle Imaging. *Physics in Medicine and Biology* **2010,** *55*, (21), 6461.

18. Ferguson, R. M.; Minard, K. R.; Krishnan, K. M. Optimization of Nanoparticle Core Size for Magnetic Particle Imaging. *Journal of Magnetism and Magnetic Materials* **2009,** *321*, (10), 1548-1551.

19. Ferguson, R. M.; Minard, K. R.; Khandhar, A. P.; Krishnan, K. M. Optimizing Magnetite Nanoparticles for Mass Sensitivity in Magnetic Particle Imaging. *Med Phys* **2011,** *38*, (3), 1619-26.

20. Reimer, P.; Rummeny, E. J.; Daldrup, H. E.; Balzer, T.; Tombach, B.; Berns, T.; Peters, P. E. Clinical Results with Resovist: a Phase 2 Clinical Trial. *Radiology* **1995,** *195*, (2), 489-96.

21. Chen, D. X.; Sun, N.; Gu, H. C. Size Analysis of Carboxydextran Coated Superparamagnetic Iron Oxide Particles Used as Contrast Agents of Magnetic Resonance Imaging. *Journal of Applied Physics* **2009,** *106*, (6), 063906-9.

22. Yu, W. W.; Falkner, J. C.; Yavuz, C. T.; Colvin, V. L. Synthesis of Monodisperse Iron Oxide Nanocrystals by Thermal Decomposition of Iron Carboxylate Salts. *Chem Commun (Camb)* **2004**, (20), 2306-7.

23. Hyeon, T.; Lee, S. S.; Park, J.; Chung, Y.; Na, H. B. Synthesis of highly crystalline and monodisperse maghemite nanocrystallites without a size-selection process. *J Am Chem Soc* **2001,** *123*, (51), 12798-801.

24. Sun, S.; Zeng, H.; Robinson, D. B.; Raoux, S.; Rice, P. M.; Wang, S. X.; Li, G. Monodisperse MFe2O4 (M = Fe, Co, Mn) nanoparticles. *J Am Chem Soc* **2004,** *126*, (1), 273-9.

25. Luigjes, B.; Woudenberg, S. M. C.; de Groot, R.; Meeldijk, J. D.; Torres Galvis, H. M.; de Jong, K. P.; Philipse, A. P.; Erné, B. H. Diverging Geometric and Magnetic Size Distributions of Iron Oxide Nanocrystals. *The Journal of Physical Chemistry C* **2011,** *115*, (30), 14598-14605.

26. Biederer, S.; Knopp, T.; Sattel, T. F.; Lüdtke-Buzug, K.; Gleich, B.; Weizenecker, J.; Borgert, J.; Buzug, T. M. Magnetization Response Spectroscopy of Superparamagnetic Nanoparticles for Magnetic Particle Imaging. *Journal of Physics D: Applied Physics* **2009,** *42*, (20), 205007.

27. Burdinski, D.; Bohlender, C.; Haex, N. Synthesis of high-performance iron oxide particle tracers for magnetic particle imaging (MPI). WO 2012/001578 A1, 2012.

28. Starmans, L. W. E.; Kok, M. B.; Sanders, H. M. H. F.; Zhao, Y.; de Mello Donegá, C.; Meijerink, A.; Mulder, W. J. M.; Grüll, H.; Strijkers, G. J.; Nicolay, K. Influence of Cell-Internalization on Relaxometric, Optical and Compositional Properties of Targeted Paramagnetic Quantum Dot Micelles. *Contrast Media Mol Imaging* **2011,** *6*, (2), 100-109.

29. Mulder, W.; Castermans, K.; van Beijnum, J.; oude Egbrink, M.; Chin, P.; Fayad, Z.; Löwik, C.; Kaijzel, E.; Que, I.; Storm, G.; Strijkers, G.; Griffioen, A.; Nicolay, K. Molecular Imaging of Tumor Angiogenesis Using αvβ3-Integrin Targeted Multimodal Quantum Dots. *Angiogenesis* **2009,** *12*, (1), 17-24.

30. Wescot, C. R.; Beltzer, J. P.; Sato, A. K. Fibrin Binding Moieties Useful as Imaging Agents. WO 02/055544 A2, 2002.

31. Marinelli, E.; Ramalingam, K.; Swenson, R.; Song, B.; Lattuada, L.; Uggeri, F.; Lorusso, V.; Aime, S.; Morosini, P.; Chaabane, L. Fibrin Binding Peptide Conjugates for Diagnostic and Therapeutic Applications. WO 2008/071679 A1, 2008.

32. Fields, G. B.; Noble, R. L. Solid Phase Peptide Synthesis Utilizing 9-Fluorenylmethoxycarbonyl Amino Acids. *International Journal of Peptide and Protein Research* **1990,** *35*, (3), 161-214.

33. Cengelli, F.; Maysinger, D.; Tschudi-Monnet, F.; Montet, X.; Corot, C.; Petri-Fink, A.; Hofmann, H.; Juillerat-Jeanneret, L. Interaction of functionalized superparamagnetic iron oxide nanoparticles with brain structures. *J Pharmacol Exp Ther* **2006,** *318*, (1), 108-16.

5.7 Supplementary information

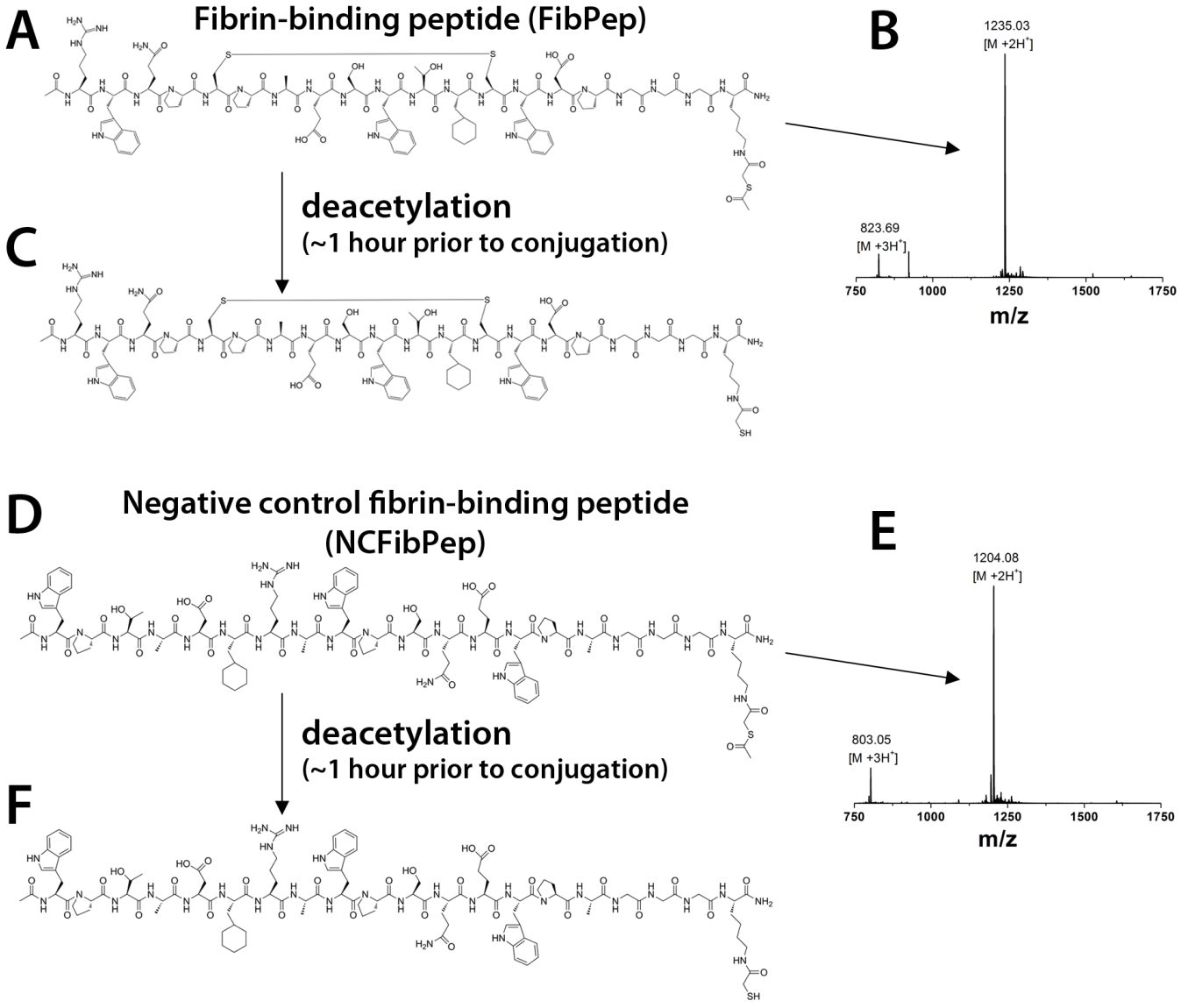

Figure S1. *Structural formulas and corresponding mass spectra of FibPep and NCFibPep. (A,B) FibPep and (D,E) NCFibPep prior to deacetylation. ~1 h before conjugation of the peptides to the ION-Micelles, the SATA group is deacetylated in order to obtain a functional thiol group that can bind to the maleimide-functionalized PEG2000-DSPE lipids on the surface of the ION-Micelles (C,F for FibPep and NCFibPep, respectively).*

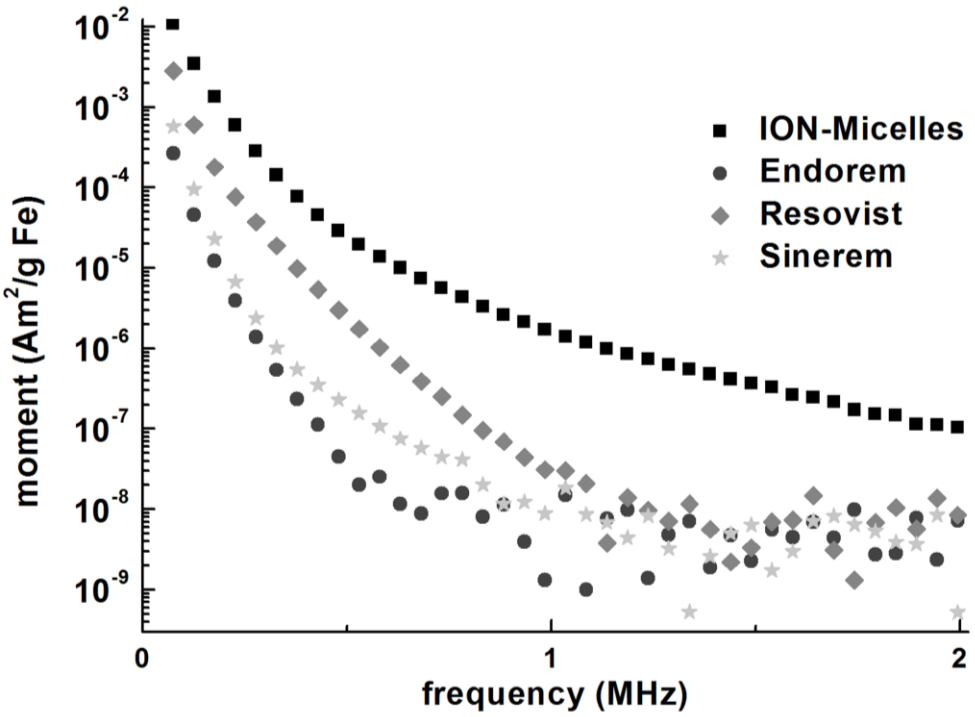

Figure S2. *Magnetic particle spectrometry in whole blood. MPS experimental data of the ION-Micelles, Endorem, Resovist and Sinerem in whole blood plotted as magnetic moment (normalized for iron content) versus frequency.*

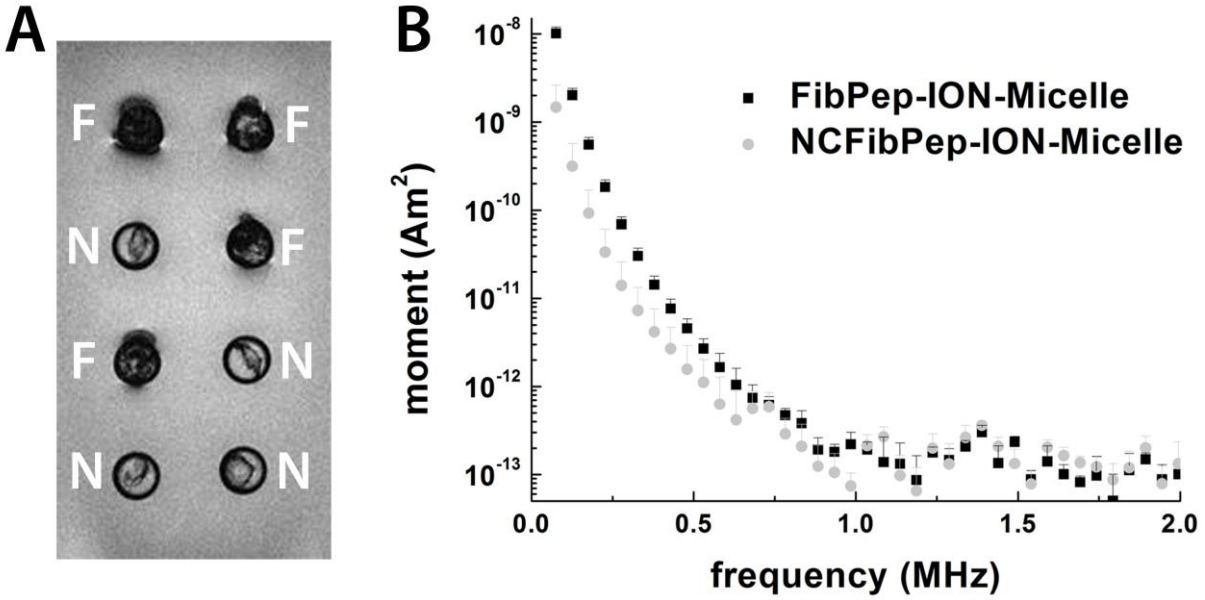

Figure S3. *MRI and MPS measurements of blood clots incubated with either FibPep-ION-Micelles or NCFibPep-ION-Micelles. (A) Transversal MR slice of the blood clots; F = clots incubated with FibPep-ION-Micelles; N = clots incubated with NCFibPep-ION-Micelles. (B) MPS spectrum of clots incubated with FibPep-ION-Micelles or NCFibPep-ION-Micelles.*

Chapter 6

Evaluation of fibrin-binding iron oxide nanoparticle micelles (FibPep-ION-Micelles) for MRI and MPI of thrombosis

Abstract

The significant role of fibrin deposition in cardiovascular and oncologic disease processes motivates efforts in the development of imaging probes that allow noninvasive visualization of pathological fibrin deposition *in vivo*. To allow fibrin-specific molecular magnetic resonance imaging (MRI) and magnetic particle imaging (MPI), we developed a fibrin-binding peptide functionalized iron oxide nanoparticle micelle (FibPep-ION-Micelle) nanoplatform. In this study, we investigated the potential of FibPep-ION-Micelles for MRI and MPI-based detection of thrombi in mice with induced carotid artery thrombosis. FibPep-ION-Micelles showed a high transversal relaxivity (>200 $mM^{-1}s^{-1}$) and a strong magnetic particle spectrometry (MPS) signal (up to 750-fold increased signal with respect to Resovist), and displayed fibrin-specific and stable binding to blood clots *in vitro*. However, accumulation of FibPep-ION-Micelles in carotid artery thrombi *in vivo* was nonspecific for fibrin. The negative control NCFibPep-ION-Micelles accumulated to similar amounts in the thrombi. The lack of fibrin specificity is likely due to nonspecific entrapment of nanoparticles in the mesh-like thrombi *in vivo.* This entrapment of the ION-Micelles significantly decreased T_2 values in the thrombi with respect to pre injection T_2 values ($p < 0.01$) and significantly increased *ex vivo* MPS thrombus signal with respect to the noninjured, contralateral carotid ($p < 0.01$). Therefore, (nontargeted) ION-Micelles might be of value for noninvasive MPI/MRI-based diagnosis, characterization and treatment monitoring of thrombosis.

This chapter is based on:

Starmans, L. W.;* Moonen, R. P.;* Aussems-Custers, E.; Daemen, M. J.; Strijkers, G. J.; Nicolay, K.; Grull, H. Evaluation of fibrin-binding iron oxide nanoparticle micelles (FibPep-ION-Micelles) for magnetic resonance imaging (MRI) and magnetic particle imaging (MPI) of thrombosis. *Under review.* *Authors contributed equally.

6.1 Introduction

Fibrin is a protein which plays an important role in blood coagulation and wound healing.[1] The protein is formed after cleavage of fibrinopeptide A from the fibrinogen Aα-chains by thrombin, which induces fibrin polymerization.[2, 3] Deposition of fibrin is a key process in a variety of pathologies. Fibrin is a main building block of thrombi,[4] which play a significant role in a variety of cardiovascular diseases, such as myocardial infarction, ischemic stroke, pulmonary embolism and deep venous thrombosis. Furthermore, fibrin deposition in atherosclerotic lesions has been shown to correlate to plaque progression and has been linked to plaque erosion and the presence of intraplaque vasa vasorum.[5-8] In addition to cardiovascular diseases, fibrin deposition occurs in a variety of malignant tumors.[9] Fibrin deposition induces formation of mature tumor stroma and provides a scaffold that facilitates tumor angiogenesis and storage of growth factors within the tumor.[9, 10] Fibrin is also known to protect cancer cells against the immune system by impeding their elimination by natural killer cells.[11] The significant role of fibrin in these cardiovascular and oncologic disease processes motivates efforts in the development of imaging probes that allow noninvasive visualization of pathological fibrin deposition *in vivo*.

Recently, we have developed an iron oxide nanoparticle micelle (ION-Micelle) platform that allows sensitive magnetic resonance imaging (MRI) and magnetic particle imaging (MPI).[12] The ION-Micelle nanoplatform consists of hydrophobic, 25 nm-sized iron oxide nanoparticles, which are encapsulated into pegylated phospholipid micelles. MPI is a relatively new diagnostic imaging modality that is able to directly visualize magnetic nanoparticles.[13] This represents a fundamentally different approach than iron oxide nanoparticle-enhanced MRI, which detects magnetic particles indirectly by measuring their effect on proton relaxation rates. MPI yields hotspot-like images similar to nuclear imaging techniques and should provide a more quantitative and sensitive alternative for molecular and cellular MRI.[14] For optimal sensitivity in MPI, the nanocrystal size of the iron oxide nanoparticles should be around 20-30 nm,[14] whereas currently employed commercially available iron oxide formulations for MPI have a core size around 4-6 nm.[15, 16] This size is too small to induce a strong signal for MPI. Magnetic particle spectrometry (MPS),[17] which essentially is zero-dimensional MPI, showed that ION-Micelles induced up to 200-fold higher signal compared to Resovist,[12] which is considered to be the most potent commercially available iron oxide formulation for MPI purposes. Thus, the ION-Micelle nanoplatform allows significantly more sensitive MPI than current commercially available iron oxide formulations.

To allow noninvasive visualization of pathological fibrin deposition *in vivo* using molecular MRI and MPI, we have functionalized the ION-Micelle nanoplatform with fibrin-binding peptides (FibPep), yielding FibPep-ION-Micelles (Fig. 1A). FibPep contains the cyclic fibrin-binding amino acid sequence RWQPCPAESWT-Cha-CWDP and binds to human and mouse fibrin with an affinity (K_d) of approximately 700 nM.[18] Previous preliminary *in vitro* fibrin-binding experiments showed that FibPep-ION-Micelles bound specifically to human plasma clots and allowed visualization and quantification of this specific binding using MRI and MPS, respectively.[12] In this study, we report on a more detailed analytical and *in vitro* characterization of the FibPep-ION-Micelle nanoplatform. Furthermore, we investigated the

potential of the FibPep-ION-Micelle nanoplatform for MRI and MPI-based detection of fibrin deposition in mice with induced carotid artery thrombosis *in vivo*.

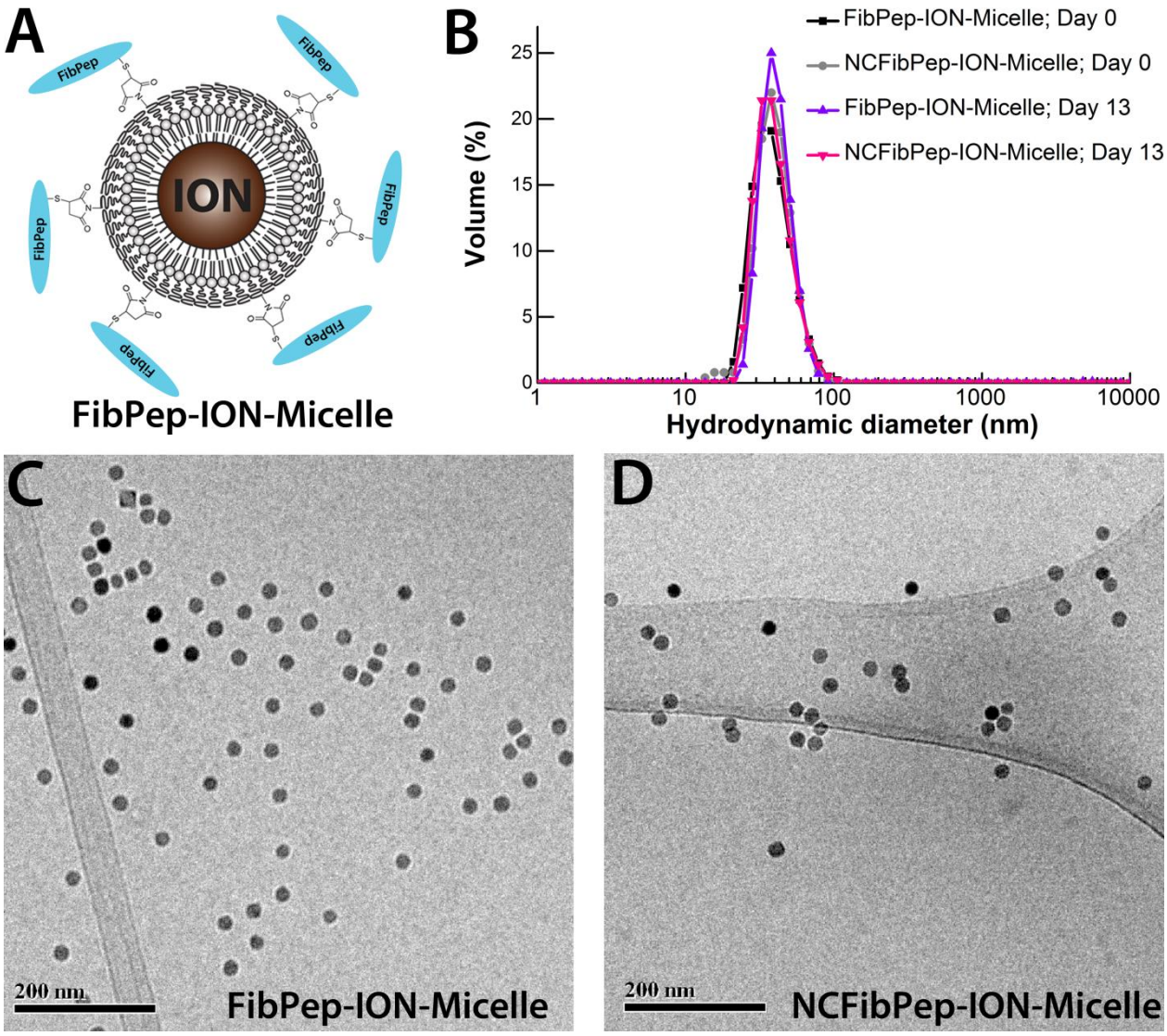

Figure 1. *(A) Schematic representation of the FibPep-ION-Micelle nanoplatform. Reproduced from Starmans and coworkers.*[12] *(B) Volume-weighted size-distribution profiles of the FibPep-ION-Micelles and NCFibPep-ION-Micelles at the day of synthesis (day 0) and at the final day of the in vivo experiments (day 13). (C, D) Representative cryo-TEM images of (C) FibPep-ION-Micelles and (D) NCFibPep-ION-Micelles.*

6.2 Results

6.2.1 Nanoparticle synthesis and characterization

Fibrin-targeted FibPep-ION-Micelles (Fig. 1A) and negative control NCFibPep-ION-Micelles were synthesized according to a previously published protocol.[12] In short, hydrophobic iron oxide nanoparticles with a core size of ca. 25 nm were synthesized using a thermal decomposition method, and, subsequently, iron oxide nanoparticles were phase-transferred by encapsulation into lipidic micelles. Finally, the iron oxide nanoparticle-micelles were functionalized by conjugation of the fibrin-binding peptide FibPep or the negative control peptide NCFibPep onto the lipidic coating of the nanoparticles.[18, 19]

The dispersion state of the synthesized nanoparticles in HEPES buffered saline (HBS, pH 7.4) was investigated using dynamic light scattering (DLS) and cryogenic transmission electron microscopy (cryo-TEM) measurements. Figure 1B shows the volume-weighted size-distribution profiles of the FibPep-ION-Micelles and NCFibPep-ION-Micelles. Immediately after synthesis of the nanoparticles, one peak was observed with a maximum intensity at a hydrodynamic diameter of 40 nm. At the conclusion of the *in vivo* experiments (13 days post synthesis), DLS was performed once more, and showed identical results for both FibPep-ION-Micelles and NCFibPep-ION-Micelles (Fig. 1B), indicating excellent intrinsic stability of the particles over the time course of the study. Cryo-TEM analysis showed that FibPep-ION-Micelles and NCFibPep-ION-Micelles were dispersed in HBS as single particles or as small aggregates of nanoparticles (Fig. 1C-D). The cryo-TEM observations correspond well to the DLS results, as a single iron oxide nanoparticle (25 nm) coated with a lipid monolayer (ca. 5-10 nm in thickness) would be expected to yield a hydrodynamic diameter of approximately 40 nm.

The potential of the ION-Micelles to generate MRI contrast was studied using proton relaxometry (1.4 T, 37 °C). FibPep-ION-Micelles and NCFibPep-ION-Micelles displayed a longitudinal relaxivity of 5.6 and 5.4 $mM^{-1}s^{-1}$ and a transversal relaxivity of 207 and 204 $mM^{-1}s^{-1}$, respectively. The high transversal relaxivity and high r_2/r_1 ratio indicate that the nanoparticles are well suited to allow sensitive detection by T_2-weighted MR imaging. MPS was performed to assess the capacity of the FibPep-ION-Micelles and NCFibPep-ION-Micelles to induce a signal for MPI purposes. Resovist was measured as a reference. Figure 2 shows that FibPep-ION-Micelles induced similar MPS signal in comparison to NCFibPep-ION-Micelles. For lower frequencies (<0.5 MHz), the (NC)FibPep-ION-Micelles generated approximately a twofold higher signal per gram iron than Resovist, whereas in the higher frequency domain the signal of (NC)FibPep-ION-Micelles was up to 750 times increased with respect to Resovist, indicating that the (NC)FibPep-ION-Micelles are potent contrast agents for MPI.

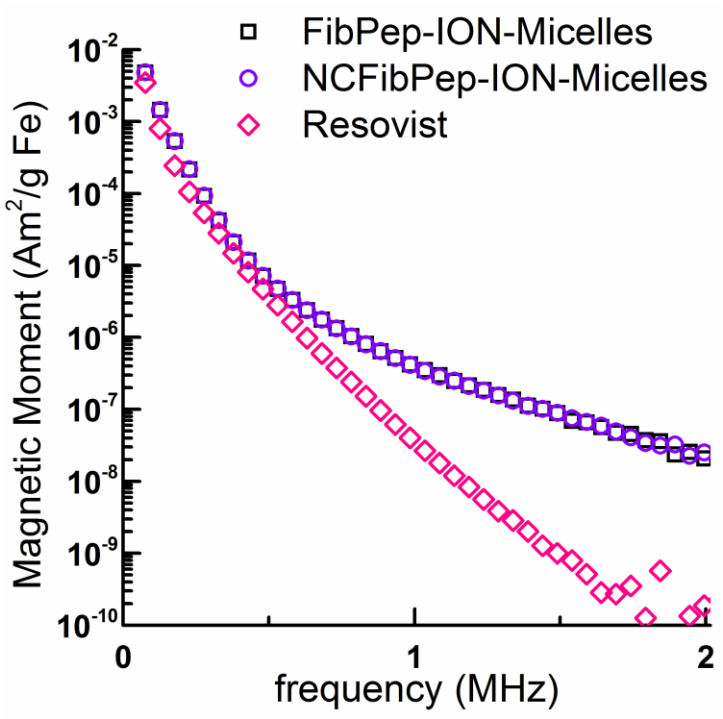

Figure 2. *MPS of FibPep-ION-Micelles, NCFibPep-ION-Micelles and Resovist. Data is plotted as magnetic moment (normalized for iron content) versus frequency. Note that the curves of FibPep-ION-Micelles and NCFibPep-ION-Micelles largely overlap.*

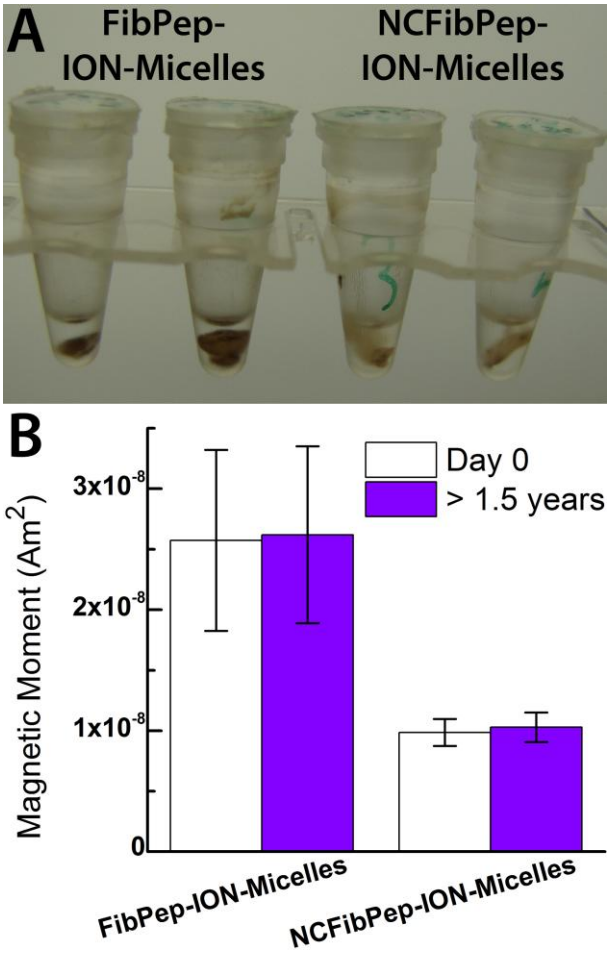

Figure 3. *(A) Photograph and (B) MPS of human plasma clots incubated with either FibPep-ION-Micelles or NCFibPep-ION-Micelles. MPS measurements were performed immediately after the incubation and washing procedure (Day 0) and after storage for more than 1.5 years (> 1.5 years). Data is expressed as mean magnetic moment of the third harmonic (76 kHz) ± SD.*

An *in vitro* human blood clot assay was performed to confirm the specific fibrin-binding capabilities of the synthesized batch of FibPep-ION-Micelles. Plasma clots were incubated with either FibPep-ION-Micelles or NCFibPep-ION-Micelles and extensively washed after incubation. Subsequently, clots were photographed and measured using MPS to determine iron oxide nanoparticle binding. The clots incubated with FibPep-ION-Micelles showed markedly increased uptake of the (brownish) colored ION-Micelles with respect to clots incubated with NCFibPep-ION-Micelles (Fig. 3A). Specific analysis of the third MPS harmonic (72.6 kHz), which is the harmonic with the highest signal amplitude, showed that FibPep-ION-Micelles displayed a 3-fold higher signal in the clots compared to NCFibPep-ION-Micelles (25.7 ± 7.5 nAm^2 and 9.9 ± 1.1 nAm^2, respectively, Fig. 3B). Thus, FibPep-ION-Micelles bound in specific fashion to the human plasma clots. Samples were stored at 4 °C and measured once more after more than 1.5 years of storage, yielding virtually identical results with respect to the initial measurements (Fig. 3B), indicating that the particles were bound to the clots in a stable fashion. Similar *in vitro* blood clot binding studies with the peptide-based SPECT-tracers ^{111}In-FibPep and ^{111}In-NCFibPep yielded a 6 to 8 fold difference between fibrin-binding ^{111}In-FibPep and the negative control peptide.[18, 19] The observed lower difference in *in vitro* blood clot uptake between FibPep-ION-Micelles and NCFibPep-ION-Micelles may possibly be attributed to reduced clot penetration and an increased nonspecific entrapment in the mesh-like clot structure of the ION-Micelle nanoparticles with respect to the much smaller peptidic fibrin-binding SPECT tracers.

6.2.2 In vivo MRI

To study the potential of the ION-Micelles to allow visualization of fibrin deposition using MPI and contrast enhanced MRI, an $AlCl_3$-induced carotid artery thrombosis mouse model was employed.[20] The $AlCl_3$-model produces wall-adherent thrombi similar to the frequently employed $FeCl_3$-injury method,[18, 19, 21] but does not cause iron-based MR signal void artifacts which hamper MRI analysis of the produced thrombi using the $FeCl_3$-model.[20] Mice were subjected to baseline MR scans following thrombus inducing surgery, and, subsequently, FibPep-ION-Micelles or NCFibPep-ION-Micelles were injected and mice underwent post injection MR scans (n=5 per group). No adverse effects were noticed following injection of the nanoparticles. One mouse of the NCFibPep-ION-Micelle group had to be excluded from MRI data analysis because of internal bleeding caused by the surgery, obscuring the carotid artery and thrombus in the MR images.

3D fast low-angle shot time-of-flight (3D-FLASH-TOF) MR images confirmed formation of thrombus in the right carotid artery, which was observed as interruption of the bright blood signal; the thrombus itself has a light gray appearance in the MR image (Fig. 4A). A 2D image of the right carotid artery (RCA) was reconstructed from the 3D dataset and was used for planning subsequent MRI scans (Fig. 4B). T_1- and T_2-weighted images and T_2 maps were successfully acquired repeatedly (Fig. 4C-D). Quantification of T_2 was preferred over T_2* because imaging in the carotid artery region requires a protocol that is robust for cardiac, respiratory and blood-flow motion.

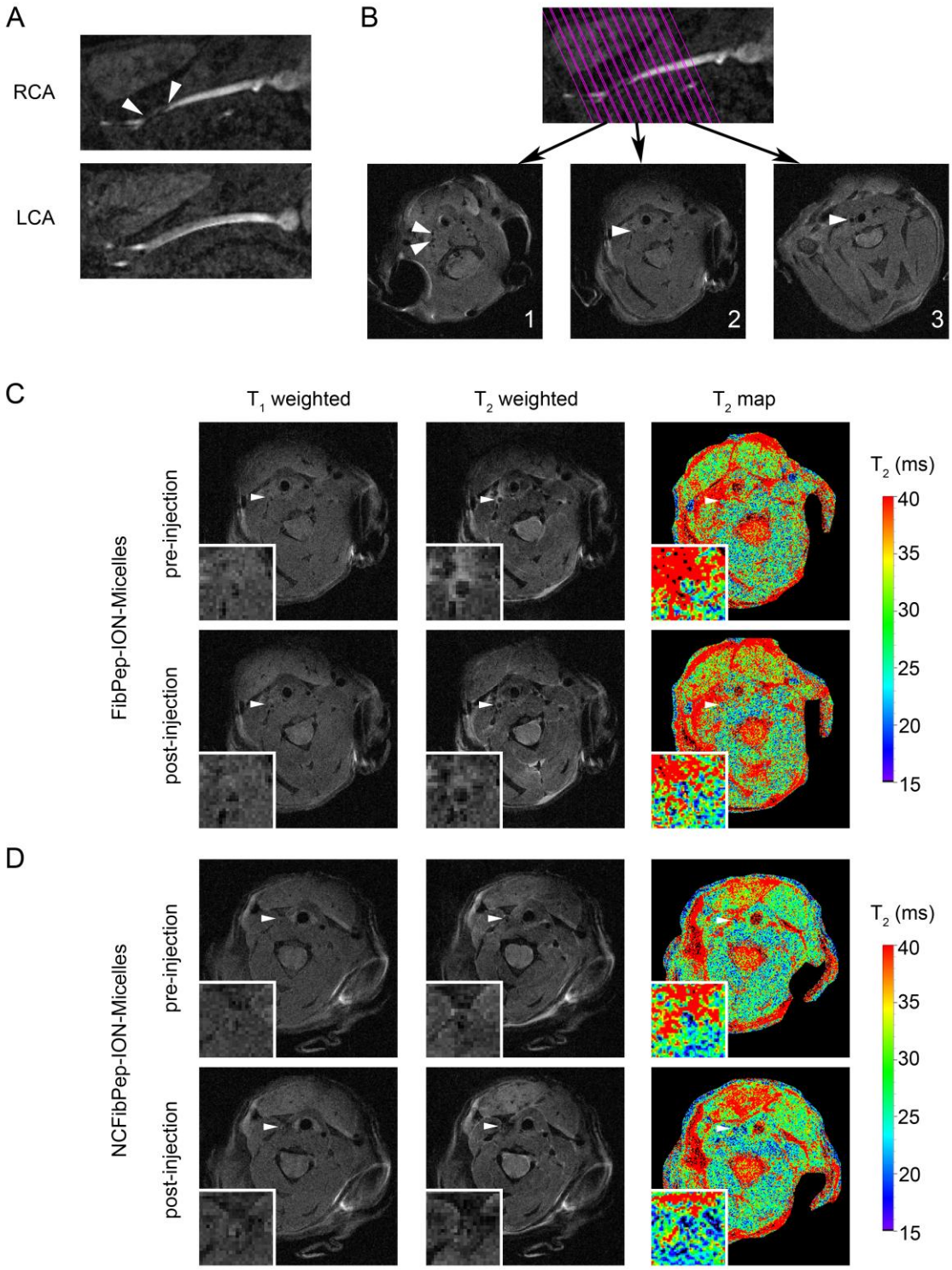

Figure 4. *In vivo MR images after thrombus induction. (A) Images of right and left carotid arteries (RCA & LCA) reconstructed from the 3D time of flight (TOF) image. The thrombus can be observed in the RCA just proximal of the bifurcation (arrowheads). (B) On the TOF image 13 parallel slices were planned perpendicular to the RCA. T_1-weighted images from three slices are shown: (1) distal from the bifurcation, (2) in the thrombus and (3) proximal to the thrombus (arrowheads: RCA). (C, D) Pre and post injection T_1- and T_2-weighted images and T_2 maps of (C) FibPep-ION-Micelles and (D) NCFibPep-ION-Micelles (arrowheads: RCA). The insets show magnifications of the RCA.*

Region of interest (ROI) analysis revealed decreased mean T_2 values in the thrombus area after injection with both FibPep-ION-Micelles (22.7 ± 1.5 ms) and NCFibPep-ION-Micelles (22.0 ± 2.6 ms) compared to pre injection values (26.5 ± 2.6 and 25.0 ± 1.5 ms, respectively) (Fig. 5). Comparison of T_2 values between mice injected with FibPep-ION-Micelles or NCFibPep-ION-Micelles revealed no significant differences for pre or post injection values (p = 0.388 and p = 0.675, respectively). This indicates that the functionalization with FibPep did not specifically enhance *in vivo* uptake of ION-Micelles in the thrombus as compared to the negative control peptide functionalized nanoparticles. Statistically, the mice injected with FibPep-ION-Micelles or NCFibPep-ION-Micelles can thus be viewed as a single group. Comparison of the combined mean thrombus T_2 values revealed a highly significant (p = 0.003) overall decrease of T_2 from 25.8 ± 2.3 ms pre injection to 22.4 ± 2.1 ms post injection of ION-Micelles (Fig. 5).

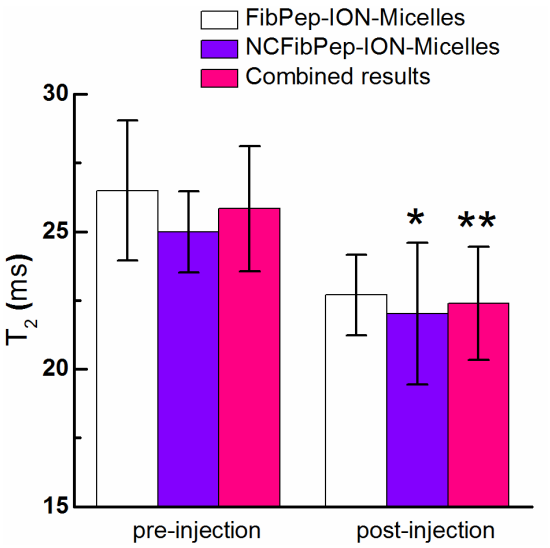

Figure 5. *In vivo T_2 (mean ± SD) of the thrombus pre and post injection with FibPep-ION-Micelles (n=5), NCFibPep-ION-Micelles (n=4) and T_2 for both contrast agents combined (n=9). T_2 values that were significantly decreased post injection compared to pre injection are marked with * (p < 0.05) or ** (p < 0.01).*

6.2.3 Ex vivo MPS and histological validation

Mice were euthanized upon completion of the MR scans (ca. 2 h post injection of ION-Micelles and 4.5 h post thrombus induction). Subsequently, the injured and noninjured, contralateral carotid arteries were excised and measured using MPS to probe ION-Micelle MPI signal. In addition, the injured and contralateral carotids of three mice that had not undergone nanoparticle injection were measured with MPS to quantify background MPS signal of the thrombosed and noninjured carotids. Specific analysis of the third MPS harmonic (Fig. 6) showed significantly increased signal for the injured carotids of mice injected with FibPep-ION-Micelles or NCFibPep-ION-Micelles (26 ± 7 and 25 ± 8 pAm^2, respectively) with respect to the contralateral carotids of these mice (9 ± 3 and 8 ± 2 pAm^2, respectively) and also with respect to both the injured and contralateral carotids of mice which did not receive nanoparticle injections (5 ± 2 and 6 ± 4 pAm^2, respectively). Thus, both the fibrin-specific and fibrin-nonspecific nanoparticle formulations showed significant accumulation in thrombi. The MPS data indicate that there was no significant difference between iron oxide nanoparticle uptake in the injured carotids of mice injected with FibPep-ION-Micelles or NCFibPep-ION-Micelles, which is in line with the above MRI findings.

Histological sections studied using autofluorescence imaging confirmed (partial) occlusion of the injured carotid arteries and absence of occlusion in the contralateral, noninjured carotid arteries (Fig. 7).

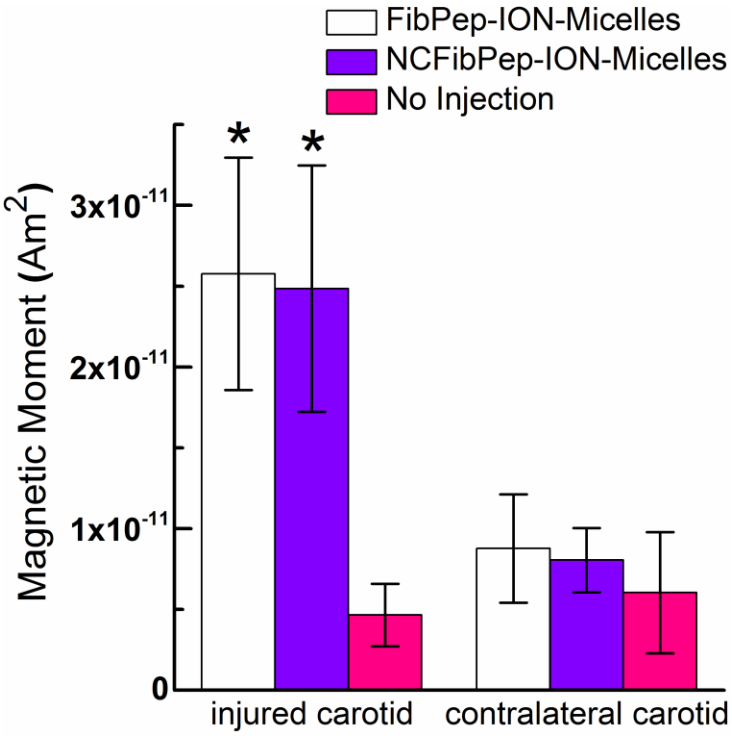

Figure 6. *MPS of excised injured and contralateral, noninjured carotid arteries following injection with FibPep-ION-Micelles (n=5) and NCFibPep-ION-Micelles (n=5) or without injection (n=3). Data is expressed as mean magnetic moment of the third harmonic (76 kHz) ± SD. * P < 0.01 versus contralateral carotid (all three groups) and injured carotid of mice which had not received an injection of ION-Micelles.*

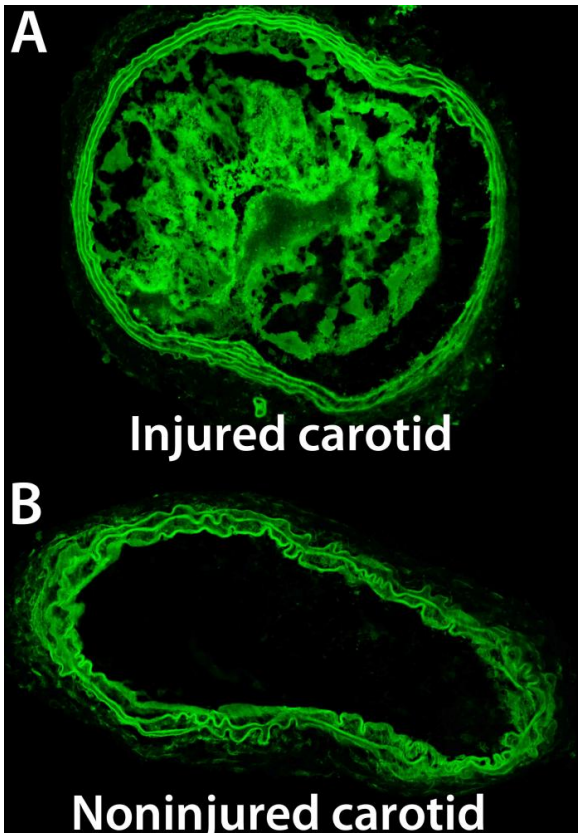

Figure 7. *Representative autofluorescence confocal microscopy images of transversal histological sections of the (A) injured carotid and (B) noninjured, contralateral carotid artery.*

6.3 Discussion

In this study, we report on the characterization and the *in vivo* evaluation of FibPep-ION-Micelles for MRI- and MPI-based detection of fibrin deposition in thrombosis. FibPep-ION-Micelles and negative control peptide (NCFibPep) functionalized ION-Micelles had a volume-weighted hydrodynamic diameter of 40 nm and displayed excellent stability over time. The nanoparticles showed high transversal relaxivity (> 200 $mM^{-1}s^{-1}$) and high signal in magnetic particle spectroscopy (MPS) experiments (up to 750 fold increased signal compared to Resovist), indicating that the FibPep-ION-Micelles are potent contrast agents for MRI and MPI purposes. In addition, FibPep-ION-Micelles displayed significantly more binding towards blood clots *in vitro* with respect to negative control peptide (NCFibPep) functionalized ION-Micelles. FibPep-ION-Micelles did not dissociate in a significant fashion from the blood clots after more than one year of incubation in buffer solution, indicating highly stable bonding between the nanoparticles and fibrin deposited in the blood clots *in vitro*.

To evaluate the potential of the FibPep-ION-Micelle nanoplatform for *in vivo* MRI- and *ex vivo* MPI-based detection of fibrin deposition, an $AlCl_3$-induced carotid artery thrombosis mouse model was employed. MR images of the carotids were acquired pre and post nanoparticle injection. Pre injection 3D-TOF images confirmed carotid artery thrombosis, whereas no signal void artifacts were observed, indicating that the $AlCl_3$-injury method induced carotid artery thrombosis without inducing metal-based signal loss. However, in contrast to the *in vitro* experiments, no significant difference in thrombus binding was observed between FibPep-ION-Micelles and negative control NCFibPep-ION-Micelles. Both FibPep-ION-Micelles and NCFibPep-ION Micelles decreased the T_2 values in the thrombus region, but there were no significant differences for pre or post injection values between the FibPep-ION-Micelle group and the group which received NCFibPep-ION-Micelles. Previous *in vitro* MRI evaluation demonstrated that particle binding occurs only on the outside of the blood clots.[12] For reasons of resolution, *in vivo* ROIs encompass the whole thrombus, the vessel wall and potentially some blood, and local changes are thus averaged out over a larger area at the cost of sensitivity. After the final MR scans, mice were euthanized and the carotids were excised and measured *ex vivo* with a magnetic particle spectrometer. FibPep-ION-Micelles and NCFibPep-ION-Micelles both displayed increased MPS signal in the injured carotid with respect to the noninjured, contralateral carotid artery. However, in line with the MRI results, no significant difference between FibPep-ION-Micelles and negative control NCFibPep-ION-Micelles was observed. Thus, the measured *in vivo* uptake of the FibPep-ION-Micelles in carotid artery thrombosis seems nonspecific for fibrin deposition.

Similar *in vivo* thrombus uptake of FibPep- and NCFibPep-ION-Micelles may have various potential causes. First, previous studies investigating ^{111}In-labeled FibPep showed that the FibPep peptide was stable in serum, but prone to degradation in kidney and liver homogenates.[18] FibPep-ION-Micelles are, unlike the small ^{111}In-labeled FibPep peptides, not expected to extravasate, encounter liver and kidney proteolytic enzymes and subsequently reenter the circulation. In addition, even though the ^{111}In-labeled FibPep peptides were susceptible to degradation by liver and kidney homogenates, ^{111}In-FibPep accumulated significantly more in carotid artery thrombi with respect to negative control peptide ^{111}In-

NCFibPep.[18] Therefore, instability of the targeting peptides on the FibPep-ION-Micelles is likely not a main factor for the identical level of uptake *in vivo* for the FibPep- and NCFibPep-ION-Micelles. Second, the lipidic micellular nanoparticle coating has a dynamic nature,[22-24] possibly enabling fibrin-bound FibPep-ION-Micelles to dissociate from the fibrin target by shedding the fibrin-bound FibPep-lipid construct from the nanoparticle. However, *in vitro* blood clot binding experiments showed that the nanoparticles were bound to the clots in a stable fashion for more than one year. Third, nanoparticles are known to accumulate nonspecifically in thrombi *in vivo*,[25, 26] likely by entrapment in the mesh-like clot structure. Consequently, nonspecific accumulation of FibPep-ION-Micelles and NCFibPep-ION-Micelles in the carotid artery thrombi most likely obscures fibrin-specific uptake effects of the fibrin-binding FibPep-ION-Micelles.

Even though the *in vivo* accumulation of FibPep-ION-Micelles in carotid artery thrombi was nonspecific for fibrin deposition, the ION-Micelles significantly decreased thrombus T_2 values and significantly increased MPS signal of the thrombi and thus were successfully able to detect thrombosis using MRI and MPS. This is most likely due to nonspecific entrapment of the nanoparticles in the thrombi *in vivo*. Such an entrapment-based strategy using (nontargeted) ION-Micelles might be valuable for noninvasive MPI-based diagnosis, characterization and treatment monitoring of thrombosis.[25, 26] With respect to MRI, suitable noncontrast enhanced alternatives for detection of thrombus such as T_1-weighted imaging are available.[27] Additional research is required to explore the potential of nontargeted ION-Micelles for MPI-based thrombosis diagnostics. Furthermore, since the FibPep-ION-Micelles did show specificity for fibrin *in vitro*, the FibPep-ION-Micelles might still find value for visualization of fibrin deposition in other pathologies, such as atherosclerosis, which do not involve large intraluminar mesh-like structures such as thrombi that may lead to high levels of nonspecific nanoparticle entrapment. Finally, the ION-Micelle platform shows high transversal relaxivity and strong MPS signal and allows conjugation to targeting ligands other than FibPep via facile maleimide-thiol chemistry, and is therefore a promising multi-purpose nanoplatform for molecular MRI and MPI strategies.

6.4 Conclusions

FibPep-ION-Micelles showed high transversal relaxivity and MPS signal, and displayed fibrin-specific and stable binding to blood clots *in vitro*. However, accumulation of FibPep-ION-Micelles in carotid artery thrombi *in vivo* was nonspecific for fibrin, as negative control NCFibPep-ION-Micelles showed similar levels of thrombus uptake. The lack of fibrin specificity is likely due to nonspecific entrapment of nanoparticles in the mesh-like thrombi *in vivo.* This nonspecific entrapment of the ION-Micelles significantly decreased T_2 values in the thrombi and significantly increased MPS thrombus signal, and therefore, (nontargeted) ION-Micelles might be of value for noninvasive MPI- and MRI-based diagnosis, characterization and treatment monitoring of thrombosis. In addition, the ION-Micelles have potential as an multi-purpose nanoplatform which allows conjugation of other ligands to tailor it for detection of a variety of other disease markers with molecular MRI and MPI.

6.5 Experimental

6.5.1 Materials

Materials were obtained from Sigma-Aldrich unless otherwise specified. Succinimidyl acetylthioacetate (SATA) was acquired from Invitrogen and Rink amide resin and 9-fluorenylmethyloxycarbonyl (Fmoc) protected amino acids were obtained from either Bachem or Novabiochem (Merck). 1,2-distearoyl-sn-glycero-3-phosphoethanolamine-N-[maleimide(polyethyleneglycol)-2000] (Mal-PEG200-DSPE) was purchased from Avanti Polar Lipids, 1,2-distearoyl-sn-glycero-3-phosphoethanolamine-N-[methoxy(polyethyleneglycol)-2000] (PEG200-DSPE) was acquired from Lipoid and near-infrared664-1,2-distearoyl-sn-glycero-3-phosphoethanolamine (NIR664-DSPE) was obtained from SyMO-Chem B.V.[28] Citrated human plasma was purchased from Sanquin, human tissue factor was obtained from Dade Behring and Resovist was acquired from Bayer Schering Pharma.

6.5.2 Peptide synthesis

SATA-modified fibrin-binding peptide FibPep (Ac-RWQPCPAESWT-Cha-CWDPGGGK[SATA]-NH_2) and a scrambled negative control peptide with C-A substitutions (NCFibPep, Ac-WPTAD-Cha-RAWPSQEWPAGGGK[SATA]-NH_2) were synthesized according to a previously published protocol.[12] In short, the amino acid sequences were synthesized on a 4-methylbenzhydrylamine hydrochloride salt rink amide resin by Fmoc solid-phase peptide synthesis and subsequently cleaved from the resin by trifluoroacetic acid: triisopropylsilane: H_2O: ethanedithiol (90.5:5:2.5:2 v/v%) for 3 h. The obtained amino acid sequences were purified by reversed-phase high-pressure liquid chromatography (RP-HPLC) on an Agilent 1200 apparatus equipped with a C18 Zorbax column. The FibPep amino acid sequence was then cyclisized (formation of a disulfide bond between the two cysteine residues) by dimethylsulfoxide:H_2O (9:1 v/v%), with pH set to 8 using n-methyl-d-glucamine, for 5 days and subsequently purified by RP-HPLC. Next, both peptides were functionalized with a SATA moiety at the lysine ε-amino group by mixing the synthesized amino acid sequences and a tenfold excess of SATA in dimethylformamide containing 3.6 v/v% triethylamine at room-temperature (RT) overnight, yielding FibPep and negative control NCFibPep. The obtained peptides were purified by RP-HPLC and analyzed using liquid chromatography-mass spectrometry (LC-MS) on an Agilent 1200 apparatus equipped with a C8 Eclipse plus column and an Agilent 6210 electrospray mass spectrometer.

6.5.3 Nanoparticle synthesis

Fibrin-binding FibPep-ION-Micelles and negative control NCFibPep-ION-Micelles were synthesized according to a previously published protocol.[12] In short, a mixture of FeO(OH) (0.11 g, 1.18 mmol, grounded), oleic acid (3.81 g, 13.5 mmol) and eicosane (0.61 g, 2.17 mmol) was heated to 360 °C (ramping rate: 3.3 °C/min) and subsequently kept at this temperature for 2 h, yielding iron oxide nanoparticles (IONs). Next, the mixture was cooled down and 10 mL of hexane was added. Subsequently, IONs were precipitated by adding 20 mL of acetone and centrifugation (4671 g, RT, 30 min). IONs were redispersed with 10 mL of hexane and 20 µL oleic acid. This precipitation-redispersion procedure was repeated twice.

IONs were subsequently encapsulated into lipidic micelles using a procedure similar to a protocol previously employed to phase-transfer quantum dots.[22, 29] PEG2000-DSPE (448 mg, 160 µmol), MAL-PEG2000-DSPE (52 mg, 18 µmol) and NIR-lipid (2.4 mg, 1.8 µmol) were dissolved in 3 mL chloroform, and IONs in hexane (2 mL, 12 mg Fe) were added. This suspension was injected into stirred, deionized water (40 mL, 80 °C) at a speed of 5 mL/hr, creating iron oxide nanoparticle-micelles (ION-Micelles). Next, large aggregates were removed by centrifugation (1500 g, RT, 5 min) and, subsequently, phospholipid micelles without iron oxide core were removed by ultracentrifugation (27440 g, RT; 15 min) using a Optima^{TM} L-90K ultracentrifuge equipped with a type 70.1 TI rotor (Beckman Coulter). The pellet containing the ION-Micelles was redispersed using HBS pH 6.7 and the ultracentrifugation procedure was repeated once more.

In parallel to the micelle coating procedure, the SATA-moiety on (NC)FibPep peptides was deacetylated using a hydroxylamine containing buffer at RT for 1 h. Immediately after deacetylation and the phase-transfer procedure, fibrin targeted FibPep-ION-Micelles were prepared by mixing half of the obtained ION-Micelle suspension with 250 nmol of deacetylated FibPep at 4 °C overnight. Nonbinding NCFibPep-ION-Micelles were formed in similar fashion using the remaining half of the ION-Micelle suspension and deacetylated NCFibPep (250 nmol). Finally, (NC)FibPep-ION-Micelles were prepared for characterization and *in vivo* application by removing any large aggregates using centrifugation (500 g, 5 min) and changing the buffer to HBS pH 7.4 using centrifugation-filtration (Vivaspin 50k MWCO, 6 mL, Sartorius Stedim Biotech). The final volume of the obtained (NC)FibPep-ION-Micelle solution was ca. 1 mL.

6.5.4 Nanoparticle characterization

The hydrodynamic diameter of the nanoparticles was measured by DLS on a Zetasizer Nano-S (Malvern). In addition, dispersion of the particles in the HBS buffer solution was studied using cryo-TEM on a FEI Tecnai F30ST (300 kV) using a cryo-holder at approximately -170 °C. Sample vitrification was performed with an automated FEI Vitrobot.

Longitudinal and transversal proton relaxivities were determined using a Minispec MQ60 NMR spectrometer (Bruker, 1.41 T, 37 °C). MPS was performed using a dedicated magnetic particle spectrometer (Philips, 10 mT, 25 kHz, 30 s measurements, RT).[17] Iron concentrations were measured using inductively coupled plasma atomic emission spectrometry (ICP-AES).

To confirm the fibrin-binding capabilities of FibPep-ION-Micelles, an *in vitro* blood clot assay was performed. Human clots were prepared by addition of 1.3 µL human tissue factor and 1.5 µL of 1M $CaCl_2$ in ultrapure water to 100 µL of citrated human plasma and subsequent incubation of this mixture at 37 °C for 30 min.[12] Blood clots were subsequently washed 3x with HBS pH 7.4. Next, 20 µL of the FibPep-ION-Micelles or NCFibPep-ION-Micelles solution (35 µg Fe per sample, n=2 per group) and 20 µL HBS pH 7.4 were added to the clots and incubated at RT for 1 h. After the incubation period, the solution was removed and the clots were washed 3x with HBS pH 7.4. The clots were then subjected to

MPS (10 mT, 25 kHz, 30 s, RT) and subsequently stored at 4 °C for more than 1.5 years. Next, clots were washed 3x with HBS pH 7.4, photographed and subjected to MPS.

6.5.5 Animal model

All procedures regarding to animals were approved by the ethical review committee of Maastricht University and were performed according to the Dutch national law and the guidelines set by the institutional animal care committee, accredited by the national department of health.

A well-established $AlCl_3$-induced carotid artery thrombosis mouse model was chosen to study *in vivo* fibrin-binding of the nanoparticles.[20] C57BL/6 mice (Charles River Laboratories, 24.5 ± 1.6 g bodyweight) were housed under standard conditions with water and food freely available and acclimatized for at least one week before the start of the experimental procedures. Prior to thrombus inducing surgery, mice were subcutaneously injected with buprenorphine hydrochloride (Schering-Plough, 0.1 mg/kg). The mice were anesthetized using isoflurane, and a segment of the right carotid artery was surgically exposed. Wall-adherent thrombus formation was subsequently induced by applying a small piece of cleaning cloth soaked in 10% $AlCl_3$ on the carotid for 5 min. Next, the cloth was removed, the carotid was washed with saline and the surgical wound was closed by a suture. Finally, a cannula filled with ca. 100 µL saline containing 50 U heparin/mL was connected to the tail vein to allow nanoparticle injection subsequent to the pre injection MR scans without requiring repositioning of the mice. The nanoparticle bolus was contained in a second cannula which was attached to the first at the time of injection.

6.5.6 In vivo MRI and ex vivo MPS of carotid thrombosis using (NC)FibPep-ION-Micelles

Mice were positioned in supine position into a 9.4 T MRI scanner equipped with a 35-mm-diameter volume transceiver coil (Bruker BioSpin GmbH) and were kept under continuous anesthesia using isoflurane (1-2%). Respiration frequency was monitored with a pressure balloon and temperature was maintained at 37 °C with a heating pad and a rectal temperature probe for feedback. ECG signal was acquired by application of ECG paste on the front paws of the mice, which were subsequently positioned onto gold-plated ECG electrodes that were connected to an ECG triggering system (Small Animal Instruments Inc).

The MRI protocol consisted of a scan of the chest and neck region with a 3D-FLASH-TOF acquisition (echo time TE = 2.5 ms, repetition time TR = 17 ms, field of view FOV = 20 x 20 x 25.6 mm^3, matrix = 200 x 200 x 256, number of averages NA = 2, flip angle FA = 20°). This 3D dataset was used to plan 13 parallel slices (thickness = 0.5 mm, slice separation 0.1 mm, FOV = 25.6 x 25.6 mm^2, matrix = 256 x 256) perpendicular to the right carotid artery, such that the last slice was positioned distal to the bifurcation (Fig. 4B). Subsequently, T_1- and T_2-weighted multi slice spin echo (NA = 2, T_1: TE/TR = 7.5/800 ms, T_2: TE/TR = 20/2000 ms) images were acquired in this slice geometry. The center slice in the thrombus was chosen for T_2 mapping which was performed with an ECG-triggered, respiratory gated, segmented, MLEV-prepared scan with fast imaging with steady-state precession (FISP) readout (40 segments of 5

echoes, TE = 2.1 ms, TR = 4.1 ms, segment TR = 2000 ms, NA = 4, FA = 30°, FOV 20 x 20 mm^2, matrix 400 x 400, zero-filling 2 x 2).[30] Images with six effective echo times (TE_{eff} = 0.2, 7.0, 14.6, 21.0, 29.0 and 35.4 ms) were acquired.

The full MRI protocol was performed twice in the same scan session. In between, at ca. 2.5 h post thrombus formation, FibPep-ION-Micelles or NCFibPep-ION-Micelles (100 µL, 175 µg Fe, n=5 per group) were injected together with the saline already present in the cannula. To this end, the cradle containing the mouse had to temporarily be removed out of the bore of the MRI scanner. By leaving the mouse fixed in the cradle its orientation was largely preserved. However, to prevent repositioning errors the MRI slice planning was repeated. The T_1- and T_2-weighted images and the T_2 map were acquired at approximately 49, 62 and 94 min post injection, respectively. After the final MR scans (ca. 2 h post nanoparticle injection), mice were euthanized. The injured and contralateral carotids were subsequently harvested and subjected to MPS measurements (10 mT, 25 kHz, 30 s, RT). Additionally, the injured and contralateral carotids of three mice, which did undergo thrombus inducing surgery but no nanoparticle injection, were excised and measured with MPS.

6.5.7 MRI data analysis

Image analysis was performed using a custom-built algorithm in Mathematica 9.0 (Wolfram Research). A region of interest (ROI) was manually drawn around the right carotid artery with thrombus on one of the T_2-weighted images of the pre injection T_2 map. The center of the artery was marked and used as a landmark to register pre and post injection images. The registration was visually inspected and corrected manually if necessary. The validity of the ROIs was additionally assessed by registration to the multi-slice T_1- and T_2-weighted images and visual inspection. Subsequently, pixel-wise mono-exponential fitting of the signal intensities at different TE_{eff} was performed. Next, the mean T_2 value of the ROI was determined, and pixels with an R^2 of fit < 0.7 were excluded from further analysis.

6.5.8 Histology

After the MPS measurements, the injured and contralateral carotid arteries were embedded in Tissue-Tek matrix (Sakura) and subsequently snap-frozen in isopentane and stored at -80 °C. The arteries were cut in transversal sections of 5 µm and covered with Fluoromount and a cover glass. Confocal fluorescence images were recorded at RT on a Leica TCS SP5 system (Leica Microsystems). Autofluorescence was measured using a 488 nm argon laser and an emission window of 530-580 nm.

6.5.9 Statistical analysis

All data represent the mean value ± standard deviation (SD). For differences between more than two groups, a 1-way ANOVA with Bonferroni's multiple comparison procedure was employed. Comparison of FibPep- and NCFibPep-ION-Micelles MRI data was done using a two-sided independent t-test and pre and post injection data were compared with a two-sided paired t-test. For all statistical analysis, values of $p < 0.05$ were considered to be significant.

6.6 Acknowledgements

This research was supported by the Center for Translational Molecular Medicine and The Netherlands Heart Foundation (PARISK, Grant 01C-202). The authors would like to thank Sander van Duijnhoven for assistance with the solid-phase peptide synthesis, Monja Kaiser for the cryo-TEM measurements, Jeannette Smulders for the ICP-AES measurements, Larry de Graaf for construction of the animal cradle and Iris Verel, Marleen Hendriks and Caren van Kammen for their support regarding the *in vivo* experiments.

6.7 References

1. Laurens, N.; Koolwijk, P.; de Maat, M. P. Fibrin structure and wound healing. *J Thromb Haemost* **2006,** *4*, (5), 932-9.
2. Mosesson, M. W. Fibrinogen and fibrin structure and functions. *J Thromb Haemost* **2005,** *3*, (8), 1894-904.
3. Weisel, J. W. Fibrinogen and fibrin. *Adv Protein Chem* **2005,** *70*, 247-99.
4. Ariens, R. A. Fibrin(ogen) and thrombotic disease. *J Thromb Haemost* **2013,** *11 Suppl 1*, 294-305.
5. Bini, A.; Fenoglio, J. J., Jr.; Mesa-Tejada, R.; Kudryk, B.; Kaplan, K. L. Identification and distribution of fibrinogen, fibrin, and fibrin(ogen) degradation products in atherosclerosis. Use of monoclonal antibodies. *Arteriosclerosis* **1989,** *9*, (1), 109-21.
6. Congiu, T.; Schembri, L.; Tozzi, M.; Guasti, L.; Maio, R. C.; Cosentino, M.; Marino, F. Scanning electron microscopy examination of endothelium morphology in human carotid plaques. *Micron* **2010,** *41*, (5), 532-6.
7. Sato, Y.; Hatakeyama, K.; Yamashita, A.; Marutsuka, K.; Sumiyoshi, A.; Asada, Y. Proportion of fibrin and platelets differs in thrombi on ruptured and eroded coronary atherosclerotic plaques in humans. *Heart* **2005,** *91*, (4), 526-30.
8. Tavora, F.; Cresswell, N.; Li, L.; Ripple, M.; Burke, A. Immunolocalisation of fibrin in coronary atherosclerosis: implications for necrotic core development. *Pathology* **2010,** *42*, (1), 15-22.
9. Rickles, F. R.; Patierno, S.; Fernandez, P. M. Tissue factor, thrombin, and cancer. *Chest* **2003,** *124*, (3 Suppl), 58S-68S.
10. Dvorak, H. F.; Nagy, J. A.; Berse, B.; Brown, L. F.; Yeo, K. T.; Yeo, T. K.; Dvorak, A. M.; van de Water, L.; Sioussat, T. M.; Senger, D. R. Vascular permeability factor, fibrin, and the pathogenesis of tumor stroma formation. *Ann N Y Acad Sci* **1992,** *667*, 101-11.
11. Palumbo, J. S.; Talmage, K. E.; Massari, J. V.; La Jeunesse, C. M.; Flick, M. J.; Kombrinck, K. W.; Jirouskova, M.; Degen, J. L. Platelets and fibrin(ogen) increase metastatic potential by impeding natural killer cell-mediated elimination of tumor cells. *Blood* **2005,** *105*, (1), 178-85.
12. Starmans, L. W.; Burdinski, D.; Haex, N. P.; Moonen, R. P.; Strijkers, G. J.; Nicolay, K.; Grull, H. Iron oxide nanoparticle-micelles (ION-micelles) for sensitive (molecular) magnetic particle imaging and magnetic resonance imaging. *PLoS One* **2013,** *8*, (2), e57335.
13. Gleich, B.; Weizenecker, J. Tomographic imaging using the nonlinear response of magnetic particles. *Nature* **2005,** *435*, (7046), 1214-7.
14. Weizenecker, J.; Borgert, J.; Gleich, B. A simulation study on the resolution and sensitivity of magnetic particle imaging. *Phys Med Biol* **2007,** *52*, (21), 6363-74.
15. Cengelli, F.; Maysinger, D.; Tschudi-Monnet, F.; Montet, X.; Corot, C.; Petri-Fink, A.; Hofmann, H.; Juillerat-Jeanneret, L. Interaction of functionalized superparamagnetic iron oxide nanoparticles with brain structures. *J Pharmacol Exp Ther* **2006,** *318*, (1), 108-16.
16. Chen, D. X.; Sun, N.; Gu, H. C. Size analysis of carboxydextran coated superparamagnetic iron oxide particles used as contrast agents of magnetic resonance imaging. *J Appl Phys* **2009,** *106*, (6).
17. Biederer, S.; Knopp, T.; Sattel, T. F.; Ludtke-Buzug, K.; Gleich, B.; Weizenecker, J.; Borgert, J.; Buzug, T. M. Magnetization response spectroscopy of superparamagnetic nanoparticles for magnetic particle imaging. *J Phys D Appl Phys* **2009,** *42*, (20).

18. Starmans, L. W.; van Duijnhoven, S. M.; Rossin, R.; Berben, M.; Aime, S.; Daemen, M. J.; Nicolay, K.; Grull, H. Evaluation of 111In-labeled EPep and FibPep as tracers for fibrin SPECT imaging. *Mol Pharm* **2013,** *10*, (11), 4309-21.

19. Starmans, L. W.; van Duijnhoven, S. M.; Rossin, R.; Aime, S.; Daemen, M. J.; Nicolay, K.; Grull, H. SPECT imaging of fibrin using fibrin-binding peptides. *Contrast Media Mol Imaging* **2013,** *8*, (3), 229-37.

20. Wolters, M.; van Hoof, R. H.; Wagenaar, A.; Douma, K.; van Zandvoort, M. A.; Hackeng, T. H.; Post, M. J.; Backes, W. H.; Kooi, M. E. MRI artifacts in the ferric chloride thrombus animal model: an alternative solution: preventing MRI artifacts after thrombus induction with a non-ferromagnetic Lewis acid. *J Thromb Haemost* **2013,** *11*, (9), 1766-9.

21. Sachs, U. J.; Nieswandt, B. In vivo thrombus formation in murine models. *Circ Res* **2007,** *100*, (7), 979-91.

22. Starmans, L. W.; Kok, M. B.; Sanders, H. M.; Zhao, Y.; Donega Cde, M.; Meijerink, A.; Mulder, W. J.; Grull, H.; Strijkers, G. J.; Nicolay, K. Influence of cell-internalization on relaxometric, optical and compositional properties of targeted paramagnetic quantum dot micelles. *Contrast Media Mol Imaging* **2011,** *6*, (2), 100-9.

23. Zhao, Y.; Schapotschnikow, P.; Skajaa, T.; Vlugt, T. J.; Mulder, W. J.; de Mello Donega, C.; Meijerink, A. Probing lipid coating dynamics of quantum dot core Micelles via Forster resonance energy transfer. *Small* **2014,** *10*, (6), 1163-70.

24. Zhao, Y.; van Rooy, I.; Hak, S.; Fay, F.; Tang, J.; Davies Cde, L.; Skobe, M.; Fisher, E. A.; Radu, A.; Fayad, Z. A.; de Mello Donega, C.; Meijerink, A.; Mulder, W. J. Near-infrared fluorescence energy transfer imaging of nanoparticle accumulation and dissociation kinetics in tumor-bearing mice. *ACS Nano* **2013,** *7*, (11), 10362-70.

25. Kim, D. E.; Kim, J. Y.; Sun, I. C.; Schellingerhout, D.; Lee, S. K.; Ahn, C. H.; Kwon, I. C.; Kim, K. Hyperacute direct thrombus imaging using computed tomography and gold nanoparticles. *Ann Neurol* **2013,** *73*, (5), 617-25.

26. Schmitz, S. A.; Winterhalter, S.; Schiffler, S.; Gust, R.; Wagner, S.; Kresse, M.; Coupland, S. E.; Semmler, W.; Wolf, K. J. USPIO-enhanced direct MR imaging of thrombus: preclinical evaluation in rabbits. *Radiology* **2001,** *221*, (1), 237-43.

27. Jansen, C. H.; Perera, D.; Makowski, M. R.; Wiethoff, A. J.; Phinikaridou, A.; Razavi, R. M.; Marber, M. S.; Greil, G. F.; Nagel, E.; Maintz, D.; Redwood, S.; Botnar, R. M. Detection of intracoronary thrombus by magnetic resonance imaging in patients with acute myocardial infarction. *Circulation* **2011,** *124*, (4), 416-24.

28. van Bochove, G. S.; Sanders, H. M. H. F.; de Smet, M.; Keizer, H. M.; Mulder, W. J. M.; Krams, R.; Strijkers, G. J.; Nicolay, K. Molecular MR Imaging of Collagen in Mouse Atherosclerosis by Using Paramagnetic CNA35 Micelles. *Eur J Inorg Chem* **2012**, (12), 2115-2125.

29. Mulder, W. J.; Castermans, K.; van Beijnum, J. R.; Oude Egbrink, M. G.; Chin, P. T.; Fayad, Z. A.; Lowik, C. W.; Kaijzel, E. L.; Que, I.; Storm, G.; Strijkers, G. J.; Griffioen, A. W.; Nicolay, K. Molecular imaging of tumor angiogenesis using alphavbeta3-integrin targeted multimodal quantum dots. *Angiogenesis* **2009,** *12*, (1), 17-24.

30. Coolen, B. F.; Simonis, F. F.; Geelen, T.; Moonen, R. P.; Arslan, F.; Paulis, L. E.; Nicolay, K.; Strijkers, G. J. Quantitative T mapping of the mouse heart by segmented MLEV phase-cycled T preparation. *Magn Reson Med* **2013,** *72*, (2), 409-17.

Chapter 7

^{89}Zr- and Fe-labeled polymeric micelles for dual modality (molecular) PET & T_1-weighted MR imaging

Abstract

Simultaneous dual modality positron emission tomography (PET) and magnetic resonance imaging (MRI) combines the high sensitivity of PET and the excellent soft tissue contrast of MRI. Dual modal PET/MR imaging probes allow quantification and full body screening of probe uptake using PET and characterization of this uptake in high resolution using MRI. In this study, we developed an ^{89}Zr- and Fe^{3+}-labeled micelle nanoplatform (^{89}Zr/Fe-DFO-micelles) for dual modality PET/MR imaging. The nanoplatform consists of self-assembling amphiphilic diblock copolymers which are functionalized with ^{89}Zr-deferoxamine (^{89}Zr-DFO) and Fe^{3+}-deferoxamine (Fe-DFO) for PET and MR purposes, respectively. ^{89}Zr displays favorable PET imaging characteristics with a 3.3 days half-life suitable for imaging long circulating nanoparticles. The nanoparticles were modified with Fe-DFO as MR T_1-contrast label instead of commonly used Gd^{3+}-based chelates. This approach avoids any potential Gd-related toxicity that may result from nanoparticle uptake in liver and spleen, thus significantly increasing the translational potential. We demonstrated the suitability of ^{89}Zr/Fe-DFO-micelles for bimodal PET/MRI in two lines of experiments. The first line of experiments entailed enhanced permeability and retention (EPR)-based tumor PET/MR imaging using (nontargeted) ^{89}Zr/Fe-DFO-micelles. The micelles showed high tumor-to-blood (10.3 ± 3.6) and tumor-to-muscle (15.3 ± 8.1) ratios at 48 h post injection. The obtained *in vivo* PET images clearly delineated tumor tissue and showed good correspondence with *ex vivo* biodistribution results. Furthermore, *in vivo* MRI allowed probing the intratumoral distribution of the ^{89}Zr/Fe-DFO-micelles at high resolution. Hence, (nontargeted) ^{89}Zr/Fe-DFO-micelles hold great potential for noninvasive dual modality imaging in oncology. The second line of experiments encompassed fibrin-specific molecular PET/MRI using fibrin-binding peptide (FibPep) conjugated ^{89}Zr/Fe-DFO-micelles. FibPep-^{89}Zr/Fe-DFO-micelles bound specifically to blood clots *in vitro* and this specific binding could be visualized by PET and MR imaging. These findings encourage further studies of the FibPep-^{89}Zr/Fe-DFO-micelle nanoplatform for *in vivo* PET/MRI of fibrin deposition in cardiovascular and neurological diseases, as well as in oncology. In conclusion, we developed a nanoparticulate platform with high translational potential that allows both EPR-based and target-specific PET/MRI, and, furthermore, holds great potential for PET/MR image guided drug delivery.

This chapter is based on:

Starmans, L. W.;* Hummelink, M. A.;* Rossin, R.; Kneepkens, E. C.; Lamerichs, R.; Donato, K.; Moonen, R. P.; Nicolay, K.; Grull, H. ^{89}Zr- and Fe-labeled polymeric micelles for dual modality (molecular) PET and T_1-weighted MR imaging. *In preparation*. *Auhors contributed equally.

7.1 Introduction

Nanomedicine, the application of nanotechnology to healthcare, is a rapidly evolving field showing great promise to improve current treatment regimes.[1] This effort resulted over the last decade in the approval of several nanomedicine formulations.[2, 3] While most approved formulations are based on drug-loaded liposomes, a plethora of nanoparticles (NP) were explored in preclinical research such as micelles,[4-6] polymersomes,[7, 8] or capsosomes[9] to name only a few examples. New theranostic approaches are based on nanoparticles that can carry a drug payload and also provide an imaging functionality that allows noninvasive imaging of the biodistribution or drug delivery process.[10-12]

Amphiphilic diblock copolymers represent a relatively new class of building blocks for drug carriers or imaging vehicles that self-assemble into different morphologies and structures such as micelles, polymersomes or vesicles, depending on the properties and size of the hydrophobic and hydrophilic part.[7, 13, 14] Synthetic amphiphilic diblock copolymers display lipid-like behavior, but have a much higher molecular weight than lipids, which can be exploited to fine-tune drug retention or size. Furthermore, they allow easy incorporation of other functionalities such as reactive side groups.[13, 15] The use of different block copolymers provides a toolbox approach to nanoparticles such as micelles, where for instance a hydrophobic drug can be incorporated in the core and imaging labels and targeting moieties such as antibodies and peptides can be conjugated to the outer shell.[4, 16-18]

In this context, we designed a novel, ^{89}Zr- and Fe^{3+}-labeled polymeric micelle-nanoplatform (^{89}Zr/Fe-DFO-micelles) for positron emission tomography (PET) and magnetic resonance imaging (MRI). This dual modal PET/MR imaging probe allows quantification and full body screening of probe uptake using PET and characterization of this uptake in high resolution using MRI. The micelle is formed via self-assembly of a mixture of polybutadiene-b-polyethyleneoxide (PBD-b-PEO) and polybutadiene-b-polyacrylicacid (PBD-b-PAA) polymers, and the acrylic acid (AA) residues are subsequently employed to functionalize the micelles with ^{89}Zr-deferoxamine (^{89}Zr-DFO) and Fe^{3+}-deferoxamine (Fe-DFO) for PET and MRI purposes, respectively (Fig. 1). Deferoxamine (DFO) is a siderophore from the bacterium *Streptomyces pilosus* and is clinically approved as treatment for iron overload.[19] In addition, DFO has been frequently employed to chelate Fe- and Zr-ions for MR and PET imaging purposes.[20-23] Zirconium-89 displays favorable PET imaging characteristics (β^+ = 22.3%; $E_{ave}(\beta^+)$ = 396.9 keV; $R_{ave}(\beta^+)$ = 1.18 mm) and has a 3.3 days half-life suitable for imaging of long circulating nanoparticles.[24-26] We conjugated Fe-DFO to the micelles as MR T_1-contrast label instead of commonly used Gd-based chelates, as these two have similar T_1 properties in MRI.[20] This approach entirely avoids Gd-related toxicity effects such as *nephrogenic systemic fibrosis* (NSF),[27, 28] which may result from uptake of Gd-bearing nanoparticles in liver and spleen. Hence, an Fe-DFO-based strategy shows much higher potential for eventual clinical translation compared to other nanoparticulate approaches that employ Gd for MR contrast.

In this study, we developed a simple protocol for the synthesis of ^{89}Zr/Fe-DFO-micelles and we characterized the micelles extensively *in vitro.* Furthermore, we investigated the potential of the ^{89}Zr/Fe-DFO-micelles for *in vivo* PET/MR imaging. For the latter, two lines of experiments were pursued.

The first part of this chapter entails the study of (nontargeted) ^{89}Zr/Fe-DFO-micelles for PET/MRI in oncology. Tumors display enhanced permeability and retention (EPR) of large molecules and nanoparticles due to poorly aligned endothelial cells in angiogenic blood vessels and the lack of lymphatic drainage in tumors.[29-31] This EPR effect thus yields a means to deliver nanoparticles in significant amounts into tumor lesions. To determine the suitability of the nanoplatform for EPR-based tumor targeting, biodistribution profiles were obtained in LS174T tumor bearing mice at 6, 48 and 120 h post injection. In addition, the potential of the ^{89}Zr/Fe-DFO-micelles for noninvasive dual modal tumor imaging was investigated in an *in vivo* PET/MRI study in LS174T tumor bearing mice. Tumors were excised post PET/MR imaging and subsequently analyzed using autoradiography and histology to corroborate the *in vivo* PET/MR imaging results.

The second part of this chapter reports on the synthesis and *in vitro* characterization of fibrin-targeted ^{89}Zr/Fe-DFO-micelles for molecular PET/MR imaging of fibrin deposition. Deposition of fibrin plays an important role in cardiovascular, oncological and neurological disease processes,[32-40] and is thus a broadly applicable target for molecular imaging purposes. To this aim, the micelles were conjugated with the fibrin-binding peptide FibPep,[41-43] yielding fibrin-targeted FibPep-^{89}Zr/Fe-DFO-micelles. As negative control, ^{89}Zr/Fe-DFO-micelles were conjugated with scrambled peptides (NCFibPep), yielding NCFibPep-^{89}Zr/Fe-DFO-micelles. To gauge the potential of the FibPep-^{89}Zr/Fe-DFO-micelles for fibrin-specific molecular imaging, an *in vitro* thrombus-binding experiment was performed using the (NC)FibPep-^{89}Zr/Fe-DFO-micelles and the thrombus uptake was subsequently visualized using PET/MR imaging.

7.2 Results and Discussion: ^{89}Zr/Fe-DFO-micelles for EPR-based PET/MR tumor imaging

7.2.1 Synthesis and characterization

Polymeric micelles were synthesized by mixing the amphiphilic diblock copolymers PBD_{1800}-b-PEO_{4000} and PBD_{1000}-b-PAA_{2200} in a 2.7:1 molar ratio in tetrahydrofuran (THF), followed by evaporation to dryness. Micelles were subsequently obtained by rehydration of the polymeric film in phosphate buffered saline (PBS). DFO complexated with Fe was conjugated to the AA residues on the micelle surface via N-hydroxysulfosuccinimide (sulfo-NHS) and 1-ethyl-3-(3-dimethylaminopropyl) carbodiimide hydrochloride (EDC)-based conjugation chemistry, yielding Fe-DFO-micelles (Fig. 1). The excess of free DFO was removed via desalting columns and centrifugal filtration. MRI negative control micelles were synthesized similarly, with Al^{3+} instead of Fe^{3+}.

Inductively coupled plasma-optical emission spectroscopy (ICP-OES) measurements showed that approximately 15% of all AA residues were functionalized with Fe-DFO, yielding ca. 3000 Fe-DFO unites per micelle. The volume-weighted hydrodynamic diameter of a Fe-DFO-micelle, as determined by dynamic light scattering (DLS), was 25 nm (Fig. 2A). Figure 2B displays a representative cryogenic transmission electron microscopy (cryo-TEM) image of the micelle solution, showing that the diblocks self-assemble into star-like micelles which are mainly dispersed as single particles and which display a densely packed PBD core of 16 ± 3 nm. The size of the micelles agrees well with the expected size based

on the respective block copolymer dimensions.[44] The sub-50 nm hydrodynamic diameter of the micelles allows high tumor penetration, even in poorly permeable tumors,[45] and therefore the Fe-DFO-Micelles are well suited for EPR-based tumor-targeting strategies.

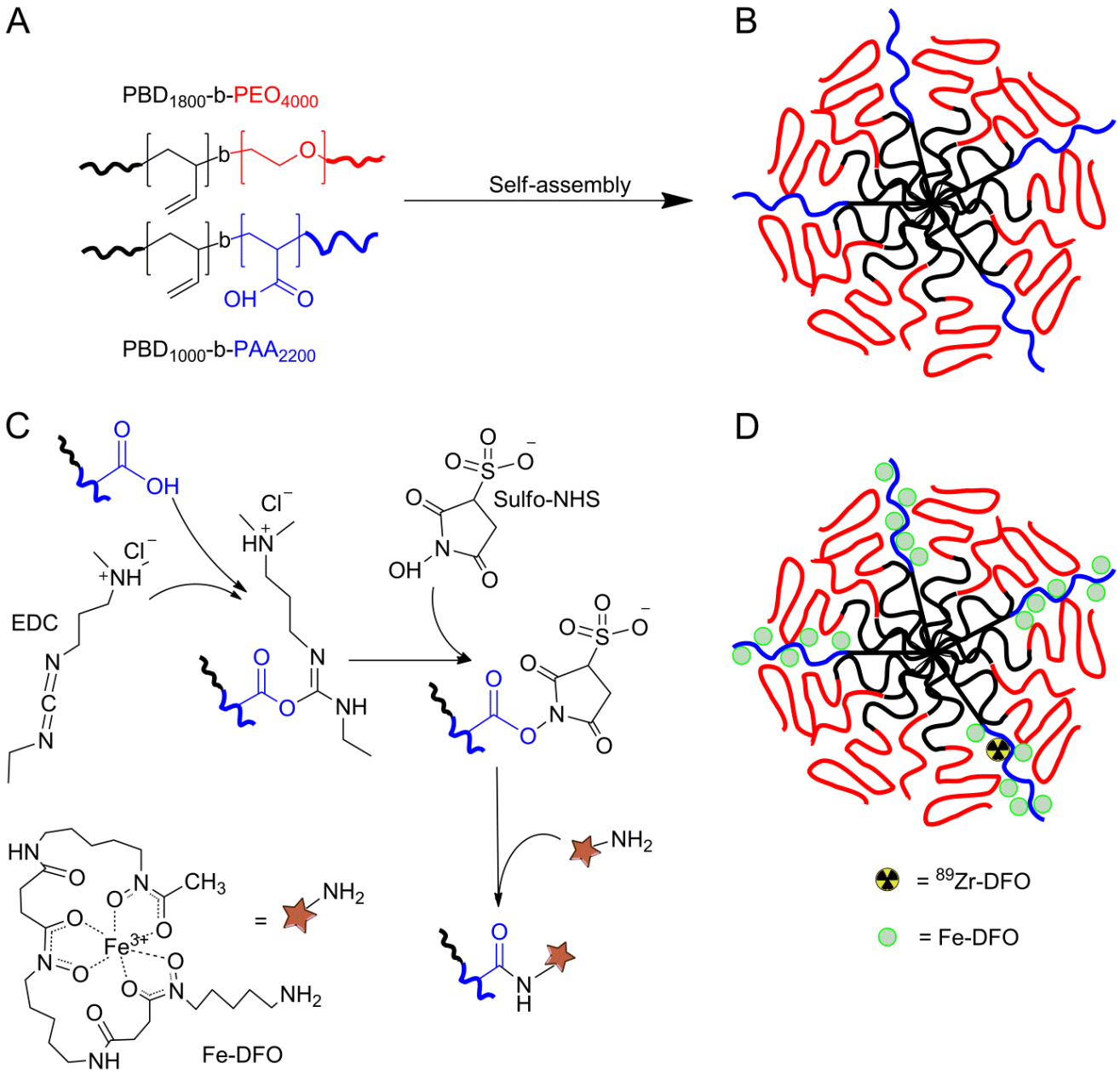

Figure 1. *Synthesis of self-assembled bimodal polymeric micelles (^{89}Zr/Fe-DFO-micelles). (A) Schematic structure of diblock copolymers PBD_{1800}-PEO_{4000} and PBD_{1000}-PAA_{2200}, which form (B) self-assembled polymeric micelles. (C) Conjugation of Fe-DFO to AA residues on the micelle surface via EDC- and sulfo-NHS-based chemistry. (D) Schematic structure of stealth bimodal polymeric micelles loaded with a radio (^{89}Zr) and paramagnetic (Fe^{3+}) label for PET and MR imaging purposes, respectively. Radiolabeling of the micelles is performed by adding ^{89}Zr-oxalic acid to the Fe-DFO-Micelles, yielding bimodal ^{89}Zr/Fe-DFO-micelles. MRI negative control particles were labeled with Al^{3+} instead of Fe^{3+}.*

The longitudinal (r_1) and transversal (r_2) relaxivities of the paramagnetic polymeric micelles were measured at 37 °C and 1.41 T. Relaxivity studies showed a longitudinal ionic relaxivity (r_1) of 2.7 $mM^{-1}s^{-1}$ and a transversal relaxivity (r_2) of 3.1 $mM^{-1}s^{-1}$ for the Fe-DFO-micelles. Since a micelle contains ca. 600 block copolymers, the longitudinal and transversal relaxivity per mM micelle was estimated to be 1620 and 1860 $mM^{-1}s^{-1}$, respectively. The low r_2 / r_1 ratio (1.1) indicates that the paramagnetic micelles are best suited for positive contrast T_1-weighted MRI. As large molecules and nanoparticles tend to tumble slower than small molecules and therefore have a larger rotational correlation time (τ_r), an increase in proton relaxivity would be expected upon conjugation of Fe-DFO to the polymeric micelles.[46, 47] However, the micelles cannot be seen as rigid spheres, since the diblock copolymer components of the micelles are quite dynamic and flexible. Therefore, the tumbling rate of the Fe-DFO moieties is still relatively high and consequently the τ_r relatively short, limiting the effect of macromolecular conjugation on the relaxivity (DFO without micelle conjugation showed r_1 = 2.2 $mM^{-1}s^{-1}$ and r_2 = 2.5 $mM^{-1}s^{-1}$). The longitudinal ionic relaxivity of the Fe-DFO-micelles is thus similar to that of commonly used Gd-based contrast agents such as Gd-DTPA (Magnevist®, 3.3 $mM^{-1}s^{-1}$) and Gd-DOTA (Dotarem®, 3.1 $mM^{-1}s^{-1}$) in water at 1.5 T and 37 °C.[48]

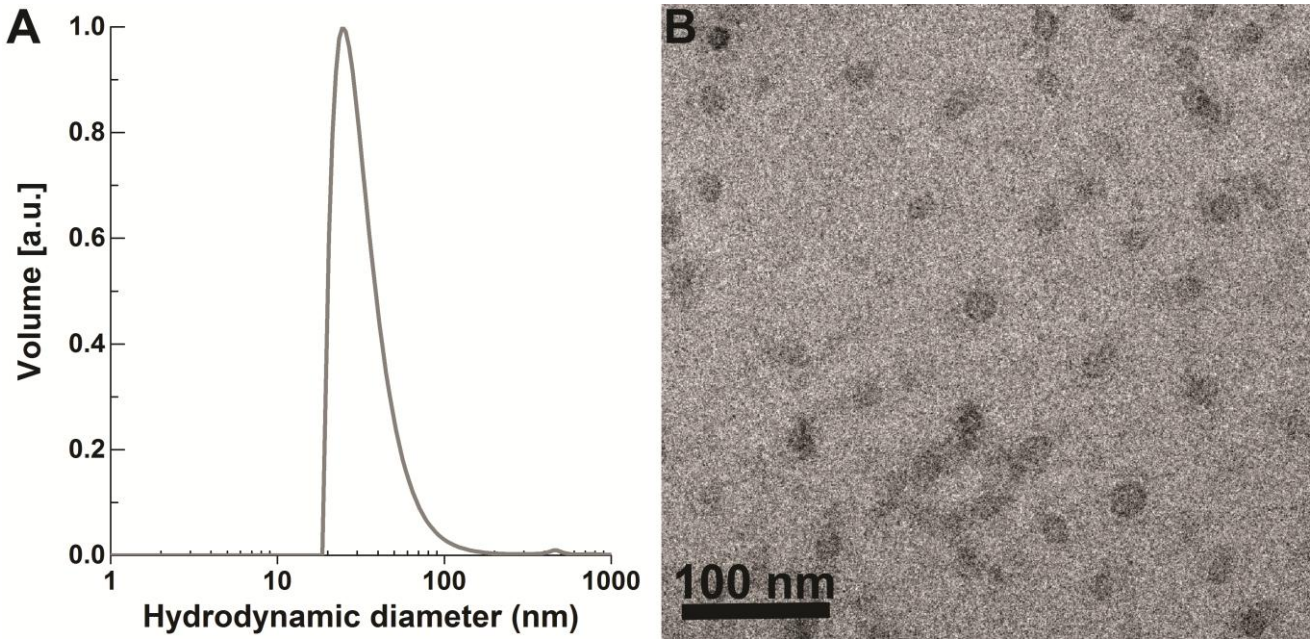

Figure 2. *(A) Volume-weighted size distribution profile of the Fe-DFO-polymeric micelles as determined by DLS. (B) Representative cryo-TEM image of the Fe-DFO-micelle solution.*

The paramagnetic micelles were successfully radiolabeled with the positron-emitter ^{89}Zr, yielding bimodal ^{89}Zr/Fe-DFO-micelles. Radiolabeling was performed following protocols developed by van Dongen and coworkers.[25, 26] Due to the high specific activity of ^{89}Zr (ca. 3 GBq/mg), a minute amount of non-Fe complexated DFO ligands on the micelle surface is sufficient for radiolabeling purposes. Radiochemical yield was 99.1 ± 0.5% (n=4) and a DTPA challenge was conducted to remove loosely

bound ^{89}Zr. Finally, the bimodal ^{89}Zr/Fe-DFO-micelles were purified through a desalting spin column and the resulting solution was concentrated. This radiolabeling procedure yields, depending on the chosen ratio of ^{89}Zr over PBD-PAA polymer, ca. one ^{89}Zr-DFO per 10 micelles. Incubation of ^{89}Zr/Fe-DFO-micelles in BALB/c mouse serum at 37 °C for seven days showed high radiochemical stability of the ^{89}Zr/Fe-DFO-micelles (>99%).

Subsequently, the ^{89}Zr/Fe-DFO-micelle and ^{89}Zr/Al-DFO-micelle solutions were diluted in human serum for further characterization *in vitro* using PET and T_1-weighted MR imaging (3 T). In Figure 3A, the ^{89}Zr/Fe-DFO-micelle samples show positive MR contrast, which is correlated to Fe concentration, while the ^{89}Zr/Al-DFO-micelle sample provides similar signal intensity as the reference serum sample. This demonstrates that ^{89}Zr/Fe-DFO-micelles can be successfully imaged with T_1-weighted MRI in a concentration range of 0.2 – 5 mM Fe. It also confirms the suitability of the ^{89}Zr/Al-DFO-micelles as MR negative control. PET imaging was performed using a small-animal PET scanner. Signal intensity decreases with a reduction in ^{89}Zr-activity and ^{89}Zr/Al-DFO-micelles yield similar signal as the ^{89}Zr/Fe-DFO-micelles (Fig. 3B). Note that the apparent relative low sensitivity of ^{89}Zr/Fe-DFO-micelle PET versus MRI in Figure 3 is a function of the ^{89}Zr- over Fe-labeling ratio, which can be changed according to preference during the radiolabeling procedure. The ^{89}Zr- over Fe-labeling ratio in this particular *in vitro* experiment was set approximately a factor 5 lower than for subsequent *in vivo* imaging experiments in order to cover a significant part of the ^{89}Zr/Fe-DFO-micelles MRI sensitivity range in this *in vitro* experiment without having to (unnecessarily) increase radiation exposure.

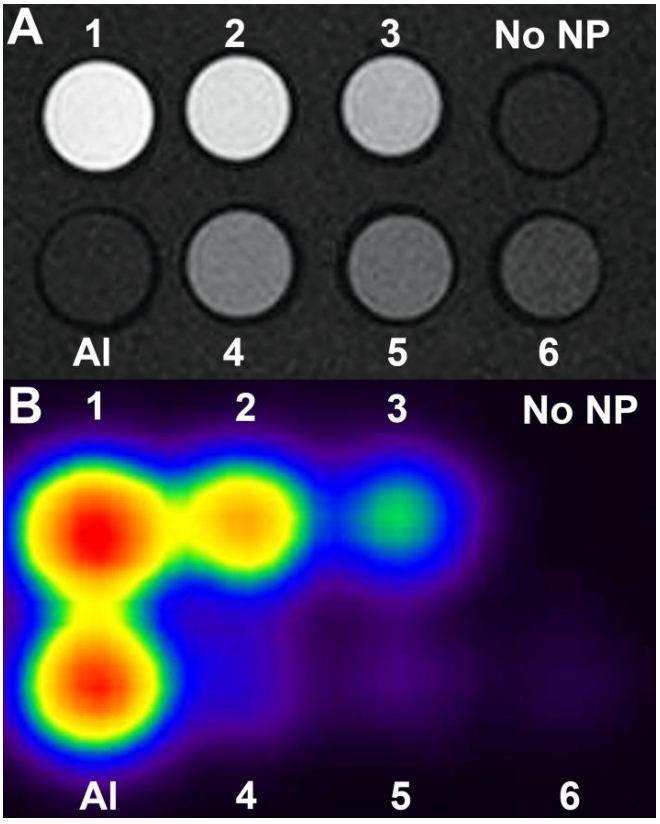

Figure 3. *In vitro PET/MRI of ^{89}Zr/Fe-DFO-micelles (1-6) and ^{89}Zr/Al-DFO-micelles (Al) in human serum, as well as human serum without nanoparticles (No NP). 1-6: [Fe] = 5, 3, 1.5, 0.8, 0.4, 0.2 mM; ^{89}Zr = 1, 0.6, 0.3, 0.14, 0.06, 0.03 MBq, respectively. Al: [Al] = 4 mM; ^{89}Zr = 1 MBq. (A) T_1-weighted MRI (3 T): ^{89}Zr/Fe-DFO-micelles show positive MR contrast, whereas ^{89}Zr/Al-DFO-micelles yield no MR contrast. (B) PET imaging: signal intensity scales with ^{89}Zr-activity.*

7.2.2 Blood kinetics and biodistribution

Pharmacokinetic profiles were assessed in non-tumor bearing BALB/c nu/nu mice. The blood circulation of the ^{89}Zr/Fe-DFO-micelles was measured at selected time-points up to 48 h. Subsequently, the mice were euthanized and a final blood sample was taken. The ^{89}Zr/Fe-DFO-micelles were well tolerated by the mice and displayed a biphasic elimination from the circulation, with an α half-life of 1 h (46%) and a β half-life of 9 h (Fig. 4A). After 24 h, 6.6 ± 1.9% injected dose per gram (% ID/g) of polymeric micelles was still circulating in blood. ^{89}Zr/Al-DFO-micelles showed similar blood elimination with respect to ^{89}Zr/Fe-DFO-micelles (Fig. 4A).

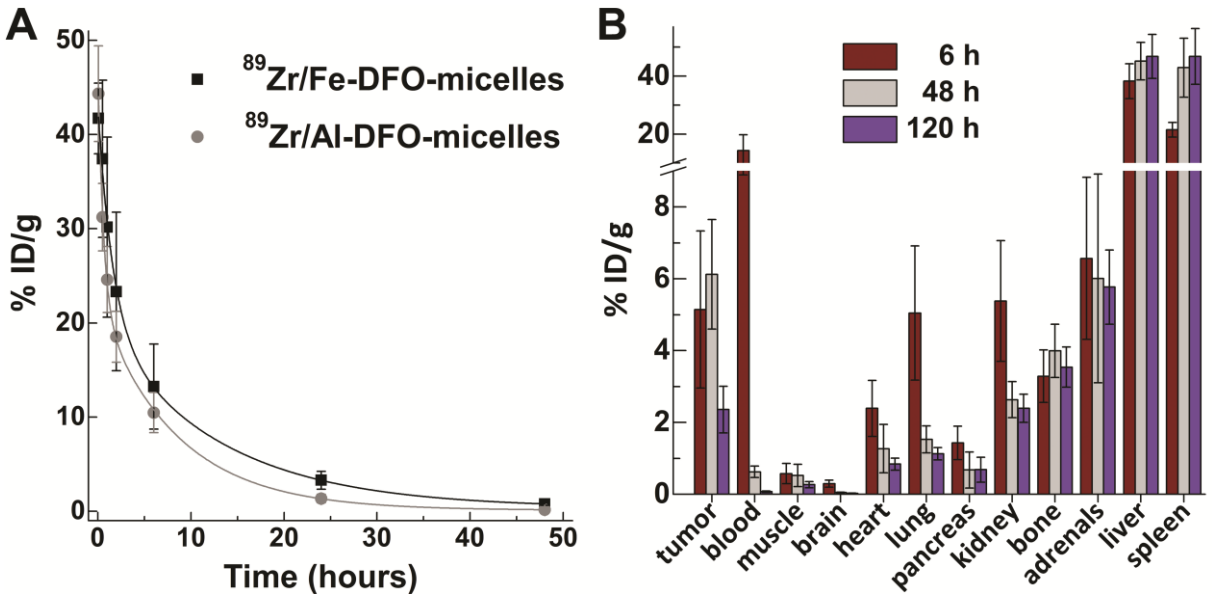

Figure 4. *(A) Blood clearance profiles of ^{89}Zr/Fe- and ^{89}Zr/Al-DFO-micelles in healthy mice. Solid lines are bi-exponential fits. (B) Biodistribution of ^{89}Zr/Fe-DFO-micelles at 6, 48 and 120 h post injection in LS174T tumor bearing mice. Data represents the mean % injected dose per gram (% ID/g) ± standard deviation (SD).*

Next, the ^{89}Zr/Fe-DFO-micelles were injected intravenously in LS174T tumor bearing mice to provide insight on EPR-based tumor uptake of the nanoparticles. The mice were divided in three groups and euthanized at 6, 48 and 120 h post injection. At 6 h, 14.4 ± 5.4% ID/g of ^{89}Zr/Fe-DFO-micelles was still present in the circulation and this value decreased to 0.6 ± 0.2% ID/g at two days post injection. The tumor uptake was 5.2 ± 2.2% ID/g after 6 h, 6.1 ± 1.5% ID/g after 48 h and 2.9 ± 0.2% ID/g after 120 h. The apparent decrease in tumor uptake at 120 h post injection was due to fast growth of the LS174T tumors, effectively diluting the concentration of already accumulated ^{89}Zr/Fe-DFO-micelles. In fact, a comparison of the absolute tumor uptake at 120 h (1.4 ± 0.6% ID/tumor) with the absolute tumor uptake at 48 h (1.4 ± 0.7% ID/tumor) shows no significant decrease in radioactivity, hence no significant nanoparticle wash-out from the tumor was observed. High tumor-to-blood (10.3 ± 3.6) and tumor-to-muscle (15.3 ± 8.1) ratios were achieved at 48 h post injection (Table 1), indicating that 48 h post

injection is a suitable time point for PET/MR imaging of EPR-based tumor uptake of ^{89}Zr/Fe-DFO-micelles in mice. Such a relatively long delay between injection and image acquisition necessitates a MR negative control strategy to assess ^{89}Zr/Fe-DFO-micelle induced MR contrast differences, since the commonly employed procedure of acquiring pre- and post-contrast MR images is not suited for the above protocol. This is due to the significant growth of the subcutaneous LS174T tumors within the 2 day delay time, rendering pre-contrast images obsolete. Employing ^{89}Zr/Al-DFO-micelles as negative control nanoparticles allows assessment of native MR tumor contrast at 48 h post injection in a control group, while still providing the ability to characterize the tumor with respect to EPR-based nanoparticle uptake using PET.

Table 1. *Tumor-to-organ ratios at 6, 48 and 120 h post injection of ^{89}Zr/Fe-DFO-micelles as determined by γ-counting.*

	6 h	**48 h**	**120 h**
Blood	0.4 ± 0.1	10.3 ± 3.6	35.7 ± 12.0
Muscle	10.9 ± 6.2	15.3 ± 8.1	9.2 ± 2.9
Brain	17.9 ± 5.3	99.8 ± 4.0	85.3 ± 24.6
Heart	2.3 ± 1.1	6.0 ± 2.9	3.0 ± 1.1
Lung	1.1 ± 0.4	4.1 ± 1.0	2.1 ± 0.6
Pancreas	3.9 ± 1.9	12.3 ± 6.6	4.2 ± 2.0
Kidney	1.0 ± 0.3	2.3 ± 0.3	1.0 ± 0.3
Bone	1.6 ± 0.7	1.5 ± 0.2	0.7 ± 0.2
Adrenals	0.9 ± 0.5	1.3 ± 0.8	0.4 ± 0.1
Liver	0.1 ± 0.1	0.1 ± 0.1	0.1 ± 0.0
Spleen	0.2 ± 0.1	0.1 ± 0.0	0.1 ± 0.0

Besides high tumor uptake, the polymeric micelles showed predominant accumulation in the liver and spleen. These results were consistent with the expected clearance via the mononuclear phagocyte system (MPS) as the micelle size (25 nm hydrodynamic diameter) prohibits glomerular filtration through the kidneys. In addition, the adrenals (6.0 ± 2.9% ID/g) showed increased activity and this phenomenon was previously also observed for other nanoparticulate agents.[49] Bone uptake (4.0 ± 0.7% ID/g) might indicate (partial) release of ^{89}Zr in circulation, as free ^{89}Zr is known to deposit in the mineralized constituents of the bone, where it is assumed to be chelated by phosphate constituents and epiphysis.[50] However, in humans injected with ^{89}Zr-DFO-labeled antibodies minimal ^{89}Zr bone-uptake is observed.[51] The faster metabolism of mice together with their less specific peptidases involving rapid degradation of ^{89}Zr-DFO are likely the root cause for the high ^{89}Zr bone uptake in mice as observed in both this work as well as in studies by others which investigated ^{89}Zr-DFO-labeled antibodies.[50] An alternative explanation for the observed bone uptake is accumulation of the ^{89}Zr/Fe-DFO-micelles in the bone marrow, which is part of the MPS and is capable of removing nanoparticles from the systemic circulation.[52]

7.2.3 In vivo PET / MR imaging

Tumor bearing mice were administered with ^{89}Zr/Fe-DFO-micelles (n=5) and ^{89}Zr/Al-DFO-micelles (n=3) and *in vivo* PET/MR imaging was performed at 48 h post micelle injection. The mice were subsequently euthanized, tumors were excised and autoradiography and histology of tumor sections was performed. Figure 5 displays a representative full-body PET image, showing clear tumor delineation. Furthermore, liver, spleen and lymph nodes showed high signal in the PET images. Lymph node uptake is a known feature for (radiolabeled, polymeric) nanoparticles.[53]

Figure 6A-C show detailed PET images of cross-sections throughout the limbs, revealing significant ^{89}Zr/Fe-DFO-micelle and ^{89}Zr/Al-DFO-micelle tumor uptake. Figure 6D-F display transverse MRI cross-sections throughout the limbs. The insert shows the corresponding T_1-map of the tumor. As can be seen on these MR images, the ^{89}Zr/Fe-DFO-micelle accumulation in the tumor seems inhomogeneous, and occurs in larger sized tumors along the tumor rim. The *ex vivo* autoradiography results (Fig. 6G-I) are in agreement with the *in vivo* imaging findings and show that the nanoparticles mainly accumulate in the tumor periphery. Yuan et al. demonstrated that the vascular pore size of the LS174T tumor could be as large as 400-600 nm, which provides an entry point for the ^{89}Zr/Fe-DFO-micelles to extravasate into the tumor interstitium.[54] The slow venous return in tumor tissue combined with poor lymphatic drainage ensures nanoparticle retention in the tumor.[29] Even though the ^{89}Zr/Fe-DFO-micelles have an ideal size to penetrate into tumors,[45] a stronger accumulation of the micelles in the periphery versus the core of the tumor was observed. This may be attributed to better perfusion of the tumor periphery and higher presence of necrosis in the tumor center.[5, 55, 56]

To quantify the difference in tumor contrast enhancement between ^{89}Zr/Fe-DFO-micelles and MRI negative control ^{89}Zr/Al-DFO-micelles, histograms of the T_1-maps were analyzed (Fig. 7A). Significant difference was found for a selection of bins, all with T_1-values shorter than 750 ms. The overall percentage of T_1-values shorter than 750 ms in tumors of mice which were injected with ^{89}Zr/Fe-DFO-micelles (12.3 ± 8.2%) was significantly higher than that of the negative MRI control ^{89}Zr/Al-DFO-micelles (3.2 ± 0.5% , $p < 0.05$), illustrating the efficacy of the ^{89}Zr/Fe-DFO-micelles to generate positive MR tumor contrast *in vivo*. Figure 7B presents the calculated PET standardized uptake values (SUVs) for tumor, liver, lymph nodes and muscle. ^{89}Zr/Fe- and ^{89}Zr/Al-DFO-micelles showed similar tumor uptake (1.27 ± 0.31 and 0.98 ± 0.24 SUV, respectively). The ^{89}Zr/Fe-DFO-micelle SUV for muscle and liver was 0.12 ± 0.03 and 6.93 ± 1.05, respectively.

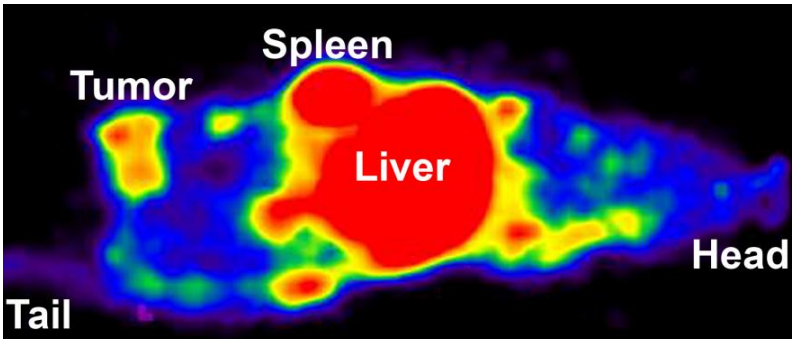

Figure 5. *Typical in vivo full-body PET coronal image at 48 h post ^{89}Zr/Fe-DFO-micelles injection, revealing significant nanoparticle accumulation in tumor. In addition, liver and spleen showed high PET signal.*

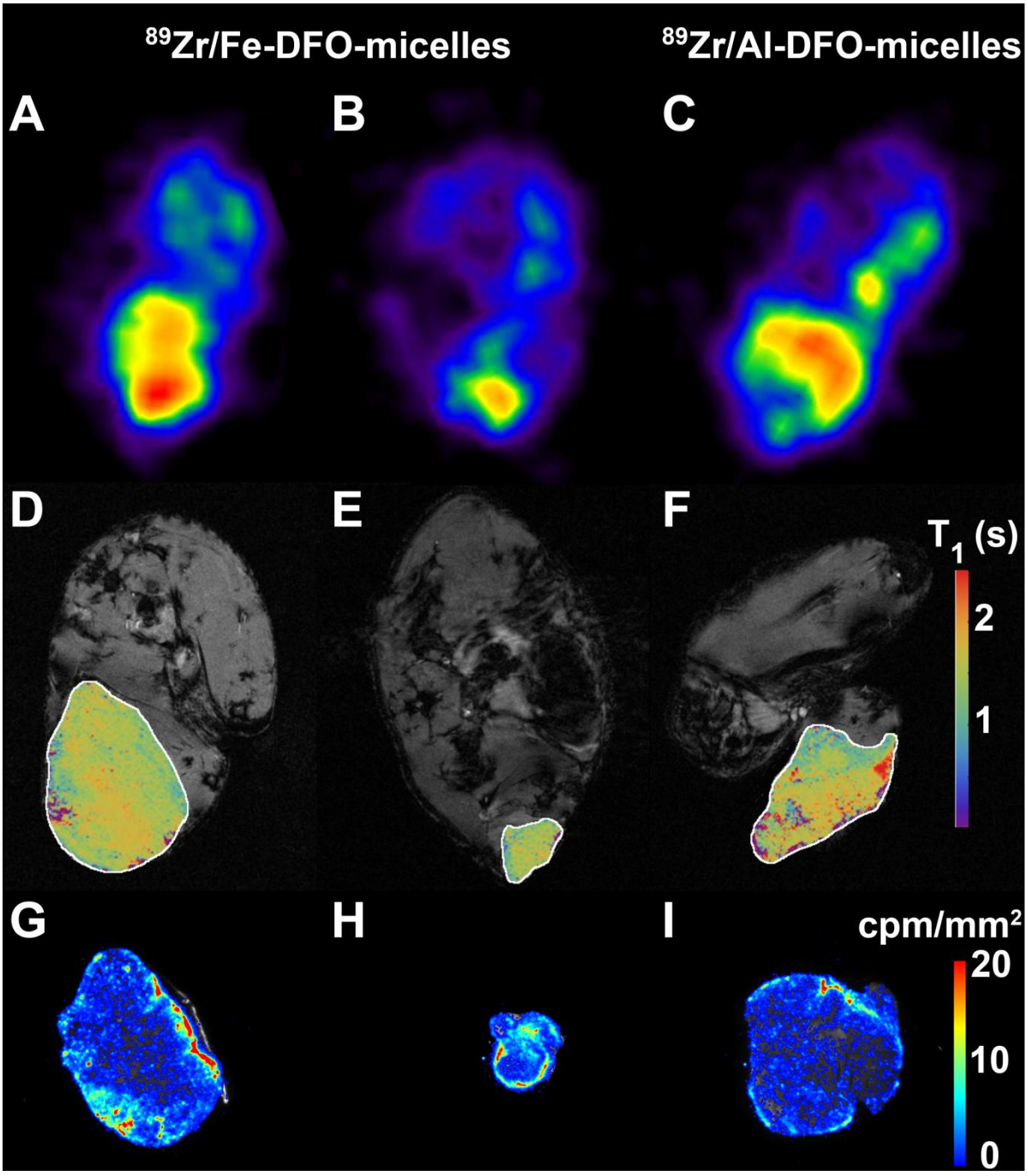

Figure 6. *Visualization of the intratumoral accumulation of ^{89}Zr/Fe- and ^{89}Zr/Al-DFO-micelles in tumor bearing mice using PET/MRI and autoradiography. Typical in vivo PET images of cross-sections throughout the limbs with predominant (A-B) ^{89}Zr/Fe-DFO-micelles and (C) ^{89}Zr/Al-DFO-micelles tumor uptake. The middle row shows T_1-weighted anatomical MR images (3 T) with quantitative T_1-map overlay (D-F) providing insight in the intratumoral distribution of the ^{89}Zr/Fe-DFO-micelles, displaying inhomogeneous intratumoral probe distribution, with lower uptake in the core versus the periphery. The bottom row shows representative ex vivo autoradiography images, displaying lower uptake of (G-H) ^{89}Zr/Fe-DFO-micelles and (I) ^{89}Zr/Al-DFO-micelles in the core of the tumor with respect to the tumor periphery.*

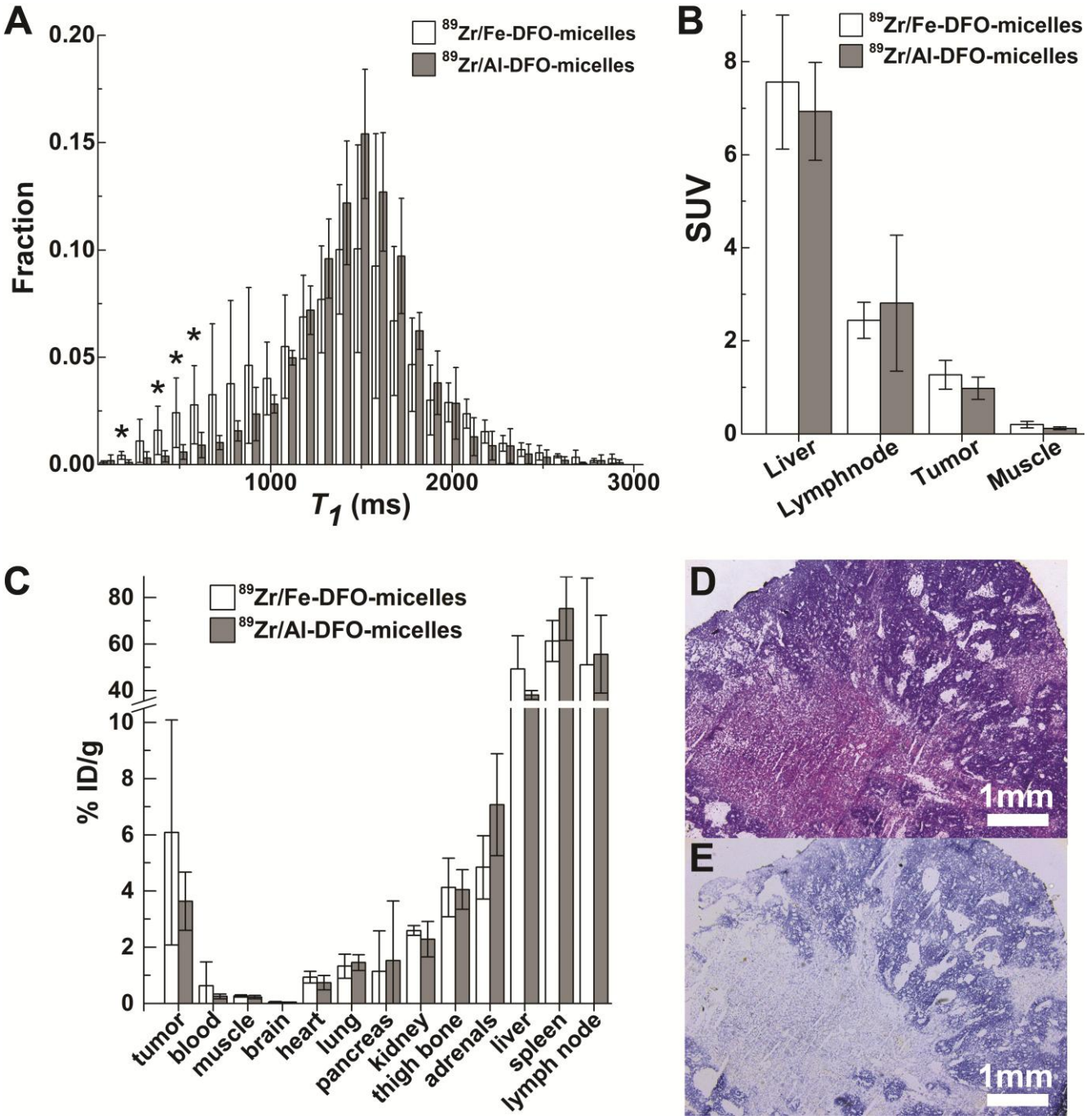

Figure 7. *(A) Histogram representation of tumoral tissue T_1-values of mice injected with ^{89}Zr/Fe- or ^{89}Zr/Al-DFO-micelles. * indicates significant difference ($p < 0.05$) between corresponding bins of the ^{89}Zr/Fe- and ^{89}Zr/Al-DFO-micelles groups. (B) Standardized uptake values (SUV) of ^{89}Zr/Fe- and ^{89}Zr/Al-DFO-micelles. (C) Biodistribution of ^{89}Zr/Fe-DFO-micelles and ^{89}Zr/Al-DFO-micelles in LS174T human colon carcinoma-bearing mice after PET/MR imaging (ca. 48 h post injection) using γ-counting. Data represents mean ± SD. Representative (D) H&E and (E) NADH-diaphorase-stained images of tumor tissue obtained 48 h post injection of ^{89}Zr/Fe-DFO-micelles.*

Figure 7C shows the obtained *ex vivo* biodistribution profiles, displaying tumor-to-muscle ratios of 22.9 (^{89}Zr/Fe-DFO-micelles) and 16.0 (^{89}Zr/Al-DFO-micelles). The MR negative control ^{89}Zr/Al-DFO-micelles showed similar biodistribution profiles with respect to the ^{89}Zr/Fe-DFO-micelles, confirming the validity of the ^{89}Zr/Al-DFO-micelles as negative control. Nanoparticle tumor accumulation inversely correlated with the size of the tumors. In the group of mice that received ^{89}Zr/Fe-DFO-micelles, the smallest tumors (n=3, sizes 48, 50, 64 mm^3) show an averaged uptake of 8.54 ± 3.07% ID/g, whereas the larger tumors (n=2, sizes 269, 616 mm^3) displayed a lower uptake of 2.70 and 2.10% ID/g, respectively. For large tumors, the well perfused periphery represents a smaller fraction of total tumor volume with respect to smaller tumors, which likely leads to a lower uptake per gram for the larger tumors.

The combined PET, MR and autoradiography results provide evidence that the vast majority of the nanoparticles did not reach the center of the tumor. Haematoxylin and eosin (H&E) stained tumor sections showed tumor heterogeneity (Fig. 7D). The periphery of the tumor reflects a high density of nuclei, whereas the core is less dense. NADH-diaphorase stained sections displayed areas with little cell viability in the center of the tumor (Fig. 7E), suggesting the presence of a necrotic core.

In summary, the bimodal polymeric micelle (^{89}Zr/Fe-DFO-micelles) nanoplatform developed in this study holds great potential for noninvasive dual modality EPR-based imaging of tumors, tumor characterization or staging. The synthesized contrast agent allowed to detect tumor lesions in a whole body fashion using PET and to investigate these lesions in high resolution using MRI, yielding additional insights regarding intratumoral distribution of the nanoparticles. These findings were subsequently confirmed by *ex vivo* autoradiography measurements and histology.

7.3 Results and Discussion: FibPep-^{89}Zr/Fe-DFO-micelles for molecular PET/MR imaging of fibrin deposition

7.3.1 Synthesis and characterization

PBD-PAA/PBD-PEO polymeric micelles were synthesized using thin film hydration, as described in the previous section. Subsequently, the acrylic acid groups were coupled to Fe-DFO and fibrin-binding peptides (FibPep) or negative control peptides (NCFibPep) via EDC-based conjugation techniques. Finally, the fibrin-targeted and negative control micelles were labeled with ^{89}Zr, yielding bimodal fibrin-targeted FibPep-^{89}Zr/Fe-DFO-micelles (Fig. 8A) suitable for molecular PET/MRI of fibrin deposition and their corresponding negative control nanoparticles (NCFibPep-^{89}Zr/Fe-DFO-micelles).

DLS measurements showed a hydrodynamic diameter of 33 nm for both FibPep- and NCFibPep-Fe-DFO-micelles (Fig. 8B). Figure 8C-D shows representative cryo-TEM images obtained for FibPep- and NCFibPep-Fe-DFO micelles, displaying that the micelles were mainly dispersed as single particles. Proton relaxometry measurements (1.41 T; 37 °C) showed a longitudinal ionic relaxivity (r_1) of 2.4 and 2.5 mM^{-1}s^1 and a transversal relaxivity of 2.8 and 2.9 mM^{-1}s^{-1} for the FibPep- and the NCFibPep-Fe-DFO-micelles, respectively. The radiochemical purity of the (NC)FibPep-^{89}Zr/Fe-DFO-micelles was > 98%. Hence, FibPep- and NCFibPep-^{89}Zr/Fe-DFO-micelles show similar characteristics with respect to size,

relaxivity and radiochemical purity, and these properties match the material characteristics observed for the non-peptide conjugated micelles described in the previous section.

7.3.2 Fibrin-specific PET/MR imaging of thrombi in vitro

To evaluate the potency of the ^{89}Zr/Fe-DFO-Micelle nanoplatform for molecular imaging purposes, an *in vitro* blood clot targeting assay was performed using the fibrin-binding FibPep-^{89}Zr/Fe-DFO-micelles and negative control NCFibPep-^{89}Zr/Fe-DFO-micelles. Blood clots were prepared by incubating a mixture of citrated human blood plasma, human tissue factor and calcium chloride. Next, clots were washed and subsequently incubated with either FibPep- or NCFibPep-^{89}Zr/Fe-DFO-micelles (n=4 per preparation). After 1 h of incubation, clots were washed three times and then subjected to PET and MR imaging measurements. Finally, ^{89}Zr clot uptake was determined using a dose calibrator, and Fe clot content was measured using inductively coupled plasma-mass spectrometry (ICP-MS).

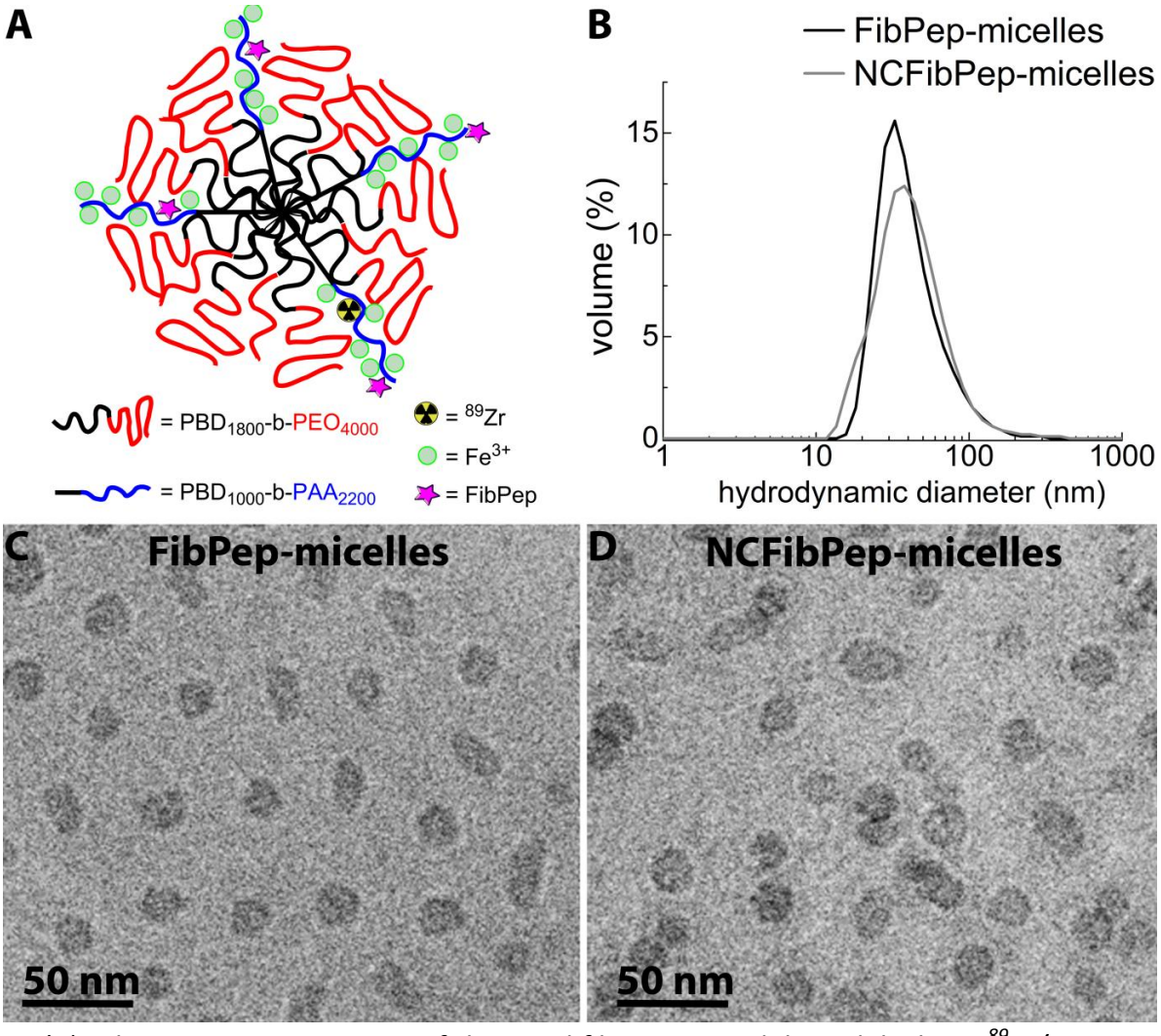

Figure 8. *(A) Schematic representation of the novel fibrin-targeted, bimodal FibPep-^{89}Zr/Fe-DFO-micelle nanoplatform. (B) Dynamic light scattering analysis of the FibPep- and NCFibPep-Fe-DFO-micelles. (C-D) Cryo-TEM images of (C) FibPep-Fe-DFO-micelles and (D) NCFibPep-Fe-DFO-micelles.*

Figure 9A shows the acquired PET image of the clots, displaying clear signal increase for FibPep-^{89}Zr/Fe-DFO-micelles incubated clots with respect to the clots which were incubated with negative control micelles, which indicates fibrin-specific clot binding of the FibPep-^{89}Zr/Fe-DFO-micelles. In addition, the obtained T_1-weighted MR image displays increased positive contrast on the clot surface for the FibPep-^{89}Zr/Fe-DFO-micelle incubated clots in comparison to the clots incubated with NCFibPep-^{89}Zr/Fe-DFO-micelles (Fig. 9B). Dose calibrator and ICP-MS measurements showed that FibPep-^{89}Zr/Fe-DFO-micelles displayed a circa twofold increase in clot binding with respect to the negative control micelles (4.7 ± 0.4% and 2.4 ± 0.4% ^{89}Zr-dose, 0.11 ± 0.02 and 0.07 ± 0.00 µg Fe, respectively; $p < 0.01$; Fig. 9C-D), confirming the PET/MR imaging findings.

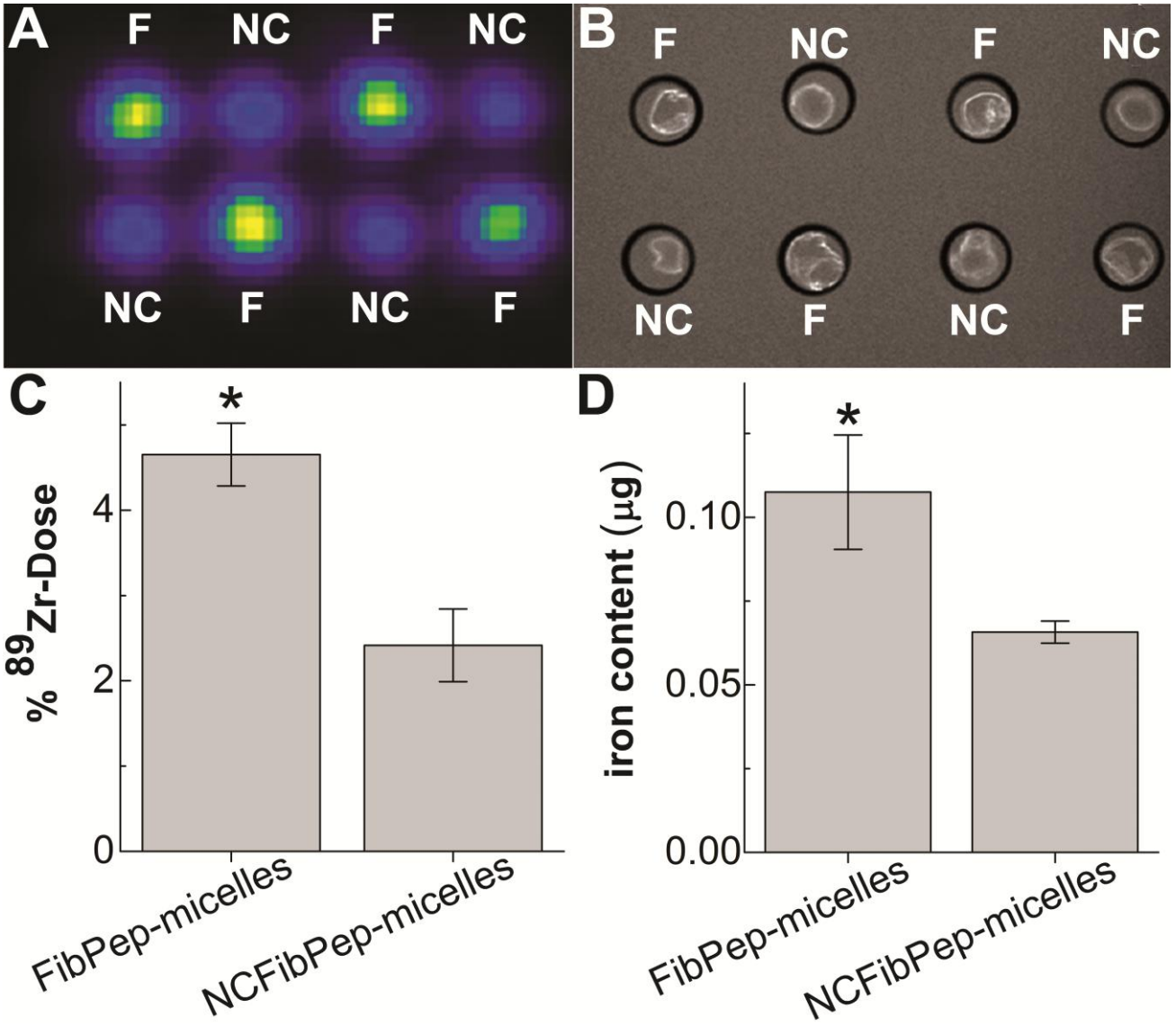

Figure 9. *(A) PET and (B) T_1-weighted MR images (9.4 T) of human blood clots incubated with fibrin-binding FibPep-^{89}Zr/Fe-DFO-micelles (F) and negative control NCFibPep-^{89}Zr/Fe-DFO-micelles (NC). (C) ^{89}Zr clot uptake expressed in percentage of incubated dose and (D) Fe clot content as determined with ICP-MS. * $p < 0.01$.*

Hence, these data underline the potential of the FibPep-^{89}Zr/Fe-DFO-Micelle nanoplatform for fibrin-specific molecular PET/MRI. In addition, these findings illustrate the benefits of combining PET and MRI for molecular imaging purposes, as MRI clearly displayed that the micelles mainly sequestered on the blood clot surface, a feature that could not be observed with PET due to the relative low spatial resolution.

7.4 General discussion

This study reports on a novel ^{89}Zr- and Fe-labeled polymeric micelle nanoplatform (^{89}Zr/Fe-DFO-micelles) for bimodal PET/MR imaging. To illustrate the potential of the ^{89}Zr/Fe-DFO-micelles as nanoplatform for PET/MRI, two lines of experiments were pursued. In the first line of experiments, (nontargeted) ^{89}Zr/Fe-DFO-micelles were employed for EPR-based tumor imaging using PET/MRI. PET/MR imaging at 48h post injection in tumor bearing mice showed clear tumor delineation on the PET scans, whereas MR imaging provided high-resolution information regarding intratumoral distribution of the nanoparticles. Hence, (nontargeted) ^{89}Zr/Fe-DFO-micelles hold great potential for noninvasive dual modality imaging in oncology. The second line of experiments entailed fibrin-specific PET/MR imaging using fibrin-targeted FibPep-^{89}Zr/Fe-DFO-micelles. These FibPep-^{89}Zr/Fe-DFO-micelles bound specifically to blood clots *in vitro* and this specific binding could be visualized by PET and MR imaging. Overall, these findings encourage further studies of the FibPep-^{89}Zr/Fe-DFO-micelle nanoplatform for *in vivo* PET/MR imaging of fibrin deposition in cardiovascular and neurological diseases, as well as in oncology.

A novelty of the synthesized nanoparticles in this study is that the micelles are tagged with Fe-DFO as a MR contrast label. Fe-FDO yields similar T_1-contrast with respect to conventional Gd-chelates, but does not have the intrinsic problem of potential Gd toxicity, which hampers clinical translation of Gd-based nanoparticles.[57] DFO is clinically approved (Desferal®) and considered safe for human use. The net iron load administered to the mice in this study is only a minor fraction (ca 5%) of the total amount of iron naturally present in the body.[58] Thus, we do not expect significant toxicity or adverse effects resulting from Fe-DFO-containing nanoparticle uptake in liver and spleen, which is in contrast to Gd-based nanoparticles that pose a risk to induce nephrogenic systemic fibrosis (NSF).

Our nanoparticle platform may find further application in image-guided drug delivery, as the micelles offer the possibility for drug loading. Hydrophobic drugs such as paclitaxel could be incorporated in the polybutadiene core of the micelle, while other (hydrophilic) drugs could be conjugated to the acrylic acid groups in the hydrophilic corona. Such an image-guided drug delivery system could be further optimized by additional conjugation of targeting ligands, such as antibodies or peptides, to the acrylic acid groups. For instance, the fibrin-targeted FibPep-^{89}Zr/Fe-DFO-micelles might be suitable to deliver cytotoxic therapeutics to solid tumors, which often display a fibrin-rich tumor stroma,[59] while allowing visualization of this therapeutic delivery using PET/MRI. Finally, the concept of nanoparticulate Fe-DFO-based T_1-MRI agents could be easily applied to other types of nanoparticles employed for MRI purposes, and thus be tailored to all kind of *in vivo* applications.

7.5 Conclusions

Overall, this work described the synthesis and characterization of a novel nanoparticulate platform (^{89}Zr/Fe-DFO-micelles) for dual modal PET/MRI. (Nontargeted) ^{89}Zr/Fe-DFO-micelles allowed noninvasive *in vivo* PET/MR imaging of EPR-based tumor uptake of the nanoparticles. In addition, FibPep-^{89}Zr/Fe-DFO-micelles allowed PET/MR visualization of fibrin-deposition in human thrombi *in vitro*. Hence, the ^{89}Zr/Fe-DFO-micelle nanoplatform is suitable for both EPR-based and target-specific PET/MRI. Our approach offers an alternative to Gd-based nanoparticles for T_1-MR imaging, thereby avoiding all potential risk associated with long-term organ retention of Gd. Thus, the ^{89}Zr/Fe-DFO-micelles show great potential for clinical translation in the setting of nanomedicine, cancer diagnostics and molecular imaging.

7.6 Experimental

7.6.1 Materials

Tetrahydrofuran (THF), dimethylsulfoxide (DMSO), phosphate buffered saline (PBS) tablets, hydrochloric acid (HCl, 2M), sodium hydroxide (NaOH, 1M), iron(III)chloride hexahydrate, aluminum(III)chloride hexahydrate, 1-ethyl-3-(3-dimethylaminopropyl) carbodiimide hydrochloride (EDC·HCl), N-hydroxysulfosuccinimide (sulfo-NHS), acetonitrile, sodium citrate, 4-(2-hydroxyethyl)piperazine-1-ethanesulfonic acid (HEPES), sodium carbonate and oxalic acid were purchased from Sigma Aldrich (USA). Polybutadiene-b-polyethyleneoxide (PBD_{1800}-b-PEO_{4000}) and polybutadiene-b-polyacrylicacid (PBD_{1000}-b-PAA_{2200}) were purchased from PolymerSource, Inc. (Canada). Deferoxamine (DFO) mesylate salt was obtained from Abcam (UK). Mouse and human serum were purchased from Innovative Research (USA). 9-fluorenylmethyloxycarbonyl-protected amino acids and Rink amide resin were purchased from either Novabiochem (Germany) or Bachem (Switzerland). Human tissue factor was obtained from Dade Behring (USA) and citrated human blood plasma was obtained from Sanquin (the Netherlands).

7.6.2 Methods: ^{89}Zr/Fe-DFO-micelles for EPR-based PET/MR tumor imaging

7.6.2.1 Micelle synthesis: Polymeric micelles were prepared using thin film hydration. PBD_{1800}-b-PEO_{4000} (92.8 mg) and PBD_{1000}-b-PAA_{2200} (18.9 mg) were dissolved in THF (8 mL) at 60 °C and evaporated to dryness by rotary evaporation (starting at 300 mbar, 40 °C). The thin film was further dried overnight under mild N_2 flow. The obtained film was then hydrated in 5.58 mL PBS (pH 7.4) at 70 °C via sonication (1h, room temperature (RT)), followed by extrusion through 0.45 µm and 0.22 µm syringe filters. Next, DFO and $FeCl_3 \cdot 6H_2O$ were separately dissolved in PBS (pH < 2) and mixed (1:1) under mechanical stirring, resulting in DFO-complexed Fe (Fe-DFO).[20, 60] Subsequently, NaOH was used to increase the pH to 7.4 and the solution was filtered over a 0.22 µm filter. EDC, sulfo-NHS and Fe-DFO were added to the polymeric micelle solution in a molar ratio of 1:10:2:3 (acrylic acid: EDC: sulfo-NHS: Fe-DFO). The pH was then adjusted to 7 and the final solution was mixed for 3 h at RT. Next, the Fe-DFO-micelles were run over a PD-10 desalting column (GE Healthcare, UK) twice and finally washed 5 times with PBS in Amicon Ultra centrifugal filters (50 kDa molecular weight cut-off (mwco)) (Millipore, USA) at 4000 g in

an Heraeus Biofuge (Thermo Scientific, USA). Al-DFO-micelles were synthesized according to a similar protocol, using $AlCl_3 \cdot 6H_2O$ instead of $FeCl_3 \cdot 6H_2O$.

7.6.2.2 Micelle characterization: Micelle hydrodynamic size was determined by dynamic light scattering (DLS) (ALV-5000/60X0 Multiple Tau Digital Time Correlator, ALV-Laser GmbH, Germany). Each sample was measured 5 times for 10 s at a scattering angle of 90°. Size distribution was determined from the autocorrelation function. Morphology and dispersion state of the micelles was determined by cryogenic transmission electron microscopy (Cryo-TEM). Sample preparation was performed by applying a 2 µL droplet of suspension to a lacy carbon film and subsequently plunge-freezing this sample into liquid ethane using a Vitrobot. Imaging was done in low-dose using a FEI TECNAI F30ST (300kV, FEI, the Netherlands) equipped with a cryoholder (sample temperature: -175°C). Iron concentration was determined by inductively coupled plasma-optical emission spectroscopy (ICP-OES) or inductively coupled plasma-mass spectrometry (ICP-MS). Aluminum concentration was determined by means of ICP-OES. The hydrophilic fraction f= 1-(M_{PBD}/M_{total}) for both employed diblocks is f=0.69, leading to self-assembly into a mixed star-like micelle with a PBD core and a mixed PEO and PAA corona. Diameter of the core is estimated to be around $d_{core} \approx 15$ nm, based on the molecular weights of PBD, and the overall diameter is approximately $d \approx 40$ nm with an estimated aggregation number of ca. 600 block copolymers per micelle.[44, 61-63]

The longitudinal (r_1) and transversal (r_2) relaxivities of the Fe-DFO-micelles were measured with a Minispec MQ60 (60 MHz, 1.41 T, Bruker, Germany). Dilution series of the original polymer suspensions were prepared in PBS and samples (180 µL) were measured at 37 °C. T_1 relaxation times were measured with an Inversion Recovery sequence and T_2 relaxation times were determined with a Carr-Purcell-Meiboom-Gill sequence (TR > $5T_1$, mono-exponential fit). Inverse T_1 and T_2 relaxation times were plotted against corresponding iron concentration, and the slope of the calculated linear fit provided r_1 and r_2, respectively.

7.6.2.3 Zirconium-89 labeling of micelles: Labeling of the micelles with ^{89}Zr was performed according to a modified protocol by Vosjan and coworkers.[26] A typical radiolabeling procedure is described: In short, 139 µL of 1 M oxalic acid and 63.4 µL of 2 M Na_2CO_3 were added to 2-5 µL of ^{89}Zr-oxalic acid solution (3-15 MBq), and incubated for 3 min at RT. Consecutively, 704 µL of 0.5 M HEPES buffer solution (pH 7.2-7.4) and 500 µL of polymeric micelle solution were added. The solution was allowed to react while gently wobbling for 1 h, yielding ^{89}Zr/Fe-DFO-micelles. Next, a DTPA-challenge (5 µL, 10 mM) was conducted for 15 min at RT. The radiolabeling efficiency was analyzed with radio-thin layer chromatography (iTLC-SG plates, Varian Inc, USA) using a 20 mM citrate : acetonitrile 9:1 (v/v) running buffer. The samples were imaged on a FLA-7000 phosphor imager (Fujifilm, Japan). The ^{89}Zr/Fe-DFO-micelles were purified through a 7 kDA mwco Zeba desalting spin column (Thermo Scientific, US). Radiochemical purity was determined by size exclusion chromatography on an Agilent Technologies HPLC 1100 series system (Agilent Technologies, US) equipped with an UV detector (260 nm and 280 nm, reference 450 nm) and a radioactive detector. The analyte was loaded on a Phenomenex BioSep-SEC-S

3000 column which was eluted with 0.1 M phosphate, 0.15 M NaCl buffer at 1 mL/min. Finally, the collected solution was concentrated in Amicon Ultra centrifuge filters. Al-DFO-Micelles were radiolabeled similarly.

Radiochemical stability was determined by incubating ^{89}Zr/Fe-DFO-micelles in 50% v/v BALB/c mouse serum in PBS at 37 °C for up to a week. After 1, 3, 24, 96 and 168 h, aliquots of the suspension were analyzed with radio-TLC. Subsequently, the supernatant was separated from the protein pellet and the radioactivity of the pellet and supernatant was measured using a dose calibrator (VDC-405, Veenstra Instruments, the Netherlands). The supernatant was then analyzed by radio-HPLC.

7.6.2.4 In vitro imaging studies: A dilution series of ^{89}Zr/Fe-DFO-micelles in human serum was prepared (six samples, [Fe] = 5, 3, 1.5, 0.8, 0.4 and 0.2 mM; ^{89}Zr = 0.98, 0.61, 0.31, 0.14, 0.06 and 0.03 MBq, respectively). Control particles were diluted in human serum (1 sample, [Al] = 4 mM; ^{89}Zr = 0.99 MBq). 300 µL of human serum without nanoparticles was used as reference sample. The eight tubes were put in a sample-holder and imaged by MR and PET. MR scans were acquired using an Achieva 3 T scanner (Philips Healthcare, The Netherlands) using a 3.5 cm solenoid receive coil (Philips Research Laboratories, Germany). A single-slice high resolution T_1-weighted anatomical image of the 8 samples was acquired (T_1-FFE, TR/TE: ~60/~20 ms, flip angle (FA): 50°, field-of-view (FOV): 30 × 50 mm, voxel size: 0.2 × 0.2 × 0.2 mm^3, number of averages (NA): 16, slice thickness: 1 mm, acquisition time: 92 s). PET scanning was performed using a small animal Mosaic PET scanner (Philips, the Netherlands), with a spatial resolution of approximately 2.5 mm. Total scan time was 51 min (listmode).

7.6.2.5 cell culture: LS174T human colon carcinoma tumor cells (ATCC, USA) were cultured in Dulbecco's modified Eagle's medium (DMEM, Invitrogen, Germany), supplemented with heat-inactivated 10% fetal bovine serum (Invitrogen), 1% Glutamax 100 (Invitrogen) and 1% pen/strep (Invitrogen) at 37 °C and 5% CO_2, in a humidified atmosphere.

7.6.2.6 Mouse xenograft model: BALB/c nu/nu nude mice (Charles River, The Netherlands) were housed under standard conditions and acclimatized for at least one week. Food and water were freely available. LS174T cells (3.0 × 10^6 cells in 100 µL PBS) were injected subcutaneously into the left hind limb. The growth of the LS174T tumors was monitored by measuring the length (*l*), width (*w*) and depth (*d*) using a caliper and the tumor volume was calculated by 0.5 × *l* × *w* × *d*. Animal studies were started when tumor volume reached 50-250 mm^3 (typically 7-10 days after tumor cell injection). All animal procedures were approved by the ethical review committee of Maastricht University (Maastricht, the Netherlands) and were performed according to the Dutch national law and the guidelines set by the institutional animal care committee, accredited by the national department of health. No adverse effects or toxicity were observed throughout the animal studies.

7.6.2.7 Blood kinetics in non-tumor bearing mice: Blood kinetics of the micelles was studied in non-tumor bearing mice. 100 µL of ^{89}Zr/Fe-DFO-micelles (n=3, 38.9 ± 0.1 mM Fe^{3+}, 0.73 ± 0.01 MBq ^{89}Zr) or

^{89}Zr/Al-DFO-micelles (n=3, 34.6 ± 0.2 mM Al^{3+}; 0.58 ± 0.01 MBq ^{89}Zr) was injected intravenously via the tail vein. Blood samples (ca. 20 µL) were collected from the vena saphena at 5 min, 30 min, 1 h, 2 h, 6 h, 24 h and 48 h post injection and weighed. Subsequently, 1 mL of water was added and the radioactivity in the collected blood samples was measured with a γ-counter (Wizard 1480, Perkin Elmer, USA) along with standards to determine the percentage injected dose per gram (% ID/g).

7.6.2.8 Biodistribution in tumor bearing mice: Fifteen LS174T tumor bearing mice were intravenously injected with ^{89}Zr/Fe-DFO-micelles (100 µL, 35.5 ± 2.3 mM Fe^{3+}, 0.56 ± 0.28 MBq ^{89}Zr). The mice were euthanized at 6 h (n=5, tumor size 256 ± 141 mm^3), 48 h (n=5, tumor size 220 ± 136 mm^3) and 120 h (n=5, tumor size 582 ± 201 mm^3) post injection and biodistribution profiles were obtained. The organs and tumors were harvested, blotted dry, weighed and subsequently 1 mL of water was added. The radioactivity in the collected organs en tumors was measured with a γ-counter to determine % ID/g and the percentage injected dose per organ (% ID).

7.6.2.9 Imaging studies: Ten LS174T tumor bearing mice were used for PET/MR imaging studies, of which two mice dropped out due to oversized tumors. One group (n=5, tumor sizes 48, 50, 64, 269, 616 mm^3) received 125 µL ^{89}Zr/Fe-DFO-micelles (14.1 ± 1.4 mM Fe^{3+}; 5.3 ± 1.2 MBq ^{89}Zr) via the tail vein, the control group (n=3, tumor sizes 95, 387, 405 mm^3) received 125 µL ^{89}Zr/Al-DFO-micelles (19.5 ± 1.4 mM Al^{3+}; 5.1 ± 0.1 MBq ^{89}Zr). At 48 h post injection, the mice were anesthetized using isoflurane (induction 3%, maintenance 1-2%) in medical air and were placed in a water-heated bed equipped with an anesthesia mask. The animal bed was placed inside a heated mouse coil. A small balloon sensor (Graseby, USA) was used to monitor the respiration rate. Body temperature was monitored via a rectal MR temperature probe which was connected to a small animal monitoring system (SA Instruments, USA). The orientation and position of the mouse in the animal bed remained fixed during transfer from the MRI to the PET scanner.

MRI protocol: MR scans were acquired using an Achieva 3 T scanner using a 3.5 cm solenoid receive coil. A fast field echo (T_1-FFE, acquisition time: 3 min) survey was acquired in the sagittal, coronal and transverse plane for tumor localization. Next, multi-slice high resolution T_1-weighted anatomical images of the tumor were acquired in sagittal direction (T_1-FFE, TR/TE: ~60/~20 ms, FA: 25°, FOV: 30 × 40 mm, voxel size: 0.7 × 0.7 × 0.7 mm^3, NA: 10, slice thickness: 1 mm, acquisition time: ~12 min). Subsequently, R_1 maps of the tumor area were acquired using a multi-slice Look-Locker sequence with EPI read-out (parameters: flip angle: 15°, TR/TE: 60/20 ms, interval time: 600 ms, FOV: 30 × 40 mm, matrix: 352 × 352, half-scan: 65%, slices: 3-5, slice thickness: 1 mm, NA: 8, acquisition time: 44 min). R_1* maps were calculated from the LL image set using an in-house created IDL-based software tool (IDL version 6.3, RSI, Colorado, USA). From the R_1* maps, the effective R_1 maps were calculated using Mathematica (Wolfram Research Inc., USA). Region of interests (ROIs) were drawn around the tumors on the accompanying T_1-FFE scan and used for tumor analysis of the obtained R_1 maps. Histograms of T_1 in the tumor were generated for each mouse and averaged for mice in the ^{89}Zr/Fe-DFO-micelle group and for mice in the ^{89}Zr/Al-DFO-micelle group. The resulting bins were compared between both groups.

PET protocol: PET imaging was performed using a small animal PET scanner (Mosaic, Philips). Total scan time was 51 min and scans were obtained in listmode. The acquired PET data was reconstructed for the calculation of standardized uptake values (SUV) using injected dose, animal weight and time of injection. Imalytics software (Philips Research, Germany) was used to determine volume of interests (VoI) via a region growing algorithm using a seed point and lower and upper thresholds, respectively. Liver and spleen were segmented manually in different slides and interpolated automatically, followed by an erosion/dilation algorithm.

After completion of the PET/MRI protocol, the animals were euthanized either by isoflurane overdose or cervical dislocation. Several organs and tissues including tumor were collected, weighed and radioactivity was measured in a γ-counter. Next, tumors were snap-frozen in isopentane at -50 °C and kept at -80 °C until further evaluation.

7.6.2.10 *Ex vivo* autoradiography and histology: The snap-frozen tumors were embedded in Shandon cryomatrix (Thermo Scientific, UK) and serial 10 µm sections were cut on a cryotome (Cryotome FSE/FE, Thermo Scientific, UK). For autoradiography measurements, sections were covered with a scintillating foil and measured for 6 h with a BetaImager DFine system (Biospace Lab, France).To allow analysis of cell viability, a nicotinamide adenine dinucleotide (NADH) diaphorase staining was performed on the tumor sections according to a previously published protocol.[64] In addition, formaldehyde-fixed (4% formaldehyde, 10 min) cryo-sections were stained with haematoxylin and eosin (H&E).

7.6.2.11 Statistical analysis: Bins of the averaged T_1 histograms for ^{89}Zr/Fe-DFO-micelles and the corresponding bins of the ^{89}Zr/Al-DFO-micelles were compared with a one-sided t-test using statistical software (SPSS, IBM, USA). In addition, a one-sided t-test was employed to test for a significant difference in the overall percentage of voxels displaying a T_1 < 750 ms between the ^{89}Zr/Fe-DFO-micelles and ^{89}Zr/Al-DFO-micelles group. Data are presented as mean ± standard deviation (SD). A difference of $p < 0.05$ was considered statistically significant.

7.6.3 Methods: FibPep-^{89}Zr/Fe-DFO-micelles for molecular PET/MR imaging of fibrin deposition

7.6.3.1 Peptide synthesis: Fibrin-binding peptide FibPep (Ac-RWQPCPAESWT-Cha-CWDPGGGK-NH_2, containing a disulfide bond between the two cysteine residues) and a scrambled version of this peptide with C-A substitutions (NCFibPep, Ac-WPTAD-Cha-RAWPSQEWPAGGGK-NH_2) were synthesized according to a previously published protocol.[42]

7.6.3.2 (NC)FibPep-^{89}Zr/Fe-DFO-Micelle synthesis and characterization: Polymeric micelles were prepared as described for the non-peptide conjugated micelles in the previous part of the methods section. Subsequently, the obtained film was hydrated in 5.58 mL of 2-(N-morpholino)ethanesulfonic acid (MES) buffer (pH 6, 70 °C) and sonicated (1h, RT), followed by extrusion through 0.45 and 0.22 µm syringe filters. To prepare the micelles for peptide and Fe-DFO conjugation, EDC (750 µmol) and sulfo-NHS (300 µmol) were added to 2 mL of the obtained micelle solution and this mixture was incubated

for 15 min. Subsequently, the EDC-sulfo-NHS activated micelles were separated from nonconjugated EDC and sulfo-NHS using PD-10 columns (2 runs; PBS pH 7.4 as eluting buffer). Immediately after collecting the micelles from the PD-10 column, half of the activated micelle solution (3 mL) was incubated with FibPep solution (1 µmol peptide in 0.2 mL of 50% DMSO and 50% ultrapure water) and Fe-DFO solution (105 µmol Fe-DFO in 0.85 mL PBS) at 4 °C for 3 h, yielding fibrin-binding FibPep-Fe-DFO-micelles. Negative control NCFibPep-Fe-DFO-micelles were obtained by conjugating NCFibPep and Fe-DFO to the remaining half of the active micelle solution in similar fashion. To prepare the micelles for *in vitro* application, nonconjugated Fe-DFO and peptides were removed from the micelle solution by two PD-10 runs and subsequent centrifuge filtration (50 kDa mwco, Amicon Ultra centrifugal filters). Finally, any precipitation/large aggregates were removed using centrifugation (2000 g; 5 min).

(NC)FibPep-Fe-DFO-micelles were subsequently characterized using DLS, cryo-TEM and ICP-MS according to procedures similar to the protocols described in the methods section for the (nontargeted) Fe-DFO-micelles. Finally, micelles were labeled with ^{89}Zr in a similar fashion as described in the previous part of the methods section, yielding bimodal fibrin-targeted FibPep-^{89}Zr/Fe-DFO-micelles and non-specific negative control NCFibPep-^{89}Zr/Fe-DFO-micelles.

7.6.3.3 Blood clot assay: Blood clots were prepared by incubating a mixture of 6 µL of human tissue factor, 4 µL of 1 M $CaCl_2$ in ultrapure water and 250 µL of citrated human plasma at 37 °C for 2 h.[43] Next, the clots were washed 3x with HEPES buffered saline (HBS) and stored at -20 °C until further use. Clots were thawed and 40 µL of FibPep-^{89}Zr/Fe-DFO-micelles or NCFibPep-^{89}Zr/Fe-DFO-micelles solution (3 µg Fe and 1.4 MBq ^{89}Zr per sample, n=4 per group) were added to the clots and incubated for 1 hr at RT. Subsequently, the solution was removed and the clots were washed 3x with HBS. The clot radioactivity was measured using a VDC-405 dose calibrator and expressed as percentage dose. Next, clots were subjected to PET and MR measurements. PET images were acquired using a small animal Mosaic PET scanner. Total scan time was 1 h (listmode). MRI was performed using a 9.4 T preclinical scanner (Bruker BioSpin, Germany) equipped with a 35 mm birdcage transceiver volume coil. T_1 weighted images were acquired using a FLASH sequence with the following settings: FA 40°, NA 10, TR/TE 90/3.2 ms, slice thickness 0.5 mm, acquisition matrix 300 x 200, reconstructed matrix 600 x 400, FOV 30 x 20 mm^2, voxel size 0.05 x 0.05 mm^2 and acquisition time 3 min. Finally, iron content of the clots was determined using ICP-MS.

7.6.3.4 Statistical analysis: For difference between two groups, data sets were compared using an unpaired 2-sides t-test (not assuming equal variances). Values of $p < 0.05$ were considered significant. Data are presented as mean ± standard deviation (SD).

7.7 Acknowledgements

This work was supported by the Center for Translational Molecular Medicine and The Netherlands Heart Foundation (PARISK, Grant 01C-202), as well as NanoNextNL (FES0901:FES HTSM). The authors would like to thank Monique Berben, Suzanne Kivits, Jeannette Smulders, Monja Kaiser, Caren van

Kammen, Carlijn van Helvert and Marije Janssen for their support with the characterization of the nanoparticles and the *in vivo* experiments.

7.8 References

1. Ferrari, M. Cancer nanotechnology: opportunities and challenges. *Nat Rev Cancer* **2005,** *5*, (3), 161-71.
2. Allen, T. M.; Cullis, P. R. Drug delivery systems: entering the mainstream. *Science* **2004,** *303*, (5665), 1818-22.
3. Wagner, V.; Dullaart, A.; Bock, A. K.; Zweck, A. The emerging nanomedicine landscape. *Nat Biotechnol* **2006,** *24*, (10), 1211-7.
4. Hoang, B.; Lee, H.; Reilly, R. M.; Allen, C. Noninvasive monitoring of the fate of 111In-labeled block copolymer micelles by high resolution and high sensitivity microSPECT/CT imaging. *Mol Pharm* **2009,** *6*, (2), 581-92.
5. Lee, H.; Hoang, B.; Fonge, H.; Reilly, R. M.; Allen, C. In vivo distribution of polymeric nanoparticles at the whole-body, tumor, and cellular levels. *Pharm Res* **2010,** *27*, (11), 2343-55.
6. Mikhail, A. S.; Eetezadi, S.; Ekdawi, S. N.; Stewart, J.; Allen, C. Image-based analysis of the size- and time-dependent penetration of polymeric micelles in multicellular tumor spheroids and tumor xenografts. *Int J Pharm* **2014,** *464*, (1-2), 168-77.
7. Photos, P. J.; Bacakova, L.; Discher, B.; Bates, F. S.; Discher, D. E. Polymer vesicles in vivo: correlations with PEG molecular weight. *J Control Release* **2003,** *90*, (3), 323-34.
8. Lee, J. S.; Feijen, J. Polymersomes for drug delivery: design, formation and characterization. *J Control Release* **2012,** *161*, (2), 473-83.
9. Chandrawati, R.; Hosta-Rigau, L.; Vanderstraaten, D.; Lokuliyana, S. A.; Stadler, B.; Albericio, F.; Caruso, F. Engineering advanced capsosomes: maximizing the number of subcompartments, cargo retention, and temperature-triggered reaction. *ACS Nano* **2010,** *4*, (3), 1351-61.
10. Jarzyna, P. A.; Gianella, A.; Skajaa, T.; Knudsen, G.; Deddens, L. H.; Cormode, D. P.; Fayad, Z. A.; Mulder, W. J. Multifunctional imaging nanoprobes. *Wiley Interdiscip Rev Nanomed Nanobiotechnol* **2010,** *2*, (2), 138-50.
11. Lammers, T.; Aime, S.; Hennink, W. E.; Storm, G.; Kiessling, F. Theranostic nanomedicine. *Acc Chem Res* **2011,** *44*, (10), 1029-38.
12. de Smet, M.; Langereis, S.; van den Bosch, S.; Grull, H. Temperature-sensitive liposomes for doxorubicin delivery under MRI guidance. *J Control Release* **2010,** *143*, (1), 120-7.
13. Discher, D. E.; Eisenberg, A. Polymer vesicles. *Science* **2002,** *297*, (5583), 967-73.
14. O'Reilly, R. K.; Hawker, C. J.; Wooley, K. L. Cross-linked block copolymer micelles: functional nanostructures of great potential and versatility. *Chem Soc Rev* **2006,** *35*, (11), 1068-83.
15. Brinkhuis, R. P.; Rutjes, F. P. J. T.; van Hest, J. C. M. Polymeric vesicles in biomedical applications. *Polym Chem-Uk* **2011,** *2*, (7), 1449-1462.
16. Alexis, F.; Pridgen, E.; Molnar, L. K.; Farokhzad, O. C. Factors affecting the clearance and biodistribution of polymeric nanoparticles. *Mol Pharm* **2008,** *5*, (4), 505-15.
17. Choi, H. S.; Liu, W.; Liu, F.; Nasr, K.; Misra, P.; Bawendi, M. G.; Frangioni, J. V. Design considerations for tumour-targeted nanoparticles. *Nat Nanotechnol* **2010,** *5*, (1), 42-7.
18. Forster, S.; Plantenberg, T. From self-organizing polymers to nanohybrid and biomaterials. *Angew Chem Int Ed Engl* **2002,** *41*, (5), 689-714.
19. Zhou, T.; Ma, Y.; Kong, X.; Hider, R. C. Design of iron chelators with therapeutic application. *Dalton Trans* **2012,** *41*, (21), 6371-89.
20. Mino, Y.; Kitagaki, H.; Sasaki, M.; Ishii, K.; Mori, T.; Yamada, K.; Nagasawa, O. Characterization of Fe(III)-deferoxamine and Mn(II)-pectin as magnetic resonance imaging contrast agents. *Biol Pharm Bull* **1998,** *21*, (12), 1385-8.
21. Schwert, D. D.; Davies, J. A.; Richardson, N. Non-gadolinium-based MRI contrast agents. *Top Curr Chem* **2002,** *221*, 165-199.
22. Verel, I.; Visser, G. W.; Boellaard, R.; Stigter-van Walsum, M.; Snow, G. B.; van Dongen, G. A. 89Zr immuno-PET: comprehensive procedures for the production of 89Zr-labeled monoclonal antibodies. *J Nucl Med* **2003,** *44*, (8), 1271-81.

23. White, D. L. Paramagnetic iron (III) MRI contrast agents. *Magn Reson Med* **1991,** *22*, (2), 309-12.
24. Holland, J. P.; Sheh, Y.; Lewis, J. S. Standardized methods for the production of high specific-activity zirconium-89. *Nucl Med Biol* **2009,** *36*, (7), 729-39.
25. Perk, L. R.; Vosjan, M. J.; Visser, G. W.; Budde, M.; Jurek, P.; Kiefer, G. E.; van Dongen, G. A. p-Isothiocyanatobenzyl-desferrioxamine: a new bifunctional chelate for facile radiolabeling of monoclonal antibodies with zirconium-89 for immuno-PET imaging. *Eur J Nucl Med Mol Imaging* **2010,** *37*, (2), 250-9.
26. Vosjan, M. J.; Perk, L. R.; Visser, G. W.; Budde, M.; Jurek, P.; Kiefer, G. E.; van Dongen, G. A. Conjugation and radiolabeling of monoclonal antibodies with zirconium-89 for PET imaging using the bifunctional chelate p-isothiocyanatobenzyl-desferrioxamine. *Nat Protoc* **2010,** *5*, (4), 739-43.
27. Broome, D. R. Nephrogenic systemic fibrosis associated with gadolinium based contrast agents: a summary of the medical literature reporting. *Eur J Radiol* **2008,** *66*, (2), 230-4.
28. Daftari Besheli, L.; Aran, S.; Shaqdan, K.; Kay, J.; Abujudeh, H. Current status of nephrogenic systemic fibrosis. *Clin Radiol* **2014,** *69*, (7), 661-8.
29. Iyer, A. K.; Khaled, G.; Fang, J.; Maeda, H. Exploiting the enhanced permeability and retention effect for tumor targeting. *Drug Discov Today* **2006,** *11*, (17-18), 812-8.
30. Maeda, H. The enhanced permeability and retention (EPR) effect in tumor vasculature: the key role of tumor-selective macromolecular drug targeting. *Adv Enzyme Regul* **2001,** *41*, 189-207.
31. Maeda, H.; Nakamura, H.; Fang, J. The EPR effect for macromolecular drug delivery to solid tumors: Improvement of tumor uptake, lowering of systemic toxicity, and distinct tumor imaging in vivo. *Adv Drug Deliv Rev* **2013,** *65*, (1), 71-9.
32. Paul, J.; Strickland, S.; Melchor, J. P. Fibrin deposition accelerates neurovascular damage and neuroinflammation in mouse models of Alzheimer's disease. *J Exp Med* **2007,** *204*, (8), 1999-2008.
33. Palumbo, J. S.; Talmage, K. E.; Massari, J. V.; La Jeunesse, C. M.; Flick, M. J.; Kombrinck, K. W.; Jirouskova, M.; Degen, J. L. Platelets and fibrin(ogen) increase metastatic potential by impeding natural killer cell-mediated elimination of tumor cells. *Blood* **2005,** *105*, (1), 178-85.
34. Dvorak, H. F.; Nagy, J. A.; Berse, B.; Brown, L. F.; Yeo, K. T.; Yeo, T. K.; Dvorak, A. M.; van de Water, L.; Sioussat, T. M.; Senger, D. R. Vascular permeability factor, fibrin, and the pathogenesis of tumor stroma formation. *Ann N Y Acad Sci* **1992,** *667*, 101-11.
35. Rickles, F. R.; Patierno, S.; Fernandez, P. M. Tissue factor, thrombin, and cancer. *Chest* **2003,** *124*, (3 Suppl), 58S-68S.
36. Tavora, F.; Cresswell, N.; Li, L.; Ripple, M.; Burke, A. Immunolocalisation of fibrin in coronary atherosclerosis: implications for necrotic core development. *Pathology* **2010,** *42*, (1), 15-22.
37. Congiu, T.; Schembri, L.; Tozzi, M.; Guasti, L.; Maio, R. C.; Cosentino, M.; Marino, F. Scanning electron microscopy examination of endothelium morphology in human carotid plaques. *Micron* **2010,** *41*, (5), 532-6.
38. Sato, Y.; Hatakeyama, K.; Yamashita, A.; Marutsuka, K.; Sumiyoshi, A.; Asada, Y. Proportion of fibrin and platelets differs in thrombi on ruptured and eroded coronary atherosclerotic plaques in humans. *Heart* **2005,** *91*, (4), 526-30.
39. Bini, A.; Fenoglio, J. J., Jr.; Mesa-Tejada, R.; Kudryk, B.; Kaplan, K. L. Identification and distribution of fibrinogen, fibrin, and fibrin(ogen) degradation products in atherosclerosis. Use of monoclonal antibodies. *Arteriosclerosis* **1989,** *9*, (1), 109-21.
40. Ariens, R. A. Fibrin(ogen) and thrombotic disease. *J Thromb Haemost* **2013,** *11 Suppl 1*, 294-305.
41. Starmans, L. W.; van Duijnhoven, S. M.; Rossin, R.; Berben, M.; Aime, S.; Daemen, M. J.; Nicolay, K.; Grull, H. Evaluation of 111In-labeled EPep and FibPep as tracers for fibrin SPECT imaging. *Mol Pharm* **2013,** *10*, (11), 4309-21.
42. Starmans, L. W.; van Duijnhoven, S. M.; Rossin, R.; Aime, S.; Daemen, M. J.; Nicolay, K.; Grull, H. SPECT imaging of fibrin using fibrin-binding peptides. *Contrast Media Mol Imaging* **2013,** *8*, (3), 229-37.
43. Starmans, L. W.; Burdinski, D.; Haex, N. P.; Moonen, R. P.; Strijkers, G. J.; Nicolay, K.; Grull, H. Iron oxide nanoparticle-micelles (ION-micelles) for sensitive (molecular) magnetic particle imaging and magnetic resonance imaging. *PLoS One* **2013,** *8*, (2), e57335.
44. Zheng, Y.; Won, Y. Y.; Bates, F. S.; Davis, H. T.; Scriven, L. E.; Talmon, Y. Directly resolved core-corona structure of block copolymer micelles by cryo-transmission electron microscopy. *J Phys Chem B* **1999,** *103*, (47), 10331-10334.

45. Cabral, H.; Matsumoto, Y.; Mizuno, K.; Chen, Q.; Murakami, M.; Kimura, M.; Terada, Y.; Kano, M. R.; Miyazono, K.; Uesaka, M.; Nishiyama, N.; Kataoka, K. Accumulation of sub-100 nm polymeric micelles in poorly permeable tumours depends on size. *Nature Nanotechnology* **2011,** *6*, (12), 815-823.

46. Strijkers, G. J.; Mulder, W. J.; van Tilborg, G. A.; Nicolay, K. MRI contrast agents: current status and future perspectives. *Anticancer Agents Med Chem* **2007,** *7*, (3), 291-305.

47. Terreno, E.; Dastru, W.; Delli Castelli, D.; Gianolio, E.; Geninatti Crich, S.; Longo, D.; Aime, S. Advances in metal-based probes for MR molecular imaging applications. *Curr Med Chem* **2010,** *17*, (31), 3684-700.

48. Vander Elst, L.; Raynaud, J.-S.; Vives, V.; Santus, R.; Louin, G.; Robert, P.; Port, M.; Corot, C.; Muller, R. Comparative Relaxivities and Efficacies of Gadolinium-based Commercial Contrast Agents. *Proc. Intl. Soc. Mag. Reson. Med.* **2013,** *21*, 746.

49. de Smet, M.; Langereis, S.; van den Bosch, S.; Bitter, K.; Hijnen, N. M.; Heijman, E.; Grull, H. SPECT/CT imaging of temperature-sensitive liposomes for MR-image guided drug delivery with high intensity focused ultrasound. *J Control Release* **2013,** *169*, (1-2), 82-90.

50. Abou, D. S.; Ku, T.; Smith-Jones, P. M. In vivo biodistribution and accumulation of 89Zr in mice. *Nucl Med Biol* **2011,** *38*, (5), 675-81.

51. Dijkers, E. C.; Oude Munnink, T. H.; Kosterink, J. G.; Brouwers, A. H.; Jager, P. L.; de Jong, J. R.; van Dongen, G. A.; Schroder, C. P.; Lub-de Hooge, M. N.; de Vries, E. G. Biodistribution of 89Zr-trastuzumab and PET imaging of HER2-positive lesions in patients with metastatic breast cancer. *Clin Pharmacol Ther* **2010,** *87*, (5), 586-92.

52. Moghimi, S. M.; Hunter, A. C.; Murray, J. C. Long-circulating and target-specific nanoparticles: theory to practice. *Pharmacol Rev* **2001,** *53*, (2), 283-318.

53. Majmudar, M. D.; Yoo, J.; Keliher, E. J.; Truelove, J. J.; Iwamoto, Y.; Sena, B.; Dutta, P.; Borodovsky, A.; Fitzgerald, K.; Di Carli, M. F.; Libby, P.; Anderson, D. G.; Swirski, F. K.; Weissleder, R.; Nahrendorf, M. Polymeric nanoparticle PET/MR imaging allows macrophage detection in atherosclerotic plaques. *Circ Res* **2013,** *112*, (5), 755-61.

54. Yuan, F.; Dellian, M.; Fukumura, D.; Leunig, M.; Berk, D. A.; Torchilin, V. P.; Jain, R. K. Vascular permeability in a human tumor xenograft: molecular size dependence and cutoff size. *Cancer Res* **1995,** *55*, (17), 3752-6.

55. Kunjachan, S.; Gremse, F.; Theek, B.; Koczera, P.; Pola, R.; Pechar, M.; Etrych, T.; Ulbrich, K.; Storm, G.; Kiessling, F.; Lammers, T. Noninvasive optical imaging of nanomedicine biodistribution. *ACS Nano* **2013,** *7*, (1), 252-62.

56. Lee, H.; Fonge, H.; Hoang, B.; Reilly, R. M.; Allen, C. The effects of particle size and molecular targeting on the intratumoral and subcellular distribution of polymeric nanoparticles. *Mol Pharm* **2010,** *7*, (4), 1195-208.

57. Langereis, S.; Geelen, T.; Grull, H.; Strijkers, G. J.; Nicolay, K. Paramagnetic liposomes for molecular MRI and MRI-guided drug delivery. *NMR Biomed* **2013,** *26*, (7), 728-44.

58. Kohgo, Y.; Ikuta, K.; Ohtake, T.; Torimoto, Y.; Kato, J. Body iron metabolism and pathophysiology of iron overload. *Int J Hematol* **2008,** *88*, (1), 7-15.

59. Yasunaga, M.; Manabe, S.; Matsumura, Y. New concept of cytotoxic immunoconjugate therapy targeting cancer-induced fibrin clots. *Cancer Sci* **2011,** *102*, (7), 1396-402.

60. Hallaway, P. E.; Eaton, J. W.; Panter, S. S.; Hedlund, B. E. Modulation of deferoxamine toxicity and clearance by covalent attachment to biocompatible polymers. *Proc Natl Acad Sci U S A* **1989,** *86*, (24), 10108-12.

61. Pispas, S.; Hadjichristidis, N. Aggregation behavior of poly(butadiene-b-ethylene oxide) block copolymers in dilute aqueous solutions: Effect of concentration, temperature, ionic strength, and type of surfactant. *Langmuir* **2003,** *19*, (1), 48-54.

62. Zupancich, J. A.; Bates, F. S.; Hillmyer, M. A. Synthesis and self-assembly of RGD-functionalized PEO-PB amphiphiles. *Biomacromolecules* **2009,** *10*, (6), 1554-63.

63. Zhulina, E. B.; Borisov, O. V. Theory of Block Polymer Micelles: Recent Advances and Current Challenges. *Macromolecules* **2012,** *45*, (11), 4429-4440.

64. Hijnen, N. M.; Heijman, E.; Kohler, M. O.; Ylihautala, M.; Ehnholm, G. J.; Simonetti, A. W.; Grull, H. Tumour hyperthermia and ablation in rats using a clinical MR-HIFU system equipped with a dedicated small animal set-up. *Int J Hyperthermia* **2012,** *28*, (2), 141-55.

Chapter 8

Summarizing discussion

Abstract

Methodologies that allow noninvasive imaging of fibrin deposition have the potential to improve clinical decision making in a number of chief medical disciplines, such as cardiology, oncology and neurology (**Chapter 1**). In this thesis, three types of fibrin-specific imaging methodologies were developed and put to a test in a preclinical setting. The first methodology comprised the development of two ^{111}In-labeled fibrin-binding peptides (FibPep and EPep) for nuclear imaging of fibrin deposition with subsequent testing in rodent thrombosis models (**Chapter 2-3**). EPep was additionally evaluated for application in the field of oncology by employing tumor xenograft mouse models (**Chapter 4**). The second methodology entailed the development of a fibrin-binding iron oxide nanoparticle micelle (FibPep-ION-Micelle) platform for molecular magnetic particle imaging (MPI) and magnetic resonance imaging (MRI) of fibrin deposition (**Chapter 5**). The FibPep-ION-Micelles were subsequently evaluated in a rodent thrombosis model (**Chapter 6**). The final strategy described in this thesis comprised of fibrin-targeted ^{89}Zr- and Fe-deferoxamine-labeled polymeric micelles (FibPep-^{89}Zr/Fe-DFO-micelles) for combined molecular positron emission tomography (PET) and MR imaging of fibrin deposition (**Chapter 7**). This chapter (**Chapter 8**) will summarize, discuss and provide a future perspective of these three developed fibrin-specific imaging methodologies.

8.1 Radiolabeled fibrin-binding peptides for nuclear imaging of fibrin deposition

Nuclear imaging has historically been the major modality in the field of fibrin-specific imaging and allows sensitive, quantitative and whole-body detection of fibrin deposits (**Chapter 1**). Owing to the minute amounts of tracers required, translational efforts to transfer novel nuclear imaging tracers from bench to bedside are typically less challenging with respect to contrast agents for other imaging modalities. Fibrin-specific nuclear imaging has evolved over the past decades from employing radiolabeled coagulation cascade proteins and radiolabeled antibodies against fibrin towards using radiolabeled fibrin-binding peptides (**Chapter 1**). Peptide-based tracers have in general several advantages over protein- and antibody-based tracers, such as low costs of production, low immunogenicity, rapid blood clearance and high tissue penetration,[1, 2] which yield a favorable competitive edge for fibrin-binding peptide tracers with respect to their protein and antibody counterparts.

In the last decade, efforts in the field of fibrin-specific imaging have mainly focused on the EP-2104R fibrin-binding peptide platform for molecular MR imaging of fibrin deposits. EP-2104R is a gadolinium-containing peptidic fibrin-binding contrast agent,[3] which binds to fibrin with a dissociation constant (K_d) of ca. 1 μM and has been investigated extensively for preclinical MR imaging of fibrin deposition in thrombi, atherosclerotic lesions and tumors.[4-9] In addition, this peptide platform was clinically used in phase I and II clinical trials for MR imaging of fibrin deposition in thrombosis.[10, 11] However, EP-2104R has not been taken into phase III clinical trials. The phase II trial found a relative low sensitivity for venous thrombosis, as only 4 out of 14 thrombi located in the venous system were detected by EP-2104R fibrin MRI.[11] Radiolabeled counterparts of the EP-2104R peptide for nuclear imaging are in several aspects better suited to take the next step with respect to translational efforts. Radionuclide-based fibrin-binding peptides provide higher sensitivity and facile whole-body detection of fibrin deposits compared to gadolinium-based fibrin-binding peptides for MR imaging. Furthermore, MR-based molecular imaging approaches using gadolinium-containing contrast agents require pre-contrast baseline MR examination in addition to the post-contrast acquisition, yielding a more complex workflow and analysis of the acquired data, as well as potential issues with patient compliance. Additionally, targeted MRI-probes labeled with gadolinium might raise concerns with respect to systemic nephrogenic fibrosis,[12] complicating translational efforts. Hence, radiolabeled fibrin-specific peptides for nuclear imaging purposes are likely more readily translatable into routine clinical application. Based on these considerations, this thesis describes the development and preclinical validation of two novel fibrin-binding peptidic tracers (FibPep and EPep) for nuclear imaging of fibrin deposition.

Chapter 2 describes a proof-of-concept study in which the novel ^{111}In-labeled fibrin-binding peptide FibPep, containing the cyclic fibrin-binding motif RWQPCPAESWT-Cha-CWDP, was developed for fibrin-specific single photon emission computed tomography (SPECT) imaging.[13] FibPep and the corresponding negative control peptide (NCFibPep) were synthesized and their fibrin-binding characteristics were investigated *in vitro*. FibPep bound to fibrin with a K_d of 0.8 μM, whereas NCFibPep

displayed at least a 100-fold lower fibrin affinity. A carotid artery thrombosis mouse model was used to evaluate the peptides *in vivo*. FibPep and NCFibPep displayed swift blood clearance and were eliminated via the urine. *In vivo* FibPep SPECT imaging allowed sensitive detection of the thrombi. The obtained e*x vivo* biodistribution profiles showed significantly increased uptake of FibPep in the thrombus-containing carotid with respect to the contralateral carotid (5.7 ± 0.7 and 0.6 ± 0.4% injected dose per gram (ID/g), respectively), whereas the negative control peptide did not (0.4 ± 0.2 and 0.3 ± 0.0% ID/g, respectively). To summarize, FibPep displayed high fibrin affinity and favourable blood clearance, and allowed sensitive detection of fibrin deposits in thrombi using *in vivo* SPECT imaging.

In a subsequent study, we developed EPep, an ^{111}In-labeled fibrin-binding peptide containing the fibrin-avid domain of EP-2104R, and sought to compare EPep and FibPep as fibrin-specific SPECT tracers (**Chapter 3**).[14] *In vitro*, EPep and FibPep showed high stability in serum, but were more prone to degradation in kidney and liver homogenate assays. Both EPep and FibPep displayed similar affinities toward mouse and human derived fibrin (K_d ≈ 1 μM), and similarly to FibPep, EPep showed rapid blood clearance, high thrombus uptake (6.8 ± 1.2% ID/g) and low non-target uptake in a mouse model of carotid thrombosis. In addition, EPep showed a comparable affinity toward rat fibrin *in vitro* and displayed high thrombus uptake in a rat model of carotid thrombosis (0.74 ± 0.39% ID/g) thus allowing visualization of the thrombi in rats using SPECT imaging. In contrast, FibPep displayed low affinity towards rat fibrin (K_d ≈ 14 μM), low thrombus uptake (0.06 ± 0.02% ID/g) in the rat carotid thrombosis model and did not allow detection of thrombi in rats using SPECT. These data suggest that the FibPep-binding epitope on the fibrin molecule is not (fully) homologous between rats and humans, and that therefore preclinical rat models of disease are not suited to gauge the clinical potential of FibPep. To summarize, both EPep and FibPep displayed comparable metabolic stability and affinity toward mouse and human fibrin, and showed high thrombus uptake in a mouse carotid thrombosis model. Therefore, both EPep and FibPep are promising tracers for fibrin SPECT imaging.

In addition to thrombus diagnostics, EPep was evaluated for SPECT imaging of fibrin deposition in tumors (**Chapter 4**). EPep SPECT imaging of BT-20 tumor bearing mice allowed visualization of fibrin deposits in the tumors, whereas mice injected with the corresponding negative control peptide (NCEPep) did not show increased tumoral SPECT signal. *Ex vivo* biodistribution showed significantly increased uptake of EPep in the BT-20 tumors compared to NCEPep (0.4 ± 0.1 and 0.1 ± 0.0% ID/g, respectively), whereas uptake in other organs was similar for both peptides. Autoradiography of BT-20 tumor sections showed marked signal for EPep which co-localized with fibrin deposits in the tumors. In MDA-MB-231 tumor bearing mice the biodistribution profiles obtained 3 h post injection displayed EPep tumor uptake (0.14 ± 0.04% ID/g) which was significantly lower with respect to EPep BT-20 tumor uptake. Histological analysis of MDA-MB-231 tumors displayed little tumor stroma and only minute levels of fibrin in the tumors, indicating fibrin-specificity of EPep tumoral uptake. To the best of our knowledge, this study is the first to report on nuclear imaging of tumoral fibrin deposition using a radiolabeled fibrin-binding peptide tracer.

In conclusion, the data presented in **Chapter 2-4** of this thesis suggest that both EPep and FibPep are promising and broadly applicable candidates for translation into clinical settings to serve as novel tools for SPECT imaging of fibrin deposition. In addition to cardiovascular and oncologic applications, as demonstrated in **Chapter 2-4**, both peptides might be of value in the field of neurology, as fibrin deposition has been implicated as a potential critical factor in Alzheimer's disease.[15] Future studies to further gauge the translational potential of EPep and FibPep might employ disease models in larger animals, such as pigs, in order to study the resolution and sensitivity aspects of EPep- and FibPep-based approaches in protocols using clinical SPECT scanners. Additionally, two other areas might be investigated to improve EPep- and FibPep-based fibrin SPECT strategies. First, the peptide dosage and its potential effects on fibrin-uptake, biodistribution and blood kinetics have not been extensively studied in this thesis. Ideally, an optimal dosage should be established that minimizes the required amount of peptide while maximizing uptake in fibrin deposits and hence detection sensitivity. The second area of potential improvement is enhancing the stability of the peptides *in vivo*, since both EPep and FibPep were found to be susceptible to degradation in mouse and rat liver and kidney homogenates *in vitro* and were mainly recovered in urine as metabolized species *in vivo*. Additional *in vitro* metabolic assays employing human microsomes might yield more insights with respect to the stability of the peptides in humans.[16] Enhanced resistance against metabolic degradation might be achieved by means of modifying the peptide structure by replacing potentially labile amino acids with their D-amino acid counterparts or by attaching a DOTA-chelator moiety at both the C- and N-termini.[17, 18] Naturally, these optimized peptides should be carefully reevaluated with respect to fibrin affinity and blood kinetics and biodistribution profiles.

Recently, Caravan and coworkers have investigated copper-64- and fluorine-18-labeled fibrin-binding peptides (FBP's) with molecular structures based on EP-2104R for PET imaging of fibrin deposition.[19-23] These FBP peptides showed roughly similar affinity towards fibrin compared to FibPep and EPep. The advantage of PET imaging with respect to SPECT is the higher spatial resolution and sensitivity in clinical settings. In addition, the emergence of dual modality PET/MRI scanners allows simultaneous acquisition of functional PET signal and high resolution anatomical and functional MR data. On the other hand, SPECT allows multi-isotope imaging,[24-26] enabling the simultaneous assessment of multiple biomarkers, which is an advantage as it allows multi-facetted analysis of complex pathologies such as atherosclerosis, cancer and Alzheimer's disease. Furthermore, SPECT/CT systems, which allow the combination of fibrin SPECT with anatomical CT, are broadly available in clinical settings. In conclusion, both the PET and SPECT peptide-based fibrin imaging approaches hold potential for clinical translation and are worthy of further exploration.

8.2 Fibrin-binding iron oxide nanoparticles micelles for MPI and MRI of fibrin deposition

MPI, which is able to directly visualize magnetic particles,[27] is a relatively young imaging modality and could serve as a radiation-free alternative for hot-spot based molecular imaging. Therefore, MPI is of significant interest in the quest to develop sophisticated noninvasive strategies to image fibrin deposition *in vivo*. Commercially available iron oxide contrast agents that are currently being employed

are not optimized for MPI, preventing MPI from reaching its full potential in terms of resolution and sensitivity. As molecular MPI applications will likely have to deal with the relative low sensitivity of MPI (with respect to nuclear imaging), optimalization of the iron oxide formulations is crucial to ensure maximal sensitivity for molecular MPI purposes. To this aim, this thesis describes the development and preclinical evaluation of a novel iron oxide nanoparticle micelle (ION-Micelle) nanoplatform for sensitive MPI, as well as the functionalisation of the ION-Micelle nanoplatform with fibrin-binding peptides (FibPep) to allow fibrin-specific molecular MPI.

In **Chapter 5**, we described the synthesis and characterization of the ION-Micelle nanoplatform, containing iron oxide cores of 25 nm, for MPI and MRI purposes.[28] ION-Micelles generated up to 200 times higher signal in magnetic particle spectrometry (MPS) measurements and showed a significantly increased transversal proton relaxivity with respect to commercially available iron oxide formulations, thus allowing more sensitive MPI and MRI. Furthermore, the potential of the ION-Micelles for fibrin-specific molecular MPI and MRI was demonstrated by *in vitro* MPS and MRI measurements of thrombi incubated with FibPep functionalized ION-Micelles (FibPep-ION-Micelles). To summarize, the data presented in **Chapter 5** underlines the potential of the ION-Micelles for sensitive MPI and MRI and warrants further evaluation of the FibPep-ION-Micelle nanoplatform for noninvasive MPI and MRI of pathological fibrin deposition *in vivo*.

In a subsequent study, FibPep-ION-Micelles were evaluated for the noninvasive detection of thrombosis using MPI and MRI (**Chapter 6**). Mice with carotid artery thrombosis were imaged by MRI pre and post injection of FibPep-ION-Micelles or the corresponding negative control NCFibPep-ION-Micelles. No significant difference in thrombus signal intensity was observed for FibPep- and NCFibPep-ION-Micelles. *Ex vivo* MPS measurements displayed significant increase in signal in the thrombosed carotid with respect to the noninjured contralateral carotid for both FibPep- and NCFibPep-ION-Micelles. However, FibPep-functionalisation did not lead to additional MPS signal in the thrombus with respect to the negative control-functionalized ION-Micelles. This nonspecific uptake of the ION-Micelles, which hampers specific imaging of fibrin deposition in the thrombus, was attributed to nanoparticle trapping in the thrombus mesh.

In conclusion, ION-Micelles might allow noninvasive detection of thrombosis using MPI by nonspecific entrapment of nanoparticles in the thrombus, regardless of peptide functionalization. Future *in vivo* MPI studies in rodent thrombosis models using the ION-Micelle nanoplatform and small-animal MPI scanners are ideally suited to further gauge the potential of the ION-Micelles for thrombus diagnostics using MPI. In addition, the fibrin-specific FibPep-ION-Micelle platform might still be of value for MPI and MRI of fibrin deposition in pathologies such as atherosclerosis and Alzheimer's disease, which do not involve large intravascular thrombi and therefore likely display lower levels of nonspecific nanoparticle entrapment.

8.3 Fe- and ^{89}Zr-labeled fibrin-binding polymeric micelles for bimodal PET/MR imaging of fibrin

Simultaneous PET/MR imaging, which combines the high sensitivity of PET and the superb soft tissue contrast of MRI, has been a topic of extensive research in the past decade.[29-31] In **Chapter 7,** we developed a fibrin-specific dual modal PET/MR nanoparticulate contrast agent (FibPep-^{89}Zr/Fe-DFO-micelles) that allows quantification and whole body screening of fibrin deposition using PET and high resolution characterization of these identified fibrin deposits using MRI. The developed contrast agent consists of amphiphilic diblock copolymers which are functionalized with the fibrin-binding peptide FibPep for targeting purposes, and equipped with ^{89}Zr-deferoxamine (^{89}Zr-DFO) and Fe^{3+}-deferoxamine (Fe-DFO) to provide PET signal and MRI contrast, respectively. Zirconium-89 displays excellent PET imaging characteristics with a 3 days half-life suitable for imaging (long circulating) nanoparticulate tracers. For T_1-MR contrast purposes, the nanoparticles were modified with Fe-DFO instead of the commonly used gadolinium-containing chelates. This approach avoids any potential gadolinium-related toxicity that may result from nanoparticle retention and degradation in excretory organs, thus significantly increasing the potential for clinical translation. To gauge the suitability of the FibPep-^{89}Zr/Fe-DFO-micelles for fibrin-specific PET/MRI, FibPep-^{89}Zr/Fe-DFO-micelles and the corresponding negative control NCFibPep-^{89}Zr/Fe-DFO-micelles were employed in an *in vitro* thrombus targeting experiment. FibPep-^{89}Zr/Fe-DFO-micelles bound in a specific fashion to human thrombi *in vitro* and allowed visualization of this specific uptake using PET and positive contrast, T_1-weighted MR imaging. Therefore, the FibPep-^{89}Zr/Fe-DFO-micelles show high potential for molecular PET/MR imaging of fibrin deposition.

Future studies should assess the *in vivo* blood kinetic and distribution profiles of the FibPep-^{89}Zr/Fe-DFO-micelles, as well as evaluate the potential for PET/MR imaging by employing animal models of diseases in which fibrin deposition plays an important role, such as atherosclerosis, cancer and Alzheimer's disease. In addition, the FibPep-^{89}Zr/Fe-DFO-micelles may also be employed for theranostic purposes, as the polybutadiene core of the polymeric micelles can be loaded with hydrophobic drugs such as paclitaxel. Such fibrin-targeted and drug-loaded ^{89}Zr/Fe-DFO-micelles might be suitable to deliver therapeutics to, for instance, solid tumors which frequently display a fibrin-rich tumor stroma,[32] while allowing visualization of this drug delivery process using PET/MR imaging.

8.4 References

1. Knight, L. C. Non-oncologic applications of radiolabeled peptides in nuclear medicine. *Q J Nucl Med* **2003,** *47*, (4), 279-91.

2. Weiner, R. E.; Thakur, M. L. Radiolabeled peptides in diagnosis and therapy. *Semin Nucl Med* **2001,** *31*, (4), 296-311.

3. Overoye-Chan, K.; Koerner, S.; Looby, R. J.; Kolodziej, A. F.; Zech, S. G.; Deng, Q.; Chasse, J. M.; McMurry, T. J.; Caravan, P. EP-2104R: a fibrin-specific gadolinium-Based MRI contrast agent for detection of thrombus. *J Am Chem Soc* **2008,** *130*, (18), 6025-39.

4. Makowski, M. R.; Forbes, S. C.; Blume, U.; Warley, A.; Jansen, C. H.; Schuster, A.; Wiethoff, A. J.; Botnar, R. M. In vivo assessment of intraplaque and endothelial fibrin in ApoE(-/-) mice by molecular MRI. *Atherosclerosis* **2012,** *222*, (1), 43-9.

5. Sirol, M.; Fuster, V.; Badimon, J. J.; Fallon, J. T.; Moreno, P. R.; Toussaint, J. F.; Fayad, Z. A. Chronic thrombus detection with in vivo magnetic resonance imaging and a fibrin-targeted contrast agent. *Circulation* **2005,** *112*, (11), 1594-600.

6. Spuentrup, E.; Buecker, A.; Katoh, M.; Wiethoff, A. J.; Parsons, E. C., Jr.; Botnar, R. M.; Weisskoff, R. M.; Graham, P. B.; Manning, W. J.; Gunther, R. W. Molecular magnetic resonance imaging of coronary thrombosis and pulmonary emboli with a novel fibrin-targeted contrast agent. *Circulation* **2005,** *111*, (11), 1377-82.

7. Spuentrup, E.; Katoh, M.; Buecker, A.; Fausten, B.; Wiethoff, A. J.; Wildberger, J. E.; Haage, P.; Parsons, E. C., Jr.; Botnar, R. M.; Graham, P. B.; Vettelschoss, M.; Gunther, R. W. Molecular MR imaging of human thrombi in a swine model of pulmonary embolism using a fibrin-specific contrast agent. *Invest Radiol* **2007,** *42*, (8), 586-95.

8. Spuentrup, E.; Katoh, M.; Wiethoff, A. J.; Parsons, E. C., Jr.; Botnar, R. M.; Mahnken, A. H.; Gunther, R. W.; Buecker, A. Molecular magnetic resonance imaging of pulmonary emboli with a fibrin-specific contrast agent. *Am J Respir Crit Care Med* **2005,** *172*, (4), 494-500.

9. Uppal, R.; Medarova, Z.; Farrar, C. T.; Dai, G.; Moore, A.; Caravan, P. Molecular imaging of fibrin in a breast cancer xenograft mouse model. *Invest Radiol* **2012,** *47*, (10), 553-8.

10. Spuentrup, E.; Botnar, R. M.; Wiethoff, A. J.; Ibrahim, T.; Kelle, S.; Katoh, M.; Ozgun, M.; Nagel, E.; Vymazal, J.; Graham, P. B.; Gunther, R. W.; Maintz, D. MR imaging of thrombi using EP-2104R, a fibrin-specific contrast agent: initial results in patients. *Eur Radiol* **2008,** *18*, (9), 1995-2005.

11. Vymazal, J.; Spuentrup, E.; Cardenas-Molina, G.; Wiethoff, A. J.; Hartmann, M. G.; Caravan, P.; Parsons, E. C., Jr. Thrombus imaging with fibrin-specific gadolinium-based MR contrast agent EP-2104R: results of a phase II clinical study of feasibility. *Invest Radiol* **2009,** *44*, (11), 697-704.

12. Kribben, A.; Witzke, O.; Hillen, U.; Barkhausen, J.; Daul, A. E.; Erbel, R. Nephrogenic systemic fibrosis: pathogenesis, diagnosis, and therapy. *J Am Coll Cardiol* **2009,** *53*, (18), 1621-8.

13. Starmans, L. W.; van Duijnhoven, S. M.; Rossin, R.; Aime, S.; Daemen, M. J.; Nicolay, K.; Grull, H. SPECT imaging of fibrin using fibrin-binding peptides. *Contrast Media Mol Imaging* **2013,** *8*, (3), 229-37.

14. Starmans, L. W.; van Duijnhoven, S. M.; Rossin, R.; Berben, M.; Aime, S.; Daemen, M. J.; Nicolay, K.; Grull, H. Evaluation of 111In-labeled EPep and FibPep as tracers for fibrin SPECT imaging. *Mol Pharm* **2013,** *10*, (11), 4309-21.

15. Paul, J.; Strickland, S.; Melchor, J. P. Fibrin deposition accelerates neurovascular damage and neuroinflammation in mouse models of Alzheimer's disease. *J Exp Med* **2007,** *204*, (8), 1999-2008.

16. Giron, M. C.; Portolan, S.; Bin, A.; Mazzi, U.; Cutler, C. S. Cytochrome P450 and radiopharmaceutical metabolism. *Q J Nucl Med Mol Imaging* **2008,** *52*, (3), 254-66.

17. Werle, M.; Bernkop-Schnurch, A. Strategies to improve plasma half life time of peptide and protein drugs. *Amino Acids* **2006,** *30*, (4), 351-67.

18. Zhang, Z.; Kolodziej, A. F.; Qi, J.; Nair, S. A.; Wang, X.; Case, A. W.; Greenfield, M. T.; Graham, P. B.; McMurry, T. J.; Caravan, P. Effect of Peptide-Chelate Architecture on Metabolic Stability of Peptide-based MRI Contrast Agents. *New J Chem* **2010,** *2010*, (34), 611-616.

19. Ay, I.; Blasi, F.; Rietz, T. A.; Rotile, N. J.; Kura, S.; Brownell, A. L.; Day, H.; Oliveira, B. L.; Looby, R. J.; Caravan, P. In vivo molecular imaging of thrombosis and thrombolysis using a fibrin-binding positron emission tomographic probe. *Circ Cardiovasc Imaging* **2014,** *7*, (4), 697-705.

20. Blasi, F.; Oliveira, B. L.; Rietz, T. A.; Rotile, N. J.; Day, H.; Looby, R. J.; Ay, I.; Caravan, P. Effect of Chelate Type and Radioisotope on the Imaging Efficacy of 4 Fibrin-Specific PET Probes. *J Nucl Med* **2014,** *55*, (7), 1157-1163.

21. Boros, E.; Rybak-Akimova, E.; Holland, J. P.; Rietz, T.; Rotile, N.; Blasi, F.; Day, H.; Latifi, R.; Caravan, P. Pycup-A Bifunctional, Cage-like Ligand for (64)Cu Radiolabeling. *Mol Pharm* **2014,** *11*, (2), 617-29.

22. Ciesienski, K. L.; Yang, Y.; Ay, I.; Chonde, D. B.; Loving, G. S.; Rietz, T. A.; Catana, C.; Caravan, P. Fibrin-targeted PET probes for the detection of thrombi. *Mol Pharm* **2013,** *10*, (3), 1100-10.

23. Uppal, R.; Catana, C.; Ay, I.; Benner, T.; Sorensen, A. G.; Caravan, P. Bimodal thrombus imaging: simultaneous PET/MR imaging with a fibrin-targeted dual PET/MR probe--feasibility study in rat model. *Radiology* **2011,** *258*, (3), 812-20.

24. Durack, J. C.; Hope, T. A.; Seo, Y.; Saeed, M.; He, J.; Wilson, M. W.; Kerlan, R. K., Jr.; Ring, E. J. Intravenous vasopressin for the prevention of nontarget gastrointestinal embolization during liver-directed cancer treatment: experimental study in a porcine model. *J Vasc Interv Radiol* **2012,** *23*, (11), 1505-12.

25. Heiba, S. I.; Kolker, D.; Mocherla, B.; Kapoor, K.; Jiang, M.; Son, H.; Rangaswamy, B.; Kostakoglu, L.; Savitch, I.; DaCosta, M.; Machac, J. The optimized evaluation of diabetic foot infection by dual isotope SPECT/CT imaging protocol. *J Foot Ankle Surg* **2010,** *49*, (6), 529-36.

26. Hijnen, N. M.; de Vries, A.; Nicolay, K.; Grull, H. Dual-isotope 111In/177Lu SPECT imaging as a tool in molecular imaging tracer design. *Contrast Media Mol Imaging* **2012,** *7*, (2), 214-22.

27. Gleich, B.; Weizenecker, J. Tomographic imaging using the nonlinear response of magnetic particles. *Nature* **2005,** *435*, (7046), 1214-7.

28. Starmans, L. W.; Burdinski, D.; Haex, N. P.; Moonen, R. P.; Strijkers, G. J.; Nicolay, K.; Grull, H. Iron oxide nanoparticle-micelles (ION-micelles) for sensitive (molecular) magnetic particle imaging and magnetic resonance imaging. *PLoS One* **2013,** *8*, (2), e57335.

29. Pichler, B. J.; Judenhofer, M. S.; Wehrl, H. F. PET/MRI hybrid imaging: devices and initial results. *Eur Radiol* **2008,** *18*, (6), 1077-86.

30. Pichler, B. J.; Wehrl, H. F.; Kolb, A.; Judenhofer, M. S. Positron emission tomography/magnetic resonance imaging: the next generation of multimodality imaging? *Semin Nucl Med* **2008,** *38*, (3), 199-208.

31. Sauter, A. W.; Wehrl, H. F.; Kolb, A.; Judenhofer, M. S.; Pichler, B. J. Combined PET/MRI: one step further in multimodality imaging. *Trends Mol Med* **2010,** *16*, (11), 508-15.

32. Yasunaga, M.; Manabe, S.; Matsumura, Y. New concept of cytotoxic immunoconjugate therapy targeting cancer-induced fibrin clots. *Cancer Sci* **2011,** *102*, (7), 1396-402.

Acknowledgements

This thesis is the result of more than 4 years of highly collaborative research and a lot of fun. This is the opportunity for me to give some shout outs to the people who have helped me along the way. Without further ado:

Herr Prof. Dr. H. Grüll (also known as Holger), how on earth can I thank you in just a few sentences? Let's try anyway: I simply could not have wished for a better supervisor, confidant and colleague. Whatever the situation, you always were willing to make time, something I really have appreciated. I am still amazed by your passion and scientific knowledge (you are truly a human Wikipedia). However, perhaps one of the things I cherished most is your willingness to teach us about the "real world", e.g. politics, strategy and things along those lines. Your openness and frank honesty in these matters has been very, very insightful! Furthermore, I have really enjoyed the freezing and non-electrifying atmosphere in the dark and snowy woods of Cochem and our discussions regarding "delicate matters" over ~~a few~~ margaritas in Savannah. I promise you that I will never be "negative" again, and I am sure that you are extremely proud that I have managed to insert some pink-like colors throughout this thesis. I wish you all the best in your future endeavors and hopefully our paths cross again in the future! Tschüss.

Prof. Klaas Nicolay, your course on molecular imaging initiated my interest in this field of research. The past 7 years in your group have been a very valuable and enjoyable experience. Thank you so much for all your advice, suggestions and guidance and I wish you all the best in the final years of your scientific career. I also would like to thank the other committee members: **Prof. Mat Daemen,** thank you for the collaboration in the PARISk project and for your valuable input regarding this thesis. **Prof. Jeff Bulte,** the time I have spent in Baltimore as a member of your group has been truly a once in a lifetime experience. Thank you for the collaboration on the iron oxide nanoparticles for MPI and for your willingness to cross the big pond to participate in my PhD committee. **Prof. Silvio Aime,** thank you so much for all the advice regarding the fibrin-binding peptides. It is true honor for me to have you on my committee. I also would like to thank you for the enjoyable time in Torino during the EMMI intensive course (and for the wine tasting in Piedmont of course!). I also would like to thank **Prof. Otto Boerman** and **Prof. Luc Brunsveld** for their willingness to take a seat in my PhD committee.

Now on to the "Philips/CPV colleagues": **Caren, Carlijn, Marleen, Marije, Melanie** and **Monique,** without your help this thesis would definitely not exist. Thank you so much for all the injections, surgeries, biodistributions etc. etc. etc. Most importantly: thank you for all the fun during the experimental work, your presence made doing the experiments a lot more entertaining ☺ I also would like to thank **Iris** for her essential support regarding the in vivo experiments and the DEC proposals. **Jo,** thank you for your help with the DEC proposals and for making me feel like an old man during our cycling trip. **Raffa,** thank you for your help regarding anything radioactive and for investing a lot of time in revising all the manuscripts which I have sent to you during the past few years. You have really been

a tremendous help! I will always remember your subtle and very kind emails to remind everyone *TO CLEAN THEIR F****NG MESS IN THE RC-LAB!!!!!!!!!!!!!!!!* **Tilman,** thank you for your help with radioactive deliveries and for making me feel bad during bootcamp. **Katia,** thanks so much for all the help with the PET, SPECT/CT and image analysis. I have really enjoyed our discussions regarding (meat)balls. **Suzanne,** thank you for keeping me radioactivity free and for all the emergency help during SPECT/CT crashes. I would like to thank **Sandra** for her support regarding cell culture, **Rolf** for the help with MR measurements and **Erica, Nicole Haex** and **Dirk Burdinski** for all their support regarding iron oxide nanoparticle synthesis. **Sander Langereis,** thank you for your advice regarding figures and for your kind willingness to always let me interrupt your (very frequent) meetings with Holger. I would like to thank **Edwin, Aaldert, Charles, Johan, Marc Robillard, René Aarnink, Wilma, Matthias, Jeannette, Monja, Peter, Jeroen, Hugo, René Beerends, Dirk Roos, Gerry** and **Frenk** for all their help, support and advice during the past few years.

I would like to take the opportunity to thank the people in the Biomedical NMR group: **Rik,** thank you for the studies we performed together in the PARISk project and for always reminding me when I was about to forget a deadline. Enjoy the married life! **Igor,** also known as beer-moustache, we have known each other a long time. I fondly remember your appetite for strawberry vodka, your special way of feeding the fish around Key West, our American Football attempts and the parties in the Federal Hill district and of course the Shampoo Club in Philly. Thank you for being my paranymph and good luck with finishing the final bits of your PhD! **Bart,** thank you for trying to make me a little bit more muscular. One day I hope to lift the same amount of weights that you do. **Marloes, Miranda** and **Tom,** thank you for all the sports activities! **Erik** and **Maarten,** thank you for your excellent supervision during my first few years in the Biomedical NMR group, you guys have laid the foundation for the work in my PhD thesis. I would like to thank **Gustav** for his input in this thesis. Good luck with your new group in Amsterdam! **Stefanie,** I want to wish you all the best in the big apple! I also want to thank **Jos** and **Shikha** for their help as interns working on the iron oxide project. **Marcus Hummelink,** you were my first and final Master student. You did an excellent job, especially considering the (lack of) supervision and the fact that you also had to spend a lot of time on the world championship rowing team. I am sure you are able to get this big consulting job after you have received your MSc-degree! **Sharonneke, Jeanine, Desiree, Abdallah, Valentina, Katrien, Floortje, Wolter, Siem, Jules, Leonie Niesen, Larry, David, Leonie Paulis, Tessa, Ot, Martijn, Richard, Bastiaan, Roel, Glenda** and all other (ex)-Biomedical NMR group members and students: thank you for making my time in this group a joy.

I would like to thank **Judith Sluimer, Eline Kooi** and **Sylvia Heeneman** for their collaboration in the PARISk project. Furthermore I would like to thank **Nico Sommerdijk** and **Paul Bomans** for giving me the opportunity to perform cryo-TEM measurements at their facilities. I also would like to thank **Jürgen Rahmer** for the *in vitro* MPI measurements in Hamburg and **Enzo Terreno**, **Lorenzo Tei** and **Mauro Botta** for the collaboration regarding nanoparticles for MRI.

Now it is time to thank my fellow PhD-students: **Anke,** thank you for helping me along in the first few years of my PhD. You really deserve the title “Mother of all AIOs”. **Mariska,** thank you for all the fun

and sorry for always bruising your shins while playing soccer. **Zanderrr**, also known as heisse weisse fish, thank you for helping me quite a bit with the peptides and with the first publication! Good luck in Nijmegen and with TagWorks. **Esther,** thank you for being the kindest roommate ever and for all the delicious baked stuff you brought over the years. Will you also bring them to my new workplace? **Pedro,** also known as Mr. Piglet**,** thank you for bringing the much needed male-spirit in our room. I enjoyed our trip to Dublin (not sure whether you can remember the evenings ;)) and thank you for all the advice regarding buying flowers. All the best @ Maastro! **Tiemen,** I really enjoyed our trip to Tennessee, Georgia and the Carolina's. The Ford Mustang was really cool! I also want to thank you for putting our hotel room on fire. Good luck with finishing your PhD! **Sin Yuin Yeo,** my sincere apologies for all my silly jokes. I really have a lot of respect for how you have handled such a complex PhD-project. I am sure you will find a fantastic job, and otherwise I suggest you keep looking for this very, very rich prince on a white horse. **Sjteffie,** I really have enjoyed the time that you were a member of our team. I wish you all the best as a clinical physicist. Aan de slag! **Nicole,** you have truly been a fantastic (role) model during our years as roommates. Your work ethic, drive and ways to get things done are off the charts. I hereby officially nominate you to become the first female CEO of Philips. I really have enjoyed being your roommate, and I am very happy that you are one my paranymphs. I wish you, Hugo and Guus all the best going forward!

Mom and **Dad,** thank you for everything that you have done for me. I could not have wished for better parents and for a better youth, and I want to thank you for always supporting me! **Laurens** and **Christopher,** thank you for being my little lovely brothers and for giving me the opportunity to develop my leadership skills ever since our youth. I realize that it took me a few years to learn that total dictatorship is (unfortunately) not the way to go. However, the forest is still mine. **Merel** and **Dionne**, thank you for being my unofficial sisters-in-law. I don't know how you can cope with those two guys and therefore I wish you both good luck. I also want to thank **Frans, Lyan** and **Marjolijn** for having me for already almost 10 years.

Last but definitely not least: **Hanneke,** you mean the world to me. Let's grow old together.

Development and Preclinical Validation of Molecular and Nanoparticulate Probes for Imaging of Fibrin

Summary

Fibrin is a main building block of thrombi, which are the underlying cause in a variety of cardiovascular diseases, such as myocardial infarction, ischemic stroke and deep venous thrombosis. Furthermore, fibrin deposition in atherosclerotic lesions has been shown to correlate to plaque progression. In addition, fibrin deposition characterizes a variety of malignant tumors. Fibrin deposition induces formation of tumor stroma and provides a scaffold that facilitates tumor angiogenesis and storage of growth factors within the tumor. The significant role of fibrin in these disease processes motivates efforts in the development of imaging probes that allow noninvasive visualization of pathological fibrin deposition *in vivo* (**Chapter 1**). In this thesis, several novel strategies to noninvasively visualize fibrin deposition have been developed.

In **Chapter 2**, a novel ^{111}In-labeled fibrin-binding peptide (FibPep) was developed. FibPep showed enhanced binding compared to negative control NCFibPep to both fibrin and blood clots *in vitro*. FibPep bound to fibrin with a dissociation constant (Kd) of 0.8 µM, whereas NCFibPep displayed at least a 100-fold lower fibrin-affinity. A $FeCl_3$-induced carotid artery thrombosis mouse model was employed to evaluate the peptides. *In vivo* single photon emission computed tomography (SPECT) imaging using FibPep allowed clear visualization of thrombi. *Ex vivo* biodistribution showed significantly increased uptake of FibPep in the thrombus-containing carotid in comparison to the noninjured carotid, whereas NCFibPep did not. In conclusion, FibPep displayed high affinity towards fibrin *in vitro* and allowed sensitive detection of thrombi using SPECT imaging. Hence, this particular imaging approach may provide a new tool to diagnose and monitor diseases such as thrombosis and cancer.

In **Chapter 3**, we developed EPep, an ^{111}In-labeled fibrin-binding tracer based on the clinically verified EP-2104R peptide, and sought to compare the potential of EPep and FibPep as tracers for fibrin SPECT imaging. Both peptide probes displayed similar metabolic stability and comparable affinities toward human and mouse derived fibrin (Kd ≈ 1 µM), and similarly to FibPep, EPep showed fast blood clearance, low nontarget uptake and high thrombus uptake in a mouse carotid thrombosis model. Furthermore, EPep showed a similar affinity toward rat derived fibrin, displayed high thrombus uptake in a rat carotid thrombosis model and allowed sensitive detection of thrombosis in rats using SPECT. In contrast, FibPep displayed lower affinity toward rat derived fibrin (Kd ≈ 14 µM) and low uptake in rat thrombi and did not allow SPECT visualization of rat carotid thrombosis. In conclusion, both peptides showed similar metabolic stability and affinity toward human and mouse derived fibrin, and displayed high thrombus uptake in a mouse thrombosis model. Therefore, both EPep and FibPep are promising tracers for translation into clinical settings to serve as novel tools for imaging of fibrin deposition.

EPep was also evaluated for SPECT imaging of fibrin deposition in cancer (**Chapter 4**). SPECT imaging of tumor-bearing mice injected with EPep allowed visualization of tumor fibrin deposits, whereas mice injected with negative control NCEPep did not show increased tumor SPECT signal. *Ex vivo* biodistribution showed significantly increased uptake of EPep in the tumor with respect to NCEPep. In addition, EPep localization within the tumor correlated with the presence of fibrin, as assessed by immunohistochemistry. In conclusion, EPep allowed specific visualization of fibrin deposition in a preclinical cancer model and therefore holds promise for clinical translation in oncologic settings.

In **Chapter 5**, a fibrin-binding contrast agent for magnetic particle imaging (MPI) and magnetic resonance imaging (MRI) was developed. MPI is able to directly visualize magnetic particles and could serve as a more sensitive and quantitative alternative to MRI. Commercially available contrast agents that are currently being employed are not optimized for MPI, preventing MPI from reaching optimal resolution and sensitivity. In this study, we developed an iron oxide nanoparticle micelle platform (ION-Micelle), containing iron oxide cores of 25 nm, for MPI purposes. ION-Micelles induced up to 200 times higher signal in magnetic particle spectrometry (MPS) measurements than commercially available iron oxide formulations and thus likely allow for more sensitive MPI. In addition, the potential of the ION-Micelles for molecular MPI and MRI was demonstrated by MPS and MRI measurements of FibPep functionalized ION-Micelles (FibPep-ION-Micelles) bound to blood clots. In conclusion, the presented data underlines the potential of the ION-Micelles for sensitive MPI and warrants further investigation of the FibPep-ION-Micelle platform for noninvasive imaging of pathological fibrin deposition *in vivo*.

FibPep-ION-Micelles were subsequently evaluated for detection of thrombosis using MPI/MRI (**Chapter 6**). Mice with carotid artery thrombosis were imaged pre- and post-injection of FibPep-ION-Micelles or negative control NCFibPep-ION-Micelles by MRI. No significant difference in signal intensity was observed for FibPep- and NCFibPep-ION-Micelles. *Ex vivo* MPS measurements showed for both groups a significant increase in signal in the thrombosed carotid with respect to the noninjured, contralateral carotid. However, FibPep-functionalization did not lead to additional accumulation in the thrombus with respect to the negative control. Nonspecific uptake was attributed to trapping of nanoparticles in the thrombus mesh, and thus specific imaging of fibrin deposition in the thrombus is hampered by this nonspecific component. In conclusion, nonfunctionalized ION-Micelles might be suitable for noninvasive detection of thrombosis using MPI by nonspecific thrombus entrapment of nanoparticles.

Simultaneous positron emission tomography (PET)/MR imaging, which allows combining the high sensitivity of PET and the high spatial resolution of MRI, has been a topic of extensive research in the past decade. To fully exploit the potential of PET/MRI, we have developed a fibrin-binding bimodal nanoparticulate contrast agent (**Chapter 7**). Polymeric micelles were synthesized via thin-film hydration and labeled with Fe^{3+} for positive MRI contrast and ^{89}Zr for PET imaging. FibPep-$^{89}Zr/Fe^{3+}$-micelles bound in a specific fashion to human thrombi *in vitro* and allowed visualization of this specific uptake using PET and positive contrast, T_1-weighted MR imaging. Therefore, the FibPep-$^{89}Zr/Fe^{3+}$-micelles show high potential for molecular PET/MR imaging of fibrin deposition in disease.

Finally, **Chapter 8** provides a summarizing discussion of the work presented in this thesis.

List of publications

Full papers

1. **Starmans, L. W.**; van Duijnhoven, S. M.; Rossin, R.; Berben, M.; Aime, S.; Daemen, M. J.; Nicolay, K.; Grull, H. Evaluation of ^{111}In-labeled EPep and FibPep as tracers for fibrin SPECT imaging. *Mol Pharm* 2013**,** *10*, (11), 4309-21.
2. **Starmans, L. W.**; Burdinski, D.; Haex, N. P.; Moonen, R. P.; Strijkers, G. J.; Nicolay, K.; Grull, H. Iron oxide nanoparticle-micelles (ION-micelles) for sensitive (molecular) magnetic particle imaging and magnetic resonance imaging. *PLoS One* 2013**,** *8*, (2), e57335.
3. **Starmans, L. W.**; van Duijnhoven, S. M.; Rossin, R.; Aime, S.; Daemen, M. J.; Nicolay, K.; Grull, H. SPECT imaging of fibrin using fibrin-binding peptides. *Contrast Media Mol Imaging* 2013**,** *8*, (3), 229-37.
4. Geelen, T.; Yeo, S. Y.; Paulis, L. E.; **Starmans, L. W.**; Nicolay, K.; Strijkers, G. J. Internalization of paramagnetic phosphatidylserine-containing liposomes by macrophages. *J Nanobiotechnology* 2012**,** *10*, 37.
5. Paulis, L. E.; Jacobs, I.; van den Akker, N. M.; Geelen, T.; Molin, D. G.; **Starmans, L. W.**; Nicolay, K.; Strijkers, G. J. Targeting of ICAM-1 on vascular endothelium under static and shear stress conditions using a liposomal Gd-based MRI contrast agent. *J Nanobiotechnology* 2012**,** *10*, 25.
6. **Starmans, L. W.**; Kok, M. B.; Sanders, H. M.; Zhao, Y.; Donega Cde, M.; Meijerink, A.; Mulder, W. J.; Grull, H.; Strijkers, G. J.; Nicolay, K. Influence of cell-internalization on relaxometric, optical and compositional properties of targeted paramagnetic quantum dot micelles. *Contrast Media Mol Imaging* 2011**,** *6*, (2), 100-9.
7. **Starmans, L. W.**; van Mourik, T.; Rossin, R.; Verel, I.; Nicolay, K.; Grull, H. Noninvasive visualization of tumoral fibrin deposition using a peptidic fibrin-binding single photon emission computed tomography tracer. *Under review.*
8. **Starmans, L. W.**;* Moonen, R. P.;* Aussems-Custers, E.; Daemen, M. J.; Strijkers, G. J.; Nicolay, K.; Grull, H. Evaluation of fibrin-binding iron oxide nanoparticle micelles (FibPep-ION-Micelles) for magnetic resonance imaging (MRI) and magnetic particle imaging (MPI) of thrombosis. *Under review.*
9. Moonen, R. P.; van der Tol, P.; Hectors, S. J.; **Starmans, L. W.**; Nicolay, K.; Strijkers, G. J. Spin-Lock MR enhances the detection sensitivity of superparamagnetic iron oxides particles. *Under review.*
10. **Starmans, L. W.**;* Hummelink, M. A.;* Rossin, R.; Kneepkens, E. C.; Lamerichs, R.; Donato, K.; Moonen, R. P.; Nicolay, K.; Grull, H. ^{89}Zr- and Fe-labeled polymeric micelles for dual modality (molecular) PET and T_1-weighted MR imaging. *In preparation*.
11. **Starmans, L. W.**; Rossin, R.; Nicolay, K.; Grull, H. Nuclear imaging strategies for visualization of fibrin deposition in disease: a comprehensive review. *In preparation.*

*Auhors contributed equally

Conference proceedings (first author only)

1. **Starmans, L. W.**; Hummelink, M. A.; Rossin, R.; Donato, K.; Moonen, R. P.; Daemen, M. J.; Nicolay, K.; Grull, H. Molecular PET/MR imaging of fibrin deposition using ^{89}Zr- and Fe^{3+}-labeled micelles. *European Molecular Imaging Meeting*, 2014, Antwerp, Belgium.
2. **Starmans, L. W.**; van Duijnhoven, S. M.; Rossin, R.; Aime, S.; Daemen, M. J.; Nicolay, K.; Grull, H. Evaluation of ^{111}In-labeled EPep and FibPep as tracers for fibrin SPECT imaging. *World Molecular Imaging Congress,* 2013, Savannah, GA, USA.
3. **Starmans, L. W.**; van Duijnhoven, S. M.; Rossin, R.; Aime, S.; Daemen, M. J.; Nicolay, K.; Grull, H. Molecular imaging of fibrin with SPECT using ^{111}In-labeled fibrin-binding peptides. *World Molecular Imaging Congress,* 2012, Dublin, Ireland.
4. **Starmans, L. W.**; Burdinski, D.; Haex, N. P.; Moonen, R. P.; Nicolay, K.; Grull, H. Synthesis, characterization and application of iron oxide nanoparticle-micelles (ION-Micelles) for sensitive molecular magnetic particle imaging (MPI) and magnetic resonance imaging (MRI). *World Molecular Imaging Congress,* 2012, Dublin, Ireland.
5. **Starmans, L. W.**; van Duijnhoven, S. M.; Rossin, R.; Aime, S.; Daemen, M. J.; Nicolay, K.; Grull, H. SPECT imaging of fibrin using fibrin-binding peptides. *Center for Translational Molecular Medicine (CTMM) Annual Meeting,* 2012, Utrecht, the Netherlands.
6. **Starmans, L. W.**; Burdinski, D.; Haex, N. P.; Moonen, R. P.; Strijkers, G. J.; Nicolay, K.; Grull, H. Iron oxide nanoparticle-micelles for sensitive molecular magnetic resonance imaging (MRI) and magnetic particle imaging (MPI). *Center for Translational Molecular Medicine (CTMM) Annual Meeting,* 2012, Utrecht, the Netherlands.
7. **Starmans, L. W.**; van Duijnhoven, S. M.; Nicolay, K.; Grull, H. SPECT imaging of thrombi using fibrin-binding peptides. *European Molecular Imaging Meeting*, 2011, Leiden, the Netherlands.
8. **Starmans, L. W.**; van Duijnhoven, S. M.; Rossin, R.; Aime, S.; Daemen, M. J.; Nicolay, K.; Grull, H. SPECT imaging of thrombi using fibrin-binding peptides. *Dutch Clinical Radiochemistry Society Meeting,* 2011, Groningen, the Netherlands.
9. **Starmans, L. W.**; van Duijnhoven, S. M.; Rossin, R.; Aime, S.; Daemen, M. J.; Nicolay, K.; Grull, H. SPECT imaging of thrombi using fibrin-binding peptides. *Center for Translational Molecular Medicine (CTMM) Annual Meeting,* 2011, Utrecht, the Netherlands.
10. **Starmans, L. W.**; Kok, M. B.; Sanders, H. M.; Zhao, Y.; Donega Cde, M.; Meijerink, A.; Mulder, W. J.; Grull, H.; Strijkers, G. J.; Nicolay, K. Influence of cell-internalization on relaxometric, optical and compositional properties of targeted paramagnetic quantum dot micelles. *12th Bi-Annual Conference on Contrast Agents and Multimodal Molecular imaging*, 2010, Mons, Belgium.
11. **Starmans, L. W.**; Kok, M. B.; Sanders, H. M.; Zhao, Y.; Donega Cde, M.; Meijerink, A.; Mulder, W. J.; Grull, H.; Strijkers, G. J.; Nicolay, K. Influence of cell-internalization on relaxometric, optical and compositional properties of targeted paramagnetic quantum dot micelles. *Benelux ISMRM Chapter Meeting,* 2010, Utrecht, the Netherlands.

Curriculum Vitae

Luc Starmans was born April 5th, 1986 in Heerlen, the Netherlands. He grew up in Schimmert, the Netherlands and completed his pre-university education (VWO) in 2004 at the Stella Maris College in Meerssen, the Netherlands. He started studying Biomedical Engineering at the Eindhoven University of Technology (TU/e) in 2004 and obtained his Bachelor of Science degree (*cum laude*) in 2007 and his Master of Science degree (with great appreciation) in 2010. During this period, he was a student member of the Biomedical Engineering Faculty Council. In addition, he was a teaching assistant for several courses in the Biomedical Engineering curriculum. Also, he was an organizing committee member of the "Cells Out of Control" scientific conference, hosted by the Protagoras study association of Biomedical Engineering (TU/e). He worked as a junior researcher in the lab of Prof. Klaas Nicolay (TU/e) on the development of nanoparticulate MR contrast agents. Furthermore, he performed a scientific internship in the group of Prof. Jeff Bulte at the Johns Hopkins University (Baltimore, MD, USA) and during this period he worked on the development of a reporter gene methodology to allow optical imaging of stem cell differentiation. His master thesis project at the Biomedical NMR group of Prof. Klaas Nicolay (TU/e) focused on the effect of cellular uptake on paramagnetic quantum dot micelles with respect to their properties for MR and optical molecular imaging.

Subsequently, he started his Ph.D. project under the supervision of prof. Holger Grüll in the Biomedical NMR group at the TU/e, in collaboration with the Oncology Solutions department at Philips Research Eindhoven. During this period he developed multiple molecular and nanoparticulate contrast agents for fibrin-specific molecular imaging with nuclear, magnetic resonance and magnetic particle imaging techniques. The principal results of this research are described in this dissertation. In addition, he participated in the *European Master in Molecular Imaging (EMMI) Intensive Programme "Design, Synthesis and Validation of Imaging Probes"* at the group of Prof. Silvio Aime (University of Torino, Italy). The Ph.D. project was part of the *Assessment of Plaque at Risk by Non-invasive (Molecular) Imaging and Modeling* (PARISk) project of the Center for Translational Molecular Medicine (CTMM), which was supported by the Dutch Heart Foundation.